Algorithmic Design and Optimization for Quantum Computation with a Qubit-Oscillator System

by

Gabriel L. Mintzer

S.B. Physics and Computer Science and Engineering, Massachusetts Institute of Technology, 2021

Submitted to the Department of Electrical Engineering and Computer Science
in partial fulfillment of the requirements for the degree of

MASTER OF ENGINEERING IN ELECTRICAL ENGINEERING AND COMPUTER SCIENCE

at the

MASSACHUSETTS INSTITUTE OF TECHNOLOGY

May 2024

Authored by:	Gabriel L. Mintzer Department of Electrical Engineering and Computer Science May 10, 2024
Certified by:	Isaac L. Chuang Professor of Physics and Professor of EECS, Thesis Supervisor
Accepted by:	Katrina LaCurts Chair, Master of Engineering Thesis Committee

Algorithmic Design and Optimization for Quantum Computation with a Qubit-Oscillator System

by

Gabriel L. Mintzer

Submitted to the Department of Electrical Engineering and Computer Science
in partial fulfillment of the requirements for the degree of

MASTER OF ENGINEERING IN ELECTRICAL ENGINEERING AND COMPUTER SCIENCE

ABSTRACT

Quantum computation has long been dominated by a digital approach using the *qubit*, which exists in a two-dimensional vector space, as its basic unit. More recently, there has been increasing interest in an analog approach, which uses as its basic unit a *qudit* in an infinite-dimensional vector space. Alongside these two approaches is a third less-studied approach, that of combining digital and analog quantum computation. This approach is perhaps best exemplified by, and most researched via, the system of a qubit coupled to a quantum harmonic oscillator, which has been realized with many of the leading platforms for quantum computation. In this thesis, we ask how machine learning and other high-level computational techniques can be employed in the design of applications of a qubit-oscillator system to implementing fundamental components of quantum technology. In order to begin to answer this question and lay the groundwork for future investigation, both with this system and with others, we demonstrate the application of such high-level computational techniques toward addressing the problems of quantum compilation, quantum sensing, and quantum error-correction with the qubit-oscillator system.

Thesis supervisor: Isaac L. Chuang
Title: Professor of Physics and Professor of EECS

Acknowledgments

I made a remark in my Fall 2020 undergraduate thesis about how strange a semester that was, a sentiment with which I still agree; however, these past few years have somehow been even more unusual than that one. Alongside the ramp-down in policies for COVID-19 mitigation, there has also been the strangeness of returning to school and research after spending half of a year in the hospital recovering from being run over by a truck in November 2021 and suffering complications. Fortunately, I received incredible support from the MIT Office of Graduate Education (OGE), and I would particularly like to thank Ms. Elizabeth Guttenberg from this office, as well as Ms. Vera Sayzew and Dr. Katrina LaCurts from the Department of Electrical Engineering and Computer Science, for their invaluable assistance as I navigated this return to MIT after such an unusual period of medical leave. I am so incredibly grateful to have had the chance to return to MIT to complete the research comprising my master's degree so soon after such a traumatic experience, and I know that I owe this victory in large part to these wonderful administrators, my therapists at Spaulding Cambridge inpatient care and the Shirley Ryan AbilityLab inpatient and outpatient care while I was in recovery, and my supportive lab, whose members kept me in the loop throughout my entire recovery process.

In particular, from my lab, I would like to thank Dr. John Chiaverini, a senior staff member in the Quantum Information and Integrated Nanosystems Group at MIT Lincoln Laboratory, for our invaluable discussions about the capabilities of the improved quantum sensing scheme that we investigated, which is featured in this work; I am also very grateful for Dr. Chiaverini's constant support throughout my recovery process. Additionally, I also owe many thanks to Dr. Susanna Todaro, a former postdoctoral researcher in our lab now working at Oxford Ionics, for her contributions to such discussions, as well as for her unwavering acquisitiveness regarding my health, both physical and mental, as I returned to lab in Fall 2022. Additionally, I owe many thanks to Dr. Jules Stuart, who was my first mentor in the lab, initiating me into both the cryogenic and room-temperature trapped-ion experiments and fueling my interest in applications of microcontrollers in lab. More recently, he completed a PhD in atomic physics at MIT and postdoctoral research with NIST at the University of Colorado, Boulder, and is now working at IonQ; he has continued to be a great help, supporting me with discussions of potential PhD programs.

My closest collaborators on the research constituting this thesis have been graduate student Ms. Jasmine Sinanan-Singh and former postdoctoral researcher, now Assistant Professor of Electrical & Computer Engineering and Computer Science at North Carolina State University, Dr. Yuan Liu. Ms. Sinanan-Singh and I worked closely on the development of the algorithm for achieving universal quantum control on a continuous-variable quantum system

in a work from spring of 2021, the beginning of my degree program, featured in Chapter 3, and we also collaborated on two complementary aspects of the work on improved quantum sensing via the use of quantum signal processing, her mostly on the theory and myself mostly on the numerical optimization of the quantum signal processing phases with machine learning, as discussed in Chapter 4. Dr. Liu also assisted with theoretical aspects for both of these projects, and he and I have since also collaborated on laying the foundation of and beginning numerical optimization for bivariable control of a bosonic system with quantum signal processing, as discussed in Chapter 5. These collaborations have proven incredibly valuable as I have been developing my understanding of continuous-variable quantum computing and the optimization of quantum signal processing algorithms with machine learning.

Additionally, on the topic of collaborations, I have spent the last year of my master's degree studies in Tokyo, Japan, engaging in quantum-computational research at the Nippon Telegraph and Telephone Corporation (NTT). Although the work is not quite finished yet, I have sketched the current state of the research project in Chapter 6, and I would be remiss not to mention my meaningful collaborations at NTT. I owe many thanks to people with whom I have worked here, including but not limited to my unit's manager at NTT, Dr. Junji Teramoto, for his gracious support of my needs as a researcher in the unit and his kind encouragement; my manager in the Computer and Data Science Lab (C & D Lab) at NTT, Dr. Yuuki Tokunaga, who has supported my more lab-specific research needs and made me feel like a full member of the group; my colleague, Dr. Tomohiro Shitara, who has graciously worked alongside and supported me; and my direct research supervisor, Dr. Suguru Endō, who has introduced me to many new topics in quantum computation and approaches to research, constantly supporting my learning in this field and my growth as an independent researcher, in addition to organizing social activities to make me feel more like a part of a greater community. I would also like to thank some of the people who have made experience possible for me logistically—namely, Ms. Christine Pilcavage, the MIT Japan coordinator, who has provided me with support as I adjust to living in Japan for such an extended period of time and introduced me to many other MIT students who have also been in Japan for months-long terms with whom I can spend time; Ms. Noriko Hirai, a temporary assistant in the C & D Lab at NTT who helped me with logistics in the group and with coordinating my return to the US in March 2024 to visit PhD programs; and Ms. Mio Kobayashi, an assistant in the C & D Lab at NTT who has supported me for the entire duration of my journey in Japan, first helping me through the labyrinthine process of obtaining my visa to come to Japan for the year-long research internship, and then helping me learn the logistics of paying bills and make other long-term preparations in Japan. Lastly for my time at NTT, I would like to sincerely thank my Japanese II instructors from MIT, Okayasu-sensei and Maekawa-sensei. Without their excellent Japanese instruction, I would have struggled so much more as I adjusted to living in Japan; I only wish that I could have taken more Japanese courses with them. I have had such a fantastic experience working on research at NTT, and I would like to carry forward many of the lessons that I have learned about research collaboration into my future research pursuits.

Finally, as far as support from my lab, I would like to express my deepest gratitude to my PI, Dr. Isaac L. Chuang, who is a Professor of Physics and Professor of Electrical Engineering at MIT. Prof. Chuang has provided me with the opportunity to work in his lab and has given me invaluable support, both while I was in the hospital and as I have been

readjusting to life on campus after my medical leave. He has also been incredibly supportive of my desire to perform research abroad and was a significant force in the arrangement of my research internship with NTT in Japan, from which I have learned so much. Moreover, my meetings with him over the last five years have undoubtedly helped to give me direction as I completed the work that now comprises this thesis, and his comments have been invaluable throughout the writing process as well.

In addition to support from individuals in my lab and at NTT, I would also like to acknowledge all of the support that I have received from friends. Prior to my accident, I was living with fellow MIT Master of Engineering degree students Ms. Erica Chiu and Mr. Albert Yue, as well as Ms. Kathryn Li, a former Rhode Island School of Design illustration student. I have appreciated Erica and Albert's support throughout my convalescence, and I also sincerely appreciate the support of my next apartment-mate and former undergraduate roommate Mr. Mihir Prasad Khambete, who was also an MIT Master of Engineering degree student a couple of years ago. He has been an incredible roommate, apartment-mate, and friend, and I so appreciate that I was able to spend my last unexpected year at MIT with him.

Even more finally, I would like to make up for an acknowledgment that I neglected in my undergraduate thesis for perceived lack of space. I would like to thank my parents for their incredible support, without which I would have struggled much more with my return to campus for the completion of my master's degree. They were with me throughout the entirety of my recovery process, moving with me from Massachusetts General Hospital to Spaulding Hospital Cambridge, and then even moving with me to the Shirley Ryan AbilityLab in Chicago for my continued rehabilitation when this became necessary. I know that we spent perhaps too much time together, and I had my frustrations (a lot of them, as they can likely recall), but I do truly appreciate their unconditional love and support and hence dedicate this master's thesis to them.

Biographical Sketch

Gabriel Mintzer was born in Des Moines, Iowa, in 1999. He received his S.B. degrees in Physics (8) and Computer Science (6-3), as well as a minor in Chinese, from MIT in February 2021 before continuing on to pursue an M.Eng. degree in Electrical Engineering and Computer Science, also at MIT. In November 2021, he was run over by a truck while returning to his apartment from lab late one night. Following this accident, Mintzer took medical leave from MIT to recover as he attended therapy for his injuries. He returned to MIT in Fall 2022 to continue his degree, and during this term, he also decided with support from his advisor to travel abroad to Japan for a year to perform additional research in quantum computation for his M.Eng. degree at the Nippon Telegraph and Telephone Corporation (NTT). In Fall 2024, Mintzer will return to the United States to begin pursuing a Ph.D. in Applied Physics at Stanford University.

Contents

List of Figures

List of Tables

Chapter 1

Introduction

Tools for computation have existed for millennia, with the first one thought to be the Sumerian abacus of Babylon, invented circa 2700 – 2300 BCE [Ifr+00]. This tool, as well as the long tradition of tools for computation that have followed, including ENIAC [Lev13] and the computer, have paved the way for the modern field of computer science. However, beginning in 1968 when Stephen Wiesner invented conjugate coding [Wie83] and continuing in 1981 when Paul Benioff and Richard Feynman presented the first proposals for models of a quantum computer [Ben82; Fey82], a new system for computation was developed. This "quantum" computing makes use of the laws of quantum mechanics to solve particular problems asymptotically more efficiently than would be possible with the original "classical" devices.

The original approach to quantum computation, and the one that still dominates today, uses *qubits*, which are well-described as two-level systems. This variety of quantum computation draws inspiration directly from the classical approach to computation with bits. The qubit approach can thus be termed a "digital" approach to computation, where the Hilbert space corresponding to a system comprised of N qubits is 2^N-dimensional. In contrast, a newer approach to quantum computation called continuous-variable quantum computation (CVQC) uses physical observables, such as the strength of an electromagnetic field or the position of a particle in space, whose numerical values belong to continuous intervals. The CVQC approach is thus termed an "analog" approach to computation, where the Hilbert spaces corresponding to the units of computation, or *qudits*, of CVQC systems are infinite-dimensional. These qudits can be implemented in many ways, but one of the most common is via a system with a quadratic potential energy, known as a quantum harmonic oscillator.

CVQC has become a topic of particular interest in quantum computation and quantum metrology research [LB99]. Some, such as McCormick et al. and Burd et al., use special continuous-variable quantum states in metrology to achieve sensitivities below the limits established by classically-behaving states [MKB+19; BSB+19]. Other motivations for studying this subject include understanding what resources are necessary to make quantum computers more powerful than classical ones [NCS18a], as well as more efficiently encoding and processing certain types of information. One particularly fascinating application that has emerged is to quantum error correction, as discussed in Gottesman et al., Flühmann et al., and Gao et al. [GKP01; FNM+19; GLC+19]. Moreover, implementations of CVQC have been considered and achieved on many of the major platforms for quantum computation, in-

cluding trapped-ion qubits [Mas+19], neutral atoms [PAS23], superconducting qubits [Pfi19], circuit QED [SQJ18], and photonic qubits [RA21].

With the strength of both the digital and analog approaches to quantum computation, there has recently been significant interest in trying to combine them in an attempt to solve certain kinds of problems more efficiently [Par+20; Mar24]. This area of study has been termed by some as Digital-Analog Quantum Computation. One leading contender for realizing this type of quantum computation is the system comprised of a qubit coupled to a quantum harmonic oscillator [YN03; Wal+04; Joh+06]. This kind of system has been realized with various platforms for quantum computation, including trapped-ion qubits [Lei+03; Man+03], cavity QED [RBH01], and superconducting qubits [Chi+04], where it has been used to probe yet unexplored areas in the field of quantum computation.

1.1 Thesis Question

In this thesis, we ask how machine learning and other high-level computational techniques can be employed in the design of applications of a qubit-oscillator system to implementing fundamental components of quantum technology.

Questions such as this one are increasingly important as we continue to search for the best system with which to implement scalable quantum technology. Although there are a number of candidate systems under consideration now, none perfectly address all of our desired applications, and it is quite possible that no single system *will* perfectly address all of these applications. As such, we need to consider carefully the strengths of each system and how best to leverage these strengths in order to achieve our goals. Toward this goal, it is imperative that we develop methods, such as those employing machine learning and high-level computational techniques, for efficiently probing the space of applications achievable with a given system. By better defining the possible applications for the systems, we will be able to clarify which systems are best applied for each kind of problem in quantum technology.

Although this research question is simple to define, it is challenging to answer. Performing an in-depth investigation of the possible applications for a specific system of quantum technology requires specialized knowledge of both the quantum model of the particular system and the methods for investigation, in this case machine learning and high-level computational techniques. This significantly limits the number of research groups that are able to consider this question.

The research on applications of machine learning and other high-level computational techniques to the design of fundamental components of quantum technology is broad but not yet well-developed with respect to any particular system for quantum computation. With regard to general applications of high-level computational techniques to quantum technology, there have been efforts to address each of the subfields that we highlight in this thesis work. For example, with regard to compilation of quantum circuits for quantum computation, Moro et al. address the application of deep reinforcement learning to quantum compilation, enabling a single precompilation procedure to learn a general strategy for approximating single-qubit unitaries [Mor+21]. With regard to quantum sensing, Cimini et al. introduce a model-free and deep-learning-based approach to optimize parameters for performing Bayesian quantum

metrology tasks [Cim+23]. Finally, with regard to quantum error-correction, Zeng et al. have proposed a bosonic code for approximate autonomous quantum error-correction that was optimized with reinforcement learning [Zen+23].

As mentioned, these works all address strategies for applying machine learning or high-level computational techniques to *general* methods in quantum technology (i.e., methods that do not specify a particular system for their implementation). Although this approach has its benefits, such as the possibility of generalization to many systems being used for quantum technology, it cannot necessarily find the best way to use a particular system for a particular task in quantum technology. To do this, it is necessary that we carefully consider the specific systems and find strategies to explore the ways in which they can be used for quantum technology. We do not explore in this manner for every system, but we do take a step toward understanding the space of applications to quantum technology enabled by a qubit-oscillator system by employing machine learning and other high-level computational techniques to efficiently probe the space of possibilities.

In particular, we approach the question of designing applications of a qubit-oscillator system by employing a combination of quantum-mechanical theory, numerical optimization, and computer modeling to design and simulate protocols for several key directions in quantum technology. Specifically, we show concretely how the qubit-oscillator system can be utilized to perform universal quantum computation, providing an algorithm and code for the decomposition of arbitrary gates into experimentally-realizable primitives; quantum sensing, both of the magnitude of displacements on an oscillator and of arbitrary functions of the oscillator's position and momentum quadratures, via machine learning of sensing parameters; and quantum error-correction of bosonic codes implemented on the oscillator, employing both quantum-mechanical theory and numerical simulations to develop and verify new methods. As such, we provide significant progress toward answering the main question posed by this thesis and demonstrating the power and versatility of the qubit-oscillator system.

1.2 Outline

In Chapter 2, this thesis first acknowledges its place as a thesis in electrical engineering and computer science by introducing some of the mathematics and physics of quantum computation used throughout the work, assuming only basic knowledge of mathematics and classical computer science. In particular, this chapter introduces the digital and analog approaches to quantum computation, as well as the tools for treating both of them together.

In the work detailed in Chapter 3, we show how a d-dimensional Hilbert space can be analytically constructed by closing off the lowest-energy states of the qubit-oscillator system, prove that first-order sideband pulses and carrier pulses comprise a universal gate set for quantum operations on the qubit-oscillator qudit, and then provide an algorithm for the decomposition of arbitrary qudit operations into this gate set.

Then in Chapter 4, we detail our work presenting a general algorithmic framework, quantum signal processing interferometry (QSPI), for using a qubit-oscillator system like that explored in Chapter 3 to perform quantum sensing at the fundamental limits of quantum mechanics. We discuss how one can perform nonlinear polynomial transformations on the oscillator's quadrature operators by generalizing quantum signal processing (QSP) from

qubits to hybrid qubit-oscillator systems and demonstrate, both theoretically and with results from numerical optimization, that we can use the QSPI sensing framework to make binary decisions on a displacement channel in the single-shot limit.

In Chapter 5, we present the seeds of our research on bivariable quantum signal processing (BiQSP), an extension to the QSPI research of Chapter 4.5.2 that would enable the design of algorithms to achieve arbitrary qubit response functions over the entirety of phase space. We show how a slight generalization of the operations available in QSPI can enable the realization of qubit response functions that are Laurent polynomials of complex exponentials of the position and momentum quadratures and present results from numerical optimization demonstrating how this capability can be used to enable the realization of the XOR gate on the position and momentum quadratures.

For our last project, we explain in Chapter 6 our most recent work on using a qubit coupled to an oscillator for quantum error-correction via engineered dissipation. We propose an experimentally-realizable scheme for error-correction of a bosonic quantum error-correcting code implemented with an oscillator based upon this idea of coupling to a qubit and demonstrate its efficacy via a number of numerical simulations performed using the QuTiP package in Python.

We conclude in Chapter 7 with some comments about the promise of this kind of quantum system and some remarks about future directions for the research presented here.

Chapter 2

Quantum Computing Background

This is, at its core, an EECS thesis about the use of classical computing techniques toward the innovation and realization of practical quantum computation. As such, it is useful to provide some background on the field of quantum computation for an audience that might be familiar with the computational but not physical aspects of this field.

Toward this goal, we will walk through the basics of some areas of quantum mechanics relevant to our exploration of the qubit-oscillator system toward use in quantum technology. First, we introduce the basics of digital quantum computation and the qubit, followed by elaboration on topics of more general relevance to quantum computation, in Sec. 2.1. Then we note the distinctions from the treatment of the other component of the system, namely the oscillator, and discuss analog quantum computation and the oscillator qudit in Sec. 2.2. With these two pieces, we are able to contextualize and understand the physics of the entire qubit-oscillator system as we proceed to investigate its applications to realizing the fundamental components of quantum technology.

2.1 Introduction to Digital Quantum Computation

To introduce the basics of quantum computation, we begin by providing the context of digital quantum computation with qubits before transitioning into more general topics in quantum computation. In Sec. 2.1.1, we introduce the basic unit of digital quantum computation, the qubit, as well as its most common visualization with the Bloch sphere. Then in Sec. 2.1.2, we introduce the idea of a quantum state in the context of qubits. Next, we introduce the concept of a quantum operator on these quantum states in Sec. 2.1.3. Afterward, we extend this theory for one qubit to that for many qubits with tensor products in Sec. 2.1.4. Finally, we introduce the fundamental ideas of quantum measurements in Sec. 2.1.5.

2.1.1 Qubits and the Bloch Sphere

We will first explain the qubit. A *qubit* is a binary unit of quantum computation, essentially the quantum equivalent of a bit.

What distinguishes a qubit from its classical, or non-quantum, counterpart is that while a bit is fully binary, meaning that it can only be fully in the zero state or fully in the one

state, the qubit, though also fundamentally binary, can additionally be in a superposition of both states simultaneously. This is to say that qubit states exist in a continuum between the two binary extremes of zero and one, often visualized as the surface of a sphere called the *Bloch sphere*. The two poles of the sphere represent these two binary extremes, or the $|0\rangle$ and $|1\rangle$ qubit states, which form the standard basis for the vector space of states, while all of the points on the sphere between the two poles represent nontrivial superpositions of these two basis states. This visualization is depicted in Figure 2.1.

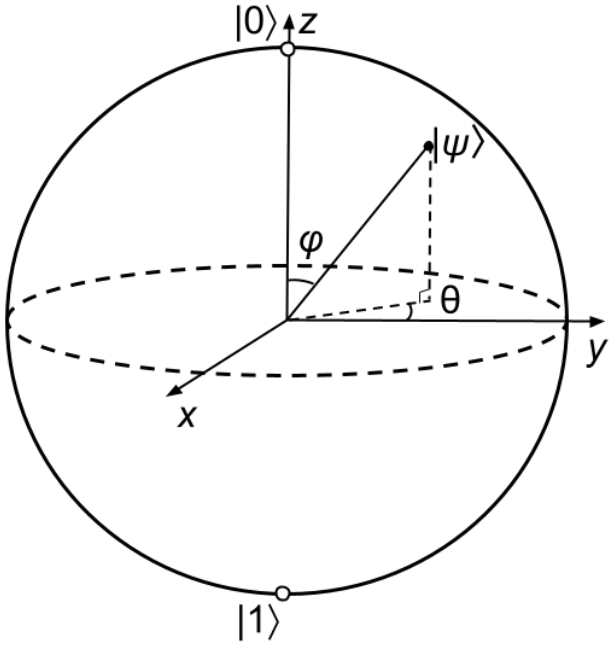

Figure 2.1: A Bloch sphere with an example state $|\psi\rangle = \alpha|0\rangle + \beta|1\rangle$ $(\alpha, \beta \in \mathbb{C})$ that is a complex superposition of the basis states $|0\rangle$ and $|1\rangle$

A qubit can be physically implemented in many ways, much as a classical bit can be implemented with any of several alternative methods, including by an electrical voltage or by a current pulse. One such approach to implementing a qubit, and the one discussed most in this work, is using an ion trapped electromagnetically by voltages applied to electrodes in an ion trap. Essentially, for a single ion, we can form a *digital*, or binary, qubit with the two long-lived electronic or spin states acting as its basis. In other words, the two long-lived states act as the two basis states of the qubit that form the poles of the Bloch sphere, $|0\rangle$ and $|1\rangle$.

For more background on the Bloch sphere, please refer to Section 1.2 of *Quantum Computation and Quantum Information* by Michael Nielsen and Isaac Chuang [NC10]. This text also includes much more information about other implementations of qubits for those who might be curious.

2.1.2 Quantum States

We have already defined a valid quantum state by the states on the Bloch sphere introduced in Sec. 2.1.1. These can be thought of as vectors in the space in which the Bloch sphere

exists, known as a *Hilbert space*. However, to distinguish this type of vector from other types of vectors, it is common and useful in physics to denote these vectors ψ as "kets" $|\psi\rangle$. Because these kets are vectors, they behave according to the same rules of linear algebra as other vectors; they can be added, multiplied by scalars, etc. For example, in the vector space shown in Fig. 2.1, we can decompose the ket $|\psi\rangle$ into the basis kets of the space $|0\rangle$ and $|1\rangle$ as $|\psi\rangle = \alpha|0\rangle + \beta|1\rangle$, as shown in the caption.

A ket is an element of a vector space, and a "bra" $\langle\psi|$ is an element of its dual space. It is useful to think about kets and bras as being elements of different but related vector spaces. Every ket can be transformed into its corresponding bra by conjugating the coefficients in its decomposition into its basis decomposition and changing the basis kets to bras. For example, for $|\psi\rangle = \alpha|0\rangle + \beta|1\rangle$, the corresponding bra is $\langle\psi| = \alpha^*\langle 0| + \beta^*\langle 1|$.

We can take inner products of quantum states by taking the bra of one state and right-multiplying it by the ket of the other state. For example, the inner product of $|\psi\rangle$ and $|\phi\rangle$ is the complex number $\langle\psi|\phi\rangle$. If the inner product of two kets ψ and ϕ is zero (i.e., $\langle\psi|\phi\rangle = 0$), then they are said to be *orthogonal*. One example of a pair of orthogonal kets is the pair $|0\rangle$ and $|1\rangle$ in Fig. 2.1, as their inner product is 0. This can be expressed as $\langle 0|1\rangle = \langle 1|0\rangle = 0$. Given this definition of the inner product, we can also define the *norm* of a ket $|\psi\rangle$ by

$$\||\psi\rangle\| \equiv \sqrt{\langle\psi|\psi\rangle}. \tag{2.1}$$

A *unit vector* is a vector $|\psi\rangle$ such that $\||\psi\rangle\| = 1$. If a vector $|\psi\rangle$ satisfies $\||\psi\rangle\| = 1$, then we say that it is *normalized*. All valid quantum states are represented by unit vector kets, and it is convenient to call dividing a ket by its norm to make it a unit vector ket *normalizing* the ket; the result, $|\psi\rangle/\||\psi\rangle\|$ is then the *normalized* form of $|\psi\rangle$. For the state $|\psi\rangle = \alpha|0\rangle + \beta|1\rangle$ shown in Fig. 2.1, normalization implies that α and β must satisfy

$$\begin{aligned}
\langle\psi|\psi\rangle &= (\alpha^*\langle 0| + \beta^*\langle 1|)(\alpha|0\rangle + \beta|1\rangle) && (2.2)\\
&= \alpha^*\alpha\langle 0|0\rangle + \alpha^*\beta\langle 0|1\rangle + \beta^*\alpha\langle 1|0\rangle + \beta^*\beta\langle 1|1\rangle && (2.3)\\
&= |\alpha|^2 + |\beta|^2 && (2.4)\\
&= 1. && (2.5)
\end{aligned}$$

A set $|i\rangle$ of vectors with index i is orthonormal if every vector in this set is a unit vector and each pair of distinct vectors in the set is orthogonal (i.e., $\langle i|j\rangle = \delta_{ij}$, where δ_{ij} denotes the Kronecker delta function that is equal to 1 when $i = j$ and 0 otherwise and i and j are both chosen from the set of indices). We usually describe a Hilbert space in terms of an "orthonormal basis" of vectors that spans the Hilbert space.

We can express kets for a qubit state in the more familiar column vector form by defining an orthogonal basis and representing the basis vectors as the unit basis vectors for the vector space $\mathbb{R}^2$. In particular, we can represent $|0\rangle$ by $\begin{bmatrix}1\\0\end{bmatrix}$ and $|1\rangle$ by $\begin{bmatrix}0\\1\end{bmatrix}$ so that the ket $|\psi\rangle$ is

given by

$$|\psi\rangle = \alpha|0\rangle + \beta|1\rangle \tag{2.6}$$

$$= \alpha \begin{bmatrix} 1 \\ 0 \end{bmatrix} + \beta \begin{bmatrix} 0 \\ 1 \end{bmatrix} \tag{2.7}$$

$$= \begin{bmatrix} \alpha \\ \beta \end{bmatrix}. \tag{2.8}$$

Note that using this convention, bras are written as row vectors, since $\langle 0|$ is represented by $\begin{bmatrix} 1 & 0 \end{bmatrix}$ and $\langle 1|$ by $\begin{bmatrix} 0 & 1 \end{bmatrix}$.

For more background on the linear algebra of quantum states, please refer to Sections 2.1.1, 2.1.4, and 2.1.6 of *Quantum Computation and Quantum Information* by Michael Nielsen and Isaac Chuang [NC10].

2.1.3 Quantum Operators

In order to understand the use of qubits in our work, we must also discuss *operators*, the quantum equivalents of classical logic gates that act on qubits rather than bits. These operators usually act on a small number of qubits, and the gates that they enact form the building blocks for more complex quantum circuits, making their implementation fundamental to the realization of quantum computation.

We refer the reader to Section 2.1 of *Quantum Computation and Quantum Information* by Michael Nielsen and Isaac Chuang for information about quantum operators, but we will summarize key details here. Additionally, some frequently used quantum gates and circuit symbols are provided on page xxx of this text [NC10], and we would recommend referring here.

Let $\hat{A}$ be a linear quantum operator. Then we can describe the operator $\hat{A}$ acting on a state $|\psi\rangle$ by writing $\hat{A}|\psi\rangle$. We often denote operators with this "hat" notation, although the hat is sometimes dropped for ease of notation. It turns out that there is a unique linear quantum operator $\hat{A}^\dagger$ with the property that the inner product of $|v\rangle$ with $\hat{A}|w\rangle$ is identical to the inner product of $\hat{A}^\dagger|v\rangle$ with $|w\rangle$. This linear operator $\hat{A}^\dagger$ is known as the *adjoint*, or the *Hermitian conjugate*, of the operator $\hat{A}$. We note some interesting properties of this adjoint. For one, we can easily observe that for any two operators $\hat{A}$ and $\hat{B}$, $(\hat{A}\hat{B})^\dagger = \hat{B}^\dagger\hat{A}^\dagger$. Additionally, by convention, if $|v\rangle$ is a ket, then we define $|v\rangle^\dagger \equiv \langle v|$ to be the corresponding bra. Given this definition, it also clearly follows that, for any operator $\hat{A}$ and vector v, $(\hat{A}|v\rangle)^\dagger = \langle v|\hat{A}^\dagger$.

If we represent the operator $\hat{A}$ as a matrix A, then taking the Hermitian conjugate of A is equivalent to taking the matrix A and mapping it to the conjugate-transpose matrix (i.e., $A^\dagger \equiv (A^*)^T$). An operator $\hat{A}$ whose adjoint is itself is known as a *Hermitian*, or *self-adjoint*, operator. All of the eigenvalues of Hermitian operators are real, and we will see in the next section that Hermitian operators are an important class of operators.

One particularly notable collection of Hermitian operators is the collection of *Pauli operators*. The Pauli operators in their matrix forms are given in Table 2.1.

One final class of quantum operators that are useful to note specially is the class of *unitary* operators. In linear algebra, a matrix U is said to be unitary if $U^\dagger U = I$, where

$$\hat{\sigma}_0 \equiv \hat{I} \equiv \begin{bmatrix} 1 & 0 \\ 0 & 1 \end{bmatrix} \quad \hat{\sigma}_1 \equiv \hat{\sigma}_x \equiv \hat{X} \equiv \begin{bmatrix} 0 & 1 \\ 1 & 0 \end{bmatrix}$$
$$\hat{\sigma}_2 \equiv \hat{\sigma}_y \equiv \hat{Y} \equiv \begin{bmatrix} 0 & -i \\ i & 0 \end{bmatrix} \quad \hat{\sigma}_3 \equiv \hat{\sigma}_z \equiv \hat{Z} \equiv \begin{bmatrix} 1 & 0 \\ 0 & -1 \end{bmatrix}$$

Table 2.1: The Pauli operators in matrix form

I represents the identity matrix. Similarly, an operator $\hat{U}$ is unitary if $\hat{U}^\dagger \hat{U} = \hat{I}$, where $\hat{I}$ here represents the identity operator. All unitary operators also satisfy $\hat{U}\hat{U}^\dagger = I$. Unitary operators are important because they leave inner products between vectors unchanged. We can check this by letting $|\psi\rangle$ and $|\phi\rangle$ be any two kets and confirming that the inner product of these two kets is identical to the inner product of $\hat{U}|\psi\rangle$ and $\hat{U}|\phi\rangle$ for an arbitrary unitary operator $\hat{U}$:

$$(\hat{U}|\psi\rangle)^\dagger(\hat{U}|\phi\rangle) = \langle\psi|\hat{U}^\dagger\hat{U}|\phi\rangle \tag{2.9}$$
$$= \langle\psi|\hat{I}|\phi\rangle \tag{2.10}$$
$$= \langle\psi|\phi\rangle. \tag{2.11}$$

These unitary operators are especially important because the reversibility of quantum mechanics implies that all processes on closed systems must evolve according to unitary dynamics (i.e., as if acted on by unitary operators).

2.1.4 Tensor Products

Given all of this mathematical background for quantum computation on a single qubit, one might ask how we can apply the theory of quantum mechanics to more complex systems, particularly those including many qubits. The key to approaching larger systems is to use the tensor product.

The *tensor product* is a method for putting vector spaces together in order to form larger vector spaces. In particular, suppose that V and W are vector spaces of dimension m and n, respectively, and for convenience, we will also assume that they are both Hilbert spaces. Then $V \otimes W$, which is read as 'V tensor W', is an mn-dimensional vector space. Moreover, the elements of $V \otimes W$ are linear combinations of 'tensor products' $|v\rangle \otimes |w\rangle$ of elements $|v\rangle \in V$ and $|w\rangle \in W$, and in particular, if $|i\rangle$ and $|j\rangle$ are orthonormal bases for the spaces V and W, then $|i\rangle \otimes |j\rangle$ is a basis for $V \otimes W$. We sometimes use the abbreviated notations $|v\rangle|w\rangle$, $|v, w\rangle$, or $|vw\rangle$ to denote the tensor product $|v\rangle \otimes |w\rangle$.

The tensor product satisfies several important and fundamental properties:

1. For an arbitrary scalar z and arbitrary elements $|v\rangle \in V$ and $|w\rangle \in W$, we have

$$z\left(|v\rangle \otimes |w\rangle\right) = \left(z|v\rangle\right) \otimes |w\rangle = |v\rangle \otimes \left(z|w\rangle\right). \tag{2.12}$$

2. For arbitrary $|v_1\rangle, |v_2\rangle \in V$ and $|w\rangle \in W$,

$$\left(|v_1\rangle + |v_2\rangle\right) \otimes |w\rangle = |v_1\rangle \otimes |w\rangle + |v_2\rangle \otimes |w\rangle. \tag{2.13}$$

3. For arbitrary $|v\rangle \in V$ and $|w_1\rangle, |w_2\rangle \in W$,

$$|v\rangle \otimes (|w_1\rangle + |w_2\rangle) = |v\rangle \otimes |w_1\rangle + |v\rangle \otimes |w_2\rangle. \tag{2.14}$$

Now, we might ask what kinds of operators act on this "tensor-product" space $V \otimes W$. Suppose that we have elements $|v\rangle \in V$ and $|w\rangle \in W$, as well as linear operators $\hat{A}$ on space V and $\hat{B}$ on space W. Then we can define the action of a linear operator $\hat{A} \otimes \hat{B}$ on the space $V \otimes W$ by

$$\left(\hat{A} \otimes \hat{B}\right)(|v\rangle \otimes |w\rangle) = \hat{A}|v\rangle \otimes \hat{B}|w\rangle. \tag{2.15}$$

Moreover, since $\hat{A} \otimes \hat{B}$ is linear, we can extend this definition to all elements of $V \otimes W$ by decomposition into basis elements:

$$\left(\hat{A} \otimes \hat{B}\right)\left(\sum_i a_i |v_i\rangle \otimes |w_i\rangle\right) \equiv \sum_i a_i \hat{A}|v_i\rangle \otimes \hat{B}|w_i\rangle. \tag{2.16}$$

As with tensor product states, if the Hilbert spaces involved are well-understood, then the tensor-product symbol is sometimes dropped for convenience of notation. In other words, the tensor-product operator $\hat{A} \otimes \hat{B}$ might also be denoted $\hat{A}\hat{B}$. This notation is often taken in the remainder of this thesis after the subproblem and the involved Hilbert spaces have been clearly presented.

There is also a convenient way to represent the tensor product of two matrices by the *Kronecker product*, but to see more on this and other topics related to the tensor product, please refer to Section 2.1.7 of *Quantum Computation and Quantum Information* by Michael Nielsen and Isaac Chuang [NC10].

2.1.5 Quantum Measurements

Finally, for the last section of this overview of quantum computation with qubits, we will discuss the topic of quantum measurements.

While we claimed that a closed quantum system evolves according to unitary evolution, a quantum measurement entails interaction with the quantum system, and so a quantum system need not undergo unitary evolution during measurement. In fact, we introduce a postulate of quantum mechanics to describe how quantum systems behave under measurement.

A quantum measurement is described by a collection $\{\hat{M}_m\}$ of measurement operators, operators acting on the state space of the system being measured. Here, the index m of the measurement operators refers to the possible measurement outcomes that may occur. Suppose that immediately before the measurement, the state of the system is $|\psi\rangle$. Then the probability that measurement m occurs is given by

$$p(m) = \langle\psi|\hat{M}_m^\dagger \hat{M}_m|\psi\rangle. \tag{2.17}$$

Correspondingly, the state of the system following the measurement is given by

$$\frac{\hat{M}_m|\psi\rangle}{\sqrt{\langle\psi|\hat{M}_m^\dagger \hat{M}_m|\psi\rangle}}. \tag{2.18}$$

The measurement operators $\{\hat{M}_m\}$ necessarily satisfy the completeness relation

$$\sum_m \hat{M}_m^\dagger \hat{M}_m = I. \tag{2.19}$$

This requirement is derived from the fact that the probabilities of all possible outcomes must sum to 1:

$$1 = \sum_m p(m) = \sum_m \langle\psi|\hat{M}_m^\dagger \hat{M}_m|\psi\rangle. \tag{2.20}$$

Before we conclude, we will work through one example of measurement, a measurement of a qubit in the computational basis. By this, we are referring to a measurement on a single qubit with two outcomes defined by the two measurement operators $\hat{M}_0 = |0\rangle\langle 0|$ and $\hat{M}_1 = |1\rangle\langle 1|$. Note that we do indeed have $\hat{M}_0^\dagger \hat{M}_0 = \hat{M}_0 = |0\rangle\langle 0|$ and $\hat{M}_1^\dagger \hat{M}_1 = \hat{M}_1 = |1\rangle\langle 1|$, so

$$\sum_m \hat{M}_m^\dagger \hat{M}_m = |0\rangle\langle 0| + |1\rangle\langle 1| = I \tag{2.21}$$

by the completeness relation. Also, note that this is called measurement in the computational basis because $|0\rangle$ and $|1\rangle$ are known as the computational basis states.

Now, suppose that the state that we are measuring is the state $|\psi\rangle = \alpha|0\rangle + \beta|1\rangle$ from Fig. 2.1. Then the probability of obtaining measurement outcome 0 is given by

$$p(0) = \langle\psi|\hat{M}_0^\dagger \hat{M}_0|\psi\rangle = \langle\psi|\hat{M}_0|\psi\rangle = |\alpha|^2. \tag{2.22}$$

Analogously, we can go through and find that the probability of measuring 1 is $|\beta|^2$.

If we measure 0, then the state after measurement is

$$\frac{\hat{M}_0|\psi\rangle}{|\alpha|} = \frac{\alpha}{|\alpha|}|0\rangle, \tag{2.23}$$

and if we measure 1, then the state after measurement is

$$\frac{\hat{M}_1|\psi\rangle}{|\beta|} = \frac{\beta}{|\beta|}|1\rangle. \tag{2.24}$$

Because the coefficients in front of the states have magnitude 1, they are only global phases and can be effectively ignored. Thus, the post-measurement state is either $|0\rangle$ if we measure 0 with probability $|\alpha|^2$ or $|1\rangle$ if we measure 1 with probability $|\beta|^2$.

For one final point about notation, assuming that the state being measured is understood, then the notation for a measurement of operator $\hat{M}$ with respect to state ψ is often abbreviated to

$$\langle\hat{M}\rangle \equiv \langle\psi|\hat{M}|\psi\rangle. \tag{2.25}$$

For more information on quantum measurements, please refer to Sections 2.2.3 – 2.2.7 of *Quantum Computation and Quantum Information* by Michael Nielsen and Isaac Chuang [NC10].

2.2 Introduction to Analog Quantum Computation

We have indicated that the topic of this thesis is answering whether the system of a qubit coupled to an oscillator is a viable platform for implementing fundamental components of quantum technology. The system of interest is comprised of both a qubit, the unit of digital quantum computation discussed in Sec. 2.1, and an oscillator *qudit*, a unit of analog quantum computation to be discussed in this section. Although the theory of digital quantum computation does provide a basis for understanding quantum computation, there are some notable differences encountered in analog quantum computation.

In this section, we walk through some of the basic theory of the quantum harmonic oscillator and its place in analog quantum computation, pointing out these differences as we encounter them. We begin by providing an overview of the nature of a quantum harmonic oscillator and its eigenspectrum in Sec. 2.2.1. Then we proceed to discuss some fundamental operators on this unit of analog quantum computation in Sec. 2.2.2. Next, we discuss some other fundamental operators in CVQC, as well as how they can aid in understanding CVQC and the hybrid qubit-oscillator system that we investigate, in Sec. 2.2.3. Afterward, we introduce some more CVQC operators that are useful for constructing states and visualize their action in Sec. 2.2.4. Finally, we conclude by presenting some useful states that we can create using these operators and that we will employ throughout this thesis in Sec. 2.2.5.

2.2.1 The Quantum Harmonic Oscillator and its Eigenspectrum

In order to understand the quantum harmonic oscillator qudit, a unit of analog quantum computation, it is beneficial to first discuss the classical analog, a simple harmonic oscillator. An example of a simple harmonic oscillator is a particle in a quadratic potential well, as given by $V(x) = \frac{m\omega^2 x^2}{2}$, where $V(x)$ denotes the potential energy of the particle. With relation to classical, or non-quantum systems, this "particle" could be a mass on a spring, which oscillates back and forth as energy is transferred between the elastic potential energy of the spring and the motional kinetic energy of the mass. This simple harmonic oscillator could also be a resonant electrical circuit, where energy is converted back and forth between the inductor and the capacitor in the circuit. Although these two systems differ, they can both be described as simple harmonic oscillators, where the total energy of the system is a continuous parameter.

These simple harmonic oscillators become *quantum harmonic oscillators* when the coupling, or interaction, with the external world becomes very small. These quantum harmonic oscillators are exemplified by electromagnetic radiation trapped in a cavity with low loss or the motional modes of a single ion, of which there are three (one for each spatial dimension).

The energy eigenstates of a QHO have a special mathematical structure. In particular, eigenstates can be labeled by $|0\rangle$, $|1\rangle$, $|2\rangle$, ..., and the eigenvalue of the state labeled $|n\rangle$, also called its eigenenergy E_n, is given by $E_n = n\hbar\omega$, where $\hbar$ denotes the reduced Planck constant and ω is the angular frequency of the oscillator. One noteworthy property of these eigenenergies is that they come in discrete multiples of $\hbar\omega$. Due to this uniformly-spaced hierarchy of eigenenergies, this collection is often referred to as the *ladder of energy eigenstates* for the quantum harmonic oscillator motional mode.

2.2.2 QHO Ladder Operators

Two useful operators for this ladder of energy eigenstates of the QHO are the operators $\hat{a}$ and its Hermitian conjugate $\hat{a}^\dagger$. These, often referred to together as *ladder operators*, can be defined for each QHO motional mode such that $\hat{a}|n\rangle = \sqrt{n}|n-1\rangle$ and $\hat{a}^\dagger|n\rangle = \sqrt{n+1}|n+1\rangle$ for each $n \in \mathbb{Z}_{\geq 0}$. The properties of increasing or decreasing the energy of the state lead to their common names of *annihilation* and *creation* operator (or *lowering* and *raising* operator if instead viewed from the perspective of decreasing and increasing n in the ladder). Using these ladder operators, this collection of motional modes can be manipulated to perform CVQC operations and hence quantum computation.

For more information on the quantum harmonic oscillator and its eigenspectrum, please refer to Sections 7.3.1 and 7.3.2 of *Quantum Computation and Quantum Information* by Michael Nielsen and Isaac Chuang [NC10]

2.2.3 Position and Momentum CVQC Operators

Beyond the ladder operators, there are a few additional operators that are very useful in the study of CVQC. Two such operators with whose classical counterparts most physicists are quite familiar are the position and momentum operators $\hat{x}$ and $\hat{p}$, which are named by their traditional classical notations but with hats to indicate that these are quantum operators.

Interestingly, each of these two operators can be expressed quite simply in terms of the ladder operators. Their definitions are as follows:

$$\hat{x} = \sqrt{\frac{\hbar}{2m\omega}}\left(\hat{a} + \hat{a}^\dagger\right) \tag{2.26}$$

$$\hat{p} = -i\sqrt{\frac{m\hbar\omega}{2}}\left(\hat{a} - \hat{a}^\dagger\right), \tag{2.27}$$

where $\hbar$ denotes the reduced Planck constant, m denotes the mass of the oscillator, and ω denotes the angular frequency of the oscillator.

These position and momentum quantum operators enable visualization of analog quantum states in the *phase-space representation*, a representation to which we will refer when exploring analog quantum states throughout this thesis. We introduce the phase-space representation in Sec. 2.2.3.1. Then we discuss a distribution often used to visualize states in this representation in Sec. 2.2.3.2.

2.2.3.1 Phase-space Representation

The position and momentum operators can also be used to define an alternate continuous-variable representation of quantum states, known as the phase space representation. This representation depicts quantum states by using the values of their position and momentum operators, with position $\hat{x}$ on the horizontal axis and momentum $\hat{p}$ on the vertical axis, as shown in Figure 2.2.

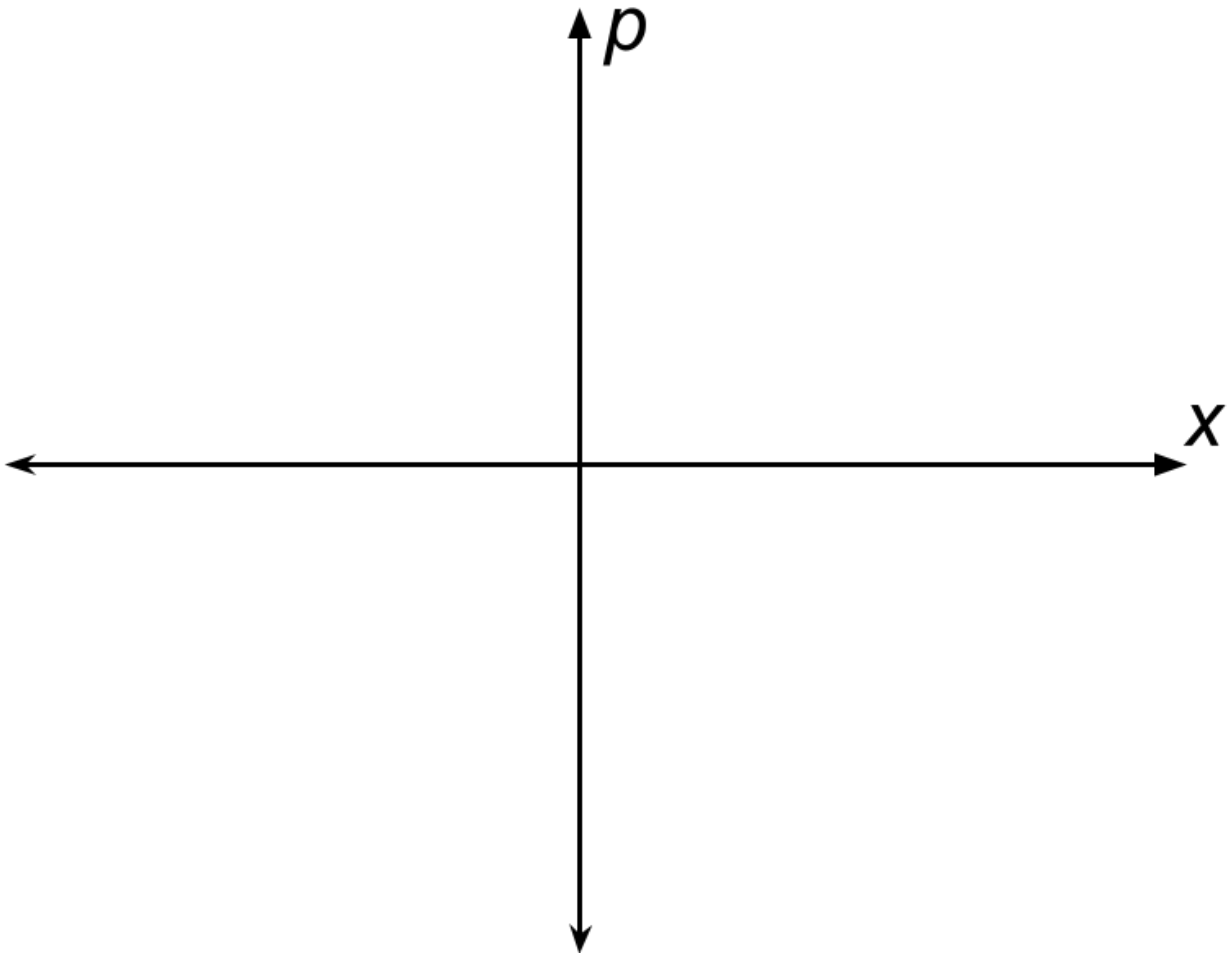

Figure 2.2: A plot showing the standard axes for the phase-space representation of a quantum state.

2.2.3.2 Wigner Quasiprobability Distribution and Wigner Plots

With this new understanding of the phase-space representation as a tool for understanding continuous-variable quantum states, one might ask what exactly can be plotted for this phase-space representation of a quantum state.

One popular quantity plotted in phase-space plots is the Wigner quasiprobability distribution. This distribution was introduced by Eugene Wigner in 1932 in order to connect the wavefunction that appears in Schrödinger's equation to a probability distribution in phase space.

The intuition for the Wigner quasiprobability distribution is as follows. Because a classical particle has a definite position and momentum, it can be represented by a point in the phase-space picture that we defined above. Moreover, given a collection of particles, the probability of finding a particle at a certain position in phase space can be specified by a probability distribution called the Liouville density. However, this reasoning fails for a *quantum* particle, as the Heisenberg uncertainty principle does not allow one to precisely specify both the position and the momentum of a particle simultaneously. Instead, the Wigner quasiprobability distribution plays an analogous role for these quantum particles, although in order to do so, it does not satisfy all the properties of a conventional probability distribution, instead sometimes taking values not allowed to classical distributions. In particular, regions in phase space where the Wigner quasiprobability distribution is negative indicate that the state does not have a classical model and are hence readily observed indicators of interference that is inherently quantum mechanical.

This distribution is defined over position and momentum as follows:

$$W(x,p) \stackrel{\text{def}}{=} \frac{1}{\pi\hbar}\int_{-\infty}^{\infty} \psi^*(x+y)\psi(x-y)e^{2ipy/\hbar}\,dy, \tag{2.28}$$

The Wigner quasiprobability distribution is often used to visualize quantum mechanical wavefunctions in phase space for continuous-variable quantum systems, and we make use of it many times in this work. We will also show several examples of its utility in the next couple of sections.

2.2.4 More Useful CVQC Operators

In this section, we will introduce a couple more useful CVQC operators and demonstrate their action on states via the use of Wigner plots in order to illustrate the utility of both. In particular, we will introduce the *displacement* operator $\hat{D}$ and the *squeezing* operator $\hat{S}$, since we make use of a slight variant of the displacement operator in Chapters 4, 5, and 6 and the squeezing operator in Chapter 6.

We first introduce the displacement operator in Sec. 2.2.4.1. Then we introduce the squeezing operator in Sec. 2.2.4.2.

2.2.4.1 Displacement Operator

The *displacement* operator $\hat{D}$ is given by

$$\hat{D}(\alpha) = \exp\left[\alpha\hat{a}^\dagger - \alpha^*\hat{a}\right] \tag{2.29}$$

for α an arbitrary complex number. The displacement operator does precisely what it sounds like it would do; the operator $\hat{D}(\alpha)$ displaces a state by the complex value $\alpha\sqrt{2}$ in phase space, where the $\sqrt{2}$ factor emerges from the definitions of $\hat{x}$ and $\hat{p}$ in terms of $\hat{a}$ and $\hat{a}^\dagger$. We can see this action by plotting the Wigner function for the vacuum state, or the ground state of the quantum harmonic oscillator, $|0\rangle$, and this state after the actions of two different displacement operators, or $\hat{D}(\alpha)|0\rangle$. These Wigner plots are shown in Fig. 2.3.

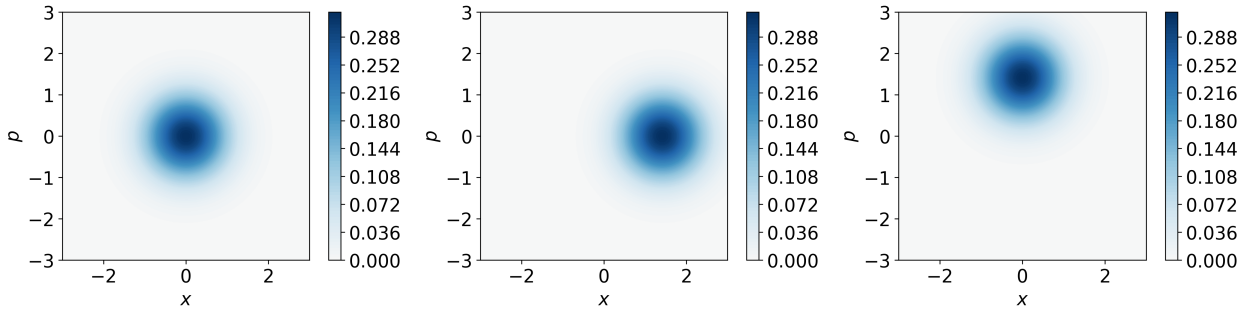

(a) Vacuum State $|0\rangle$ (b) Displaced State $\hat{D}(1)|0\rangle$ (c) Displaced State $\hat{D}(i)|0\rangle$

Figure 2.3: The vacuum state $|0\rangle$ (Fig. 2.3a) and the same state state after undergoing the actions of the displacement operator $\hat{D}(1)$, resulting in the state $\hat{D}(1)|0\rangle$ (Fig. 2.3b, and $\hat{D}(i)$, resulting in the state $\hat{D}(i)|0\rangle$ (Fig. 2.3c).

The state $\hat{D}(\alpha)|0\rangle$ is often denoted $|\alpha\rangle$ and is known as the "coherent state" with magnitude α. This state is also an eigenstate of the operator $\hat{a}$ with eigenvalue α (i.e., $\hat{a}|\alpha\rangle = \alpha|\alpha\rangle$).

2.2.4.2 Squeezing Operator

The *squeezing* operator $\hat{S}$ is given by

$$\hat{S}(\zeta) = \exp\left[\frac{1}{2}\left(\zeta^*\hat{a}^2 - \zeta\hat{a}^{\dagger 2}\right)\right]. \tag{2.30}$$

for ζ an arbitrary complex number. The squeezing operator also does precisely what it sounds like it would do; the operator $\hat{S}(\zeta)$ "squeezes" a state according to the complex value ζ in phase space, where the argument of ζ determines the axis of the squeezing and the magnitude of ζ determines the magnitude of the squeezing along this axis. We can see this action by plotting the Wigner function for the vacuum state, or the ground state of the quantum harmonic oscillator, $|0\rangle$, and this state after the actions of two different displacement operators, or $\hat{S}(\zeta)|0\rangle$. These Wigner plots are shown in Fig. 2.4.

2.2.5 More Useful CVQC States

With the displacement operator $\hat{D}$ and the squeezing operator $\hat{S}$, we can create many useful kinds of states. We will illustrate a couple of them that we investigate further in this thesis in this section. We begin by introducing the *squeezed coherent state*

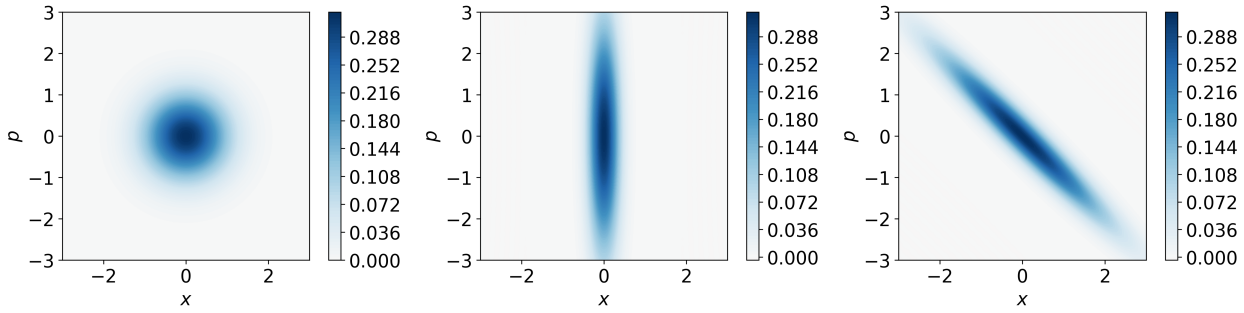

(a) Vacuum State $|0\rangle$ (b) Squeezed State $\hat{S}(1)|0\rangle$ (c) Squeezed State $\hat{S}(i)|0\rangle$

Figure 2.4: The vacuum state $|0\rangle$ (Fig. 2.4a) and the same state state after undergoing the actions of the squeezing operators $\hat{S}(1)$, resulting in $\hat{S}(1)|0\rangle$ (Fig. 2.4b, and $\hat{S}(i)$, resulting in the state $\hat{S}(i)|0\rangle$ (Fig. 2.4c).

One example is the state known as a *squeezed coherent state*. This state is defined by a displacement parameter α and a squeezing parameter ζ, where the displaced coherent state $|\alpha, \zeta\rangle$ is given by

$$|\alpha, \zeta\rangle = \hat{D}(\alpha)\hat{S}(\zeta)|0\rangle. \tag{2.31}$$

We provide the Wigner plot for an example squeezed coherent state with magnitude $\alpha = 1$ and squeezing level $\zeta = 1$ in Fig. 2.5.

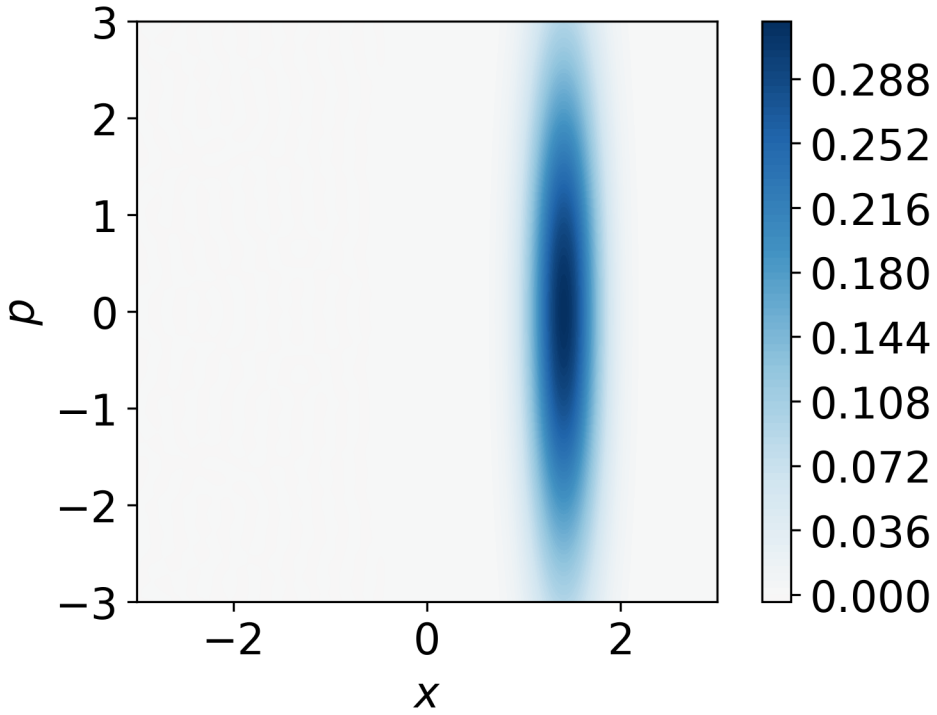

Figure 2.5: Wigner plot for the squeezed coherent state $|\alpha = 1, \zeta = 1\rangle = \hat{D}(1)\hat{S}(1)|0\rangle$.

The statistics of these states have been studied carefully, and they have proven quite useful

for quantum sensing in the Laser Interferometer Gravitational-Wave Observatory (LIGO) experiment for increasing sensitivity of the sensing device to gravitational waves [Cav81; Aas+13].

Another useful state for sensing that we can define, and to which we will refer in Chapters 4 and 6, is the cat state. The cat state is defined by

$$|\psi_{\text{cat}}(\alpha_{\text{cat}})\rangle = \frac{1}{\sqrt{\mathcal{N}(\alpha_{\text{cat}})}} \left(|\alpha_{\text{cat}}\rangle + |-\alpha_{\text{cat}}\rangle\right), \tag{2.32}$$

where α_{cat} is the amplitude of the state and $\mathcal{N}(\alpha_{\text{cat}})$ is an appropriately-chosen normalization factor. This state is illustrated in Fig. 2.6 for $\alpha_{\text{cat}} = 1$.

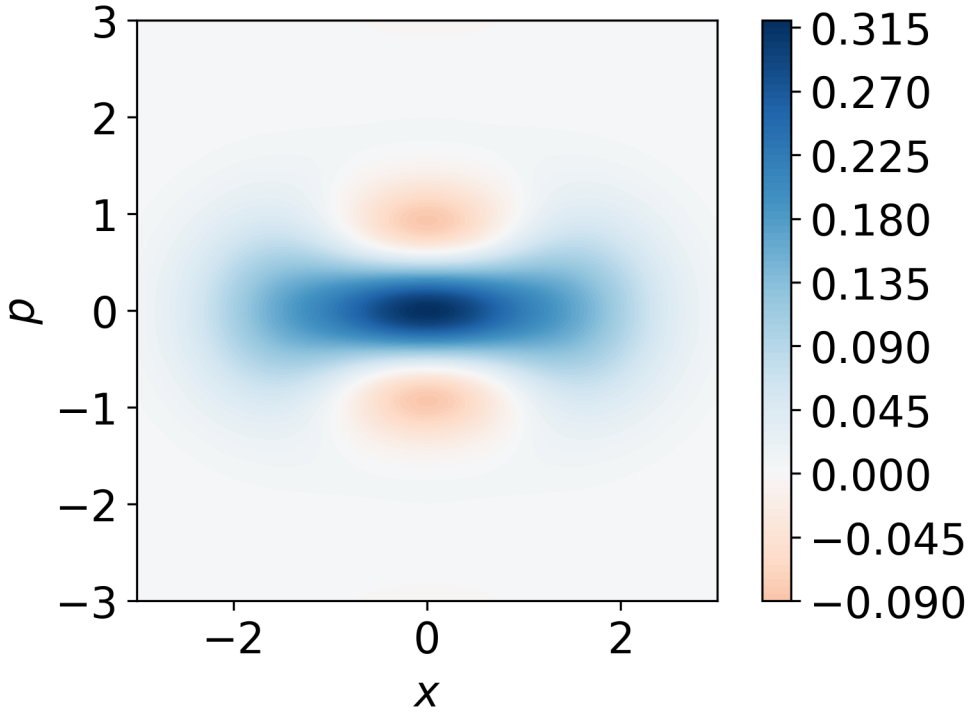

Figure 2.6: A plot of the Wigner quasiprobability distribution of a cat state $\frac{1}{\sqrt{\mathcal{N}}}(|\alpha\rangle + |-\alpha\rangle)$, where $\mathcal{N}$ is the appropriately-chosen normalization constant and $\alpha = 1$ so that the coherent lobes are located at $(x, p) = (\pm\sqrt{2}, 0)$ in phase space. Note the red negative regions of interference in the Wigner quasiprobability distribution, which indicate the quantum-mechanical nature of this state.

Cat states have standard use cases in the fields of quantum sensing and quantum error-correction, and we will discuss these in more detail in Chapter 4 and Chapter 6, respectively.

Both of these kinds of CVQC states are quite useful for quantum technology that operates using CVQC, and we use them in several research directions that we discuss in this thesis.

Chapter 3

Constructing Qubits from Quantum Harmonic Oscillator Qudits

Here, we take our first step toward the goal of using high-level computational techniques in order to improve the application of CVQC to solving problems of practical utility. In order to do so, we consider both theoretically and numerically the new realization of a qudit by the coupling of a qubit to a quantum harmonic oscillator, as introduced in Sec. 1. We term this unit of computation a *quantum-oscillator qudit* or "QO-qudit." The fundamental principles of such a qudit demonstrate how the ideas underlying the quantum harmonic oscillator (QHO) and continuous-variable quantum computation (CVQC) can be applied in order to construct more powerful units of quantum computation.

This section is based on a paper that I co-authored about this research project, which is published in *Physical Review A* [Liu+21]. The parts of this manuscript to which I solely contributed are approximately copied here with some additional background sections to which I contributed with others. Small changes have been made to highlight the computational aspects, and additional sections have been added to discuss relevant physical background.

In order to better appreciate our approach toward this goal, we first examine the physics of each of the component of a QO-qudit that we have not discussed yet beyond the qubit and the quantum harmonic oscillator, namely the manner in which the two are coupled, or the Jaynes-Cummings model, in Sec. 3.1. Then in Sec. 3.3, we introduce the qubit-oscillator coupling Hamiltonian in the context of our work and derive the available unitary operations as a starting point for the rest of the discussion. Next, we describe a general strategy for finding unitary operations that are closed for arbitrary d-QO-qudits in Sec. 3.4. A constructive universality proof of the QO-qudit operations is then given in Sec. 3.5. In order to make our construction practical for implementation, we give an explicit algorithm for this construction and show an example for an 8-QO-qudit in Sec. 3.6, where the theoretical bound on the number of pulses is also supported numerically up to a 46-QO-qudit. Finally, we summarize all of our results for QO-qudits in Sec. 3.7 and discuss potential future directions to explore.

3.1 Introduction to the Jaynes-Cummings Model

Having lain the fundamental background for both the qubit and the quantum harmonic oscillator in the preliminaries, we will now introduce the physical model that couples these two components together and hence underlies the qudit, which we term a quantum-oscillator qudit, or QO-qudit. This coupling arises via a model known in quantum physics as the *Jaynes-Cummings (JC) model*.

We first introduce this JC model and provide some historical background in Sec. 3.1.1. Then in Sec. 3.1.2, we present the Hamiltonian for the JC model and discuss some of the relevant underlying physics in greater detail.

3.1.1 Background on the Jaynes-Cummings Model

The *Jaynes–Cummings (JC) model* is a theoretical model in the field of quantum optics with broad applications in the fields of quantum computation and atomic physics. This model describes a system comprised of a two-level atom and a mode of an optical cavity with a discrete set of eigenvalues and eigenstates, one example of which is a quantum harmonic oscillator.

The JC model was originally developed in 1963 by Edwin Jaynes and Fred Cummings as a purely quantum mechanical model for these types of systems, which had previously only been modeled semi-classically (i.e., with the two-level atom modeled quantum-mechanically but the cavity mode modeled classically) [JC63].

3.1.2 Jaynes-Cummings Hamiltonian

An important part of understanding the JC model is understanding its energy, or its *Hamiltonian*.

For this discussion, as we derive the expression for the JC Hamiltonian and its implications for the qubit-oscillator system, we will take the two basis states of the qubit to be the ground state $|g\rangle$ and the excited state $|e\rangle$. The relevant operators to consider now are the *raising and lowering operators of the atom*, $\hat{\sigma}_+ = |e\rangle\langle g|$ and $\hat{\sigma}_- = |g\rangle\langle e|$, as well as the *atomic inversion operator* $\hat{\sigma}_z = |e\rangle\langle e| - |g\rangle\langle g|$.

With this discussion in mind, the Hamiltonian that models the energy of the full system is given by

$$\hat{H} = \hat{H}_{\text{field}} + \hat{H}_{\text{atom}} + \hat{H}_{\text{int}}, \tag{3.1}$$

where $\hat{H}_{\text{field}}$ represents the free-field Hamiltonian, $\hat{H}_{\text{atom}}$ represents the atomic excitation Hamiltonian, and $\hat{H}_{\text{int}}$ represents the Jaynes–Cummings interaction Hamiltonian. If we take the quantized radiation field to consist of a single bosonic mode and, for convenience, set the vacuum field energy to zero, then we find the following:

$$\hat{H}_{\text{field}} = \hbar\omega_c \hat{a}^\dagger \hat{a} \tag{3.2}$$

$$\hat{H}_{\text{atom}} = \hbar\omega_a \frac{\hat{\sigma}_z}{2} \tag{3.3}$$

$$\hat{H}_{\text{int}} = \frac{\hbar\Omega}{2} \hat{E}\hat{S}, \tag{3.4}$$

where ω_c represents the angular frequency of the mode, ω_a represents the atomic transition frequency, $\hat{E}$ represents the field operator of the radiation field $\hat{E} = \hat{E}_0(\hat{a} + \hat{a}^\dagger)$, and $\hat{S}$ represents the polarization operator that couples the atom to the field $\hat{S} = \hat{\sigma}_+ + \hat{\sigma}_-$.

Now, to solve for the interaction Hamiltonian $\hat{H}_{\text{int}}$, we switch our considerations from the Schrödinger picture to the interaction picture defined by the choice $\hat{H}_0 = \hat{H}_{\text{field}} + \hat{H}_{\text{atom}}$. By doing so, we find

$$\hat{H}_{\text{int}} = \frac{\hbar\Omega}{2}\left(\hat{a}\hat{\sigma}_- e^{-i(\omega_c+\omega_a)t} + \hat{a}^\dagger\hat{\sigma}_+ e^{i(\omega_c+\omega_a)t} + \hat{a}\hat{\sigma}_+ e^{-i(-\omega_c+\omega_a)t} + \hat{a}^\dagger\hat{\sigma}_- e^{i(-\omega_c+\omega_a)t}\right). \tag{3.5}$$

This Hamiltonian is tricky to solve analytically, and we note that there are both quickly-oscillating components with $(\omega_c + \omega_a)$ in the exponent and slowly-oscillating components with $(-\omega_c + \omega_a)$ in the exponent. In order to obtain a Hamiltonian that results in a solvable model, we apply the rotating-wave approximation and ignore the quickly-oscillating so-called "counter-rotating" terms with $(\omega_c + \omega_a)$ in the exponent, as these terms couple states of relatively large energy difference, meaning that the mixing of these states will be small.

Ignoring these terms and returning to the Schrödinger picture, we find a more tractable Hamiltonian for the JC model:

$$\hat{H}_{\text{JC}} = \hbar\omega_c\hat{a}^\dagger\hat{a} + \hbar\omega_a\frac{\hat{\sigma}_z}{2} + \frac{\hbar\Omega}{2}(\hat{a}\hat{\sigma}_+ + \hat{a}^\dagger\hat{\sigma}_-). \tag{3.6}$$

We can denote the state of the system by $|e/g,\, i\rangle$, where the first element describing the state is the state of the qubit (e for excited or g for ground) and the second element is the state of the oscillator (i.e., the label for its eigenstate in the QHO ladder).

Now, we find that under this model, there are oscillations induced between the states $|e,\, n-1\rangle$ and $|g,\, n\rangle$ with frequency $\frac{\sqrt{n}\Omega}{2}$. This discrete spectrum of frequencies is a purely quantum effect not seen with the semi-classical treatment of the system, and we exploit it in this work in order to demonstrate how universal computation can be achieved on QO-qudits.

3.2 Quantum Computing with Quantum-oscillator Qudits (QO-Qudits)

Now that we have analyzed the key interaction underlying a QO-qudit, as well as a key property, we will consider how we can use QO-qudits to perform CVQC.

Quantum harmonic oscillators are promising resources for quantum computation, owing to the infinite number of available states and their ubiquitous presence in nature as molecular vibrations [TV02], solid-state phonons [AM76], and optical/microwave cavities [BGO20]. The high dimensionality of oscillators provides not only a starting point for various bosonic quantum error-correcting codes [CLY97; GKP01; CMM99; Mic+16; NCS18b; Alb+18; NGJ20] but also a natural physical platform for universal quantum computation [Got99; Zho+03; NCS18a]. It is therefore desirable to achieve universal control over quantum harmonic oscillators. However, direct transitions driven between Fock states of a single oscillator will leak states outside of any finite computational space of an oscillator, due to its equally spaced and open ended spectrum. This means controlling the entire infinite dimensional

Hilbert space of an oscillator requires an infinite amount of energy and is thus highly unphysical.

In contrast to the infinite dimensions of oscillators, quantum computation often relies on a closed *finite* dimensional Hilbert space to represent quantum states and perform unitary operations on these states such that they remain inside the computational space [NC10]. By truncating the oscillator to a low energy subspace and performing computation inside this finite dimensional subspace, the unphysical requirement to the amount of control resources can be alleviated. It is both satisfying and somewhat surprising that the most elegant way to truncate an oscillator is to couple it to a qubit (a two-level system), the simplest primitive of quantum computation. The conversions between continuous-variable [BV05] and discrete-variable states enabled by the qubit+oscillator systems have spurred many important developments in the field. On the one hand, such qubit+oscillator systems have been used to realize various quantum error-correcting codes by encoding finite dimensional qubits into continuous-variable bosonic modes, including the GKP code [Pir+06; Mot+17; Flü+19], the binomial code [Mic+16], and the cat code [Ofe+16]. On the other hand, it has been shown that continuous-variable states can be transferred into multi-qubit states using primitive operations common to trapped ion systems [Has+21].

There are different ways to couple a qubit to an oscillator, and one of the most common couplings is described by the Jaynes-Cummings (JC) interaction [SK93] due to its broad applicability. Based on the JC Hamiltonian, Law and Eberly [LE96] demonstrated how arbitrary single-mode Fock states can be prepared by using sideband and carrier transitions in an alternating fashion. This idea was further extended by Mischuck and Mølmer to synthesize arbitrary unitary operations in a qubit-oscillator system by decomposing the unitary into many state-preparation protocols [MM13]. A different approach was taken to achieve universality for a resonantly coupled superconducting cavity to an artificial atom, despite the requirement of a slow adiabatic crossover for cavity states from the coupled to the uncoupled regime [Str12]. Moreover, universal control over an oscillator is also discussed beyond the JC interaction. For example, a simple quantum circuit was proposed to realize universal control by carefully engineering a partially resonant and partially dispersive coupling between an auxiliary three-level system and an oscillator [San05]. Universal control was also demonstrated for an oscillator coupled to a qubit fully dispersively [Kra+15], by combining a selective number-dependent arbitrary phase operation with a displacement operation on the oscillator.

In the various protocols developed over the past two decades on universal control over oscillators, the question of how to close an arbitrary finite dimensional subspace of an oscillator was investigated far less frequently. Childs and Chuang [CC00] showed that the lowest two levels of the oscillator can be closed to form a four dimensional Hilbert space where arbitrary unitary operations can be realized. This closed, truncated space has been used to experimentally implement the Deutsch-Josza algorithm on a trapped ion quantum computer [Gul+03; Sch+03]. One of the key ideas in their construction is to synchronize the rotations on the two Bloch spheres associated with the two 2-dimensional subspaces, using dynamical decoupling by a four-pulse sequence adapted from nuclear magnetic resonance [VC05].

The more recent work of Mischuck and Mølmer [MM13] constructed arbitrary unitary operations in the lowest $(n+1)$-dimensional subspace of an oscillator (for any $n \in \mathbb{Z}$) by decomposing the unitary into a series of modified state preparation protocols. Each state

preparation unitary is then synthesized without leaking states in the computational space to the outside. They further proved arbitrary two-qudit gates are possible by coupling two oscillators to the same qubit, enabling qudit-based quantum computation. By synthesizing arbitrary independent sideband transitions in each sideband subspace using a truncated Fourier series on the rotation angles [PK06], they demonstrated the ability to realize an arbitrary unitary on the $(n+1)$-dimensional subspace, using $O(n^{18.5}\delta^{-3})$ pulses (together with a large prefactor), where δ is the error of the synthesized unitary with respect to the target unitary. This employs a powerful technique from optimal control theory, with further efficiencies gained through numerical optimization. On the other hand, the use of optimal control theory and optimization renders the protocol *approximate* in nature. Similar ideas for truncating the oscillators has been employed in the context of perfectly generating atomic coherence from optical coherence in a recent work [GS20].

In the present work, we address the same challenge raised by [MM13], but we seek to solve the problem of closing off the $(n+1)$-dimensional oscillator subspace using a formalism which is fully analytical, sans results from optimal control theory or optimization. This allows us to fully understand the algebraic structures present in the JC Hamiltonian and how they may be exploited with explicit algorithms. Also, having protocols which are exact opens the door to understanding trade-offs and potential impact of errors. In principle, the powerful optimization techniques of [MM13] could also be deployed on top of a fully analytical solution to improve its scaling. Moreover, from the viewpoint of control theory, we would like our control set to be as simple as possible. Ideally, we want to use a finite set of basic control operations (e.g., laser frequencies) regardless of the dimension of the computational space, as opposed to the constructions such as those employing a dispersive coupling Hamiltonian where the number of control frequencies increases linearly with the dimension of the computational space [Kra+15].

We produce an analytical solution by building on the approach of Ref. [CC00] to systematically close off an arbitrary $(n+1)$-dimensional low energy subspace of an infinite dimensional oscillator via coupling to a single qubit; further, we construct universal unitary operations within this subspace *fully analytically* using only first-order sideband and carrier pulses. This analytical construction of a unitary relies on exploiting algebraic structures in the problem. The key structures arise from the well-known fact that the full Hilbert space of the qubit+oscillator is naturally partitioned into an infinite number of 2-dimensional subspaces, and only the subspace at the boundary leaks states in the computational space to the outside. We exploit these structures by constructing a set of elementary $SU(2)$ rotations on these arrays of 2-dimensional subspaces as the instruction set for constructing arbitrary unitaries. We give a recursive protocol to construct such elementary $SU(2)$ rotations by cleaning each 2D subspace one by one without accumulating any errors. Due to this recursive fashion, we refer to the construction process as *recursive cleaning* and designate the qudits constructed as *qubit-oscillator qudits* (QO-qudits). It should be noted that our recursive cleaning construction is applicable to a larger class of Hamiltonian beyond the JC interaction, but we will use the JC interaction for the ease of discussion. Also, note that the qubit doubles the Hilbert space of the truncated oscillator resulting in a larger $d = 2(n+1)$ dimensional space. We prove universal control on this enlarged space, and this naturally implies universal control on the $(n+1)$-dimensional truncated oscillator, which is a subspace of the enlarged d-dimensional space. We shall use the notation d-QO-qudit to represent a

qubit coupled to a truncated oscillator with Fock levels $\{|0\rangle, |1\rangle, |2\rangle, \ldots, |n\rangle\}$. This convention is consistent with previous work in Ref. [CC00], despite doubling the dimension of the computational space in Refs. [Kra+15; MM13].

3.3 Theoretical Model for the QO-Qudits

For completeness, we give a short review of the Hamiltonian used in our analysis. Note that we do not use the hat notation for operators in this section (i.e., we do not denote the operator A by $\hat{A}$) because we instead take the notation that operators with no hat operate on the sideband qubit manifold that we will introduce in more detail, while the operators with tildes operate on the carrier qubit manifold, also to be introduced in more detail. The total Hamiltonian of the system is given by $H = H_0 + H_I$, where $H_0 = \hbar\omega_0\sigma_z/2 + \hbar\omega_z a^\dagger a$ is the non-interacting Hamiltonian of the qubit and oscillator. The interaction between the qubit and the oscillator can be described by a spin-1/2 particle interacting with an electromagnetic (EM) field,

$$H_I = -\vec{\mu}\cdot\vec{B}, \tag{3.7}$$

where $\vec{\mu} = \mu\vec{\sigma}/2$ is the magnetic moment and $\vec{B} = Bx\cos(kz - \omega t + \Phi)$ is the magnetic field associated with the external drive. In the second quantized form, the position $z = z_0(a + a^\dagger)$, where z_0 is the characteristic length of the oscillator's ground state motional wave function, a and $a^\dagger$ are the annihilation and creation operators of the oscillator.

Under the dipole approximation $\eta \equiv kz_0 \ll 1$ and abandoning the fast rotating terms, we can expand Eq. (3.7) into power series of η. Depending on the frequency of the external drive ω, the following unitary operations that couple different states of the QO-qudits may be implemented. Denote the computational basis of the QO-qudit as $\{|\alpha, n\rangle\}$ where $\alpha = 0, 1$ labels the two qubit states, and $n = 0, 1, 2, \ldots$ labels the oscillator levels. When $\omega = \omega_0$, the EM field couples the lower and upper levels of the qubit directly, leading to a carrier pulse V_c that performs the same rotation $P(\theta, \phi)$ in each subspace $\{|0, n\rangle, |1, n\rangle\}$

$$V_c(\theta, \phi) = \exp\left[i\frac{\theta}{2}(e^{i\phi}\sigma^+ + e^{-i\phi}\sigma^-)\right] = \bigoplus_{n=0}^{\infty} P(\theta, \phi), \tag{3.8}$$

where $P(\theta, \phi)$ is a single qubit rotation around an axis with angle ϕ in the xy-plane by an amount θ. We can likewise couple each pair of $\{|0, n\rangle, |1, n-1\rangle\}$ $(n = 1, 2, \ldots)$ states using the first-order red sideband transition by setting $\omega = \omega_0 - \omega_z$, leading to

$$V_s(\theta, \phi) = \exp\left[i\frac{\theta}{2}(e^{i\phi}\sigma^+ a + e^{-i\phi}\sigma^- a^\dagger)\right] = \bigoplus_{n=1}^{\infty} Q_n(\theta, \phi). \tag{3.9}$$

In the above, $\sigma^\pm = (\sigma_x \pm i\sigma_y)/2$ and σ_x, σ_y, σ_z are the Pauli operators of the qubit. The rotation angle θ and rotation axis ϕ are given by

$$\theta = -\frac{\mu B t \eta^m}{2\hbar m!}, \tag{3.10}$$

$$\phi = \Phi + (m \mod 4)\frac{\pi}{2}, \tag{3.11}$$

with $m = 0$ for the carrier pulse and $m = 1$ for the first-order sideband pulse, where t is the pulse duration. Note the red sideband performs a n-dependent rotation Q_n along the same axis defined by ϕ but by a different rotation angle on each 2D subspace. The first-order blue sideband as well as higher order sideband transitions can be similarly derived. Since the blue sideband pulse can be obtained by conjugating the red sideband pulse using a carrier π-pulse, we only need to consider the carrier and the red sideband pulses. In the following, we will show that V_c and V_s as defined in Eqs. (3.8) and (3.9) are sufficient to generate arbitrary unitary operations in QO-qudits.

An energy level diagram of the qubit-oscillator system as well as relevant transitions are labeled in Fig. 3.1, with the definition of a d-QO-qudit explicitly shown. To simplify the discussion, we partition the Hilbert space of a d-QO-qudit into sets of two-dimensional subspaces in two different ways based on the action of the red sideband pulse and the carrier pulse. Each two-dimensional subspace can be viewed as a single qubit. The sideband qubit manifold (sQM) are spanned by states $\{|0,\, j\rangle\,,\, |1,\, j-1\rangle\}_{j=1}^{n}$ where each subspace is labeled by its corresponding value of j. We do not include states $|0,\, 0\rangle$ and $|1,\, n\rangle$ in sQM because they remain intact during the sideband operation (up to a parity phase). The carrier qubit manifold (cQM) are spanned by $\{|0,\, j\rangle\,,\, |1,\, j\rangle\}_{j=0}^{n}$, where j start from 0 instead of 1. According to the above definition, there are n nontrivial 2D subspaces in the sQM and $(n+1)$ nontrivial 2D subspaces in the cQM. To differentiate the unitary operations on these two qubit manifolds, we will use a tilde when referring to the cQM.

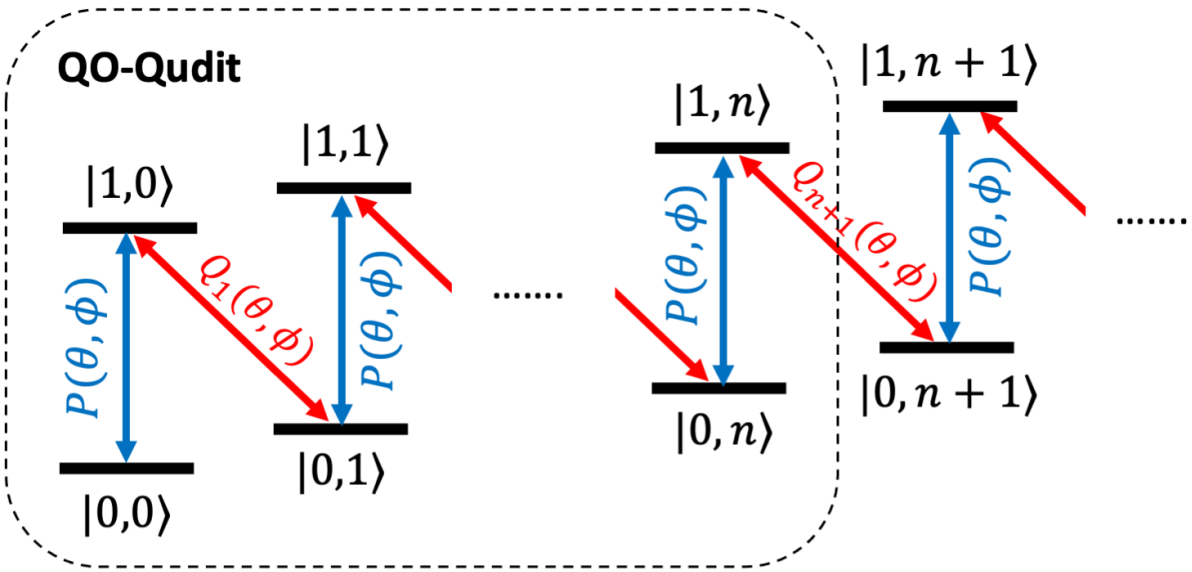

Figure 3.1: Energy level diagram in a d-QO-qudit. The first index in the state label represents the qubit state and the second represents the oscillator Fock level. Red arrows indicate states that are coupled through red sideband transitions (forming the sQM), while blue arrows indicate states coupled through the carrier pulse (forming the cQM).

3.4 Closing Off an Infinite-dimensional Harmonic Oscillator

The first step toward constructing a QO-qudit is to close off a low energy subspace of the oscillator, which serves as the computational space. The closedness of a computational space means that any the states inside it will not leak to any states outside while performing any quantum computations. This is an important step to accomplish since any leakage will result in a non-unitary evolution of the computational space and ruin the computation immediately. In general, this is difficult to achieve because there are infinitely many states outside of the finite computational space for an oscillator, which suggests that we may need to eliminate infinitely many coupling amplitudes between the computational space and its orthogonal space. This general condition, nevertheless, is greatly simplified in our case due to the partition of the full Hilbert space into many 2D subspaces. Moreover, since each unitary operation may leak states outside, there is leakage possibly at every step in performing quantum computation as is the case in Ref. [MM13]. We take a different approach here by selecting a subset of unitary operations such that the closedness of the computational space is always guaranteed. We will describe in detail how this can be accomplished in the following.

In particular, in Sec. 3.4.1, we present a method by which we close off a transition in order to realize a finite Hilbert space. Then in Sec. 3.4.2, we discuss *conjugacy classes*, a related component that is fundamental to our recursive cleaning proof.

3.4.1 Close Off the Transition on the Boundary

From Fig. 3.1, we first note that all carrier transitions $P(\theta, \phi)$ do not leak states in the d-QO-qudit outside for any d. As a result, we need only focus on the sideband pulses. The only sideband transition that leaks states is the $Q_{n+1}(\theta, \phi)$ transition on the boundary that couples the $|1, n\rangle$ state inside to the state $|0, n+1\rangle$ outside of the QO-qudit. It is therefore sufficient to shut off the coupling between these two states. We can calculate explicitly the matrix elements of Q_{n+1} to be

$$Q_{n+1}(\theta, \phi) = \begin{bmatrix} \cos\theta_{n+1} & ie^{-i\phi}\sin\theta_{n+1} \\ ie^{i\phi}\sin\theta_{n+1} & \cos\theta_{n+1} \end{bmatrix}, \tag{3.12}$$

where $\theta_{n+1} = \frac{\sqrt{n+1}}{2}\theta$. When driving a multiple of 2π pulse from $|0, n+1\rangle$ to $|1, n\rangle$, i.e., $\theta_{n+1} = \pi k$ where k is an integer, we can decouple these two states since $\sin\theta_{n+1} = 0$. The smallest θ (shortest pulse, $k = 1$) that can realize this decoupling is

$$\theta = \frac{2\pi}{\sqrt{n+1}}, \tag{3.13}$$

which gives

$$Q_{n+1}\left(\frac{2\pi}{\sqrt{n+1}}, \phi\right) = \begin{bmatrix} -1 & 0 \\ 0 & -1 \end{bmatrix}. \tag{3.14}$$

This constraint also guarantees that the operation on $|1, n\rangle$ is trivial (up to a parity phase), which is why we exclude it from the subspaces of the sQM.

3.4.2 Conjugacy Class

It may be argued that the above requirement on θ to be discrete special values seems to significantly constrain the number of possible unitaries we can apply, and thus hampers the universality of the QO-qudit. However, this is not the case because conjugating a closed sideband pulse using an arbitrary unitary operation leads to another closed unitary operation, i.e., an operation $F = U^\dagger G U$ will be closed for an arbitrary unitary U if the given unitary G is closed. In the case of $SU(2)$, F will be a rotation on the Bloch sphere by the same angle θ as the original rotation G, but along a different axis defined by U. This concept of the *conjugacy class* of a given unitary operation provides us enough flexibility to construct new unitaries and is the key idea behind our recursive cleaning proof, which we shall discuss in detail in the next section.

3.5 Universality Proof

With a closed computational space (QO-qudit) established, we next construct arbitrary unitary operations on this subspace using the operations given in Eqs. (3.8) and (3.9) subject to the closedness condition, which we refer to as the universality of the QO-qudit. We prove the QO-qudit universality in this section in two different pictures. We give some intuition of the proof in the Hamiltonian picture in Sec. 3.5.1. We then move to the unitary picture and give explicit constructions for arbitrary QO-qudit unitary operations in two steps, as is described in Sec. 3.5.2 and Sec. 3.5.3. In particular, we first reduce the QO-qudit universality to *elementary* $SU(2)$ rotations in sQM in Sec. 3.5.2. Then we give explicitly constructions for such elementary $SU(2)$ rotations in the sQM in Sec. 3.5.3.

3.5.1 Intuition in the Hamiltonian Picture

One of the well-known criteria for the universality of qudit-based quantum computation is the ability to perform arbitrary $SU(2)$ rotations between any two levels in the qudit space [Got99; BOB05]. In the Hamiltonian picture, this means we need to obtain the full $\mathfrak{su}(d)$ Lie algebra with $(d^2 - 1)$ elements that generates the $SU(d)$ group of the d-QO-qudit. Matrix representations of such generators are also known as the generalized Gell-Mann matrices (GGMs) [BK08] which are all Hermitian (See Appendix A for a definition of GGMs). In the special case of a qubit, $d = 2$, there are three generators, i.e., the Pauli matrices. Similar to the qubit case, these GGMs can be classified into three categories denoting the rotation of x, y, and z type, respectively. Moreover, the z type GGMs may be obtained by multiplying the x and y types. We will give an argument on how to generate all the GGMs of a single d-QO-qudit. The aim of this section is mainly to convey an intuition of our proof. In the next several sections we will provide a rigorous proof in the unitary picture.

As we noted before, the first observation from Fig. 3.1 is that the sideband pulse (or the carrier pulse) naturally partitions the d-QO-qudit into n small 2D subspaces (again states $|0, 0\rangle$ and $|1, n\rangle$ are discarded). In other words, the Hamiltonian that generates the sideband pulse can be written as a direct sum of n GGMs. By controlling the phase in Eq. (3.11),

the n GGMs can either be of x or y type. Therefore, one simple idea to generate a single clean GGM is to cancel the other $(n-1)$ GGMs in the direct sum by dynamical decoupling. The $\sqrt{n}$ dependency of the Rabi frequency for each subspace in the sideband pulse provides a possibility for such decoupling to be done. To see this more clearly, imagine that we have the GGM H_n for the d-QO-qudit in the sideband manifold

$$H_n = 0_1 \oplus \cdots \oplus \Sigma_k \oplus \cdots \oplus 0_n \oplus h_{n+1} \oplus \cdots , \tag{3.15}$$

where 0_n is a null Hamiltonian in the n^{th} subspace, $\Sigma_k \in \{\sigma_x, \sigma_y\}$, $h_{n+1} = \hat{\boldsymbol{r}}_{n+1} \cdot \boldsymbol{\sigma}$ is some arbitrary Hamiltonian in the $(n+1)^{\text{th}}$ subspace defined by a unit vector $\hat{\boldsymbol{r}}_{n+1}$. Our goal is then to create the corresponding GGM H_{n+1} for the $(d+2)$-QO-qudit

$$H_{n+1} = 0_1 \oplus \cdots \oplus \Sigma_k \oplus \cdots \oplus 0_n \oplus 0_{n+1} \oplus h_{n+2} \oplus \cdots \tag{3.16}$$

Recall that we can always flip the sign of a single-qubit Hamiltonian by conjugating it using an $SU(2)$ rotation along an axis that is perpendicular to the Hamiltonian. One simple example of such phase flip is $X^\dagger Z X = -Z$, where $X = i\sigma_x$. We may therefore use such dynamical decoupling trick to flip the phase of h_{n+1} in Eq. (3.15) by conjugating it with a set of red sideband pulse V_s such that

$$h_{n+1} + (V_s^\dagger)_{n+1} h_{n+1} (V_s)_{n+1} = h_{n+1} - h_{n+1} = 0_{n+1}. \tag{3.17}$$

This reproduces the 0_{n+1} term in Eq. (3.16). This conjugation of course also alters Σ_k in Eq. (3.15) into a different Hamiltonian, but the deviation from Σ_k may be cleaned again by conjugating using another set of red sideband pulses to fully recover Eq. (3.16). These step can be repeated recursively to obtain GGMs for any n in the sQM manifold, and this is also the main technique we will use in our proof in the next few sections.

The decoupling described above will enable us to generate GGMs that couple two adjacent states $\{|0,\, j\rangle\,, |1,\, j-1\rangle\}$, but it remains to generate other GGMs that couple states far from each other. This leads to our second observation from Fig. 3.1: alternatively applying the GGMs in the sQM and those in the cQM can couple states far apart together, provided that we can access the cQM GGMs. We will show in the next section how rotations in the cQM can be generated from those in the sQM. These GGMs then give us the universality for the full $SU(d)$ group of a d-QO-qudit.

3.5.2 From Clean Elementary $SU(2)$ Rotations in sQM to QO-Qudit Universality

In this section, we will start from the qudit criteria in Ref. [Got99; BOB05], and show that arbitrary $SU(2)$ rotations between any two levels in the QO-qudit can be obtained from a set of clean elementary $SU(2)$ rotations in sQM alone. This is accomplished in two steps as follows. First, in Sec. 3.5.2.1, we reduce the QO-qudit universality to the ability to construct *arbitrary clean* $SU(2)$ rotations in *both* sQM and cQM. Secondly, by a basis transformation from the sQM to the cQM, combining with dynamical decoupling [VC05], we show that constructing *arbitrary clean* $SU(2)$ rotations in both sQM and cQM can be further reduced to the construction of *elementary clean* $SU(2)$ rotations *solely* in the sQM in Sec. 3.5.2.2.

3.5.2.1 Arbitrary clean $SU(2)$ rotations in sQM and cQM implies QO-qudit universality

We define an arbitrary clean $SU(2)$ rotation in the k^{th} subspace of sQM for a d-QO-qudit ($d = 2(n+1)$) as

$$U_n^{(k)} = I_1 \oplus I_2 \oplus \cdots \oplus W_k \oplus \cdots \oplus I_n, \tag{3.18}$$

which performs a nontrivial arbitrary $SU(2)$ rotation W_k in the k^{th} sideband subspace and leaves the other sideband qubits unchanged, i.e., acted by an identity operation. Similarly, an arbitrary clean $SU(2)$ rotation in the k^{th} subspace of the cQM is likewise denoted as

$$\tilde{U}_n^{(k)} = \tilde{I}_0 \oplus \tilde{I}_1 \oplus \cdots \oplus \tilde{W}_k \oplus \cdots \oplus \tilde{I}_n, \tag{3.19}$$

where tilde is used to distinguish it from the case of sQM above. Also, note that $\tilde{U}_n^{(k)}$ is a direct sum of $(n+1)$ carrier qubits, while $U_n^{(k)}$ is composed of n sideband qubits, which is evident from Fig. 3.1.

For the QO-qudit universality, we require arbitrary unitary operations V_t between any two levels, say $|\alpha, p\rangle$ and $|\beta, q\rangle$, where $p \leq q$ without loss of generality and α, $\beta = 0$ or 1. In the following, we give explicit constructions in the case of $\alpha = 0, \beta = 1$; the other three cases ($\alpha = \beta = 0$, $\alpha = \beta = 1$, $\alpha = 1$ and $\beta = 0$) may be constructed in a similar way.

If $p = q$, V_t simply corresponds to a clean $SU(2)$ rotation $\tilde{U}_n^{(p)}$ in the cQM given by Eq. (3.19). In the case of $p < q$, there is no single rotation in Eq. (3.18) or (3.19) that can produce the coupling between $|0, p\rangle$ and $|1, q\rangle$. However, we may first realize a unitary $\tilde{U}_n^{(p)}$ such that the $SU(2)$ rotation in its p^{th} subspace $\tilde{W}_p$ satisfies $\tilde{W}_p = V_t$. We may then perform a sequence of Pauli X gates to swap the state $|1, p\rangle$ with $|0, p+1\rangle$, and then $|0, p+1\rangle$ with $|1, p+1\rangle$ and so on, until finally $|1, q\rangle$ is reached. Such a sequence of swap operations can be easily realized by chaining multiple clean $SU(2)$ rotations in Eq. (3.18) and Eq. (3.19) together. The overall pulse sequence to realize V_t between $|0, p\rangle$ and $|1, q\rangle$ (with the rest state unaltered) is then

$$[U_n^{(p+1)}\tilde{U}_n^{(p+2)} \cdots U_n^{(q-1)}\tilde{U}_n^{(q)}]^\dagger \cdot \tilde{U}_n^{(p)} \cdot [U_n^{(p+1)}\tilde{U}_n^{(p+2)} \cdots U_n^{(q-1)}\tilde{U}_n^{(q)}], \tag{3.20}$$

where $W_k = \tilde{W}_k = X$ in all $U_n^{(k)}$ and $\tilde{U}_n^{(k)}$ for $k = p+1, p+2, \ldots, q-1, q$. $X = i\sigma_x$ is the usual Pauli X gate.

3.5.2.2 Elementary clean $SU(2)$ rotations in sQM implies arbitrary clean $SU(2)$ rotations in sQM and cQM

In the above, we have shown that QO-qudit universality can be constructed from a set of clean arbitrary $SU(2)$ rotations in sQM and cQM given by Eq. (3.18) and Eq. (3.19). Now we will show that such clean arbitrary $SU(2)$ rotations may be constructed solely from a set of elementary clean $SU(2)$ rotations in sQM alone.

We first define an *elementary* clean $SU(2)$ rotation $V_n^{(k)}$ in sQM (for the k^{th} subspace) for a d-QO-qudit ($d = 2(n+1)$)

$$V_n^{(k)} = I_1 \oplus I_2 \oplus \cdots \oplus \Sigma_k \oplus \cdots \oplus I_n, \tag{3.21}$$

where $\Sigma_k = \{X, Y, I, -I\}$. It is now straightforward to see how an *arbitrary* clean $SU(2)$ rotation $U_n^{(k)}$ in Eq. (3.18) may be obtained from Eq. (3.21) and sideband transitions using refocusing.

The basic idea of refocusing has been presented in the Hamiltonian picture in Sec. 3.5.1, we shall state it here again in the unitary picture here. For an arbitrary single qubit rotation $U(\theta, \phi)$ in the xy-plane, we first note that by conjugating with Z gate, we can reverse the rotation direction $ZU(\theta, \phi)Z = U(-\theta, \phi)$. Therefore, the following pulse sequence would effectively cancel the effect of $U(\theta, \phi)$ and produce an identity operation

$$U(\theta, \phi) \cdot Z \cdot U(\theta, \phi) \cdot Z = I. \tag{3.22}$$

Now, note that an arbitrary rotation W_k on the k^{th} subspace of sQM in Eq. (3.18) can be decomposed as two rotations with rotation axis lying in the xy-plane (see Appendix B). Therefore, it suffices to assume $W_n^{(k)}$ is a rotation with an axis in the xy-plane. Imagine we start from a sideband transition in Eq. (3.9), where (θ, ϕ) are properly chosen such that the sideband rotation in the k^{th} subspace satisfies $Q_k(2\theta, \phi) = W_n^{(k)}$. And this also means for all other subspaces, there are nontrivial rotations that are not the identity operation. We will use refocusing to eliminate those unwanted rotations in the other subspaces as follows. From Eq. (3.21), we may construct the following unitary $\boldsymbol{Z}_n^{(k)}$

$$\boldsymbol{Z}_n^{(k)} = Z_1 \oplus Z_2 \oplus \cdots \oplus Z_{k-1} \oplus I_k \oplus Z_{k+1} \oplus \cdots \oplus Z_n, \tag{3.23}$$

which applies a Pauli Z gate to each sideband qubit except the k^{th} one (trivially acted upon by identity). The following construction achieves Eq. (3.18)

$$U_n^{(k)} = V_s(\theta, \phi)\boldsymbol{Z}_n^{(k)\dagger}V_s(\theta, \phi)\boldsymbol{Z}_n^{(k)}, \tag{3.24}$$

since $Q_j(\theta, \phi) \cdot Z_j \cdot Q_j(\theta, \phi) \cdot Z_j = I$ for all $j \neq k$. While for the k^{th} subspace,

$$Q_k(\theta, \phi) \cdot I_k \cdot Q_k(\theta, \phi) \cdot I_k = Q_k(2\theta, \phi) = W_k. \tag{3.25}$$

This completes our construction of Eq. (3.18) from Eq. (3.21).

We now turn to construct arbitrary clean rotations in the cQM. This is facilitated by the fact that alternations of $\pm I$ in the sQM is equivalent to I and Z gates in the cQM up to a difference in the local parity. As an example, this is illustrated in Fig. 3.2 for the first four sideband qubits being $-I_1 \oplus I_2 \oplus -I_3 \oplus I_4$. They are equivalent to a gate sequence of $\tilde{Z}_0 \oplus -\tilde{Z}_1 \oplus \tilde{Z}_2 \oplus -\tilde{Z}_3$ for the first four carrier qubits.

In general, this conversion from the sQM to the cQM is described by

$\tilde{W}_{i-1}$	W_i	W_{i-1}
$\tilde{Z}$	$-I$	$+I$
-$\tilde{Z}$	$+I$	$-I$
$\tilde{I}$	$+I$	$+I$
-$\tilde{I}$	$-I$	$-I$

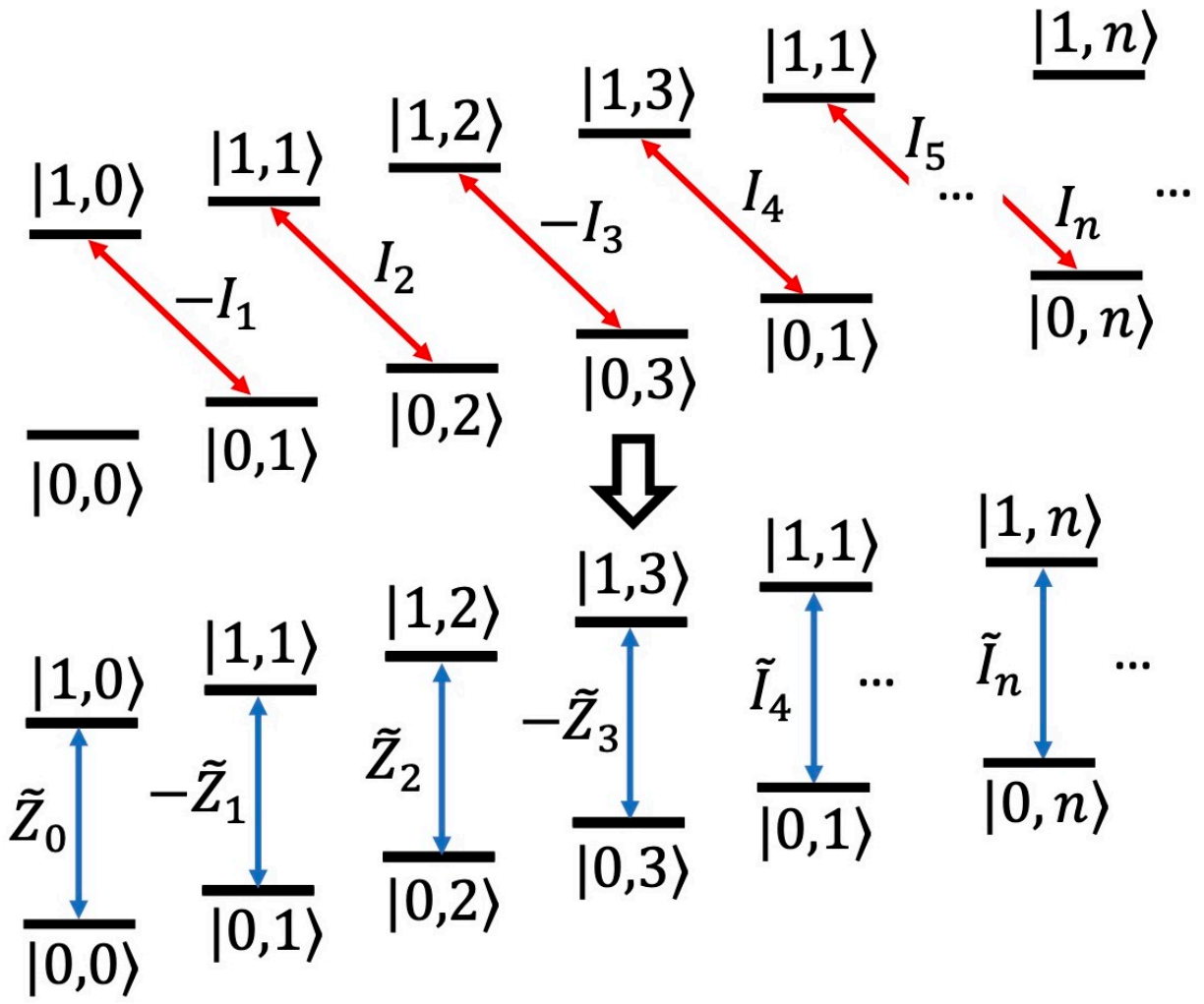

Figure 3.2: Translating between operations on sideband subspaces and carrier subspaces. The top energy diagram represents the unitary $-I_1 \oplus I_2 \oplus -I_3 \oplus I_4 \oplus \cdots \oplus I_n \oplus \cdots$ acting on sideband subspaces which translates to the bottom energy diagram of $\tilde{Z}_0 \oplus -\tilde{Z}_1 \oplus \tilde{Z}_2 \oplus -\tilde{Z}_3 \oplus \tilde{I}_4 \oplus \cdots \oplus \tilde{I}_n \oplus \cdots$.

The above conversion also means that the $\{I, -I\}$ in each subspace from 1 to $(n+1)$ in sQM is equivalent to $\{\tilde{I}, \tilde{Z}\}$ in subspaces from 0 to n in the case of cQM. Therefore, it is guaranteed that we can obtain the following unitary $\tilde{\boldsymbol{Z}}_n^{(k)}$ in cQM

$$\tilde{\boldsymbol{Z}}_n^{(k)} = \tilde{Z}_0 \oplus \tilde{Z}_1 \oplus \cdots \oplus \tilde{Z}_{k-1} \oplus \tilde{I}_k \oplus \tilde{Z}_{k+1} \oplus \cdots \oplus \tilde{Z}_n, \tag{3.26}$$

which performs a Pauli Z gate on all carrier qubits of a d-QO-qudit, except the k^{th} qubit where it performs the identity. It follows that for a clean arbitrary unitary in Eq. (3.19) where the k^{th} subspace has a nontrivial rotation $\tilde{W}_k$ (assuming it is in xy-plane without loss of generality), we may choose a carrier pulse in Eq. (3.8) with (θ, ϕ) properly such that the carrier transition on each carrier qubit $P(2\theta, \phi) = \tilde{W}_k$. The following construction

reproduces $\tilde{U}_n^{(k)}$

$$\tilde{U}_n^{(k)} = V_c(\theta,\, \phi)\tilde{\boldsymbol{Z}}_n^{(k)\dagger}V_c(\theta,\, \phi)\tilde{\boldsymbol{Z}}_n^{(k)}, \tag{3.27}$$

due to Eq. (3.22) for all carrier subspaces except the k^{th} one, and for the k^{th} subspace,

$$P(\theta,\, \phi)\cdot\tilde{I}_k\cdot P(\theta,\, \phi)\cdot\tilde{I}_k = P(2\theta,\, \phi) = \tilde{W}_k. \tag{3.28}$$

This completes our construction of Eq. (3.19) from Eq. (3.21). Specifically, by choosing $\tilde{W}_k$ to be a rotation on the k^{th} carrier qubit with a closed trajectory on its Bloch sphere, we can accumulate an arbitrary Berry phase on the $|0,\, k\rangle$ state. Combining many such Berry phase rotations together for different k, we immediately realize the SNAP gate in Ref. [Kra+15].

3.5.3 Construction for the Clean Elementary $SU(2)$ Rotations in sQM

In this section, we begin by giving a *recursive* proof in Sec. 3.5.3.1 for how to construct the *elementary* clean $SU(2)$ rotations in the sQM, as in Eq. (3.21). Our proof utilizes the repeated pattern of the oscillator's spectrum. In doing so, we first give the base case of a two-level oscillator coupled to a qubit, and then show how to clean up each subspace into the elementary operations for an $(n+1)$-level oscillator recursively. We then provide bounds on the number of sideband pulses required in our construction in Sec. 3.5.3.2.

3.5.3.1 Recursive proof

Our claim is that we can construct arbitrary clean rotations upon any 2D subspace in the sQM manifold of a d-QO-qudit (again $d = 2(n+1)$), $V_n^{(k)} = I_1 \oplus I_2 \oplus \cdots \oplus \Sigma_k \oplus \cdots \oplus I_n \oplus \cdots$ with $\Sigma_k \in \{X,\, Y,\, -I\}$, $k \leq n$. When $n \leq 2$, we provide a direct construction. For $n = 1$, we can easily select $(\theta,\, \phi)$ such that $V_1^{(1)} = V_s(\theta,\, \phi) = \Sigma_1$. For $n = 2$, we will directly construct $I_1 \oplus X_2$ and $X_1 \oplus I_2$. Obtaining Y instead of X simply corresponds to mapping every red sideband pulse $V_s(\theta,\, \phi) \mapsto V_s(\theta,\, \phi + \frac{\pi}{2})$, and obtaining $-I$ instead of X is done by repeating the sequence as $X^2 = -I$ (note we define $X = i\hat{\sigma}_x$ throughout the paper). The following pulse sequences use conjugation to orchestrate clean rotations on the first two subspaces in 4 pulses:

$$\begin{aligned} &V_s\left(\sqrt{2}\pi,\, \phi_1\right) V_s\left(\frac{\pi}{2},\, 0\right) V_s\left(\sqrt{2}\pi,\, \phi_1\right) V_s\left(-\frac{\pi}{2},\, 0\right) \\ &\qquad = X_1 \oplus I_2 \oplus \cdots \end{aligned} \tag{3.29}$$

$$\begin{aligned} &V_s\left(2\pi,\, \phi_2\right) V_s\left(\frac{\pi}{2\sqrt{2}},\, 0\right) V_s\left(2\pi,\, \phi_2\right) V_s\left(-\frac{\pi}{2\sqrt{2}},\, 0\right) \\ &\qquad = I_1 \oplus X_2 \oplus \cdots \end{aligned} \tag{3.30}$$

where $\phi_1 = \cos^{-1}\left(\cot\frac{\pi}{\sqrt{2}}\right)$ and $\phi_2 = \cos^{-1}\left(\cot\sqrt{2}\pi\right)$.

An example pulse sequence for $n = 2$ is shown in Fig. 3.3. For $n > 2$, we provide a recursive construction that also makes use of conjugation sequences to manipulate particular subspaces without disturbing others.

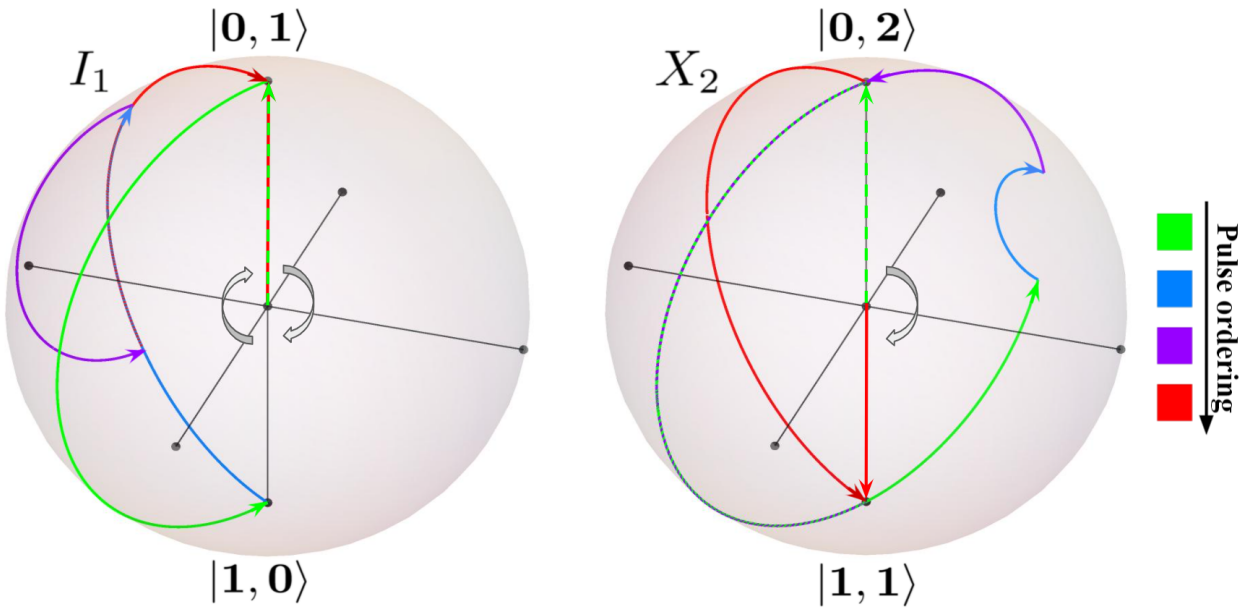

Figure 3.3: A pulse sequence for $n = 2$ to realize $I_1 \oplus X_2$ in the first two sQM subspaces. Each Bloch sphere represents an sQM subspace spanned by the states at the North and South pole. The initial Bloch vector in dashed green (pointing towards North pole) is rotated to the final Bloch vector in solid red with the four pulse sequence from Eq. (3.30).

Base Case We begin by cleaning (taking to the identity) two subspaces μ_1, $\mu_2 \in M = \{1, \ldots, n\} \setminus k$ with the constraint:

$$\sqrt{\frac{k}{\mu_1}},\ \sqrt{\frac{k}{\mu_2}} \notin \mathbb{Z}. \tag{3.31}$$

Using red sideband pulses $V_s(\theta, \phi)$, we can construct

$$\begin{aligned} U_2 &= V_s\left(\frac{2\pi}{\sqrt{\mu_1}}, 0\right) V_s\left(\frac{\pi}{\sqrt{\mu_2}}, \frac{\pi}{2}\right) V_s\left(\frac{2\pi}{\sqrt{\mu_1}}, 0\right) V_s\left(\frac{-\pi}{\sqrt{\mu_2}}, \frac{\pi}{2}\right) \\ &= \Omega_1^{(2)} \oplus \cdots \oplus I_{\mu_1} \oplus \cdots \oplus I_{\mu_2} \oplus \cdots \oplus \Omega_k^{(2)} \oplus \cdots \oplus \Omega_n^{(2)} \oplus \cdots \end{aligned} \tag{3.32}$$

where the order of μ_1, μ_2, k is arbitrary. Note that U_2's subscript and $\Omega^{(2)}$'s superscript denote how many subspaces have been cleaned to the identity. With the constraint on μ_1, μ_2 in Eq. (3.31), it is guaranteed that $\Omega_k^{(2)} \neq \pm I_k$. This is important since $\pm I$ each are the only element in their conjugacy class; if $\Omega_k = \pm I_k$, then we can never change Ω_k via conjugation. Our construction relies on using conjugated pulse sequences, so we must avoid $\Omega_k = \pm I_k$ at this step if we want it to be any other rotation.

Recursive step Assume we have cleaned j ($j < n$) subspaces indicated by the set $M_j = \{\mu_1, \mu_2, \ldots, \mu_j\}$. Then, ignoring order in the direct sum, we have

$$U_j = \bigoplus_{\mu_i \in M_j} I_{\mu_i} \oplus \Omega_k^{(j)} \oplus \bigoplus_{m \in M \setminus M_j} \Omega_m^{(j)} \tag{3.33}$$

We then choose a $\mu \in M \setminus M_j$ and clean $\Omega_\mu^{(j)}$ next. To do this we will move from $SU(2)$ into $SO(3)$ using the group homomorphism $R : SU(2) \to SO(3)$ by identifying $\vec{s} \in \mathbb{R}^3$ with $s \in \mathfrak{su}(2)$ via $\vec{s} \leftrightarrow s = \vec{s} \cdot \vec{\sigma}$, with Pauli matrices $\vec{\sigma}$. Then, any $Q(\theta, \phi) \in SU(2)$ is mapped to a rotation about an axis $\vec{r}$ through angle θ, $R_{\vec{r}}(\theta) \in SO(3)$ corresponding to $s \mapsto Q^\dagger s Q$.

In order to clean $R\left(\Omega_\mu^{(j)}\right) = R_{\vec{\mu}}(\theta_\mu)$, we choose an axis $\vec{\mu}_\perp \perp \vec{\mu}$ and note the following dynamical decoupling sequence

$$R_{\vec{\mu}}(\theta_\mu)\left[R_{\vec{\mu}_\perp}(\pi) R_{\vec{\mu}}(\theta_\mu) R_{\vec{\mu}_\perp}(-\pi)\right] = R_{\vec{\mu}}(\theta_\mu) R_{\vec{\mu}}(-\theta_\mu) = I, \tag{3.34}$$

which cleans the μ^{th} subspace. To find the red sideband pulses that perform $R_{\vec{\mu}_\perp}(\pi)$ on the μ^{th} subspace, we must decompose $R_{\vec{\mu}_\perp}(\pi)$ into rotations about axes in the xy-plane. Red sideband pulses $V_s(\theta, \phi) = \bigoplus_{n=1}^{\infty} Q_n(\theta, \phi)$ can be decomposed into $SU(2)$ rotations, $Q_n(\theta, \phi)$ which are mapped to a $SO(3)$ rotation $R_{\vec{\phi}}(\sqrt{n}\theta)$ where $\vec{\phi} = (\cos\phi, \sin\phi, 0)$ lies in the xy-plane. We decompose $R_{\vec{\mu}_\perp}(\pi)$ into $R_{\vec{a}}(\theta_a) R_{\vec{b}}(\theta_b)$ where $\vec{a}$, $\vec{b}$ lie in the xy-plane (see Appendix B). Then, the inverse mapping $R^{-1} : R_{\vec{a}}(\theta_a) R_{\vec{b}}(\theta_b) \mapsto Q_\mu\left(\frac{\theta_a}{\sqrt{\mu}}, \phi_a\right) Q_\mu\left(\frac{\theta_b}{\sqrt{\mu}}, \phi_b\right)$ specifies the necessary red sideband pulses. Thus, setting $C = V_s\left(\frac{\theta_a}{\sqrt{\mu}}, \phi_a\right) V_s\left(\frac{\theta_b}{\sqrt{\mu}}, \phi_b\right)$, we find

$$U_{j+1} = U_j C U_j C^\dagger = \bigoplus_{\mu_i \in M_{j+1}} I_{\mu_i} \oplus \Omega_k^{(j+1)} \bigoplus_{m \in M \setminus M_{j+1}} \Omega_m^{(j+1)}, \tag{3.35}$$

where I_{μ_i} are unaffected by the action of C and $\mu = \mu_{j+1}$ is added to set of cleaned subspaces M_j in Eq. (3.33) to give M_{j+1} in Eq. (3.35). By repeating this procedure $(n-3)$ times built on the base case, we can clean all the subspaces of the d-QO-qudit except the k^{th} which we shall deal with in the final step below.

Final step When $j = n-1$, we have cleaned all but the k^{th} subspaces in the d-QO-qudit. To transform $\Omega_k^{(n-1)}$ into Σ_k, we examine the problem in $SO(3)$ taking $R(\Omega_k^{(n-1)}) = R_{\vec{k}}(\theta_k)$ and $R(X) = R_x(\pi)$. WLOG, we only consider $\Sigma_k = X$ since Y belongs to the same conjugacy class and $X^2 = -I$ so we can simply perform our construction for X twice to achieve $-I$. We once again use conjugation to maintain the cleaned subspaces while taking advantage of the fact that the conjugacy classes of $SO(3)$ each consist of all rotations by the same angle, $C(\theta) = \{R_{\vec{r}}(\theta) | \forall \vec{r} \in \mathbb{R}^3\}$, demonstrated in Fig. 3.4b. Using a pair of conjugations

$$\begin{aligned} &\left[R_{\vec{r}_1}(\theta_1) R_{\vec{k}}^l(\theta_k) R_{\vec{r}_1}(-\theta_1)\right]\left[R_{\vec{r}_2}(\theta_2) R_{\vec{k}}(\theta_k) R_{\vec{r}_2}(-\theta_2)\right] \\ =&R_{\vec{k}_1}(l\theta_k) R_{\vec{k}_2}(\theta_k) \end{aligned} \tag{3.36}$$

we can rephrase the problem as finding $\vec{k}_1$, $\vec{k}_2$ such that $R_{\vec{k}_1}(l\theta_k) R_{\vec{k}_2}(\theta_k) = R_x(\pi)$, given $l = \left\lceil \frac{\pi}{\theta_k} \right\rceil - 1$ to guarantee rotation by an angle close to π. We can always find satisfactory $\vec{k}_1$, $\vec{k}_2$ because the triangle inequality on the sphere states that a composition of two rotations $R_{\vec{a}}(\alpha) R_{\vec{b}}(\beta) = R_{\vec{c}}(\gamma)$ results in a rotation by an angle less than the sum of angles, $|\gamma| \leq |\alpha + \beta|$ as shown in Fig. 3.4a. So, by choosing l we guarantee that we can achieve an angle of at least π, and with judicious choice of $\vec{k}_1$, $\vec{k}_2$ we can achieve a rotation by π about any axis. To find the necessary red sideband pulses, we decompose $R_{\vec{r}_1}(\theta_1)$ and $R_{\vec{r}_2}(\theta_2)$ as before and use the inverse mapping, $R_{\vec{r}_1}(\theta_1) \mapsto Q_k\left(\frac{\theta_{a,1}}{\sqrt{k}}, \phi_{a,1}\right) Q_k\left(\frac{\theta_{b,1}}{\sqrt{k}}, \phi_{b,1}\right)$

and $R_{\vec{r}_2}(\theta_2) \mapsto Q_k\left(\frac{\theta_{a,2}}{\sqrt{k}}, \phi_{a,2}\right) Q_k\left(\frac{\theta_{b,2}}{\sqrt{k}}, \phi_{b,2}\right)$. Setting $C_p = V_s\left(\frac{\theta_{a,p}}{\sqrt{\mu}}, \phi_{a,p}\right) V_s\left(\frac{\theta_{b,p}}{\sqrt{\mu}}, \phi_{b,p}\right)$, $p \in \{1, 2\}$ we find

$$V_n^{(k)} = C_1 U_{n-1}^l C_1^\dagger C_2 U_{n-1} C_2^\dagger = I_1 \oplus I_2 \oplus \cdots \oplus X_k \oplus \cdots \oplus I_n \oplus \cdots \tag{3.37}$$

Thus, we can construct elementary sQM rotations in a d-QO-qudit where $d = 2(n+1)$ for any n.

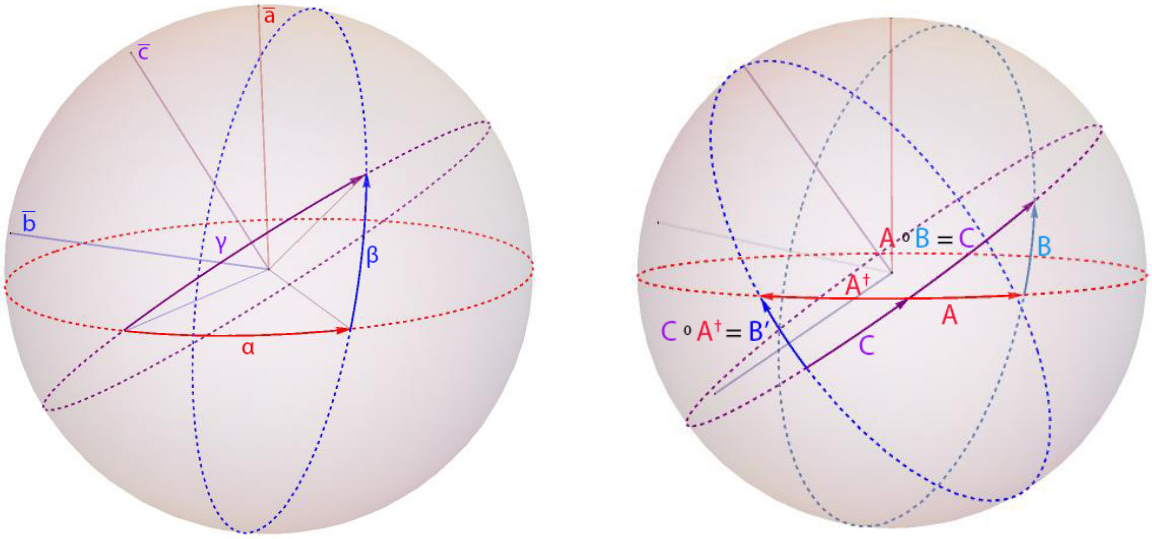

(a) (b)

Figure 3.4: (a) Composition of rotations $R_{\vec{a}}(\alpha)R_{\vec{b}}(\beta) = R_{\vec{c}}(\gamma)$ and (b) conjugation of a rotation B by A produces B' which has the same angle as B due to the congruent triangles formed by ABC and $A^\dagger B' C$.

3.5.3.2 Bounds on the number of pulses required

Now that we have shown we can create the elementary sQM rotations, we would like to bound the number of red sideband pulses needed to create $V_n^{(k)}$ in this section. One intuition is that the number of pulses required will increase at least exponentially as n increases, since each step in the recursion will cost at least a constant number of pulses due to the conjugation procedure. We shall analyze this more precisely in the following.

To create the identity on any set of $(n-1)$ subspaces in the sQM of a d-QO-qudit, we only need $\sim 2^n$ pulses. At the j^{th} recursive step we use $|U_{j+1}| = 4 + 2|U_j|$ pulses, where $|U_j|$ denotes the number of pulses in the sequence. We can see this by examining Eq. (3.35) which uses $|U_j|$ twice and both C, $C^\dagger$ are made up of two red sideband pulses by definition. We begin with 2^2 pulses at the base step U_2, and at each step j we have $|U_j| = \sum_{d=2}^{j} 2^d = 2^{j+1} - 4$. Thus, to clean $j = n-1$ subspaces to identity, we need $(2^n - 4)$ pulses. In the final step, a total of $8 + (l+1)|U_{n-1}| = (l+1)(2^n - 4) + 8$ is required to construct $V_n^{(k)}$ in Eq. (3.37).

In order to bound l, we must understand how the base step and each recursive step j transforms $\Omega_k^{(j)}$ into $\Omega_k^{(j+1)}$. For notation clarity, $(U_j)_m = \Omega_m^{(j)}$ indicates the $SU(2)$ rotation upon the m^{th} subspace in U_j (as defined in Eq. (3.32) and Eq. (3.33)). $\Omega_m^{(j)}$ maps to the $SO(3)$ rotation $R_{\vec{m}_j}\left(\theta_m^{(j)}\right)$. We take the C, μ, U_j, U_{j+1} as defined in the recursive step above. In the following we will show the conditions such that $\theta_k^{(j)} \geq \frac{\pi}{t}$ for all $j < n$ for some $t > 2$ and $t \in \mathbb{Z}$.

In the base step, we can easily calculate the rotation angle of $\Omega_k^{(2)} = R_{\vec{k}_2}\left(\theta_k^{(2)}\right)$ from Eq. (3.32):

$$\begin{aligned}\theta_k^{(2)} =& 2\cos^{-1}\left\{\frac{1}{2}\left[1+\cos\left(2\pi\sqrt{\frac{k}{\mu_1}}\right)\right.\right.\\ &\left.\left.-2\cos\left(\pi\sqrt{\frac{k}{\mu_2}}\right)\sin^2\left(\pi\sqrt{\frac{k}{\mu_1}}\right)\right]\right\}. \end{aligned} \tag{3.38}$$

We can always choose μ_1, $\mu_2 < k$ such that $\theta_k^{(2)} \geq \frac{\pi}{2}$. For $k \sim 1$, this can be easily calculated explicitly. For general k, if we simply take μ_1 as the number closest to $\frac{k}{2}$ that abides by the base case constraint, then Eq. (3.38) is approximately

$$\theta_k^{(2)} = 2\cos^{-1}\left[\frac{1}{2}\left(1+\cos\left(2\sqrt{2}\pi\right)-2\cos\left(\pi\sqrt{\frac{k}{\mu_2}}\right)\sin^2\left(\sqrt{2}\pi\right)\right)\right]. \tag{3.39}$$

Thus, for $\theta_k^{(2)} \geq \frac{\pi}{2}$, we obtain a periodic condition $0.18 < \sqrt{\frac{k}{\mu_2}} - 2z < 0.74$, $z \in \mathbb{Z}$, which can be easily fulfilled for a range of $\mu_2 < k$.

We will show the conditions such that $\theta_k^{(j+1)} \geq \frac{\pi}{t}$ if we have $\theta_k^{(j)} \geq \frac{\pi}{t}$ at each recursive step.

Recall, at the j^{th} step we perform $U_{j+1} = U_j C U_j C^\dagger$ where $C = V_s\left(\frac{\theta_a}{\sqrt{\mu}}, \phi_a\right) V_s\left(\frac{\theta_b}{\sqrt{\mu}}, \phi_b\right)$. Restricting our attention to the k^{th} subspace, we examine C and its action upon $\Omega_k^{(j)} = R_{\vec{k}_j}\left(\theta_k^{(j)}\right)$ in the $SO(3)$ picture:

$$\begin{aligned}(C)_k &\mapsto R_{\vec{a}}\left(\theta_a\sqrt{\frac{k}{\mu}}\right) R_{\vec{b}}\left(\theta_b\sqrt{\frac{k}{\mu}}\right)\\ &:= R_{\vec{r}_{ab}}\left(\theta_{ab}\right), \end{aligned} \tag{3.40}$$

$$\begin{aligned}\left(CU_jC^\dagger\right)_k &\mapsto R_{\vec{r}_{ab}}\left(\theta_{ab}\right) R_{\vec{k}_j}\left(\theta_k^{(j)}\right) R_{\vec{r}_{ab}}\left(-\theta_{ab}\right)\\ &:= R_{\vec{k}_{ab}}\left(\theta_k^{(j)}\right), \end{aligned} \tag{3.41}$$

where

$$\vec{k}_j \cdot \vec{k}_{ab} = \left(\vec{k}_j \cdot \vec{r}_{ab}\right)^2 + \left[1 - \left(\vec{k}_j \cdot \vec{r}_{ab}\right)^2\right] \cos\theta_{ab} \tag{3.42}$$

$$\begin{aligned}\theta_{ab} =& 2\cos^{-1}\left\{\frac{1}{2}\left[\cos\left(\frac{\theta_a}{2}\sqrt{\frac{k}{\mu}}\right)\cos\left(\frac{\theta_b}{2}\sqrt{\frac{k}{\mu}}\right)\right.\right.\\ &\left.\left. - \left(\vec{a}\cdot\vec{b}\right)\sin\left(\frac{\theta_a}{2}\sqrt{\frac{k}{\mu}}\right)\sin\left(\frac{\theta_b}{2}\sqrt{\frac{k}{\mu}}\right)\right]\right\}\end{aligned} \tag{3.43}$$

Recall, $\vec{a}$, $\vec{b}$, θ_a, θ_b are found by decomposing $R_{\vec{\mu}_\perp}(\pi) = R_{\vec{a}}(\theta_a) R_{\vec{b}}(\theta_b)$ into two rotations about axes in the xy-plane. Using these definitions we can write the outcome of $\Omega_k^{(j+1)} \mapsto R_{\vec{k}_{j+1}}\left(\theta_k^{(j+1)}\right) = R_{\vec{k}_j}\left(\theta_k^{(j)}\right) R_{\vec{k}_{ab}}\left(\theta_k^{(j)}\right)$ in $SO(3)$. We write explicitly our condition for $\theta_k^{(j+1)}$:

$$\begin{aligned}\theta_k^{(j+1)} =& 2\cos^{-1}\left[\frac{1}{2}\left(1 - \vec{k}_j\cdot\vec{k}_{ab} + \left(1 + \vec{k}_j\cdot\vec{k}_{ab}\right)\cos\theta_k^{(j)}\right)\right]\\ \geq& \frac{\pi}{t}\end{aligned} \tag{3.44}$$

Substituting $\vec{k}_j \cdot \vec{k}_{ab}$ with Eq. (3.42) into Eq. (3.44), we can rewrite the condition as a constraint on θ_{ab} or on $\vec{r}_{ab}$:

$$\begin{aligned}|\vec{k}_j \cdot \vec{r}_{ab}| &\geq \sqrt{\frac{\cos\frac{\pi}{2t} - 1}{\cos\theta_k^{(j)} - 1}}\\ \cos\theta_{ab} &\geq \frac{1 - 2\cos\frac{\pi}{2t} - \cos\theta_k}{1 - \cos\theta_k^{(j)}}\end{aligned} \tag{3.45}$$

This indicates that we need $R_{\vec{r}_{ab}}(\theta_{ab})$ to not be close to $R_{\vec{k}_{j,\perp}}(\pi)$ where $\vec{k}_{j,\perp} \perp \vec{k}_j$. When $t \sim 2^4$ and $|\theta_k^{(j)}| \geq \frac{2\pi}{t}$, this condition is quite flexible and restricts $\cos\theta_{ab} > -0.873$ or $|\vec{k}_j \cdot \vec{r}_{ab}| > 0.26$. And when $|\theta_k^{(j)}| \geq \frac{4\pi}{t}$, $\cos\theta_{ab} > -0.967$ or $|\vec{k}_j \cdot \vec{r}_{ab}| > 0.128$. At worst, when $|\theta_k^{(j)}| = \frac{\pi}{t}$, the restriction is that $\cos\theta_{ab} > -\frac{1}{2}$ or $|\vec{k}_j \cdot \vec{r}_{ab}| > \frac{1}{2}$. When $\mu \ll k$ or $\mu \gg k$, the conjugation rotations C affect the k^{th} and μ^{th} subspaces very differently due to the rotation $(C)_\mu$ and $(C)_k$ being composed of rotations about the same axes, but by very different angles, indicated by the ratio of $\frac{k}{\mu}$. Thus, by changing how we decompose C into rotations in the xy-plane, we can ensure the flexibility of $R_{\vec{r}_{ab}}(\theta_{ab})$. When $\mu \sim k$, specifically, when $\sqrt{\frac{k}{\mu}} \sim 1$, θ_{ab} will be close to π because $(C)_\mu$ is a rotation by π. Thus, the only way to ensure $\theta_k^{(j)}$ is maintained, is to clean such μ when $\vec{\mu}\cdot\vec{k}_j \lesssim \frac{1}{2}$, i.e. $(U_j)_\mu$ and $(U_j)_k$ are rotations about different enough axes. Also, note that $\frac{1}{2}$ is a worst case scenario, when $(U_j)_k$ is a rotation by precisely $\frac{\pi}{t}$, and from our discussion of Eq. (3.45) this constraint becomes relaxed quickly. We also note that when $\mu \gg k$, the effect of the conjugation sequence upon the k^{th} subspace is negligible and so $\vec{k}_{ab} \sim \vec{k}_j \implies \theta_k^{(j+1)} \sim 2\theta_k^{(j)}$.

In order to roughly bound l for asymptotically large n, we consider two different cases: $k \ll n$ or $k \sim n$. When k is much less than $n \gg 1$, l is bounded by 4 by choosing $t = 4$. This

is because the majority of recursive steps involve $\mu \gg k$, thus we have many choices in the order of the cleaning to almost double the angle on the k^{th} subspace at a given step. Thus, whenever $\theta_k^{(j)} \sim \frac{\pi}{t}$, we can clean a subspace such that $\theta_k^{(j)} \sim \frac{2\pi}{t}$, which provides an ideal constraint from Eq. (3.45) for the next recursive step. And so we can improve the angle on the k^{th} space to ensure cleaning subspaces near k can be done optimally. When $k \gg 1$, we have the opposite situation because for large k, $\Delta_k = \sqrt{k+1} - \sqrt{k} \approx \frac{1}{2\sqrt{k}}$. Thus, on the order of $\sqrt{k}$ pulses are needed to separate the rotations on the k^{th} and $(k+1)^{\text{st}}$ subspaces. However, by cleaning the subspaces outside the range $k \pm \sqrt{k}$, we are in effect separating the subspaces near k from each other, albeit slower than directly applied pulses. This is because $(C)_k$, $(C)_{k+1}$ perform almost the same rotation and differ slightly in the angle by on the order $\frac{1}{\sqrt{k}}$. Thus, at every recursive step, we build up a difference in the axis of rotation between the k and $k+1$ subspace of about $\frac{1}{k}$. So after $\sim \frac{k}{2}$ recursive steps, we build up a difference of $\sim \frac{1}{2}$, the necessary difference for the worst case scenario in maintaining $\theta_k^{(j+1)}$ when $\theta_k^{(j)} = \frac{\pi}{t}$. Of course, we cannot guarantee that all subspaces within $k \pm \sqrt{k}$ can be optimally separated from k at the same time, and so $k \leq t \leq k^{2\sqrt{k}}$ to capture the worst case scenarios of cleaning between one and $2\sqrt{k}$ subspaces while their axes of rotation are parallel to the k^{th} subspace's axis of rotation at each recursive step. Therefore, as it is highly unlikely that the $2\sqrt{k}$ subspaces will all be exactly parallel to k and given our freedom to clean subspaces, the majority of which are not near the k^{th}, in any order, we generally bound l by k^2.

In summary, a total of $(l+2)(2^n-4)+8$ sideband pulses are needed to construct any clean elementary $SU(2)$ rotation in sQM in Eq. (3.37), where l is roughly $O(k^2)$ and k is the subspace index ($1 \leq k \leq n$). We know the decomposition of an arbitrary $d \times d$ unitary operation needs at most $d(d-1)/2$ two-level unitaries [NC10], and each two-level unitary can be further constructed from roughly d clean elementary $SU(2)$ rotations in sQM as described in Sec. 3.5.2 (Eqs. (3.21), (3.23), (3.24), (3.26), and (3.27)). Thus, the total number of control pulses needed for an arbitrary $d \times d$ unitary operation is $O(d^5 2^{d/2})$, or equivalently $O(n^5 2^n)$ in terms of n since $d = 2(n+1)$. Note that this scaling comes from a worst case estimation, and for typical unitaries one might expect a better scaling.

3.6 Algorithms and Examples

We have also implemented an algorithm according to the above constructive proof to produce composite pulse sequences that can realize arbitrary elementary clean $SU(2)$ unitary operations. We describe our algorithm in detail in Sec. 3.6.1, where an example construction of clean elementary Pauli X gate for an 8-QO-qudit (3 subspaces in sQM and 4 subspaces in cQM) is given. We then present in Sec. 3.6.2 more extensive numerical results on the construction of clean elementary Pauli X gates in d-QO-qudits ($d = 2(n+1)$) for all $n \leq 22$ and demonstrate the agreement between numerical and theoretical bounds on the number of sideband pulses.

3.6.1 An Algorithm for Constructing Gates on QO-Qudits

Following is an algorithm for constructing a gate with identity operations I on all of the subspaces apart from subspace k, which has an X or Y gate (i.e., $I_1 \oplus \cdots \oplus \Sigma_k \oplus \cdots \oplus I_n$, where $\Sigma_k \in \{X, Y\}$). This algorithm parallels the recursive procedure described in Sec. 3.5.3.1; however, we do not implement the strategies described in Sec. 3.5.3.2 but rather rely on empirical optimization over the four degrees of freedom described at the end of Sec. 3.6.1 to achieve efficient pulse sequences.

Note that we adopt the convention of using the $SO(3)$ representation in which a rotation about unit vector $\hat{r}$ by angle θ is represented by $R_{\hat{r}}(\theta)$ throughout the description of the algorithm. Once our sequence involves only rotations about unit vectors in the xy-plane, we can convert each rotation into the $SU(2)$ representation $V_s(\theta, \phi)$ for red sideband pulses.

1. Construct an ordered pulse sequence S_I (order goes from left to right) that results in the operation $I_1 \oplus \cdots \oplus \Omega_k \oplus \cdots \oplus I_n$.

   (a) Select distinct $\mu_1, \mu_2 \in \mathbb{Z}$ with $1 \leq \mu_1, \mu_2 \leq n$ such that $\sqrt{\frac{k}{\mu_1}}, \sqrt{\frac{k}{\mu_2}} \notin \mathbb{Z}$.

   (b) Initialize S_I to be the four-pulse sequence

   $$S_I \leftarrow \left\{ R_{\hat{y}}\left(\frac{\pi}{\sqrt{\mu_1}}\right), R_{\hat{x}}\left(\frac{2\pi}{\sqrt{\mu_2}}\right), R_{\hat{y}}\left(\frac{\pi}{\sqrt{\mu_1}}\right), R_{\hat{x}}\left(-\frac{2\pi}{\sqrt{\mu_2}}\right) \right\} \tag{3.46}$$

   that leaves I_{μ_1} and I_{μ_2} on subspaces μ_1 and μ_2 unchanged while rotating subspace k.

   (c) For each subspace m apart from k, μ_1, and μ_2 (i.e., for each $m \in \mathbb{Z}$ with $1 \leq m \leq n$, excluding k, μ_1, and μ_2), suppose that the operation on this subspace is Ω_m after the application of pulse sequence S_I. If $\Omega_m = I_m$, continue to the next such m. Otherwise, let $\hat{r}_m$ and θ_m be the axis and angle of the rotation induced by Ω_m, respectively, and then set

   $$S_I \leftarrow \left\{ S_I, R_{\hat{r}_m^{\perp}}\left(-\frac{\pi}{\sqrt{m}}\right), S_I, R_{\hat{r}_m^{\perp}}\left(\frac{\pi}{\sqrt{m}}\right) \right\}, \tag{3.47}$$

   where $\hat{r}_m^{\perp}$ is any unit vector perpendicular to $\hat{r}_m$.
   Continue to the next such m and repeat, using the operation Ω_m on subspace m following the application of the updated sequence S_I.

2. Use pulse sequence S_I to place an X or Y gate on subspace k.

   (a) Letting θ_k be the angle corresponding to rotation Ω_k and $\hat{r}_k$ the corresponding axis, calculate $l = \lceil \frac{\pi}{\theta_k} \rceil - 1$, and define the components of unit vectors $\hat{\alpha}$ and $\hat{\beta}$

as follows. If the desired gate Σ_k is X, then we have

$$\alpha_1 = \cos\frac{l\theta_k}{2}\csc\frac{\theta_k}{2} \tag{3.48}$$

$$\alpha_2 = \csc\frac{\theta_k}{2}\sqrt{-\cos^2\frac{\theta_k}{2} + (1-\beta_2^2)\sin^2\frac{l\theta_k}{2}} \tag{3.49}$$

$$\alpha_3 = -\beta_2\csc\frac{\theta_k}{2}\sin\frac{l\theta_k}{2} \tag{3.50}$$

$$\beta_1 = \cos\frac{\theta_k}{2}\csc\frac{l\theta_k}{2} \tag{3.51}$$

$$\beta_3 = \csc\frac{l\theta_k}{2}\sqrt{-\cos^2\frac{\theta_k}{2} + (1-\beta_2^2)\sin^2\frac{l\theta_k}{2}}, \tag{3.52}$$

where β_2 is a free real parameter with

$$|\beta_2| \leq \sqrt{1 - \frac{\cos^2\frac{\theta_k}{2}}{\sin^2\frac{l\theta_k}{2}}} \tag{3.53}$$

such that all of the components of $\hat{\alpha}$ and $\hat{\beta}$ are real. Note that this range is guaranteed to be nonempty because it follows from the definition of l by $l = \lceil\frac{\pi}{\theta_k}\rceil - 1$ that

$$\sin^2\frac{l\theta_k}{2} \geq \cos^2\frac{\theta_k}{2}. \tag{3.54}$$

Similarly, if the desired gate Σ_k is Y, then we have

$$\alpha_1 = -\csc\frac{\theta_k}{2}\sqrt{-\cos^2\frac{\theta_k}{2} + (1-\beta_1^2)\sin^2\frac{l\theta_k}{2}} \tag{3.55}$$

$$\alpha_2 = \cos\frac{l\theta_k}{2}\csc\frac{\theta_k}{2} \tag{3.56}$$

$$\alpha_3 = \beta_1\csc\frac{\theta_k}{2}\sin\frac{l\theta_k}{2} \tag{3.57}$$

$$\beta_2 = \cos\frac{\theta_k}{2}\csc\frac{l\theta_k}{2} \tag{3.58}$$

$$\beta_3 = \csc\frac{l\theta_k}{2}\sqrt{-\cos^2\frac{\theta_k}{2} + (1-\beta_1^2)\sin^2\frac{l\theta_k}{2}}, \tag{3.59}$$

where β_1 is a free real parameter with

$$|\beta_1| \leq \sqrt{1 - \frac{\cos^2\frac{\theta_k}{2}}{\sin^2\frac{l\theta_k}{2}}} \tag{3.60}$$

such that all of the components of $\hat{\alpha}$ and $\hat{\beta}$ are real, where this range is nonempty for the same reason as that provided above.

(b) For $\hat{\beta}$, calculate

$$\hat{r}_\beta = \frac{\hat{r}_k \times \hat{\beta}}{\left\| \hat{r}_k \times \hat{\beta} \right\|}, \tag{3.61}$$

$$\theta_\beta = \cos^{-1}\left(\hat{r}_k \cdot \hat{\beta} \right), \tag{3.62}$$

and calculate $\hat{r}_\alpha$ and θ_α similarly for $\hat{\alpha}$. Finally, the desired sequence is now

$$\begin{aligned} S_I \leftarrow \Bigg\{ & R_{\hat{r}_\beta}\left(-\frac{\theta_\beta}{\sqrt{k}}\right),\, S_I^l,\, R_{\hat{r}_\beta}\left(\frac{\theta_\beta}{\sqrt{k}}\right), \\ & R_{\hat{r}_\alpha}\left(-\frac{\theta_\alpha}{\sqrt{k}}\right),\, S_I,\, R_{\hat{r}_\alpha}\left(\frac{\theta_\alpha}{\sqrt{k}}\right) \Bigg\}, \end{aligned} \tag{3.63}$$

where S_I^l denotes the l-fold repetition of the sequence S_I.

To obtain a sequence with $\Sigma_k = -I$, the algorithm can be carried out for $\Sigma_k = X$ and the resulting sequence repeated, since throughout this work we define $X = i\sigma_x$, and $(i\sigma_x)^2 = -I$.

Note that the rotation unit vectors $\hat{r}_m^\perp$, $\hat{r}_\beta$, and $\hat{r}_\alpha$ need not be in the xy-plane, and so the rotations about these vectors might not be achievable by a single rotation with axis in the xy-plane. However, these rotations—and, more generally, any rotation $R_{\hat{r}}(\theta)$—can also be algorithmically decomposed into an equivalent pair of xy-plane rotations according to the subroutine in Appendix C. With this subroutine, any rotations about axes not in the xy-plane are converted into sequences of two rotations about axes in the xy-plane, thus ensuring that all rotations in our final sequence are about axes in the xy-plane. Finally, these rotations about axes in the xy-plane in $SO(3)$ notation of the form $R_{\hat{r}}(\theta)$ with $\hat{r} = \langle r_1,\, r_2,\, 0 \rangle$ can be converted into the form of red sideband pulses $V_s(\theta,\, \phi)$ by the equivalence

$$R_{\hat{r}}(\theta) \leftrightarrow V_s(\theta,\, \mathrm{atan2}\,(r_2,\, r_1)), \tag{3.64}$$

where atan2 denotes the standard 2-argument arctangent function.

Finally, it is worth noting that there are four primary degrees of freedom in this algorithm—namely,

i. the choice of μ_1, μ_2 for the initial four-pulse S_I sequence;

ii. the order in which the operators on the remaining subspaces are converted to the identity;

iii. the axis $\hat{r}_m^\perp$ of the rotation used to conjugate S_I when converting the operator on subspace m to the identity; and

iv. the angle ϕ in each decomposition of a rotation about an axis $\hat{r}$ not in the xy-plane into a sequence of two rotations about axes $\hat{r}_1$ and $\hat{r}_2$ in the xy-plane.

These degrees of freedom can be chosen accordingly to empirically minimize the number of pulses in the sequence by ensuring that θ_k is near π after Step 1 of the algorithm, which in turn minimizes l and thus minimizes repetition of the S_I sequence.

This algorithm has been written in Python, and the code [Min21] has been used to generate sequences of red sideband pulses of the the form $V_s(\theta, \phi)$ that produce the gates $I_1 \oplus I_2 \oplus X_3$ and $I_1 \oplus I_2 \oplus Y_3$. The resulting parameters for the sequences are provided in Table 3.1.

$I_1 \oplus I_2 \oplus X_3$		$I_1 \oplus I_2 \oplus Y_3$	
θ	ϕ	θ	ϕ
-1.0956	-2.8651	-1.3098	-2.7835
$-\pi/\sqrt{3}$	0.4867	$-\pi/\sqrt{3}$	0.4210
$\sqrt{2}\pi$	$\pi/2$	$\sqrt{2}\pi$	$\pi/2$
π	0	π	0
$\sqrt{2}\pi$	$\pi/2$	$\sqrt{2}\pi$	$\pi/2$
$-\pi$	0	$-\pi$	0
$\pi/\sqrt{3}$	0.4867	$\pi/\sqrt{3}$	0.4210
1.0956	-2.8651	1.3098	-2.7835
-1.8073	-0.3267	-1.4071	-2.6391
-2.0499	$-\pi$	-1.2674	0
$\sqrt{2}\pi$	$\pi/2$	$\sqrt{2}\pi$	$\pi/2$
π	0	π	0
$\sqrt{2}\pi$	$\pi/2$	$\sqrt{2}\pi$	$\pi/2$
$-\pi$	0	$-\pi$	0
2.0499	$-\pi$	1.2674	0
1.8073	-0.3267	1.4071	-2.6391

Table 3.1: Pulse sequences for $I_1 \oplus I_2 \oplus X_3$ and $I_1 \oplus I_2 \oplus Y_3$

3.6.2 Numerical Scaling of the Number of Pulses

To support the theoretical bound we derived on the construction in Sec. 3.5.3.2, we also use our code to generate pulse sequences to construct gates of the form $I_1 \oplus I_2 \oplus \cdots \oplus I_{n-1} \oplus X_n$ up to the lowest 23 Fock levels of the oscillator, i.e., 22 subspaces in sQM (excluding states $|0, 0\rangle$ and $|1, n\rangle$ from the sQM because they undergo trivial transformations in red sideband pulses). We plot the total number of sideband pulses used in each case as a function of n, as is shown in Fig. 3.5. The approximate linear dependence in log-scale empirically demonstrates the exponential scaling of the number of pulses with the QO-qudit dimension (or the truncated oscillator dimension), which is consistent with the bound proven in Sec. 3.5.3.2. Note the small deviation of the numerical results from exact exponential scaling in Fig. 3.5 is a manifestation of the several degrees of freedom mentioned in Sec. 3.6.1 that we can tune, which yields a slightly different number of pulses for each n. Also note the gates $I_1 \oplus I_2 \oplus \cdots \oplus I_{n-1} \oplus X_n$ synthesized here are all elementary $SU(2)$ rotations in the sQM, so the polynomial prefactor n^5 (as described in Sec. 3.5 for an arbitrary $n \times n$ unitary) does not apply.

3.7 Conclusions

We have shown that an infinite dimensional harmonic oscillator can be truncated to a finite dimensional subspace $(n + 1)$ for any $n \in \mathbb{Z}$ by coupling to a single qubit, to form a d-dimensional QO-qudit for $d = 2(n + 1)$. A recursive construction is given to synthesize

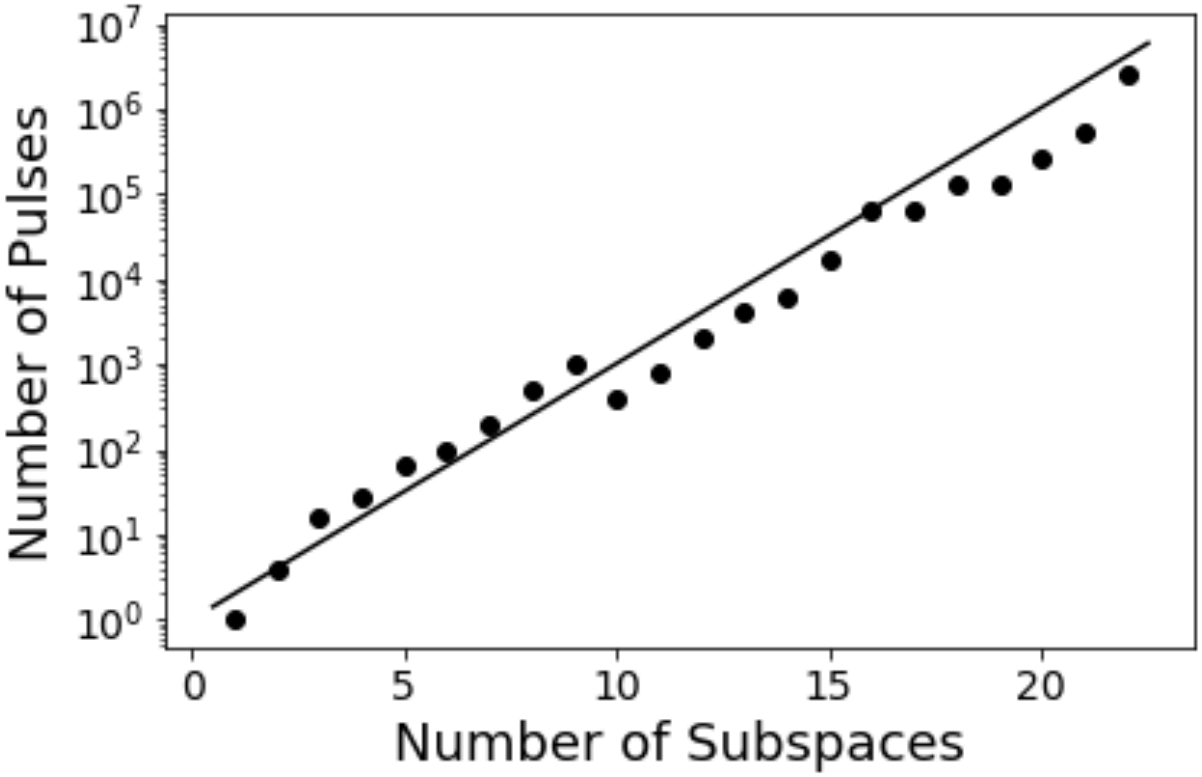

Figure 3.5: Lengths of pulse sequences for constructions of gates of the form $I_1 \oplus I_2 \oplus \cdots \oplus I_{n-1} \oplus X_n$ up to 22 subspaces, where the solid line indicates the theoretical scaling of 2^n for n subspaces. The small deviation of the numerical points from the theoretical bound is due to the degrees of freedom for tuning our algorithm, as detailed in Sec. 3.6.1.

arbitrary unitary operations in the QO-qudit using only the red sideband and the carrier pulses *fully analytically*. These control pulses used in our construction are routinely available in a Jaynes-Cummings type interaction as is easily realized in many physical platforms including trapped ions. The ability to synthesize arbitrary unitary operations in a d-QO-qudit immediately implies universal control on the corresponding truncated oscillator. At the heart of our construction is the utilization of the naturally repeated pattern in the spectrum of an oscillator. This repeated pattern allows us to recursively clean each two-dimensional subspace by the dynamical decoupling technique. To analyze the scaling of our construction, a bound on the number of sideband pulses required to accomplish the construction is derived. It is shown that the number of sideband pulses scales exponentially as the dimension d of a QO-qudit with a low degree polynomial prefactor depending on d.

We believe the exponential scaling derived is optimal and cannot be reduced to a polynomial scaling, if the synthesized unitary is completely arbitrary and is constructed fully analytically as in our work. From the viewpoint of complexity theory, it also indicates the task of closing a low energy subspace in an oscillator and construct an arbitrary unitary operation to *arbitrary precision* is exponentially hard. The exponential scaling of the number of pulse also translates to an exponential scaling of total energy required. Therefore, closing a

finite dimensional low energy subspace of the oscillator does *not* surmount the unphysically infinite amount of energy requirement on the universal control of an oscillator. However, following [MM13], numerical optimizations may be used to reduce pulse requirements, and it is likely that significant simplifications can be realized for specific unitaries, especially those with additional structure.

It should be noted that our construction should work for a larger class of Hamiltonians beyond the JC Hamiltonian. One example is for trapped ions beyond the deep Lamb-Dicke regime where the Rabi frequency of the subspaces are proportional to the Legendre polynomial, instead of a simple $\sqrt{n}$ dependence as discussed above. It would be interesting to generalize this to other Hamiltonians where unbounded bosonic systems are utilized for quantum computation, such as transmon+microwave cavity in the superconducting architecture. Moreover, by hybridizing the unitaries constructed under the Fock basis in this work with various continuous-variable type operations, more efficient and powerful operations are likely to arise.

Our discussions presented above assume perfectly isolated qubit-oscillator systems. In practical applications, the qubit-oscillator system may be coupled to an external noisy environment, leading to the presence of quantum noise in QOQ. In such noisy cases, the scheme proposed above cannot be directly applied. However, this can be circumvented by combining our protocol with proper quantum error-correcting codes. For example, depending on the nature of the quantum noise (system-bath coupling), a subspace of our qubit-oscillator system may be identified that is immune to the noise produced by the environment. Therefore, our protocol can be applied to the decoherence-free subspace [LCW98] of the qubit-oscillator system. More generally, we may use our protocol to implement arbitrary unitary operations directly on the *logical qubits/qudits* (instead of the Fock levels) defined by a given quantum error-correcting code to get rid of the possible errors induced by coupling to external environment. Any unitary operations on these logical states can be implemented by our protocol, as is guaranteed by the universality proven in Sec. 3.5.

As a final note on this project, our work suggests that the combination qubit+bosonic system may serve as a hardware-efficient quantum resource for both computational and information storage. Going beyond a single QO-qudit, our constructions may be generalized to include interactions between two QO-qudits, such that we could realize QO-qudit-based universal quantum computation, as was pioneered in Ref. [MM13]. We hope that analytic approaches, such as those demonstrated here, will lead to further understanding of the algebraic structure of the tensor product of QO-qudits.

Chapter 4

Quantum Sensing with Quantum Signal Processing

Now that we have demonstrated the utility of such hybrid quantum systems as the one used for constructing the quantum-oscillator qudits, or QO qudits, as well as how we can use high-level computational techniques to decompose gates on these qudits into primitives for the achievement of universal quantum computation, we will proceed to explain another application of such hybrid quantum systems to a different field of quantum technology, namely that of quantum sensing.

This section is based on a paper that I co-first-authored about this research project, which is currently prepublished on arXiv and under review for publishing in Quantum Journal [Sin+23]. The parts of this manuscript to which I solely contributed are copied here with some additional background sections to which I contributed with others. Small changes have been made to highlight the computational aspects, and additional sections have been added to discuss relevant physical background.

In this chapter, we first provide background on the field of quantum sensing in Sec. 4.1. Then we introduce quantum signal processing (QSP) in Sec. 4.2. With the foundation of QSP lain, we proceed to introduce the goals of our own work in Sec. 4.3. Next, we lay out the problem that we aim to solve in Sec. 4.4. In Sec. 4.5, we introduce our new approach of applying quantum signal processing to the qubit oscillator for interferometry. Then we explain how this QSP approach to interferometry can be applied to answering decision problems in quantum sensing in Sec. 4.6. To support the theory presented here, we next present numerical results for making binary decisions about the magnitude of displacements on an oscillator in Sec. 4.7. Finally, we summarize our results and discuss future directions for the work on applying this qubit-oscillator system to address other kinds of quantum-sensing problems in Sec. 4.8.

4.1 Background

Sensing and metrology are fundamental pursuits of science and technology, and quantum systems have been used to advance metrological precision to new bounds [CC16; Bot+22; Rou+23; GLM04]. Typical quantum sensing protocols involve manipulation of quantum

coherence and entanglement followed by measurement to extract useful classical information from quantum systems.

The efficiency of different quantum sensing protocols varies by construction. At a high level, any sensing protocol can be assessed by the space and time resource requirements (e.g., the size of the quantum sensor, the length of the sensing protocol, any required repetition of the experiments) that it needs in order to achieve a given sensitivity in the sensing task, for example estimating a given parameter to a certain precision. The intrinsically probabilistic nature of quantum systems necessarily introduces uncertainty into the measurement result of any sensing protocol, leading to the so-called standard quantum limit (SQL). In the SQL, the standard deviation of the estimated parameter scales inversely as the square-root of the space and time resources employed, as is familiar in processes involving shot noise.

By leveraging non-classical properties of quantum states like entanglement [Boi+08; Til+10] and general quantum correlations [Bra+18] or using coherent sampling of the signal and adaptive feedback [BW00; Gór+20; Mar+22], sensitivity in parameter estimation can be improved beyond the SQL to approach a more fundamental physical limit, the Heisenberg limit (HL). The HL dictates that the scaling of precision with total sensing time t can be no better than $1/t$; equivalently, with N probes used in an experiment, the precision scales no better than $1/N$.

In fact, this fundamental physical limit has been achieved by a number of sensing protocols. One of the oldest and best-known is the interferometric protocol known as cat-state sensing, named after Schrödinger's cat for its use of superpositions of two distinct macroscopic states, such as the all-spin-up and all-spin-down states in a multi-atom system. This protocol, first realized for spin-states in 1996 by Bollinger et al., achieves the optimal bound for frequency uncertainty of an N-particle system [Bol+96]. This optimal HL bound, equal to $(NT)^{-1}$, where T is the time for a single repetition of the protocol, is achieved by modifying the Ramsey technique [Ram50] to use a maximally correlated GHZ state and a different final measurement operator. As it achieves the HL limit, this variety of cat-state sensing for spin systems has found broad application in precision phase sensing for atomic clocks [Mar+22; Kau+21], where variational quantum algorithms are incorporated into multi-qubit Ramsey interferometry to iteratively optimize the sensing precision.

However, many other parameters of interest, such as electric fields [Des+23], can be better sensed by bosonic modes (e.g., photonic and phononic oscillators) than by spin systems. Bosonic sensors have been employed to perform precision sensing of small displacements to bosonic oscillators, and there have been many advances investigating the advantages of utilizing bosonic resource states [Pen+16; DTW17]. Gilmore et al. have found that coupling the spins of a trapped-ion crystal to their collective motional mode offers sub-SQL sensing performance, with the quantum enhancement achieved through interferometry of highly-entangled spin-motion cat states [Gil+21]. Using the interference between squeezed light, the Advanced LIGO [Tse+19] experiment can detect the space-time curvature changes induced by gravitational waves. Interferometric phase estimation using entanglement, coherent sampling, and adaptive feedback approaches the exact Heisenberg limit [Dar+18], and similar results have been experimentally found using just a single bosonic mode [Wan+19].

Additionally, coupling bosonic modes to other degrees of freedom can transfer information from one subsystem to another in order to facilitate more convenient measurement than the direct measurement of the bosonic modes themselves [Gie22]. In spectroscopy, entangled cat-

state laser sources have also been used to enhance signals by an order of magnitude [Kir+11]. Beyond the single-mode case, it has been demonstrated that the entanglement of many modes can provide HL-sensing enhancement for parameter estimation [ZZS18; Kwo+22]. Furthermore, various efficient HL-scaling Hamiltonian learning protocols have been proposed, including some on bosonic systems, that can be rephrased as multi-parameter estimation problems [Li+23; Hua+23].

Beyond parameter estimation, there are many other sensing applications that have been left largely unexplored, for example, single-shot decision making. For such decision-making problems, the underlying signal can happen rarely, such as the case of gravitational wave detection [CC16], and it is therefore crucial to obtain useful information in the single-shot limit. When events are rare, many iterative protocols for parameter estimation and learning [DGN22; Hua+23; Zho+18; Sug+23; RC21; Ros+22; Gór+20] are challenged. Protocols for discrete decision problems (such as classification) on multiple bosonic modes have been developed in Ref. [ZZ19; Xia+21] by using variational algorithms for state preparation and signal decoding with notable performance gain enabled by multi-mode entanglement. Despite the success of bosonic systems and cat-state sensing for parameter estimation, a unified protocol for general sensing tasks with provable speedup is unknown, particularly in scenarios where decisions must be made in the single-shot limit. Though there are many broad results concerning the optimal bounds on precision in quantum channel discrimination problems, there are few analyses of resource scaling in the single sample regime [Mey+23; Tan+08; Pir+19].

Protocols for realizing such general sensing tasks should generally build on the ability to perform transformations of the underlying signal. Not surprisingly, transformation of classical signals has been extensively studied in the context of *signal processing* in electrical engineering [OS10], where state-of-the-art classical algorithms have been developed to design a variety of *filters* that transform the underlying classical signals tailored to the desired purposes [PM72; Ant18]. Inspired by classical signal processing, quantum signal processing (QSP) algorithms [LYC16; LC19; Kik+23; RC22; Don+22; Ros+23; MW23; Lan23; RCC23; Mar+23; WDL22; Mar+21; Yu+22] can achieve arbitrary polynomial transformations on one or more quantum amplitudes, as will be explained further in the introduction to QSP provided in the following section.

4.2 Quantum Signal Processing (QSP)

Quantum signal processing (QSP) is an algorithmic framework in the field of quantum computation that generalizes results related to composite pulse sequences. In particular, the fundamental idea of QSP is to interleave two distinct kinds of single-qubit rotations, namely a *signal* rotation operator W, and a *signal processing* rotation operator S. There are two common conventions for the choice of these two operators, and the one taken in this work is known as the Wx convention. In this convention, the W operator is taken to be

$$W(a) = \begin{bmatrix} a & i\sqrt{1-a^2} \\ i\sqrt{1-a^2} & a \end{bmatrix}, \tag{4.1}$$

which represents an x-rotation by angle $\theta = -2\cos^{-1} a$, and the S matrix is taken to be

$$S(\phi) = e^{i\phi\hat{Z}}, \tag{4.2}$$

which represents a z-rotation by angle -2ϕ.

For a tuple of phases $\vec{\phi} = \{\phi_0, \phi_1, \ldots, \phi_d\} \in \mathbb{R}^{d+1}$, and using the Wx convention, the QSP operation sequence $U_{\vec{\phi}}$ is defined as

$$U_{\vec{\phi}} = e^{i\phi_0\hat{Z}} \prod_{k=1}^{d} W(a) e^{i\phi_k\hat{Z}}. \tag{4.3}$$

Although perhaps not immediately evident, the utility of QSP lies in how it can be used to transform the input a to the signal operator W. For example, if we take $\vec{\phi} = \{0, 0\}$, we obtain a trivial transformation of a with no processing (i.e., $U_{\vec{\phi}} = W(a)$. If we examine the probability of a $|0\rangle$ qubit staying unchanged (i.e., $p = \langle 0|U_{\vec{\phi}}|0\rangle$) under such a QSP operation as a function of $\theta = -2\cos^{-1} a$, we find a sinusoid, namely $p = \cos^2(\frac{\theta}{2})$.

This is fairly simple, but let us now examine what happens if we take a more complex QSP sequence for constructing $U_{\vec{\phi}}$. Suppose that we take $\vec{\phi} = \left\{\frac{\pi}{2}, -\eta, 2\eta, 0, -2\eta, \eta\right\}$, where $\eta = \frac{1}{2}\cos^{-1}(-\frac{1}{4})$. In this case, we find a different, and perhaps more useful, probability of the $|0\rangle$ state remaining unchanged as a function of θ:

$$\begin{aligned} p &= |\langle 0|U_{\vec{\phi}}|0\rangle|^2 \\ &= \frac{1}{8}\cos^2\left(\frac{\theta}{2}\right)\left(3\cos^8\left(\frac{\theta}{2}\right) - 15\cos^6\left(\frac{\theta}{2}\right) + 35\cos^4\left(\frac{\theta}{2}\right) - 45\cos^2\left(\frac{\theta}{2}\right) + 30\right). \end{aligned} \tag{4.4}$$

This probability is plotted with the probability resulting from the trivial QSP sequence in Fig. 4.1. Note that this function has the useful property that the qubit measures 0 for a wide range of signal values before a sharp transition to measuring 1 for θ greater than approximately $\frac{2}{3}\pi$. As such, we are able to use such a QSP sequence as a filter sensitive to specific values of θ, a property that has many potential applications, such as improving image contrast in MRI, and this particular sequence is well-known in the field of nuclear magnetic resonance as the "BB1" pulse sequence.

This property of being able to obtain useful functions of a, and hence θ, in the probability of the operator $U_{\vec{\phi}}$ leaving the state $|0\rangle$ unchanged is not a coincidence. In fact, it is perhaps one of the most important results in quantum signal processing that with an appropriate choice of the phases $\vec{\phi}$, $P(a) = \langle 0|U_{\vec{\phi}}|0\rangle$ can achieve most polynomials. This result is summarized in the following theorem.

Theorem 1 (Quantum Signal Processing)**.** *The QSP sequence $U_{\vec{\phi}}$ produces a matrix that can be expressed as a polynomial function of a:*

$$e^{i\phi_0\hat{Z}} \prod_{k=1}^{d} W(a) e^{i\phi_k\hat{Z}} = \begin{bmatrix} P(a) & iQ(a)\sqrt{1-a^2} \\ iQ^*(a)\sqrt{1-a^2} & P^*(a) \end{bmatrix} \tag{4.5}$$

for $a \in [-1, 1]$, and a $\vec{\phi}$ exists for any polynomials P, Q of a such that

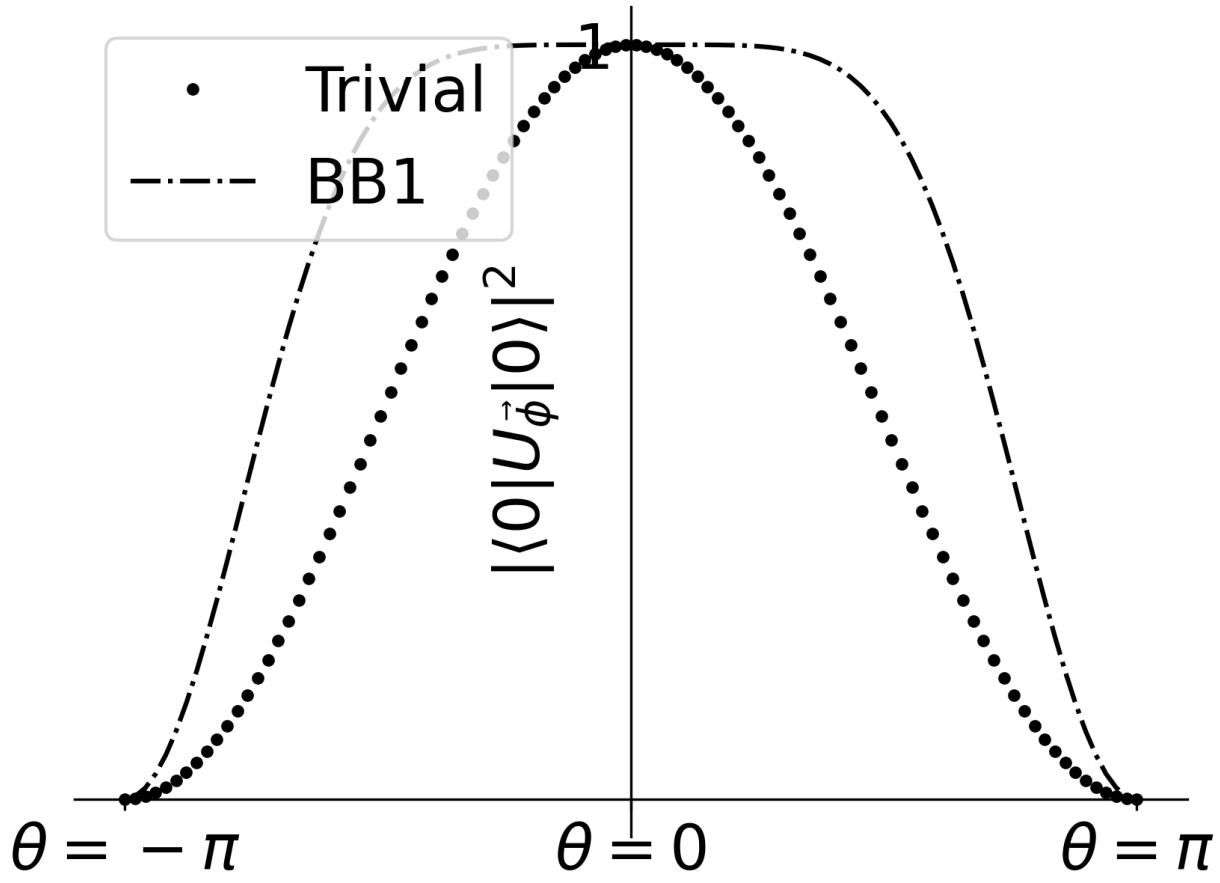

Figure 4.1: The transition probabilities for the initial state $|0\rangle$ to itself after the application of the trivial QSP sequence, $e^{\frac{i\theta\hat{X}}{2}}$, (dotted) and the QSP sequence for the BB1 protocol (dotted dashed). Note that the probability of remaining in the $|0\rangle$ state remains near 1 for a significantly wider range around 0 for the BB1 protocol as compared with the trivial protocol.

1. $\deg(P) \leq d$, $\deg(Q) \leq d-1$,

2. *P has parity d mod 2 and Q has parity $(d-1)$ mod 2,*

3. $|P|^2 + (1-a^2)|Q|^2 = 1$.

This QSP theorem demonstrates the power of the QSP framework for designing useful functions for signal processing in quantum computation. Given the triumphs of classical and quantum signal processing, we wonder if it might it be possible to adopt the philosophy of filter design to bosonic systems such that quantum signals on oscillators can be transformed for general sensing tasks.

4.3 Contributions

In the present work, we develop a novel algorithmic protocol for general quantum sensing tasks beyond parameter estimation using interferometric bosonic modes in a manner that enables *systematic and analytically predictive improvement* of single-shot decision error beyond what is possible with traditional sensing protocols. This *QSP interferometry (QSPI)* protocol builds on a theory of bosonic QSP that can perform polynomial transformation on the block-encoded quadrature operators of bosonic modes using qubit rotations and qubit-oscillator entangling gates [Hal+05; Eic+22]. The core of our QSPI protocol lies in these polynomial transformations generating nonclassical resource states for interferometery. Just as in typical Ramsey experiments [Ram50], the signal being sensed in a QSPI experiment is queried only once, and the power of quantum enhancement comes from generating a nonclassical resource state by increasing the QSP circuit length. The feature of only querying the signal only once distinguishes our work from much prior art [DGN22; Hua+23; Li+23; BW00]. The single sample feature (only one measurement is needed) of our protocol further distinguishes our work from [Mey+23; Pir+19].

We demonstrate the performance of the QSPI protocol with a theoretical analysis demonstrating its optimal extraction of binary decision information about a quantum displacement channel, which allows for the achievement of HL-like scaling (see Def. 1). As a concrete pedagogical example, we focus on the task of distinguishing whether a displacement channel has a displacement amount above or below a given threshold. Thus we are deciding between two sets of channels, i.e. the set of displacement channels above and below the threshold amount. This framework for quantum channel discrimination (QCD) problems opens the avenue to asking more complicated QCD questions that can decide between multiple hypotheses at the same time.

Note that such decision problems are ideal for qubit-oscillator systems because we desire a single-shot measurement that answers a question about the channel acting on a bosonic quantum state with high probability. Given that the qubit is naturally binary under classical projection measurement, extracting a yes/no answer from the qubit should be much faster than extracting a continuous-valued answer by measuring the oscillator. This intuition is satisfied by our construction.

4.4 A Binary Bosonic Decision Problem

In this section, we first set up some notation and define quantum decision-making problems in displacement sensing, as well as what HL-like behavior is for decision problems, in Sec. 4.4.1. In Sec. 4.4.2, we review the basics of a typical displacement-sensing protocol based on cat-state interferometry, highlighting its advantages and limitations in order to motivate why a more general sensing scheme is required.

4.4.1 Quantum Decision-Making for a Displacement Channel

We consider a quantum sensing problem in a joint qubit-oscillator system subjected to a unitary displacement channel S_β

$$S_\beta := \begin{bmatrix} e^{i\beta\hat{p}} & 0 \\ 0 & e^{i\beta\hat{p}} \end{bmatrix}, \tag{4.6}$$

where we have written S_β under the joint qubit-oscillator tensor product form such that $S_\beta = I \otimes e^{i\beta\hat{p}}$ and β is the amount of the position kick acting on the oscillator; $e^{i\beta\hat{p}} |x\rangle_{\text{osc}} = |x-\beta\rangle_{\text{osc}}$ for a position eigenstate $|x\rangle_{\text{osc}}$ (the subscript "osc" refers to "oscillator" to distinguish it from the qubit register). The symbol := used here represents the definition of a quantity, and $\hat{x}$, $\hat{p}$ are the oscillator's canonical position and momentum operators, respectively.

On the joint system, we assume the resource gates are arbitrary single-qubit rotations $R_X(2\theta) := e^{i\theta\hat{\sigma}_x}$ and a fixed qubit-oscillator entangling gate

$$\mathcal{D}_c(i\kappa/\sqrt{2}) = e^{i\kappa\hat{x}\hat{\sigma}_z} \tag{4.7}$$

parameterized by κ, where $\mathcal{D}_c(i\kappa/\sqrt{2})$ is a conditional displacement gate that imparts a momentum kick $\pm\kappa$ to the oscillator depending on the qubit state being $|0\rangle$ or $|1\rangle$. $\hat{\sigma}_x, \hat{\sigma}_z$ are the single-qubit Pauli matrices. This entangling gate is derived from the usual definition of a more general conditional displacement gate in phase space $\mathcal{D}_c(\alpha) := e^{(\alpha\hat{a}^\dagger - \alpha^*\hat{a})\hat{\sigma}_z}$ (the conditional version of the displacement gate introduced in Eq. 2.29) by setting $\alpha = i\kappa/\sqrt{2}$. Moreover, the gate in Eq. (4.7) is an operator with support on the infinite-dimensional qubit-oscillator joint Hilbert space. When acting on a position eigenstate of the oscillator $|x\rangle_{\text{osc}}$, the gate given in Eq. (4.7) reduces to $e^{i\kappa x\hat{\sigma}_z}$, which is simply a 2×2 operator acting on the qubit. Throughout the paper, we take $\hbar = 1, m = 1, \omega = 1$ for m the mass of the oscillator and ω its angular frequency, in order to simplify our expressions. This means the fundamental length of the oscillator $\sqrt{\hbar/m\omega} = 1$; as a result, κ, which should be in units of inverse β, is unitless. Additionally, we will use $\hat{x}$, $\hat{p}$ and x, p to distinguish the two different ways of using position and momentum as operators or real numbers. The product of $\kappa\hat{x}$ on the right-hand side of Eq. (4.7) means the gate itself will be periodic in the oscillator position x with a period of $T_x = \frac{2\pi}{\kappa}$.

With these notations established, we are ready to define the quantum decision-making problem on the displacement channel:

Main Problem (Quantum Binary Decision-Making for a Displacement Channel)**.** *Given* $\beta_{\text{th}} > 0$*, construct a quantum circuit by using the resource gates* R_X *and* $\mathcal{D}_c(i\kappa/\sqrt{2})$ *a*

maximum of d times for some κ to determine whether $|\beta| > \beta_{\text{th}}$ or $|\beta| < \beta_{\text{th}}$ with only a single query to S_β, such that the probability of making an erroneous decision, p_{err}, is small.

Clearly, the probability p_{err} of erroneous decision will depend on $\kappa, \beta_{\text{th}}$, and d. Due to the periodicity of Eq. (4.7) in x, any unitary constructed from repeated applications of $\mathcal{D}_c(i\kappa/\sqrt{2})$ and R_X will be periodic in x with the same period T_x. As will be discussed in Sec. 4.5.3 (also see Fig. 4.4), the periodicity in x for the $\mathcal{D}_c(\cdot)$ gate results in a period of $T_x/2$ for p_{err} in terms of the sensing parameter β. This allows us to define a restricted region $\left(-\frac{\pi}{2\kappa}, \frac{\pi}{2\kappa}\right)$ where the sensing problem will be discussed. This notion of periodicity is similar to the concept of a "unit cell" in solid state physics [AM76]. Therefore, it is necessary to choose κ to be small enough such that $\beta \in \left(-\frac{\pi}{2\kappa}, \frac{\pi}{2\kappa}\right)$ (in particular, β_{th} as well). However, κ cannot be too small, or else $\mathcal{D}_c(i\kappa/\sqrt{2})$ will become too close to the identity operator, and its action on the qubit-oscillator system will not be effective. In the rest of the paper, we assume that κ has been fixed with these conditions satisfied. Furthermore, (as detailed in Appendix E) p_{err} is an even function of β; therefore, we only consider the case of $\beta_{\text{th}} > 0$, as given in Main Problem.

Once we are given β_{th} and have fixed κ as described above, it is instructive to consider how p_{err} scales as the number of resource gates d in the sensing protocol. In the single-shot limit, since we are only allowed to query the signal S_β once, it is not difficult to see that the most general single-shot decision-making protocol is as given in Fig. 4.2a, where a state preparation routine is first used to prepare the joint qubit-oscillator system at some entangled quantum state, after which the signal of interest occurs to the oscillator. In the end, a signal decoding operation is applied to create some interference followed by a single-qubit measurement to extract the answer to the decision problem. Inspired by the definition of HL scaling in parameter estimation tasks, as discussed in Sec. 4.1, we define HL-like scaling for the Main Problem:

Definition 1 (HL-like Scaling for Binary Decision error in the Main Problem.)**.** *A sensing protocol achieves Heisenberg-limit-like (HL-like) scaling for binary decision-making with a displacement channel in the Main Problem if the resulting $p_{\text{err}} \sim O(1/d)$ up to a factor of polylog$(1/d)$.*

Note that Ref. [ZZS18] provides a different definition of Heisenberg scaling on multiple bosonic modes for parameter estimation problems based on total photon numbers. In our case, there is not a one-to-one correspondence between d and the average photon number, because the latter will depend on how the resource gates $R_X, \mathcal{D}_c(i\kappa/2)$ are used for a fixed d. Thus, our primary resource is sensing time. Literature for quantum state and channel discrimination has placed broad bounds on the optimal error probability [Hel69; Pir+19; Mey+23], but these works are often lacking analysis of the resource requirements to achieve a given error. Just as for parameter estimation, the Heisenberg-limit is defined as comparing to using classical states for the estimation task; for single-shot decision making, the classical analogue is akin to binary amplitude shift keying where the signal-to-noise ratio increases as $\sqrt{t}$ for t the signal integration time and thus limits the bit error rate to scale with $1/\sqrt{t}$ [Yan21].

In the following section, we will consider a concrete realization of the general single-shot decision-making protocol (Fig. 4.2b), the cat state sensing protocol, to gain some intuition.

4.4.2 Intuition from Cat-State Sensing

The intuition for building a QSP interferometer comes from the cat-state protocol for sensing small displacements. A typical sensing scheme is shown in Fig. 4.2b where a Hadamard gate and a controlled displacement $\mathcal{D}_c(i\kappa/\sqrt{2}) = e^{i\kappa\hat{x}\hat{\sigma}_z}$ are first used to prepare an entangled state of the qubit-oscillator joint system from an initial qubit state $|\downarrow\rangle$ and oscillator state $|0\rangle_{\text{osc}}$ (first dashed blue box). The subscript c in $\mathcal{D}_c(\cdot)$ means the displacement is controlled by the qubit. Then the underlying signal (a displacement $S_\beta = e^{i\beta\hat{p}}$) is applied to the oscillator and followed by another controlled displacement and a Hadamard gate (inverse of the previous dashed blue box). Finally, a qubit Z-basis measurement is performed.

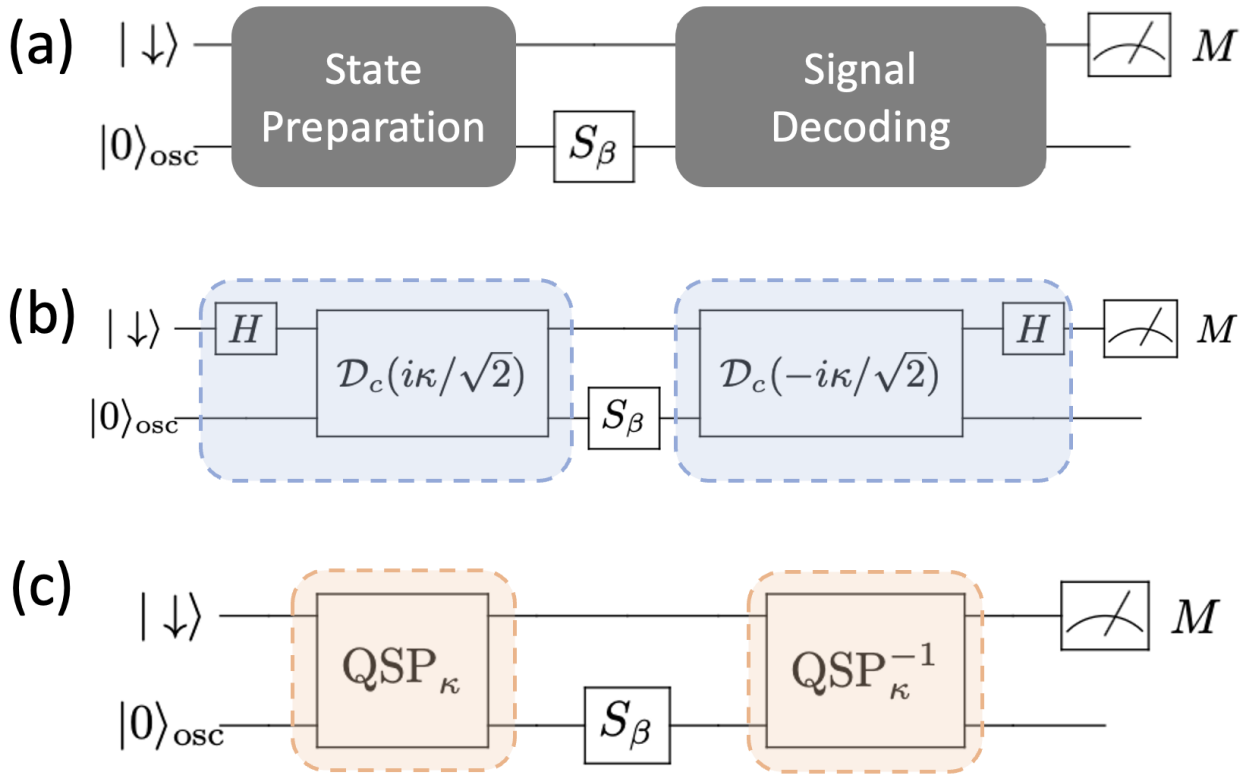

Figure 4.2: The most general single-shot decision-making protocol (a), and two realizations comparing the traditional cat-state sensing protocol (b) with the novel bosonic QSP interferometric protocol (c). In (c), the QSP operator creates an optimal sensing state, which then probes the signal S_β and is finally un-created to produce desired interference, which is followed by a measurement on the qubit.

Using the commutation relationship between $\hat{x}$ and $\hat{p}$ we have the following relation

$$e^{i\kappa\hat{x}}e^{i\beta\hat{p}} = e^{i\beta\hat{p}}e^{i\kappa\hat{x}}e^{-i\kappa\beta}, \tag{4.8}$$

which simplifies the final state of the joint qubit-oscillator system before the measurement to

$$|\Psi_{\text{out}}\rangle = (\cos(\kappa\beta)\,|\downarrow\rangle + i\sin(\kappa\beta)\,|\uparrow\rangle) \otimes e^{-i\beta\hat{p}}\,|0\rangle_{\text{osc}}\,, \tag{4.9}$$

provided that the initial state is $|\downarrow\rangle \otimes |0\rangle_{\text{osc}}$. Therefore, the displacement β is encoded in the amplitude of the ancilla qubit, where the measurement probability p of the qubit in $|\downarrow\rangle$ is

$$p = \text{Prob}[M = \downarrow] = \cos^2(\kappa\beta). \tag{4.10}$$

Since κ is known, we can repeat this sensing protocol multiple times in order to obtain an estimate of this probability, which will then tell us the value of β.

More concretely, by repeating the protocol N times, the standard deviation for estimating β is given by $\Delta\beta$:

$$\Delta\beta = \frac{\Delta p}{\left|\frac{dp}{d\beta}\right|} = \frac{1}{2\kappa\sqrt{N}} \tag{4.11}$$

where $\Delta p = \sqrt{\frac{p(1-p)}{N}}$ is the standard deviation on p, estimated by performing N experiments with a Bernoulli distribution, and the total time t for repeating the sensing protocol N times will be $t \propto N$. An interesting observation immediately follows from Eq. (4.11): for fixed N, $\Delta\beta$ improves roughly as $1/\kappa$, where κ is the displacement amount of the $\mathcal{D}_c(\cdot)$ gate. The physical intuition is that the cat state's small interference features in phase space have a characteristic length of $1/\kappa$. As a result, the sensitivity on estimating a spatial variation in β improves as $1/\kappa$. It follows that taking κ large would be beneficial to making high-sensitivity measurements. Such large κ can be realized in several ways, depending on the physical platform. For example, in trapped ions, a large κ may be realized by increasing the laser pulse intensity or by increasing the pulse duration [Hal+05].

Despite its favorable sensing scaling in κ for displacement sensing, the cat-state sensing protocol has some limitations. First, for fixed κ, $\Delta\beta$ decreases as $\frac{1}{\sqrt{N}}$ (or $\frac{1}{\sqrt{t}}$) as the number of classical repetitions N increases. This is the typical shot noise statistical convergence rate corresponding to the SQL and is sub-optimal as compared with HL scaling. Second, aside from parameter estimation on β, the cat-state sensing protocol is not particularly useful if we are only interested in learning partial information about the properties of β, for example determining if β is above or below a given threshold value β_{th}. Since only partial information is needed in such scenarios, it is expected that more efficient sensing protocols exist.

As alluded to earlier in the Introduction, filter designs in classical signal processing and advancement in quantum algorithms provide possibilities for overcoming the two aforementioned limitations such that: 1) Heisenberg-limited scaling can be achieved for parameter estimation, where $\Delta\beta \propto 1/N$; and 2) the resulting sensing protocol works for other sensing tasks that only extract partial information about β. The intuition is as follows: recall that the key feature of bosonic cat-state sensing is producing a fine-grained interference pattern in phase space that is sensitive to the displacement signal. If the N incoherent repetitions of the cat-state sensing protocol can be concatenated together into a *single-shot coherent protocol* which coherently manipulates the phase space interference pattern beyond that produced by the simple cat-state interferometer, then the coherent sensing state can be made sensitive to the partial information that we seek from the signal. In the next section, we give a construction of a novel QSP interferometer that circumvents the above two limitations and achieves HL-like behavior for decision problems.

4.5 Quantum Signal Processing Interferometry

Before presenting the QSPI construction, we first formulate a theory of bosonic QSP by alternating single-qubit rotations with controlled-displacement operations in Sec. 4.5.1 and show how to utilize this bosonic QSP approach as the basic building block to produce general sensing algorithms. Building upon the bosonic QSP theory for polynomial transformations of quadrature operators as well as the cat state sensing protocol above, we define and construct a novel QSP interferometer on hybrid qubit-oscillator platforms and present a new QSPI Theorem in Sec. 4.5.2. Detailed analysis of the behavior of the QSP interferometer for a displacement operator is discussed in Sec. 4.5.3.

4.5.1 Bosonic QSP Formalism

Coupling a bosonic oscillator to a qubit is a useful approach for achieving universal control of the oscillator [Kra+15]. It has been shown that simple Jaynes-Cummings type interactions can achieve universal control on an arbitrary low-energy d-dimensional subspaces of an oscillator [MM13; Liu+21]. By using an alternative dispersive coupling, universal control on oscillators has also been demonstrated using the echoed-controlled displacement operator [Eic+22]. Here, we draw a connection between these control protocols with quantum signal processing to develop a bosonic QSP formalism as a basic building block for the rest of the paper.

Quantum signal processing relies on two components: 1) a block-encoding of the signal operator; and 2) the ability to impart an arbitrary phase shift to the block-encoded operator. Block-encoding simply means embedding the target operator inside a known and accessible subspace of a unitary matrix. Methods for block-encoding on qubit devices are mostly limited to linear combination of unitaries [CW12; Ber+15], and block-encoding of a general Hamiltonian seems to be difficult. It might thus seem that such block-encoding will be especially challenging in our case, as we need to block-encode an entire oscillator (with infinite dimension) into a unitary matrix in order to perform QSP on the oscillator. Surprisingly, some physical interactions between quantum systems can provide natural block-encodings of one system in the basis of the other for qubit-oscillator systems, as is stated formally in Lemma 2.

Lemma 2 (Qubitization of a Bosonic Mode via Qubit-oscillator Physical Interaction)**.** *Coupling between a qubit Pauli operator $\hat{\sigma}_z$ and a bosonic mode's quadrature operators, $h(\hat{x}, \hat{p})$, naturally block-encodes the bosonic mode's unitary evolution operator $\omega(\hat{x}, \hat{p}) = e^{-ih(\hat{x},\hat{p})t}$.*

The above statement immediately follows if we write the resulting unitary under the representation of the qubit's $SU(2)$ matrix,

$$W_z := e^{-ih(\hat{x},\hat{p})\hat{\sigma}_z t} = \begin{bmatrix} \omega(\hat{x}, \hat{p}) & 0 \\ 0 & \omega^{-1}(\hat{x}, \hat{p}) \end{bmatrix}. \tag{4.12}$$

Note that the choice of $\hat{\sigma}_z$ here is only a convention, and any coupling can always be rotated into the $\hat{\sigma}_z$ representation. Also, note that $\omega(\hat{x}, \hat{p})$ is an *operator* on the oscillator rather than a complex number.

Now, given the qubitization of a bosonic mode, we are ready to state a bosonic quantum signal processing theorem that summarizes the achievable polynomial transformations on the quadrature operator $\omega(\hat{x}, \hat{p})$, as defined in Lemma 2.

Theorem 3 (Bosonic Quantum Signal Processing)**.** *The following quantum circuit parameterized by $\vec{\theta} = \{\theta_0, \ldots, \theta_d\}$ achieves a block-encoding of a degree-d Laurent polynomial transformation on $\omega(\hat{x}, \hat{p})$ as $F(\omega)$*

$$Q_{\vec{\theta}}(\omega) = e^{i\theta_d \hat{\sigma}_x} \prod_{j=0}^{d-1} W_z e^{i\theta_j \hat{\sigma}_x} = \begin{bmatrix} F(\omega) & iG(\omega) \\ iG(1/\omega) & F(1/\omega) \end{bmatrix}, \tag{4.13}$$

where (setting $t = 1$ for simplicity)

$$F(\omega) = \sum_{n=-d}^{d} f_n \omega^n = \sum_{n=-d}^{d} f_n e^{-ih(\hat{x}, \hat{p})n} := f(\hat{x}, \hat{p}), \tag{4.14a}$$

$$G(\omega) = \sum_{n=-d}^{d} g_n \omega^n = \sum_{n=-d}^{d} g_n e^{-ih(\hat{x}, \hat{p})n} := g(\hat{x}, \hat{p}). \tag{4.14b}$$

for $n = \{-d, -d+2, -d+4, \ldots, d\}$, $f_n, g_n \in \mathbb{R}$, $F(\omega)F(1/\omega) + G(\omega)G(1/\omega) = 1$, and $h(\hat{x}, \hat{p})$ is an analytical function of the bosonic mode's quadrature operators. Inversely, given $F(\omega)$ in Eq. (4.14a) and $F(\omega)F(1/\omega) < 1$, there exists $\vec{\theta} = \{\theta_0, \ldots, \theta_d\}$ such that the construction in Eq. (4.13) block-encodes $F(\omega)$.

The proof of Theorem 3 follows from the normal QSP proof on single qubit [LC19] or the periodic function formulation [Haa19] once $Q_{\vec{\theta}}(\omega)$ is expanded under the infinite sets of eigenstates of $h(\hat{x}, \hat{p})$. A detailed proof can be found in App. D. Note that a recursive relationship for computing the coefficients f_n and g_n from the phase sequence $\vec{\theta}$ is given in App. F. We also note that despite the similarity to single-qubit QSP, bosonic QSP is formally an infinite-dimensional theorem.

In general, $h(\hat{x}, \hat{p})$ can be any physically realizable Hamiltonian of the oscillator (i.e., not only finite degree polynomials but also analytic functions). To the lowest order, $h(\hat{x}, \hat{p})$ can be a linear function of $\hat{x}$ and $\hat{p}$, which generates a displacement in the phase space: $h(\hat{x}, \hat{p}) = \alpha\hat{a}^\dagger - \alpha^*\hat{a}$. Coupling h to a qubit Pauli operator generates a qubit-controlled displacement. Consider the special case where a simple qubit-oscillator coupling naturally arises on cQED hardware [Bla+04] or in trapped ions [Mon+96]; we have $h(\hat{x}, \hat{p})t = -\kappa\hat{x}$, where t denotes the duration of the qubit-oscillator interaction or coupling, which generates a displacement operator to boost the oscillator momentum by an amount of κ. From Lemma 2, it is readily realized that the physical dynamics generated from this coupling Hamiltonian form a block-encoding of the oscillator operator $\omega := e^{i\kappa\hat{x}}$. Combined with Theorem 3, we have

$$F(\omega) = \sum_{n=-d}^{d} f_n e^{i\kappa\hat{x}n} := f(\hat{x}), \tag{4.15a}$$

$$G(\omega) = \sum_{n=-d}^{d} g_n e^{i\kappa\hat{x}n} := g(\hat{x}), \tag{4.15b}$$

where $n = \{-d, -d+2, -d+4, \ldots, d\}$, and d is the degree of QSP, as specified in Theorem 3. The achievable functions and parity constraints upon $Q_{\vec{\theta}}(\omega)$ for $\omega \in \mathbb{C}$ are described in [Haa19]. Note that in this case ω is a unitary operator that maps oscillator position $x \in (-\infty, \infty)$ to the complex unit circle, so $f(\hat{x})$ and $g(\hat{x})$ are periodic functions with a period $T_x = \frac{2\pi}{\kappa}$. For an integer m:

$$f(\hat{x} + mT_x) = f(\hat{x}), \tag{4.16a}$$
$$g(\hat{x} + mT_x) = g(\hat{x}). \tag{4.16b}$$

The overall construction of the bosonic QSP circuit from Theorem 3 is shown in Fig. 4.3, where the conditional displacement operator and single qubit rotations are performed repeatedly. Since this construction performs an arbitrary degree-d real Laurent polynomial on ω with definite parity, it follows that the resulting functions $f(\hat{x})$ and $g(\hat{x})$ have flexibility to achieve a wide class of functions on $\hat{x}$ in the interval $\left[-\frac{\pi}{\kappa}, \frac{\pi}{\kappa}\right]$ that admit at most a degree-d Fourier expansion, as in Eq. (4.14a) and Eq. (4.14b). Note that the numerical and experimental realization of such conditional displacements in Ref. [Eic+22] for universal control of oscillators provides an example of the expressivity of such a bosonic QSP construction. The ability to obtain such nonlinear transformations on oscillator quadrature operators forms the basis of the QSP interferometry, as we will discuss next.

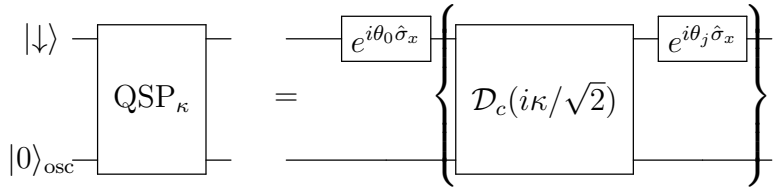

Figure 4.3: A bosonic QSP circuit composed of single-qubit rotations and controlled displacement operations, where the form of $\mathcal{D}_c(i\kappa/\sqrt{2})$ is given in Eq. (4.7). The gates inside the bracket are repeated d times for different θ_j ($j = 1, 2, \ldots, d$) in order to obtain a degree-d Laurent polynomial.

4.5.2 QSP Interferometry

Building on the ability to perform polynomial transformations on a bosonic oscillator's quadrature operators using QSP in Sec. 4.5.1 and Theorem 3, we construct a QSP interferometry (QSPI) protocol in this section by combining two bosonic QSP sequences.

A QSP interferometry protocol is defined as follows:

Definition 2 (Degree-d Quantum Signal Processing Interferometry (d-QSPI)). *Given an underlying bosonic signal unitary $S_\beta = e^{ih_\beta(\hat{x},\hat{p})}$, where $h_\beta(\hat{x}, \hat{p})$ is a finite-degree Hermitian polynomial of the quadrature operators $\hat{x}$, $\hat{p}$ parameterized by $\beta \in \mathbb{R}$, a degree-d quantum signal processing interferometry (d-QSPI) protocol for S_β is defined as the protocol in Fig. 4.2c, or $Q_{\vec{\theta}}^{-1}(\omega) S_\beta Q_{\vec{\theta}}(\omega)$, where $Q_{\vec{\theta}}(\omega)$ is given by Eq. (4.13). Furthermore, we define the joint qubit-oscillator state created by $Q_{\vec{\theta}}(\omega)$ as the QSPI sensing state $|\tilde{Q}\rangle = Q_{\vec{\theta}}(\omega) |\downarrow\rangle \otimes |0\rangle_{\text{osc}}$.*

It is readily recognized that the QSPI protocol described in Definition 2 is a simple generalization of the usual cat-state interferometry protocol, where the cat-state preparation is replaced by an arbitrary bosonic QSP transformation. The QSPI protocol may also be viewed as a parameterized version of typical quantum parameter estimation and discrimination protocols, which involve optimization of a cost function over probe states and measurement operators [Hel69]. Each d-QSPI protocol is entirely characterized by the angle sequence $\vec{\theta}$, where the first QSP sequence QSP_κ in Fig. 4.2c prepares the optimal sensing state while the second QSP sequence QSP_κ^{-1} transforms over the measurement probes. Thus, we will minimize our cost function, the probability of decision error, over the QSP angle sequence. In this perspective, our protocol is restricted to be symmetric in the state preparation and measurement procedures (because QSP_κ and QSP_κ^{-1} in Fig. 4.2c are parameterized by the same set of phase angles), but given the symmetry of the response function we seek this restriction simply makes the optimization more feasible. This choice is also motivated by the success of Ramsey-type protocols, which treat the state preparation and measurement steps symmetrically, but our bosonic QSP framework is able to handle more general approaches taken in other quantum estimation/discrimination schemes by using a different set of QSP angles for the signal decoding operator.

As an interferometer, the unitary operation realized by a d-QSPI must be a linear combination of many elementary unitaries, where the interference among them performs some desired quantum sensing task. To make the interferometry aspect of QSPI more vivid and to reveal how individual unitaries (or "paths") interfere, it is useful to identify what such elementary unitaries look like in QSPI. Because each matrix element of the bosonic QSP constructed in Eq. (4.13) is a linear combination of ω^n for different $n \in [-d, d]$, we define a *QSPI elementary transformation* on the signal S_β under the basis ω^n:

Definition 3 (QSPI Elementary Transformation)**.** *An elementary QSPI transformation $S_{\beta,nm}(\hat{x}, \hat{p})$ on S_β is defined as follows:*

$$S_{\beta,nm}(\hat{x}, \hat{p}) := \omega^{-n} S_\beta \omega^m, \tag{4.17}$$

for some $\omega = e^{-ih(\hat{x},\hat{p})}$ acting on a bosonic mode and for integers n, m.

From a basis-set-expansion point of view, Eq. (4.17) is equivalent to expanding the unknown operator S_β under the basis set $\{\omega^n\}$, where $S_{\beta,nm}(\hat{x}, \hat{p})$ is simply the resulting matrix element (despite its infinite-dimensional nature). In the special case of $\omega = e^{i\kappa\hat{x}}$, Eq. (4.17) can be viewed as a plane-wave expansion of S_β for a set of discrete reduced momenta nk for integer n, which is similar to the k-point sampling technique in the numerical study of periodic solid-state systems [AM76], where k determines the low-energy cutoff, while the upper limit of n dictates the high-energy cutoff. We will see in the following that this high-energy cutoff is directly related to the QSP degree d that is being used in our construction.

With the elementary transformation defined, we are now ready to present the QSPI transformation theory that describes how QSPI acts as an interferometer:

Theorem 4 (QSP Interferometry Theorem)**.** *A d-QSPI protocol for a bosonic signal unitary S_β performs a transformation to S_β such that the resulting unitary is a linear combination*

of $(d+1)^2$ *elementary transformations* $S_{\beta,nm}(\hat{x},\,\hat{p})$ *as defined in Def. 3*

$$Q_{\vec{\theta}}^{-1}(\omega)S_\beta Q_{\vec{\theta}}(\omega) = \sum_{n,\,m=-d}^{d} C_{nm}S_{\beta,\,nm}(\hat{x},\,\hat{p}), \tag{4.18}$$

where C_{nm} *is a complex coefficient matrix defined from the original QSP coefficients by*

$$C_{nm} = \begin{bmatrix} f_n f_m + g_{-n}g_{-m} & i(f_n g_m - g_{-n}f_{-m}) \\ i(f_{-n}g_{-m} - g_n f_m) & g_n g_m f_{-n}f_{-m} \end{bmatrix}, \tag{4.19}$$

which serves as a complex weight to its associated elementary transformation $S_{\beta,nm}$ *in order to produce the desired interference.*

The proof of the theorem follows by direct multiplication of the left-hand side of Eq. (4.18). □

The right-hand side of Eq. (4.18) is a sum of $(d+1)^2$ terms, each weighted by a complex coefficient matrix C_{nm}, as defined in Eq. (4.19); this readily reveals that the resulting unitary of a d-QSPI protocol is essentially a giant interferometer of $(d+1)^2$ elementary components. Note that each element of C_{nm} is always quadratic in terms of f and g (either a product of two f or two g with different subscripts); this is simply a consequence of the fact that the QSP sensing state $|\tilde{\mathrm{Q}}\rangle$ prepared in Fig. 4.2c is perturbed by S_β before interfering with itself. In this fashion, the original QSP coefficients f_n, g_n can be tuned such that the desired interference pattern is produced by the protocol for any quantum sensing purpose. Note that there is no approximation, such as truncating the dimension of the infinite dimensional oscillators, in our formalism, since we explicitly work with the oscillator quadrature operators, and the physical regularization of the infinite dimensional transformation is provided by a finite-energy initial state (for example, a vacuum state).

Theorem 4 characterizes at the operator level how QSPI works, but it is not clear what or how much information can be extracted from the entire protocol via measurement. We discuss the measurement aspect in the following.

Just as in any interferometry protocol, we are interested in extracting information about S_β by performing some *measurement* after the protocol, where the measurement outcome contains information about the parameter β. It is possible to measure oscillators directly using homodyne/heterodyne detection or by performing a photon-number-resolved measurement. Such measurements will often provide *local* information on the phase-space distribution of the oscillator wave function. Alternatively, it is much easier (and typically faster) to measure the ancilla qubit directly. Such a qubit measurement implies a partial trace over the bosonic quadrature operator and therefore will provide useful *global* information about the oscillator. Extracting such global information is crucial to performing decision-making regarding the underlying signal parameter β, as we will see in Sec. 4.6.1. For the ease of discussion, we define the QSPI response function as follows:

Definition 4 (QSPI Response Function)**.** *A QSPI response function is defined as the probability distribution over the signal parameter* β *after a projective measurement on the ancilla qubit as* $\mathbb{P}(\beta) = \| \langle\phi_1|\, Q_{\vec{\theta}}^{-1}(\omega)S_\beta Q_{\vec{\theta}}(\omega)\, |\phi_0\rangle\, |0\rangle_{\mathrm{osc}} \|^2$*, where* $|\phi_0\rangle$ *and* $|\phi_1\rangle$ *are the initial and final state of the ancilla qubit and the oscillator is assumed to start from vacuum* $|0\rangle_{\mathrm{osc}}$*.*

QSPI response functions, or simply the response functions, as defined in Definition 4, characterize the complicated interference pattern between two oscillator states that are perturbed by S_β. The signature of such interference is cast onto the qubit measurement probability. In our case, the unitary channel that we wish to distinguish is a displacement of the oscillator perpendicular to W_z's displacement direction. The effect of the displacing signal S_β can be understood as convolving the QSP sensing state $|\tilde{\mathrm{Q}}\rangle$ with a shifted version of itself. Thus, for an optimal choice of the QSP polynomial, we expect to be sensitive to a certain range of displacements. This protocol takes Ramsey interferometry protocols as in [Gil+21; Mar+22] as inspiration. In fact, Eq. (4.10) in Sec. 4.4.2 can be viewed as a simple response function for cat-state sensing, since it can be realized by a degree-1 QSPI protocol, as we will see in the next section.

4.5.3 QSPI Protocols for Displacement Sensing

We examine the outcome for the qubit state in our generalized QSP sensing protocol for displacement sensing in Sec. 4.5.3.1. Then we use the degree-1 case as an example to connect to the cat-state sensing protocol in Sec. 4.5.3.2.

4.5.3.1 General Theory of QSPI Displacement Sensing

We shall drop $\vec{\theta}$ subscripts from Q from here on for simplicity. The sensing sequence, also from Fig. 4.2c, is given by:

$$U(\beta, \omega) = \mathrm{Q}^{-1}(\omega) S_\beta \mathrm{Q}(\omega), \tag{4.20}$$

where $\mathrm{Q}^{-1}(\omega) = \mathrm{Q}^\dagger(1/\omega)$. Using Eq. (4.8), we may rewrite Eq. (4.20) as

$$U(\beta, \omega) = \mathrm{Q}^{-1}(\omega) S_\beta \mathrm{Q}(\omega) = S_\beta \mathrm{Q}^\dagger(1/\omega') \mathrm{Q}(\omega), \tag{4.21}$$

where

$$\omega' = \omega e^{-i\kappa\beta} = e^{i\kappa(\hat{x}-\beta)}. \tag{4.22}$$

The right-hand side of Eq. (4.21) reveals a key insight: the total QSPI protocol reduces to a product of $\mathrm{Q}^\dagger(1/\omega')\mathrm{Q}(\omega)$ (up to an irrelevant global phase S_β), which is a QSP sequence interfering with a shifted version of itself $\omega \to \omega'$ by a constant phase $e^{-i\kappa\beta}$, as defined in Eq. (4.22). It is this β-dependent shift that allows the extraction of useful information on β from the interferometry.

In order to find the response function for the probability of measuring the qubit in the ground state after the sensing protocol, we must integrate over the probability distribution in phase space. Let us denote the upper left matrix element of U as $U_{00} = e^{i\beta\hat{p}}\big[f(-\hat{x}+\beta)f(\hat{x}) + g(\hat{x}-\beta)g(-\hat{x})\big]$, then the measurement probability of the qubit being at state $|\downarrow\rangle$ is

$$
\begin{aligned}
&\mathbb{P}(M =\downarrow |\beta) \\
&= || \langle\downarrow| \mathrm{Q}^{-1} S \mathrm{Q} |\downarrow\rangle |0\rangle_{\mathrm{osc}} ||^2 \\
&= \langle 0|_{\mathrm{osc}} (U_{00})^\dagger U_{00} |0\rangle_{\mathrm{osc}} \\
&= \int_{-\infty}^{\infty} dx \, |[f(-x+\beta)f(x) + g(x-\beta)g(-x)] \, \psi_0(x)|^2 \, .
\end{aligned} \tag{4.23}
$$

where $\psi_0(x) = \pi^{-1/4} e^{-x^2/2}$ is the vacuum state of the oscillator, and we have used real numbers x as the argument of $f(\cdot)$ and $g(\cdot)$ since everything has been written under the position representation. Thus, $\mathbb{P}(M =\downarrow |\beta)$ is a function of our signal parameter β and the original QSP phase angles. We may now tailor the shape of the QSP Laurent polynomial such that the qubit response $\mathbb{P}(M =\downarrow |\beta)$ scales optimally versus β.

Using the Laurent polynomial expressions from Eq. (4.14a) and Eq. (4.14b) and explicitly evaluating the integration with respect to x, we can alternatively write Eq. (4.23) as a series sum

$$
\mathbb{P}(M =\downarrow |\beta) = \sum_{s=-d}^{d} c_s v(\beta)^s \tag{4.24}
$$

for $v(\beta) = e^{i(2\kappa)\beta}$ and $c_s \in \mathbb{R}$ being a function of κ

$$
\begin{aligned}
c_s = &\sum_{n,\, n',\, r=-d}^{d} (f_n f_{n'} + g_n g_{n'}) \\
&\times (f_{n+2s} f_{n'+2r} + g_{n+2s} g_{n'+2r}) e^{-\kappa^2 (r-s)^2}
\end{aligned} \tag{4.25}
$$

where n, n' are either all odd or all even depending on the parity of d. It follows that the response function of the qubit $\mathbb{P}(M =\downarrow |\beta)$ is a degree-d Laurent polynomial with respect to the new "signal" operator $v(\beta, \kappa) = e^{i(2\kappa)\beta}$. See Appendix E for a proof.

Figure 4.4: Pictorial illustration of how in the bosonic QSP interferometric protocol, the qubit measurement enacts a duality between a polynomial transformation on the bosonic quadrature operators and a polynomial transformation on the sensing parameter β via QSPI.

Therefore, apart from parity and normalization constraints, we may design the qubit response $\mathbb{P}(M =\downarrow |\beta)$ by choosing f_n and g_n such that we approach the desired Fourier series of a function of β. This relationship also reveals an interesting duality between the QSP polynomial transformation on phase space quadrature and the polynomial transformation on the signal parameter β in the response function, which is highlighted in Fig. 4.4 and summarized as Theorem 5.

Theorem 5 (QSPI for Displacement Sensing). *Given a degree-d QSPI protocol with the block-encoded quadrature operator $\hat{\omega} = e^{i\kappa\hat{x}}$ (periodic with a period of $\left[-\frac{\pi}{\kappa}, \frac{\pi}{\kappa}\right]$ with respect to x), a degree-d response function $\mathbb{P}(v) := \sum_s c_s v^s$, with $v = e^{i(2\kappa)\beta}$ as its argument, is well-defined where $\beta \in [-\frac{\pi}{2\kappa}, \frac{\pi}{2\kappa}]$. Conversely, given a degree-d real Laurent polynomial transformation (defined in Eq. (4.24) with c_s as its coefficients) on $v = e^{i(2\kappa)\beta}$ where $\beta \in \left[-\frac{\pi}{2\kappa}, \frac{\pi}{2\kappa}\right]$ as the desired response function that satisfies the following necessary conditions,*

$$\sum_{s=-d}^{d} c_s = 1, \quad c_s = c_{-s}, \tag{4.26a}$$

$$0 \leq \sum_s c_s v(\beta)^s \leq 1, \tag{4.26b}$$

there exists a d-QSPI protocol as in Fig. 4.2c that realizes the desired response function.

We will now sketch a proof of the above theorem. From [Haa19], we know for a given QSPI protocol characterized by $\vec{\theta}$ that $f(x)$ and $g(x)$ are well-defined, and thus the forward direction of Theorem 5 is trivial.

On the other hand, it is in general challenging to provide sufficient conditions for response functions such that they can be realized by the QSPI protocol using a set of phase angles $\vec{\theta}$. Here for the reverse direction of Theorem 5, we resort to only necessary conditions on the response function.

Because the response function is necessarily a probability on the qubit and involves a integral over the bosonic coordinates, there are additional constraints on the response function. First, from the response function's relevant parity and normalization constraints on c_s as defined in Eq. (4.24), Eq. (4.26a) can be derived. Secondly, beyond the parity and normalization constraints, we must also impose an additional constraint on possible sets of c_s due to the response function being a probability, which requires Eq. (4.26b) to be satisfied for all $\beta \in \mathbb{R}$. □

Let us make additional remarks on the reverse direction of Theorem 5. The reason that it is challenging to ascertain a set of sufficient conditions on the response function is due to the nonlinear transformation of F, G in Eq. (4.23). Inverting the system of polynomial equations in Eq. (4.25), even in the large κ limit where decay coefficients vanish, appears analytically intractable. From our construction in Eq. (4.14), it can be inductively shown that $f_{-d} = g_d = 0$, and from [Haa19], $F(\omega)$ determines $G(\omega)$ up to $\omega \mapsto 1/\omega$. Thus, for fixed κ, we may reduce Eq. (4.25) to a system of d independent equations with d unknowns, but searching for solution sets of such polynomial equations is difficult and often infeasible analytically.

4.5.3.2 Example: Cat State Sensing

For the degree $d = 1$ case, and $\{\theta_0, \theta_1\}$ as the QSP phase angles, the QSPI response function is

$$\mathbb{P}(M = 0|\beta) = c_0 + c_1 v + c_{-1} v^{-1} \tag{4.27}$$

where

$$c_0 = \cos^4(\theta_0) + \sin^4(\theta_0) \tag{4.28}$$

$$c_1 = c_{-1} = \cos^2(\theta_0)\sin^2(\theta_0). \tag{4.29}$$

Evidently, this is a degree-1 Laurent polynomial of the argument $v = e^{i(2\kappa)\beta}$, where all of the polynomial coefficients are real. Also, we note that the measurement probability is independent of θ_1 (or, in general, θ_d for a d-QSPI protocol) per the construction. Furthermore, by choosing $\theta_0 = \pi/4$, we recover exactly the cat state sensing protocol with $\mathbb{P}(M = 0|\beta) = \cos^2(\kappa\beta)$. Thus, the cat state sensing protocol is indeed a special case of a 1-QSPI protocol!

We can also view the cat-state sensing protocol for a displacement of κd as the trivial case of choosing all zero rotation angles for R_X in a d-QSPI protocol. In this case, the average photon number in the prepared state after state prepatation unitary in Fig. 4.2a will be $n_{\text{photon}} \propto \kappa^2 d^2$. Therefore, Def. 1 reduces to $p_{\text{err}} \sim O(1/\sqrt{n_{\text{photon}}})$. This agrees with the results in Sec. 4.4.2 and Fig. 4.6 (vide infra) that cat states are not efficient resource states for the Main Problem.

4.6 Binary Decision-Making Using QSPI

Now, we have established the QSPI protocol and its response function as a polynomial transformation of the signal. To demonstrate its potential for general sensing tasks, we derive an explicit expression for the response function for a binary decision problem on the displacement parameter in Sec. 4.6.1. Following this analysis, we delve deeper into the limitations of cat-state sensing for decision-making in Sec. 4.6.1.1. Lastly, we analyze analytically the decision quality and sensing complexity in Sec. 4.6.2.

4.6.1 Binary decision for displacement sensing

For a classical binary decision using measurement of a single qubit, we want the QSPI response function to be either 1 or 0 depending on the value of the signal displacement relative to β_{th}. In particular, one such target qubit response function is the step function

$$P_{\text{ideal}}(\beta) = \begin{cases} 1, & 0 \le |\beta| < \beta_{\text{th}} \\ 0, & \beta_{\text{th}} < |\beta| \le \frac{\pi}{2\kappa}. \end{cases} \tag{4.30}$$

If such an ideal qubit response function is realized, then the binary decision sensing protocol has no error. However, in practice, only a finite-degree polynomial approximation to this function is available and lead to decision errors. In the following, we give basic definitions to quantify the decision errors.

For ease of discussion, Fig. 4.5 plots the ideal response function (red) in contrast to a typical polynomial approximation generated by the QSPI protocol (black) as a function of the underlying displacement β. The approximated response function features a steep yet finite slope centered about β_{th}. There are usually some small oscillatory patterns for small

β and for $\beta_{\text{th}} < |\beta| < \frac{\pi}{2\kappa}$. Deviations of $P_{\text{approx}}(\beta)$ from $P_{\text{ideal}}(\beta)$ across the entire range of $\left[-\frac{\pi}{2\kappa}, \frac{\pi}{2\kappa}\right]$ quantify the overall probability of making the wrong decision. We define the following quantity as *decision error density*:

$$\begin{aligned} p_{\text{err}}(\beta_{\text{th}}, \kappa) &= \frac{\kappa}{\pi} \int_{-\frac{\pi}{2\kappa}}^{\frac{\pi}{2\kappa}} |P_{\text{approx}}(\beta) - P_{\text{ideal}}(\beta)| \, d\beta \\ &= p_{\text{err, FN}}(\beta_{\text{th}}) + p_{\text{err, FP}}(\beta_{\text{th}}). \end{aligned} \tag{4.31}$$

This quantity can be split into two contributions according to β_{th} as follows:

$$p_{\text{err, FN}}(\beta_{\text{th}}) = \frac{2\kappa}{\pi} \int_0^{\beta_{\text{th}}} (1 - P_{\text{approx}}(\beta)) \, d\beta, \tag{4.32a}$$

$$p_{\text{err, FP}}(\beta_{\text{th}}) = \frac{2\kappa}{\pi} \int_{\beta_{\text{th}}}^{\pi/2\kappa} P_{\text{approx}}(\beta) d\beta. \tag{4.32b}$$

The former, $p_{\text{err, FN}}(\beta_{\text{th}})$, defined in Eq. (4.32a), is the false-negative (FN) error (also called Type-II error in hypothesis testing) and is indicated by the grey region in Fig. 4.5, while the latter, $p_{\text{err, FP}}(\beta_{\text{th}})$, defined in Eq. (4.32b), is the false-positive (FP) error (Type-I error) and is highlighted in orange in Fig. 4.5 [Hel69]. Our goal in designing the response function is to find QSP phase angles that minimize the total decision error in Eq. (4.31).

Substituting Eq. (4.24) into Eq. (4.31), the error probability can be written explicitly as

$$p_{\text{err}}(\beta_{\text{th}}, \kappa) = \sum_{s=-d}^{d} c_s H_s(\beta_{\text{th}}, \kappa), \tag{4.33}$$

where we have defined

$$H_s(\beta_{\text{th}}, \kappa) = \frac{2\kappa\beta_{\text{th}}}{\pi} + \text{sinc}\,(\pi s) - \frac{4\kappa\beta_{\text{th}}}{\pi} \text{sinc}\,(2\kappa s \beta_{\text{th}}) \tag{4.34}$$

as a function of $(\beta_{\text{th}}, \kappa)$, and the definition of c_s is given in Eq. (4.25). Eq. (4.33) is the central metric for the binary decision problem in displacement sensing.

Additionally, note that κ and β_{th} always appear together in Eq. (4.34) as a product, which suggests there is a scale-invariance in the definition of H_s in the sense that the displacement length scale can be measured in units of $1/\kappa$ and only this relative length scale with respect to $1/\kappa$ is meaningful. Toward this end, we introduce a dimensionless parameter η to quantify $\beta_{\text{th}} = \eta\frac{\pi}{\kappa}$. It is evident that the dynamic range for the signal β will be $\eta \in [-0.5, 0.5]$, as is suggested by the horizontal axis of Fig. 4.5. However, the dependence of the coefficients c_s on κ in Eq. (E.8) means p_{err} is still κ-dependent, which in turn suggests the optimal sensing QSPI phase angles depend on κ.

Lastly, note that *some* information is inevitably lost when in the final step of the sensing protocol we trace out the oscillator part of the system with the qubit measurement, leaving only the qubit part of the system. However, by selecting the QSPI phases so as to engineer the polynomials F and G in ω (Eq. 4.14a and Eq. 4.14b) prior to measurement, we are able to maximize the proximity of the response-function polynomial in β after measurement to the ideal step-function response with transition at β_{th} (and hence minimize p_{err}). In this way, we

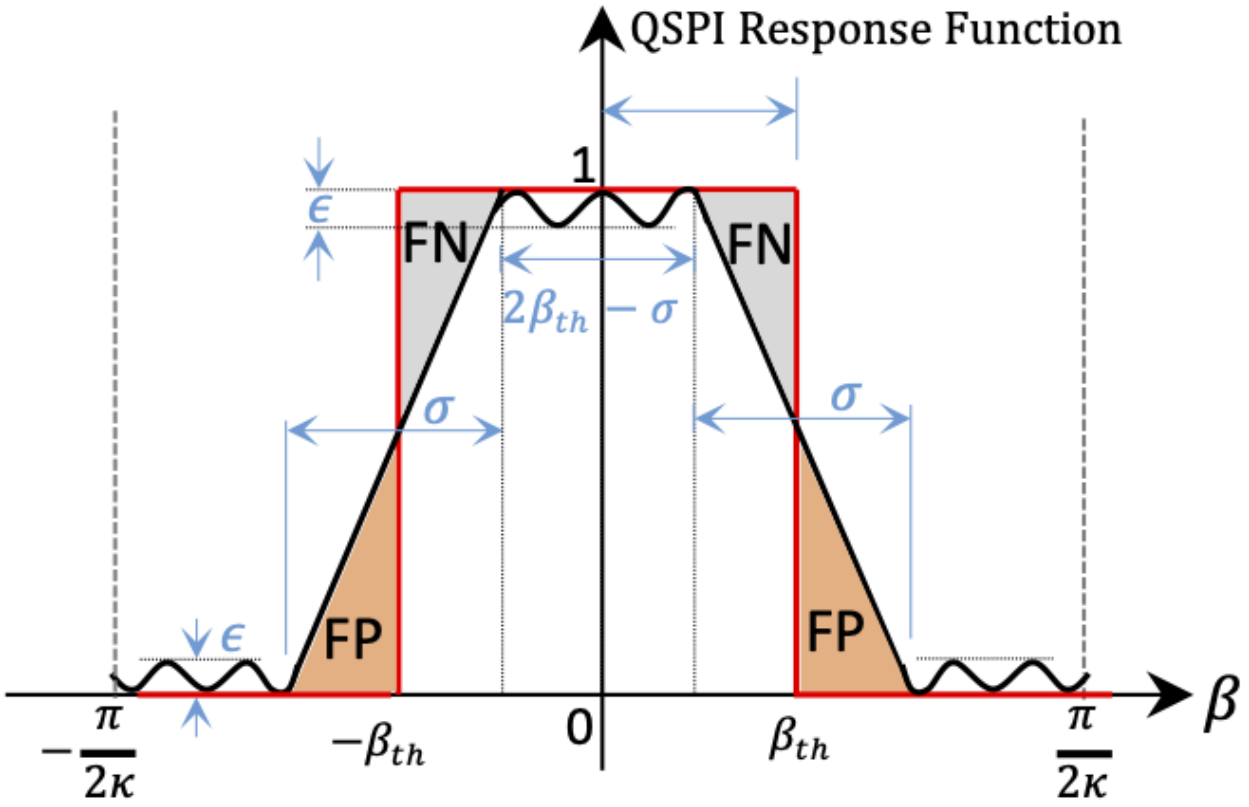

Figure 4.5: Schematic of erroneous decision making probability (from the response function) as the difference between the ideal response function (solid red) and a polynomial approximated response function (solid black). For an event defined as "the displacement is below threshold β_{th}", the integrated erroneous probability is composed of two parts: i) missing the event while it actually happened (false-negative, FN, Type-II error, grey-shaded area), ii) reporting the event when it did not happen (false-positive, FP, Type-I error, orange-shaded area). Note that the effective detection signal range is $\left[-\frac{\pi}{2\kappa}, \frac{\pi}{2\kappa}\right]$.

ensure that the *relevant* global displacement information is transferred from the oscillator to the qubit, allowing for the efficient extraction of a decision about the displacement magnitude without the need to directly read out the oscillator's state (which would require many samples and measurements).

4.6.1.1 Limitations of Cat State for Decision Making

As we have seen in Sec. 4.5.3.2 and in Fig. 4.2b, the cat-state sensing protocol corresponds to a degree $d = 1$ QSPI. It has also been shown in Eq. (4.11) in Sec. 4.4.2 that the cat state sensing protocol achieves the celebrated Heisenberg-limited sensing for parameter estimation. In this section, we will characterize the performance of cat-state sensing protocol for *decision-making* and reveal its limitations in this regard.

For degree $d = 1$ QSPI, the integrated probability of making the wrong decision per unit signal can be calculated as

$$p_{\text{err}} = \frac{1}{4\pi}\big[\sin(2\beta_{\text{th}}\kappa - 4\theta_0) + \sin(2\beta_{\text{th}}\kappa + 4\theta_0) \tag{4.35}$$

$$+ (\pi - 4\beta_{\text{th}}\kappa)\cos(4\theta_0) - 4\beta_{\text{th}}\kappa - 2\sin(2\beta_{\text{th}}\kappa) + 3\pi\big]. \tag{4.36}$$

We would like to minimize p_{err} overall by choosing θ_0 appropriately. The global minimum is found to be the following when $\theta_0 = \pi/4$ (regardless of β_{th} and κ):

$$p_{\text{err}}|_{\theta_0=\frac{\pi}{4}} = \frac{1}{2} - \frac{\sin(2\kappa\beta_{\text{th}})}{\pi}. \tag{4.37}$$

On the other hand, supposing that we perform no rotation on the qubit, or $\theta_0 = 0$, we obtain $\mathbb{P}(M = \downarrow |\beta) = 1$, which gives

$$p_{\text{err}}|_{\theta_0=0} = 1 - \frac{2\kappa\beta_{\text{th}}}{\pi}. \tag{4.38}$$

This makes sense because this scenario is equivalent to making a decision that the displacement is always below β_{th}, and therefore there is only false positive error and the error probability should decrease as β_{th} is increased. Moreover, when $\beta_{\text{th}} = \frac{\pi}{2\kappa}$, which is on the boundary of the sensing range, p_{err} drops to zero.

A comparison of the scaling of p_{err} versus β_{th} between the best decision $\theta_0 = \pi/4$ and the ignorant decision $\theta_0 = 0$ is shown in Fig. 4.6. It can be seen that the optimal sensing strategy significantly reduces p_{err} when $\beta_{\text{th}} < \beta^*_{\text{th}}$, while it performs worse than the naïve guess for $\beta_{\text{th}} > \beta^*_{\text{th}}$ where $\beta^*_{\text{th}} = \frac{\chi}{2\kappa}$ for χ being the solution to the transcendental equation $\frac{\pi}{2} - x + \sin(x) = 0$. The optimal sensing protocol works best for $\beta_{\text{th}} = \frac{\pi}{4\kappa}$, where it gives $p_{\text{err}} = \frac{1}{2} - \frac{1}{\pi}$. This simple example also demonstrates the non-trivial complexity of decision problems, even for the simplest such problems.

The above analysis also reveals that the minimum p_{err} achieved by the cat-state sensing protocol is always a constant regardless of the value of the displacement κ or the size of the cat state for a threshold $\beta_{\text{th}} = \frac{\pi}{4\kappa}$. This behavior is in drastic contrast with parameter estimation tasks, where a larger cat state will have finer interference fringes in phase space and therefore achieve Heisenberg-limited estimation accuracy for very small displacements

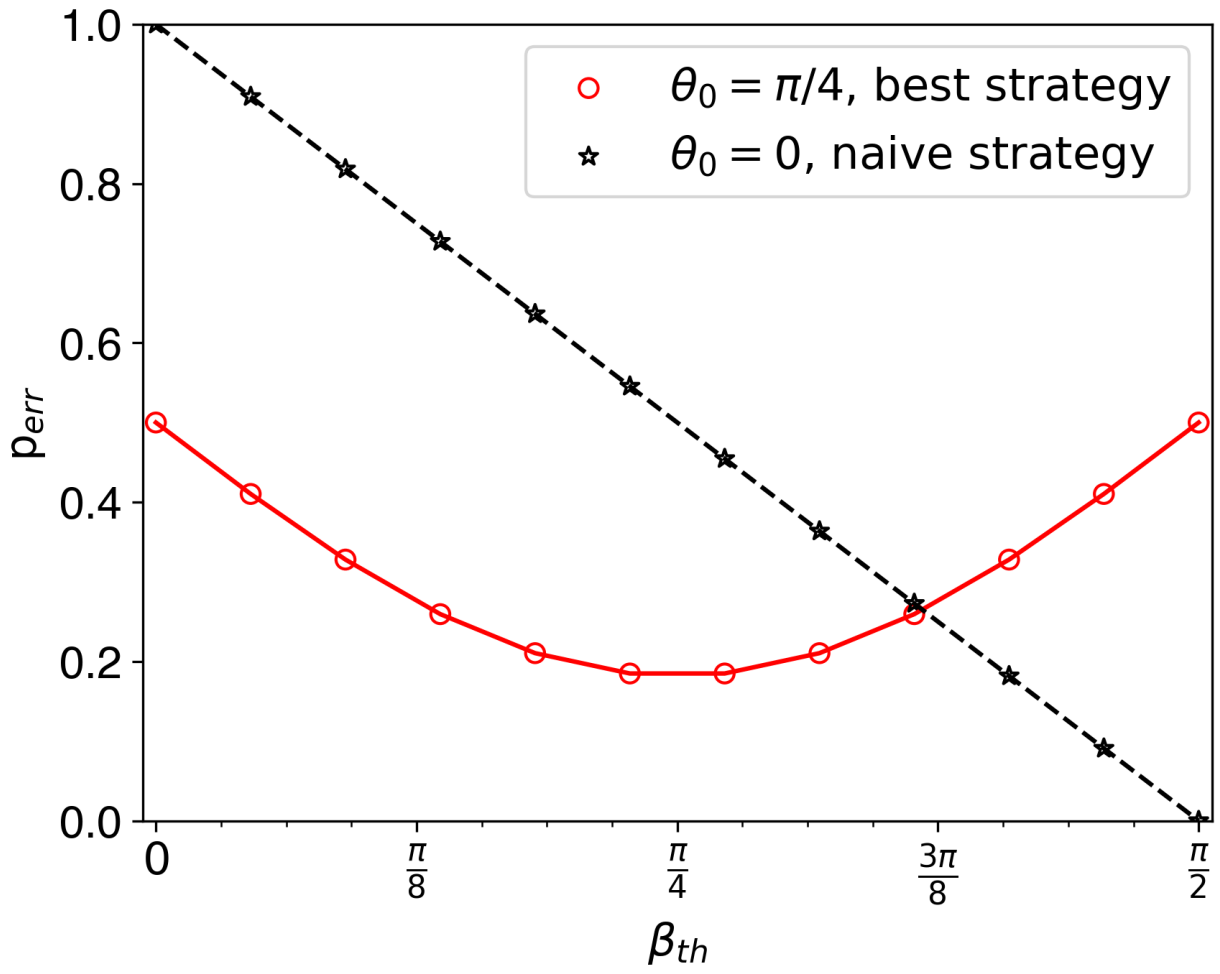

Figure 4.6: The probability of making wrong decision versus the decision threshold β_{th}. Data shown for a binary decision of displacement sensing using degree-1 bosonic QSP with $\kappa = 1$, comparing the best ($\theta_0 = \pi/4$, red circle) and the naïve ($\theta_0 = 0$, black star) sensing protocol.

(Eq. (4.11) of Sec. 4.4.2). An intuitive reason why decision-making with a larger cat-state does not help is that the integration in Eq. (4.31) smears out the local information in the oscillator wave function (e.g., the fine interference fringes), meaning that globally, a larger cat-state behaves the same as a smaller cat-state for the binary decision.

4.6.2 Algorithmic Complexity for Binary Decision

Given the definition of the decision error density $p_{\text{err}}(\beta_{\text{th}}, \kappa)$, in this section, we would like to understand some fundamental limits on how $p_{\text{err}}(\beta_{\text{th}})$ scales with the degree of the QSP. This determines the algorithmic complexity of making a high-quality binary decision using a QSPI protocol.

To do this, we first construct a composite function that exactly reproduces $P_{\text{ideal}}(\beta)$ (red trace in Fig. 4.5) in the relevant sensing range of $\left[-\frac{\pi}{2\kappa}, \frac{\pi}{2\kappa}\right]$. In particular, consider

$$P_{\text{ideal}}^{\text{sign, sin}}(\beta) = \frac{\text{sign}\left[\sin(\kappa(\beta_{\text{th}} - \beta))\right] + \text{sign}\left[\sin(\kappa(\beta_{\text{th}} + \beta))\right]}{2}, \tag{4.39}$$

where $\text{sign}(\cdot)$ is the sign function. We use the superscript $^{\text{sign, sin}}$ to distinguish the current construction from other possible constructions for $P_{\text{ideal}}(\beta)$.

With this, it can be shown (Appendix G) that to achieve a target faulty-decision probability p_{err}, the required QSP polynomial degree d to approximate $P_{\text{ideal}}^{\text{sign,sin}}(\beta)$ must have

$$d \propto \frac{1}{\kappa p_{\text{err}}} \log\left(\frac{1}{\kappa p_{\text{err}}}\right). \tag{4.40}$$

For small p_{err}, $\log\left(\frac{1}{p_{\text{err}}}\right) \ll \frac{1}{p_{\text{err}}}$. Therefore, the total faulty-decision probability can be solved from Eq. (4.40)

$$p_{\text{err}} \propto \frac{1}{\kappa d} \log(d). \tag{4.41}$$

Recall that in a standard parameter estimation task, Heisenberg-limited scaling is defined when the standard deviation for estimating the underlying parameter scales as $1/t$ where t is the total time for the sensing protocol (also see discussions in Sec. 4.4.2). Here for our case of binary decision making, analogous to parameter estimation, Eq. (4.41) suggests that our QSPI protocol can achieve a similar Heisenberg-limited scaling where the probability of making the wrong decision decreases as $1/d$ (up to a logarithmic factor of $\log(d)$), where d is proportional to the runtime of the sensing protocol. More strictly speaking, the appearance of the $\log(d)$ factor in Eq. (4.41) will make the actual scaling slightly worse than the Heisenberg limit, as is corroborated by numerical evidence in Sec. 4.7.

4.7 Numerical Results and Discussions

Building on the fundamental theory and analytical analysis of the quantum signal processing interferometry, in this section we provide numerical evidence to support our analytical findings for binary decision-making on displacement channels and to demonstrate the advantage of the QSPI protocol for quantum sensing tasks.

A key task to construct the desired QSPI protocol is to find the corresponding QSPI phase angles $\vec{\theta}$ as in Definition 2. For a given decision problem, the existing analytic angle-finding algorithms for QSP [GW04; Cha+20] cannot be directly applied in QSPI to realize the optimal response function due to reasons mentioned in Sec. 4.5.3.1. In this section, we resort to numerical optimization algorithms, which are capable of carrying out such multi-variable approximate optimization tasks on a reasonable timescale to find the QSPI angles. See Ref. [MLS23] for the source code and related data accompanying this work. The rest of this section is organized as follows. Sec. 4.7.1 presents the response function from our numerical optimization, while Sec. 4.7.2 further exhibits the favorable Heisenberg-limited scaling for the error decision probability from these numerical solutions. In Sec. 4.7.3, we discuss features of the Wigner function of the optimal sensing states $|\tilde{\mathrm{Q}}\rangle$ as defined in Definition 2.

4.7.1 QSPI Phases for Binary Decisions

As discussed, we seek a QSPI protocol that generates a response function approximating a step function with sharp transitions at $\pm\beta_{\mathrm{th}}$, as given in Eq. (4.30). We approximate the ideal response function via machine optimization of the phases θ_j in Eq. (4.13) to minimize the objective function p_{err} in Eq. (4.31) and Eq. (4.33) for different degrees d. We use the standard Nelder-Mead optimization algorithm as implemented in Python in the `scipy` optimization package with convergence defined to take place whenever either p_{err} or every QSPI rotation angle in $\vec{\theta}$ changes by at most 10^{-5} radians in a single step of optimization.

Using this learned QSPI phase sequence, we can now define an explicit experimental protocol for sensing a displacement as follows

Protocol 1 QSPI Sensing

1. **Parameter selection:** Given β_{th} and a range of the signal $\beta \in (0, \beta_{\text{max}})$, pick $\kappa = \frac{\pi}{2\beta_{\text{max}}}$ such that β_{th} and β fall in the first period of the effective sensing range $\left[0, \frac{\pi}{2\kappa}\right)$ (Fig. 4.5). In our discussion, we have picked $\kappa = \frac{\pi}{4\beta_{\text{th}}}$, assuming that $\beta_{\text{max}} = 2\beta_{\text{th}}$.

2. **Numerical optimization/phase learning on classical computers:** Perform classical optimization for the desired QSPI phases given this β_{th} and κ using the code in the QSPI repository [MLS23]. Denote the output phase angles of the code by $\vec{\theta}$.

3. **Experimental realization on quantum systems:** Using the experimental implementations of qubit rotations and controlled displacements by κ, implement the experimental sensing protocol corresponding to the learned QSPI phases $\vec{\theta}$:

   (a) **QSPI State Preparation:** Prepare the QSPI sensing state according to Eq. (4.13) and Fig. 4.3.

      i. Perform a qubit rotation by θ_0.

      ii. For $1 \leq j \leq d$:

         A. Perform a controlled displacement by κ.

         B. Perform a qubit rotation by θ_j.

   (b) **Signal:** Apply the unknown displacement signal for sensing to the oscillator in the qubit-oscillator system.

   (c) **QSPI Signal Decoding:** Undo the preparation of the QSPI sensing state for readout.

      i. For $d \geq j \geq 1$:

         A. Perform a qubit rotation by $-\theta_j$.

         B. Perform a controlled displacement by $-\kappa$.

      ii. Perform a qubit rotation by $-\theta_0$.

   (d) **QSPI Readout:** Measure the ancilla qubit under the Pauli-Z basis once.

Given the QSPI sensing protocol Protocol 1, we compute the corresponding response function based on converged optimization results for $\kappa = \frac{1}{2048}$, $\beta_{\text{th}} = \frac{\pi}{4\kappa}$ and plot this as a function of β in Subfig. 4.7(a) for degrees $d = 1$, 5, 9, and 13, with Subfigs. 4.7(b) and 4.7(c) zoomed in for the small and large β regions, respectively. As shown in the figure, when $d = 1$, the response function simply takes the shape of a $\cos(\cdot)$ function. As the degree of the QSPI protocol increases, not only does the slope of the falling edge become steeper, but also, more ripples are observed in the wings, as highlighted in panels (b) and (c) of Fig. 4.7. These ripples are a common feature for finite-degree polynomial approximations to discontinuous functions.

Furthermore, a closer observation of the response function reveals that a d-QSPI protocol

has precisely $(d-1)$ local minima or maxima of its corresponding response function in the interval $\left[0, \frac{\pi}{2\kappa}\right)$. This is expected because a degree-d polynomial on β has at most $(d-1)$ turning points. From a signal processing perspective, such qubit response functions serve as low-pass filters on the signal parameter β [OS10]. We note that filters have been widely used in classical decision-making [KV16], where filter functions (or impulse response) of the desired shape can be implemented as infinitely smooth analytical functions (such as the Butterworth or Chebyshev filters) or as finite-degree polynomials. The former class of filters are often called infinite impulse response because an exact realization of the response would require an infinite order polynomial, while the latter are named finite impulse response. Our QSPI protocol can therefore be viewed as a quantum circuit realization of a finite impulse response (finite-degree filter) on a classical parameter β which parameterizes a quantum process (the underlying displacement signal). There is efficient classical algorithm, the Parks-McClellan algorithm, that designs optimal finite-order polynomial filters [PM72]. It is interesting to ask whether there might exist a quantum version of the Parks-McClellan algorithm for filter design. Another question is to what extent our QSPI protocol can realize classical filters of a given degree. Sufficient conditions provided in Theorem 5 will shed more light on these questions.

4.7.2 Heisenberg-limited Scaling in Decision Quality

To analyze our results and compare with the traditional displacement-sensing approaches, we plot the decision error of the QSPI protocol against its degree d on a log-log plot, as shown in Fig. 4.8. This plot illuminates an interesting relationship between the QSPI protocol degree and the associated response function. From the figure, we can see that the numerical data points can be fitted by a linear black dashed line, demonstrating a power-law trend for p_{err} vs. degree d. The fitting reveals a slope of roughly $\alpha = -0.82 \pm 0.02$ which is close to the HL-like scaling as defined in Definition 1. This power-law fit does not precisely fit all of the points, and it exhibits a parity-dependence with respect to the probability of error. The slope is slightly worse than the exact Heisenberg limit (green dotted line), while still clearly outperforming the standard quantum limit, a deficiency that is consistent with the additional logarithmic factor $\log(d)$, as explained in Eq. (4.41) of Sec. 4.6.2. To make a more direct comparison, we also fit all data points for $d \geq 5$ using the analytical scaling in Eq. (4.41) (blue dashed line). The discrepancy between the analytical expectation and numerical data occurs because our analytical scaling is derived in the large d limit, where we assume the major source of error p_{err} is from the falling edge, as seen in Fig. 4.7 (also see discussion in Appendix G).

One final point is that although we were able to obtain numerical results and verify them, this brute-force optimization method does have several clear challenges. For example, to numerically optimize the sequence of phases minimizing the loss function (p_{err}), one must select an initial value for each of the phases as a starting point. It is possible that a sequence of initial values in the vicinity of a local minimum is selected and then the optimization procedure never escapes from the neighborhood around the local minimum. This problem becomes especially challenging for longer QSP sequences, where the search space is likely to contain more local minima. We attempt to address this difficulty by seeding with multiple distinct random initial phase sequences and iterating on only a subset with the least p_{err}.

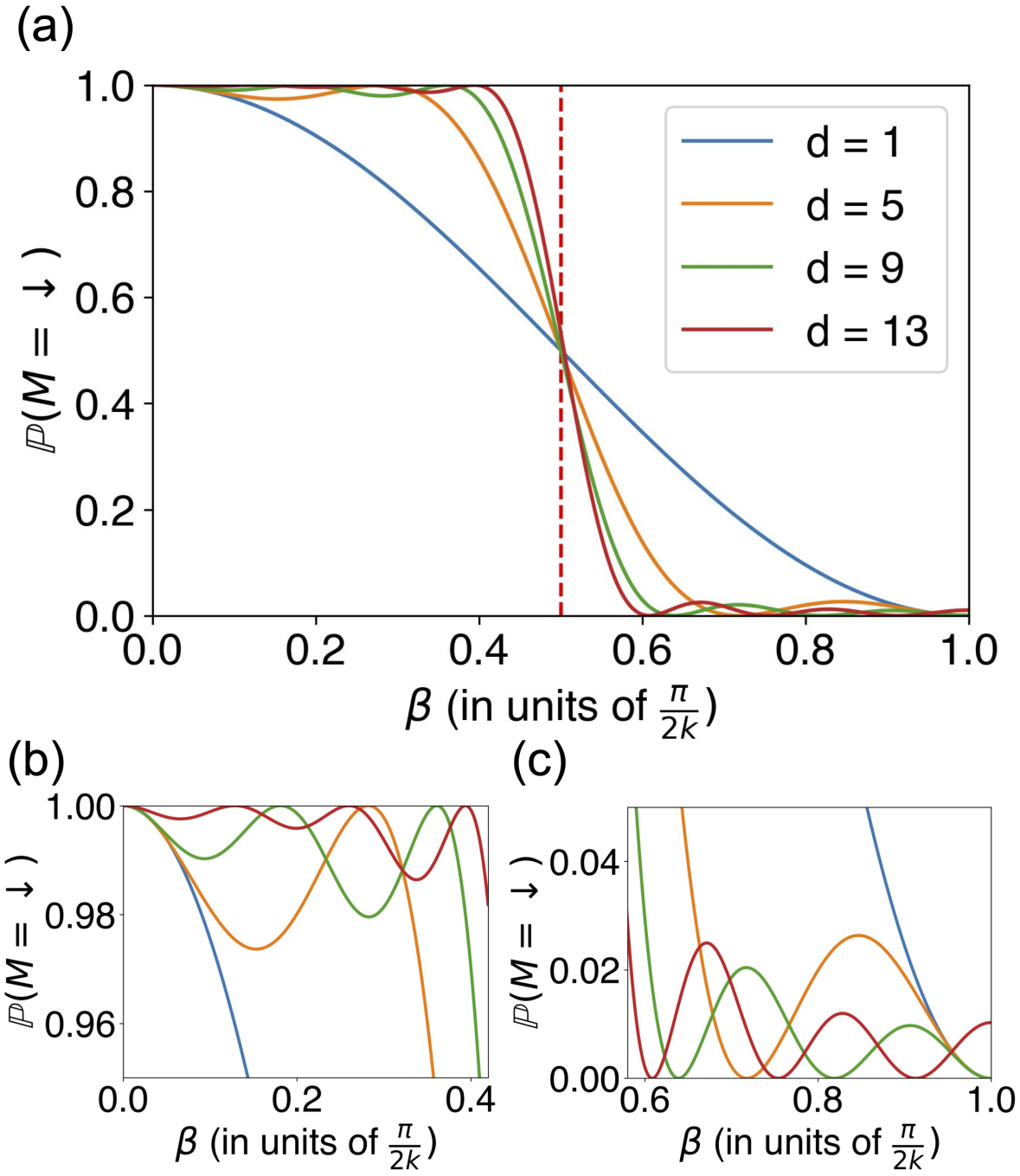

Figure 4.7: (a) Example response functions for various degrees d for distinguishing a displacement with $\beta_{\text{th}} = 0.25 \cdot \frac{\pi}{\kappa}$, where $\kappa = 1/2048$, using QSPI phases from numerical optimization. (b, c) Magnified plots of the response function shown in (a) around $\mathbb{P}(M = \downarrow) = 0$ and $\mathbb{P}(M = \downarrow) = 1$, demonstrating that the response function for a d-QSPI protocol has $(d-1)$ turning points in the interval $\left[0, \frac{\pi}{2\kappa}\right)$.

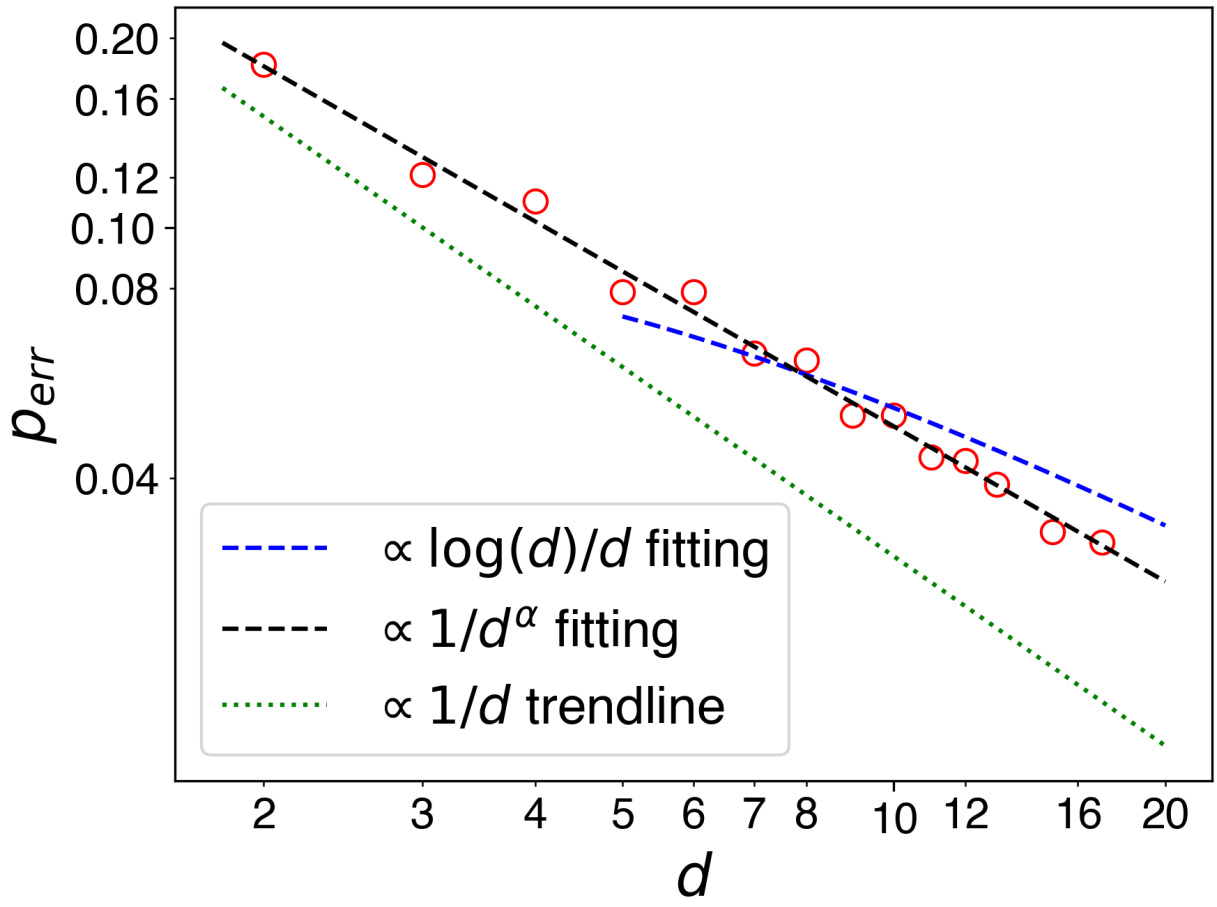

Figure 4.8: Log-log scale plot of p_{err} versus the QSPI protocol degree d (red circles). The best-fit power-law scaling (black dashed line) has a slope of $\alpha = -0.82 \pm 0.02$, indicating $p_{\text{err}} \propto d^{-0.82\pm0.02}$. Best-fit theoretical scaling from Eq. (4.41) using data for $d \geq 5$ is shown with a blue dashed line. The $\propto 1/d$ HL scaling is shown with a green dotted line for comparison.

Thus, we are able to increase the likelihood that we find a phase sequence that has not been trapped in a local minimum, allowing us to discern the optimal scaling of the decision error with QSPI degree.

4.7.3 Wigner Function of Optimal QSPI Sensing States

Given the numerically optimized phases for optimal QSPI sensing states, we may now visualize the resulting states to gain intuition about why their properties allow them to outperform cat states for our decision problems, as we describe in this section.

Although we learned the QSPI phases for the small $\kappa = 1/2048$ in order to best decouple the c_s coefficients and hence facilitate the optimization of the phases, bear in mind the discussion of the coupling of κ and β in Eq. (E.8) and realize that we can adjust our choice of κ and the corresponding β with only minimal fine-tuning of the phases learned for the original value of κ. As such, for clearer visualization of low-degree states on the Wigner plots, we increase the scale of our problem by setting $\kappa = 0.15\sqrt{2}$ and setting $\beta_{\text{th}} = \frac{\pi}{4\kappa} = \frac{5\pi}{3\sqrt{2}}$. For each degree d, we use the phase sequence learned for $\kappa = \frac{1}{2048}$ as our initial phase sequence and resume optimization until convergence for the new value of κ. This change to κ results in minimal change to the QSPI phases during the optimization, with the majority of them differing by less than 1% relative to their original values. The Wigner plots for F and G (Eq. (4.14)) for the newly optimized states resulting from these d-QSPI protocols with $\kappa = 0.15\sqrt{2}$ are shown for $d = 5$, 9, and 13 in Subfigs. 4.9(d) – 4.9(i) in the lower half of Fig. 4.9.

To compare these QSPI states with cat states, we plot F (Eq. (4.14a)) for cat states constructed with the same number $d-1$ of displacements by κ in Subfigs. 4.9(a) – 4.9(c) in the upper panel of Fig. 4.9. We see immediately that the interference patterns (regions with large contrast and Wigner negativity) for the cat state and QSPI state of same degree d differ significantly. The cat states display interference fringes from their two displaced coherent states that oscillate with a frequency of $\sqrt{2}d\kappa/\pi$ along the x-axis. Thus, cat states corresponding to higher degree d have higher-frequency fringes; this is what makes cat states effective sensors of very small displacements perpendicular to the coherent-state displacement in parameter-estimation protocols [Gil+21] but not optimal for making global decisions. In fact, cat states have a constant probability of error p_{err} across all d for a given β_{th} and κ, as explained in Sec. 4.6.1.1.

This trade-off between high and low frequency features appears in Bayesian approaches to estimation problems as well since without prior information, one must consider a flat prior over some fixed region and resolve ambiguities at the cost of devoting resources to low frequency features [Gór+20; BW00]. Often, probe states achieving Heisenberg scaling are optimal for local estimation, but only in a small neighborhood around the true value as we see for the cat state interferometry. If there is no prior information about which small neighborhood of the response function is being examined, then there is *fringe ambiguity*. Thus, the decision problem we address is akin to resolving fringe ambiguity issues in parameter estimation, and our QSPI response function provides a way of interpolating between local and global estimation regimes. For example, in interferometric phase estimation one must restrict their prior to an interval $2\pi/(\lambda_+ - \lambda_-)$, where $\lambda_\pm$'s are extreme eigenvalues of gen-

erator related to signal oracle, as phases differing by a multiple of $2\pi/(\lambda_+ - \lambda_-)$ cannot be distinguished without additional resources [Gór+20]. This trade off between local and global estimation is also pointed out in [Mey+23; Mar+22] where the short period of probe state dynamics in n-qubit GHZ states offer optimal local estimation in a range $2\pi/n$ but cannot distinguish parameter values differing by a multiple of $2\pi/n$. Since the spacing between ambiguous fringes is known for such problems, one could design efficient low-degree quantum filters that discriminate only as precisely as necessary by choosing the optimal response function for the given spacing.

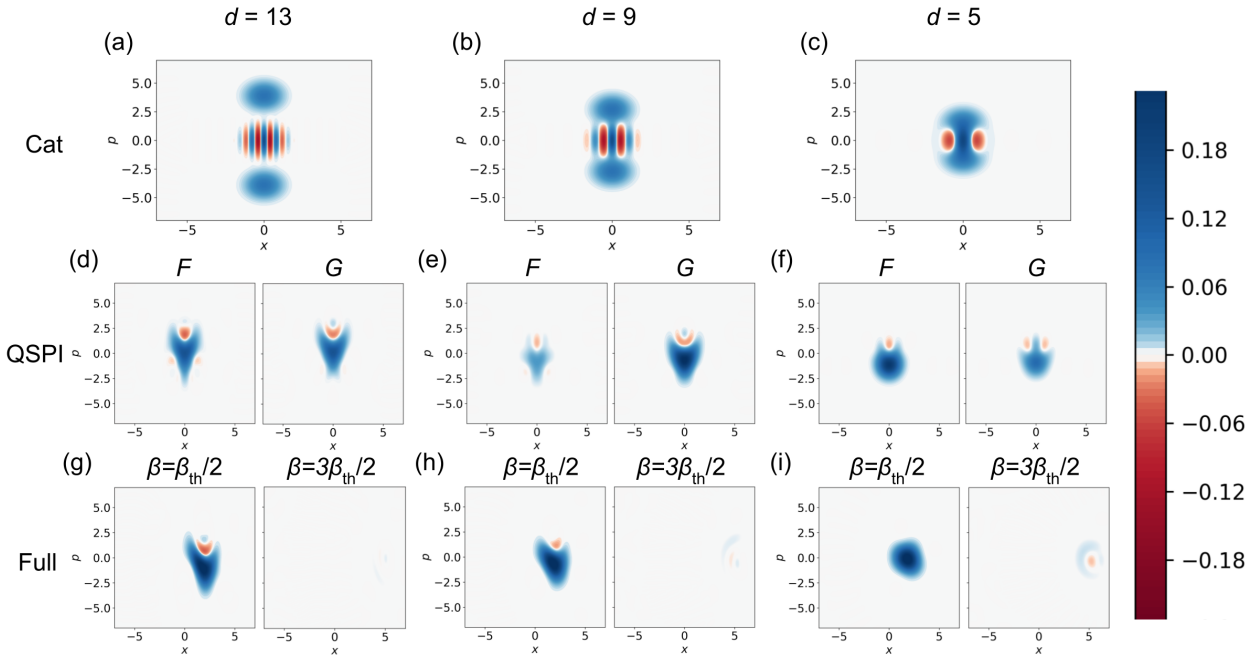

Figure 4.9: Wigner plots of F for the cat state (Figs. 4.9(a), 4.9(b), and 4.9(c)), F and G for the optimal QSPI sensing state (Figs. 4.9(d), 4.9(e), and 4.9(f)), and the oscillator state resulting after the entire protocol is applied with displacements of $\beta = \frac{1}{2}\beta_{\text{th}}$ and $\beta = \frac{3}{2}\beta_{\text{th}}$ conditioned on the qubit being in the $|\downarrow\rangle$ state (Figs. 4.9(g), 4.9(h), and 4.9(i)) with $\kappa = 0.15\sqrt{2}$ and $\beta_{\text{th}} = \frac{\pi}{4\kappa} = \frac{5\pi}{3\sqrt{2}}$ constructed for $d = 13$, 9, and 5. Note the significant differences between the Wigner plots for the cat states and those for the QSPI sensing states, which do not closely resemble any known classes of quantum states. While the cat states all appear very similar but with more distance between their two coherent state parts and more interference fringes at the center as the degree d increases, the optimal sensing states have a more complex interference pattern for improved decision-making. As expected, the final oscillator state after the sensing protocol conditioned on the qubit being in the $|\downarrow\rangle$ state represents a probability close to 1 for a displacement by $\beta = \frac{1}{2}\beta_{\text{th}}$ but a small probability for a displacement by $\beta = \frac{3}{2}\beta_{\text{th}}$, matching the behavior of the calculated response functions, shown for $\kappa = \frac{1}{2048}$ in Fig. 4.7. A symmetrical logarithmic scale, where the scaling is logarithmic in both the positive and negative directions from a small linearly-scaling range around zero, is used as the color scheme in order to increase the contrast of finer features of the Wigner quasiprobability distribution.

The physical intuition for this improved decision-making of the QSPI states stems from the lower-frequency features shown in the Wigner contrast plot. The spacing between sharp-Wigner-contrast features which appear consistently in the upper half of plots in Subfigs. 4.9(d) and 4.9(f) around ($x \approx \pm 1$, $p \approx 1$) indicates the placement of sharp thresholds in the response function. This is why the cat-state response function places sharp thresholds with frequency $d\kappa/\pi$. In comparison, for general QSPI states, the interplay between asymmetric F and G is more complicated to analyze than for the F and G of cat states, but as we see in Fig. 4.9, the spacings between sharp Wigner features shown in Subfigs. 4.9(d) and 4.9(e) remain larger than those of the cat states shown in Subfigs. 4.9(a) and 4.9(b), respectively. Notice that the Wigner extent is also smaller for QSPI states as compared with that of cat states. This is because cat states are maximally extended in phase space for the given energy of the protocol by naïvely shifting the wave packet along one direction, while the QSPI state devotes some of the energy to creating a more complicated and optimized interference pattern phase space as compared to the simple sinusoid with Gaussian envelope that the cat state creates.

Subfigs. 4.9(g) – 4.9(i) then depict the final oscillator state after performing the entire QSPI displacement-sensing protocol with displacements by $\beta = \frac{1}{2}\beta_{\text{th}}$ and $\beta = \frac{3}{2}\beta_{\text{th}}$, conditioned on the qubit being in the $|\downarrow\rangle$ state. We note from these subfigures that the quasiprobability distribution exhibits primarily constructive interference to give a total $|\downarrow\rangle$-measurement probability of nearly 1 when the QSPI sensing protocol is applied for a displacement by $\beta = \frac{1}{2}\beta_{\text{th}}$, while the Wigner quasiprobability distribution exhibits primarily destructive interference to give a total $|\downarrow\rangle$-measurement probability of nearly 0 when the QSPI sensing protocol is applied for a displacement by $\beta = \frac{3}{2}\beta_{\text{th}}$ (hence the nearly empty Wigner plots). These behaviors agree with our theoretical analysis and solve the Main Problem stated in Sec. 4.4.1.

In particular, we also show in Table 4.1 the probabilities of measuring $|\downarrow\rangle$ for the qubit state after performing the entire protocol with both the d-QSPI sensing states for $d = 5$, 9, and 13 and the corresponding cat states for reference. Note that according to simulation results (and as predicted in Sec. 4.6.1.1), the probability of detection does not change with degree d for the cat state, so we provide only one probability. Note also from the results shown in the table that although the cat state performs well for sensing a displacement by β_{th} (with $\kappa = 0.15\sqrt{2}$ and $\beta_{\text{th}} = \frac{\pi}{4\kappa} = \frac{5\pi}{3\sqrt{2}}$), its performance is already matched with only a 5-QSPI state. Moreover, while the cat state's displacement-sensing performance remains constant with increasing degree d, the d-QSPI state's performance improves, so the 9- and 13-QSPI states outperform the cat state; moreover, performance of d-QSPI states for this displacement-sensing task will continue to improve as d increases further.

4.8 Conclusion

In this work, we present a general framework for single-shot quantum sensing using continuous-variable systems by establishing a theory of quantum signal processing interferometry. The basics of this construction are a generalization of QSP to systems with a qubit coupled to a quantum harmonic oscillator. The controlled displacement operation between the qubit and the oscillator forms a natural block-encoding of the displacement operator on the oscillators,

Sensing State	$\mathbb{P}(M = \downarrow \mid \beta = \frac{1}{2}\beta_{\text{th}})$	$\mathbb{P}(M = \downarrow \mid \beta = \frac{3}{2}\beta_{\text{th}})$
Cat State	0.957	0.035
QSPI 5	0.956	0.035
QSPI 9	0.976	0.021
QSPI 13	0.982	0.016

Table 4.1: The probability of measuring the qubit in the $|\downarrow\rangle$ state after applying the entire sensing protocol with displacements by $\frac{1}{2}\beta_{\text{th}}$ (below threshold) and $\frac{3}{2}\beta_{\text{th}}$ (above threshold) using the cat state (independent of degree d) and the d-QSPI states for $d = 5$, 9, and 13, where $\kappa = 0.15\sqrt{2}$ and $\beta_{\text{th}} = \frac{\pi}{4\kappa} = \frac{5\pi}{3\sqrt{2}}$. These values are calculated from a numerical simulation of the QSPI protocol with a Fock-level truncation of $N = 500$ and using a grid with a unit cell size of 0.2×0.2. The numbers in the table are confirmed to converge to the given significant figures with respect to both Fock-level truncation N and grid spacing by performing the same calculations with larger N and finer grids.

via which arbitrary polynomial transformations on the oscillator's quadrature operator can be efficiently implemented. The flexibility of QSP provides the basis for our algorithmic QSPI sensing protocol. A measurement on the qubit induces a qubit response function that is a polynomial transformation of the signal parameters that we would like to sense. By tuning the QSPI phase angles to design appropriate response functions, useful information about the signal parameters can be extracted efficiently.

The QSPI sensing protocol is analyzed in detail for a binary decision problem on a displacement channel with theoretical bounds on the sensing-circuit and sampling complexity. These binary decision oracles are then used to construct a composite protocol for parameter estimation via classical binary search and majority vote. Our sensing scheme is applied to determine if a displacement on the oscillator is greater or smaller than a certain threshold, and Heisenberg-limited behavior is derived analytically and observed numerically for this application.

While we have demonstrated Heisenberg-limited scaling for a binary decision on a displacement channel, the sensing protocol can be further improved. One immediate task is to determine if there exist non-optimization-based algorithms for finding QSPI phase angles that achieve a general QSPI response function. This goal implies the need to find not only necessary but also sufficient conditions on QSPI for the backward direction of Theorem 5. Moreover, the sensing protocol for a single canonical variable of the oscillator can be generalized to two conjugate canonical variables of position and momentum simultaneously, allowing for the realization of quantum sensing in the entirety of phase space for the oscillator. Due to the Heisenberg uncertainty principle, tradeoffs between sensitivity in the position and momentum quadratures may be imposed using squeezing operations depending on the particular sensing task. In addition, the sensing power can be further enhanced by coherently manipulating multiple bosonic modes [ZZS18; Kwo+22], which can likely be coupled together with beamsplitters. In this context, tradeoffs between available quantum resources, such as space (number of oscillators) and time (sensing circuit depth), would be interesting to investigate.

The algorithmic QSPI-based quantum sensing protocol presented in this work opens many

possibilities for useful applications. For example, bosonic modes appear in many physical systems, such as in molecular vibrations and light-matter interactions under confined conditions. The displacement-sensing scheme presented here can be used to sense any chemical environment change in molecules, as long as the change leads to an effective displacement operation on molecular vibrations, as in the case of ro-vibrational coupling [Pek34], or a displacement on photonic modes, as in polariton chemistry [Rib+18; Xio23]. The flexibility of designing response functions can be used to deal with situations where the underlying signal has some prior distribution. Our framework also can be used to study the few-shot regime and connect local and global estimation strategies as in [Mey+23]; we show a new perspective for solving such metrology problems by focusing on response function filter design (as opposed to optimization over more abstract POVMs).

We note that the decomposition of composite sensing tasks, such as parameter estimation, into a series of decision problems provides ample room for the incorporation of hybrid quantum-classical algorithms into the sensing framework. For example, sophisticated adaptive strategies can be built in to gradually change the precision and shape of the decision filter and hence reduce the sensing cost. Lastly, Heisenberg-limited sensing is prone to quantum noise. It would be useful to analyze the stability of our QSPI-based continuous-variable sensing protocol in the presence of quantum noise [DGN22; Xu+23a]. Realistic noise models on hardware containing bosonic degrees of freedom could be incorporated into numerical simulations as well [Bra+23]. Both photon loss and heating (common to superconducting and trapped-ion hardware, respectively) will cause the behavior of the filter to change if quantum error-correction is not incorporated into the QSP sequences [DJK15; EMD11; DKG12]. A potential future direction of interest would be to study the behavior of QSPI under noisy conditions or to extend the QSPI protocol so that it is compatible with error-correction [Zho+19].

Chapter 5

Constructing Arbitrary Polynomials in Phase Space With Bivariable Quantum Signal Processing

The work in Chapter 4 suggests that we can design standard QSP sequences that alternate echo-controlled displacement gates acting on a qudit with rotations on a qubit to which the qudit is coupled in order to achieve universal control of the quantum system wave function in position. In other words, we can use an optimization algorithm in order to learn a sequence of phases for the qubit rotations such that we can realize any polynomial in position for the qubit response function.

This might lead one to wonder if there is a generalization of this approach that provides more complete control, not only over the qubit response function in position but also in momentum. This would imply complete control of the qubit response function over all of phase space, which might have yet broader applications. In order to investigate this topic, we introduce a new model for quantum computation interleaving qubit rotations with echo-controlled displacements by both real and purely imaginary quantities on a coupled qudit.

This research has not yet been completed or previously published and is still under investigation, but we demonstrate its potential by employing machine optimization to learn sequences of qubit rotations to interleave with the echo-controlled displacements in order to implement an XOR gate on the position and momentum quadratures in phase space. The idea for this bivariable QSP was proposed by Dr. Yuan Liu, and a few more details are provided in the a work currently in preparation [Liu+24].

In Sec. 5.1, we reframe the problem from Chapter 4 in the context of all of phase space in order to motivate this research direction. Then in Sec. 5.2, we lay out some fundamental definitions in this bivariable QSP. In Sec. 5.3, we use these definitions to prove constructively that bivariable QSP performs a Laurent polynomial transformation on its inputs. In Sec. 5.4, we introduce an example problem that makes use of the bivariable nature of bivariable QSP to address a different kind of sensing problem, and we share the numerical results for this problem in Sec. 5.5. Finally, in Sec. 5.6, we share some conclusions about the possibilities for bivariable QSP, as well as ideas for future directions.

5.1 Reframing the Sensing Problem of Chapter 4

We have remarked that the idea of being able to realize arbitrary qubit response functions over all of phase space could have wide-ranging applications in quantum sensing. In order to demonstrate one example, we first consider how the sensing problem that we solved with our displacement-sensing scheme as presented in Chapter 4 can be reframed as a problem of realizing a particular qubit response function over the coupled oscillator's entire phase space.

Recall that in Chapter 4, we aimed to decide using a coupled qubit whether or not an oscillator had been displaced by at least some threshold value β_{th}. In this chapter, we addressed the displacement-sensing problem by considering the ideal response function over the displacement coordinate, or the position, alone. We provided this response function as

$$P_{\text{ideal}}(x) = \begin{cases} 1, & 0 \leq |x| < \beta_{\text{th}} \\ 0, & \beta_{\text{th}} < |x| \leq \frac{\pi}{2\kappa}. \end{cases} \tag{5.1}$$

in Eq. (4.30).

The key here to reframing this displacement-sensing problem as one of realizing a particular qubit response function over the coupled oscillator's phase space is to introduce a momentum coordinate to the desired qubit response function so that rather than reading as in Eq. (5.1), it reads as

$$P_{\text{ideal}}(x,p) = \begin{cases} 1, & 0 \leq |x| < \beta_{\text{th}} \\ 0, & \beta_{\text{th}} < |x| \leq \frac{\pi}{2\kappa}. \end{cases} \tag{5.2}$$

In this new framing, if we can realize arbitrary qubit response functions over the entirety of phase space, then we should be able to provide a working protocol for solving the displacement-sensing protocol proposed in Chapter 4, as desired.

5.2 Bivariable Quantum Signal Processing (BiQSP)

Having demonstrated how the sensing problem introduced in Chapter 4 can be reframed as a problem of producing a target response function over all of phase space, we now formalize an approach to quantum signal processing over all of phase space rather than over position alone.

The first step is to define the form of the bivariable QSP, or BiQSP, protocol being considered. In order to achieve control in both dimensions, we need to be able to perform some kind of QSP operation like that introduced for the QSPI sensing work in Chapter 4 but on the momentum quadrature rather than position quadrature. We achieve this by allowing controlled displacement operations in both position and momentum interleaved in a particular manner that we will explain.

In analogy with the controlled-displacement gate for the position quadrature given in Eq. (4.7), we also define a controlled-displacement gate for the momentum operator, as

follows:

$$W_z^{(\kappa)}(\hat{x}) := \mathcal{D}_c\left(-i\frac{\kappa}{2}\right) = e^{-i\frac{\kappa}{2}\hat{x}\otimes\hat{\sigma}_z} = \begin{bmatrix} e^{-i\frac{\kappa}{2}\hat{x}} & 0 \\ 0 & e^{i\frac{\kappa}{2}\hat{x}} \end{bmatrix} = \begin{bmatrix} w(\hat{x}) & 0 \\ 0 & w^{-1}(\hat{x}) \end{bmatrix}, \tag{5.3a}$$

$$W_z^{(\lambda)}(\hat{p}) := \mathcal{D}_c\left(-\frac{\lambda}{2}\right) = e^{-i\frac{\lambda}{2}\hat{p}\otimes\hat{\sigma}_z} = \begin{bmatrix} e^{-i\frac{\lambda}{2}\hat{p}} & 0 \\ 0 & e^{i\frac{\lambda}{2}\hat{p}} \end{bmatrix} = \begin{bmatrix} v(\hat{p}) & 0 \\ 0 & v^{-1}(\hat{p}) \end{bmatrix}, \tag{5.3b}$$

where $w := w(\hat{x}) = e^{-i\frac{\kappa}{2}\hat{x}}$ and $v := v(\hat{p}) = e^{-i\frac{\lambda}{2}\hat{p}}$.

Note that each of these two "signal operators" can be viewed as a block-encoding of a momentum displacement ($W_z^{(\kappa)}(\hat{x})$) or a position displacement ($W_z^{(\lambda)}(\hat{p})$).

Now, for the general form, consider the following unitary constructed from both unitary operators defined above alternated with x rotations on the qubit:

$$U_d = e^{i\phi_0\hat{\sigma}_x}\prod_{j=1}^{d} W_z^{(\kappa)} e^{i\phi_j^{(\kappa)}\hat{\sigma}_x} W_z^{(\lambda)} e^{i\phi_j^{(\lambda)}\hat{\sigma}_x} \tag{5.4}$$

$$= \begin{bmatrix} F_d(w,\, v) & iG_d(w,\, v) \\ iG_d(w^{-1},\, v^{-1}) & F_d(w^{-1},\, v^{-1}) \end{bmatrix}. \tag{5.5}$$

Given this construction of the bosonic bivariable QSP protocol in Eq. (5.4), we would first like to prove constructively that U_d implements a bivariable Laurent polynomial transformation on w and v in the following form:

$$F_d(w,\, v) := \sum_{r,\, s=-d}^{d} f_{r,\, s} w^r v^s, \tag{5.6a}$$

$$G_d(w,\, v) := \sum_{r,\, s=-d}^{d} g_{r,\, s} w^r v^s, \tag{5.6b}$$

where $f_{r,\, s}$ and $g_{r,\, s}$ are complex coefficients determined by the phase angles $\{\phi_j^{(\kappa)}, \phi_j^{(\lambda)}\}$. Note that because w and v do not commute (due to the noncommutativity of $\hat{x}$ and $\hat{p}$), the order of the terms in Eq. (5.6) matters. In the rest of this document, we illustrate the main results of this constructive proof, taking the above way of writing out the bivariable Laurent polynomial to be canonical.

5.3 Constructive Proof of BiQSP Laurent Polynomial Transformation

In order to demonstrate constructively that U_d implements a bivariable Laurent polynomial transformation on w and v, and in order to facilitate the design of protocols using this framework for control over phase space, we derive a set of recursive formulae for computing the coefficients of the F and G polynomials in this bivariable setting given an initial phase ϕ_0 and two sequences of phases $\{\phi_j^{(\kappa)}\}$ and $\{\phi_j^{(\lambda)}\}$.

To do so, we expand the expression given in Eq. (5.4) and match terms. Doing so yields the following recursive formulae for the coefficients. The formulae fall into different cases depending on the values of r and s relative to d because the degrees with nonzero coefficients at each step are limited, and these different cases are illustrated in Figure 5.1.

Working through the algebra, the formulae in these different cases are then given by the following in Eqs. 5.7 – 5.9:

1. If $r = -d$ or $r = -d-1$, then

$$f'_{rs} = \begin{cases} -g_{r+1,\,s+1} e^{-i(s+1)\frac{\lambda\kappa}{4}} \cos\phi_{d+1}^{(\kappa)} \sin\phi_{d+1}^{(\lambda)}, & s = -d,\ -(d+1) \quad (5.7a) \\ -g_{r+1,\,s-1} e^{-i(s-1)\frac{\lambda\kappa}{4}} \sin\phi_{d+1}^{(\kappa)} \cos\phi_{d+1}^{(\lambda)} & |s| \le d-1 \quad (5.7b) \\ \quad -g_{r+1,\,s+1} e^{-i(s+1)\frac{\lambda\kappa}{4}} \cos\phi_{d+1}^{(\kappa)} \sin\phi_{d+1}^{(\lambda)}, & \\ g_{r+1,\,s-1} e^{-i(s-1)\frac{\lambda\kappa}{4}} \sin\phi_{d+1}^{(\kappa)} \cos\phi_{d+1}^{(\lambda)}, & s = d,\ d+1. \quad (5.7c) \end{cases}$$

2. If $|r| \le d-1$, then

$$f'_{rs} = \begin{cases} -f_{r-1,\,s+1} e^{i(s+1)\frac{\lambda\kappa}{4}} \sin\phi_{d+1}^{(\kappa)} \sin\phi_{d+1}^{(\lambda)} & s = -d,\ -(d+1) \quad (5.8a) \\ \quad -g_{r+1,\,s+1} e^{-i(s+1)\frac{\lambda\kappa}{4}} \cos\phi_{d+1}^{(\kappa)} \sin\phi_{d+1}^{(\lambda)}, & \\ f_{r-1,\,s-1} e^{i(s-1)\frac{\lambda\kappa}{4}} \cos\phi_{d+1}^{(\kappa)} \cos\phi_{d+1}^{(\lambda)} & |s| \le d-1 \quad (5.8b) \\ \quad -f_{r-1,\,s+1} e^{i(s+1)\frac{\lambda\kappa}{4}} \sin\phi_{d+1}^{(\kappa)} \sin\phi_{d+1}^{(\lambda)} & \\ \quad -g_{r+1,\,s-1} e^{-i(s-1)\frac{\lambda\kappa}{4}} \sin\phi_{d+1}^{(\kappa)} \cos\phi_{d+1}^{(\lambda)} & \\ \quad -g_{r+1,\,s+1} e^{-i(s+1)\frac{\lambda\kappa}{4}} \cos\phi_{d+1}^{(\kappa)} \sin\phi_{d+1}^{(\lambda)}, & \\ f_{r-1,\,s-1} e^{i(s-1)\frac{\lambda\kappa}{4}} \cos\phi_{d+1}^{(\kappa)} \cos\phi_{d+1}^{(\lambda)} & s = d,\ d+1. \quad (5.8c) \\ \quad -g_{r+1,\,s-1} e^{-i(s-1)\frac{\lambda\kappa}{4}} \sin\phi_{d+1}^{(\kappa)} \cos\phi_{d+1}^{(\lambda)}, & \end{cases}$$

3. If $r = d$ or $r = d+1$, then

$$f'_{rs} = \begin{cases} -f_{r-1,\,s+1} e^{i(s+1)\frac{\lambda\kappa}{4}} \sin\phi_{d+1}^{(\kappa)} \sin\phi_{d+1}^{(\lambda)}, & s = -d,\ -(d+1) \quad (5.9a) \\ f_{r-1,\,s-1} e^{i(s-1)\frac{\lambda\kappa}{4}} \cos\phi_{d+1}^{(\kappa)} \cos\phi_{d+1}^{(\lambda)} & |s| \le d-1 \quad (5.9b) \\ \quad -f_{r-1,\,s+1} e^{i(s+1)\frac{\lambda\kappa}{4}} \sin\phi_{d+1}^{(\kappa)} \sin\phi_{d+1}^{(\lambda)}, & \\ f_{r-1,\,s-1} e^{i(s-1)\frac{\lambda\kappa}{4}} \cos\phi_{d+1}^{(\kappa)} \cos\phi_{d+1}^{(\lambda)}, & s = d,\ d+1. \quad (5.9c) \end{cases}$$

With these analytic formulae for computing the coefficients of F and G resulting from a given initial phase ϕ_0 and pair of phase sequences $\{\phi_j^{(\kappa)}\}$ and $\{\phi_j^{(\lambda)}\}$ recursively in this bivariable setting, we have now proven constructively that U_d implements a bivariable Laurent polynomial transformation on w and v. Although we are currently in the process of proving that the above construction is general enough to realize arbitrary polynomial transformations in the oscillator's phase space efficiently, these formulae already provide us with an analytic basis for performing numerical optimization of the phases for realizing a given target qubit response function.

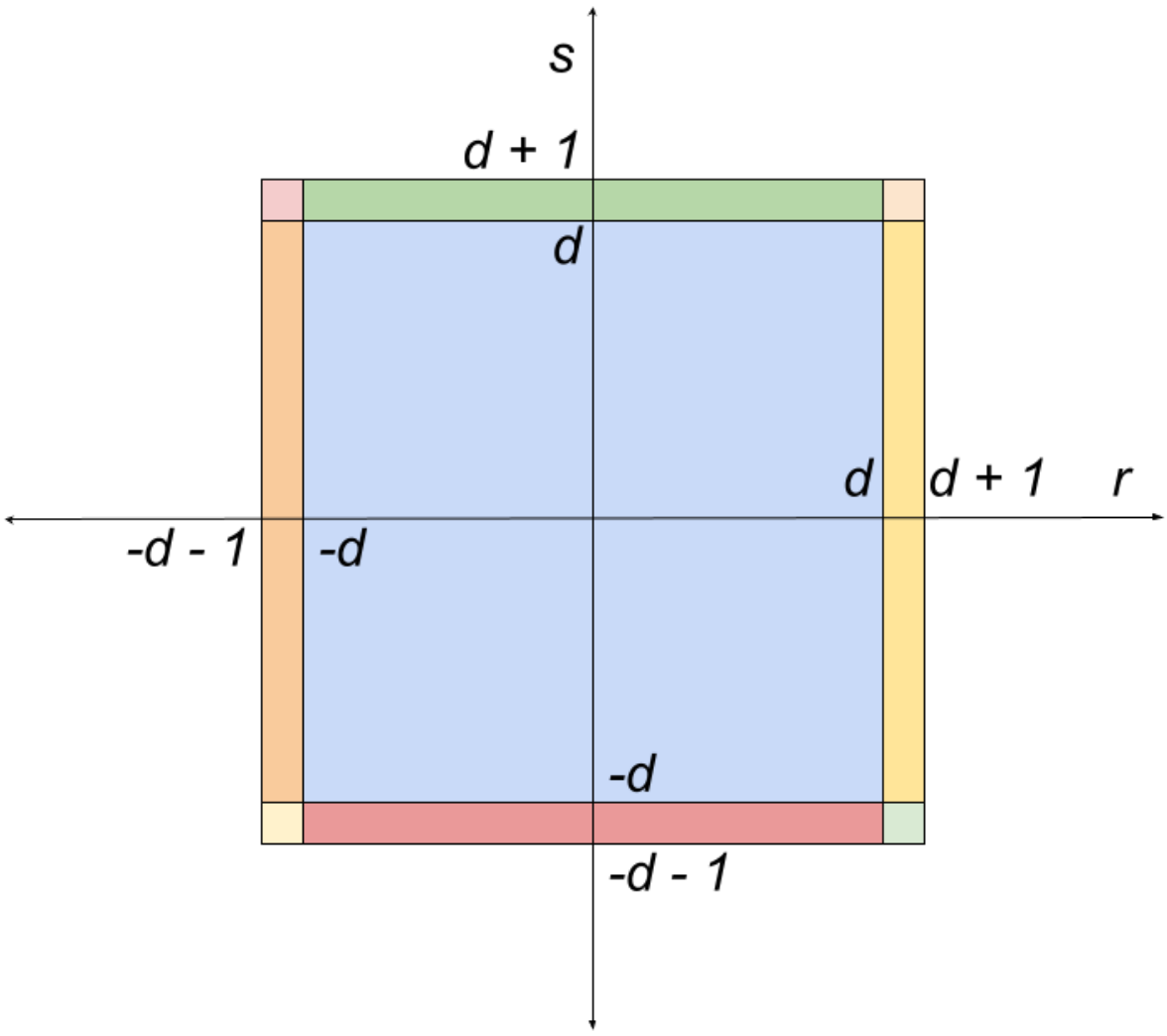

Figure 5.1: Illustrating the nine different cases for r and s in the recursion for computing the f and g coefficients of Eq. (5.6) in BiQSP. The colors exist only to distinguish the nine different cases and have no more specific relevance.

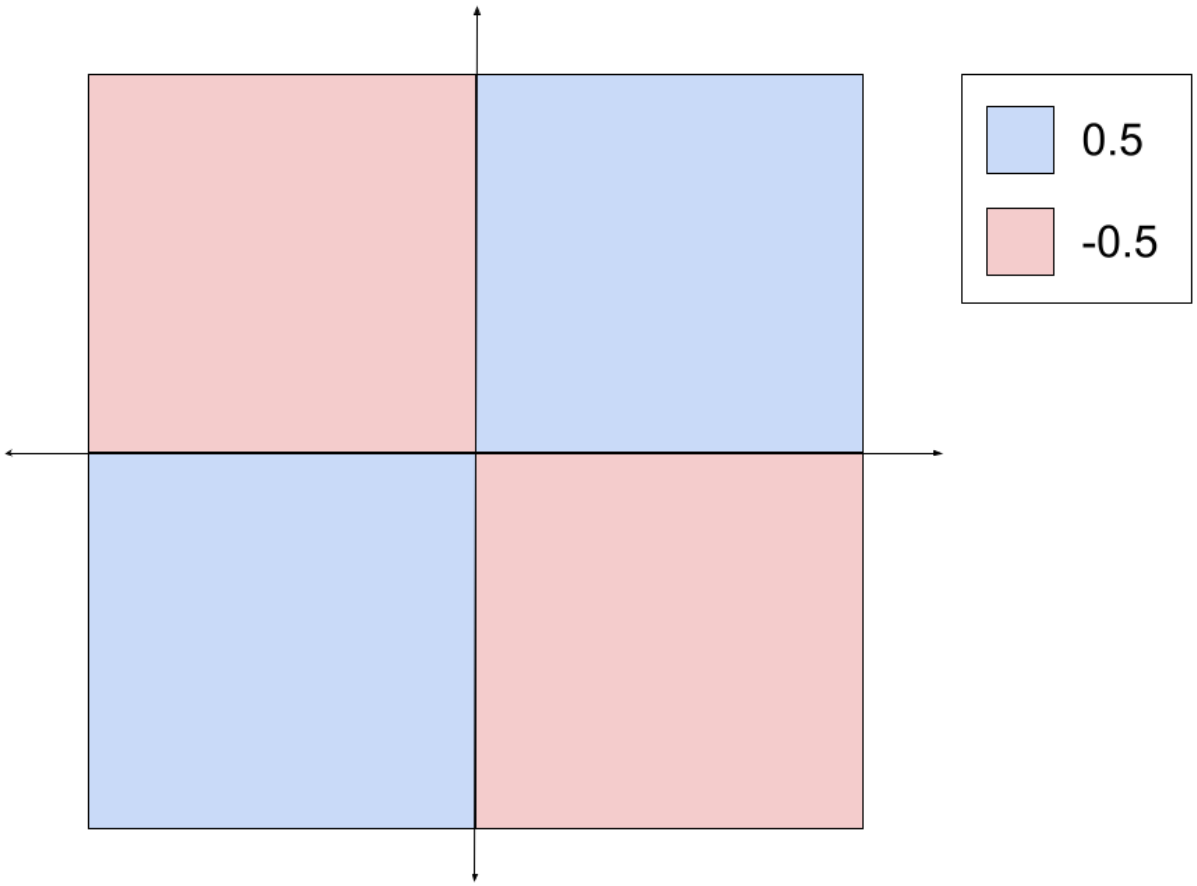

Figure 5.2: A visualization of the XOR function defined in Eq. (5.10) over all of phase space.

5.4 Example Test Problem

As mentioned, we would now like to use these analytic formulae in order to perform numerical optimization for realizing a target qubit response function. In Chapter 4, we numerically optimize a sequence of phases for realizing a qubit response function for solving a displacement sensing problem. Though this direction is fruitful and suggests a broader field of designing QSP response functions to solve sensing problems on its own, a wider range of sensing problems can be addressed if we make use of BiQSP and the analytic formulae for the Laurent polynomial coefficients.

One simple test problem that challenges the ability of BiQSP to implement a nontrivial function in phase space is the idea of implementing an XOR qubit response function on the position and momentum quadratures. To be more specific, suppose that we would like to implement the following qubit response function in Eq. (5.10):

$$XOR(x,p) = \begin{cases} \frac{1}{2}, & x \cdot p > 0 \\ -\frac{1}{2}, & x \cdot p < 0. \end{cases} \tag{5.10}$$

For visual reference, this qubit response function is also shown in Fig. 5.2.

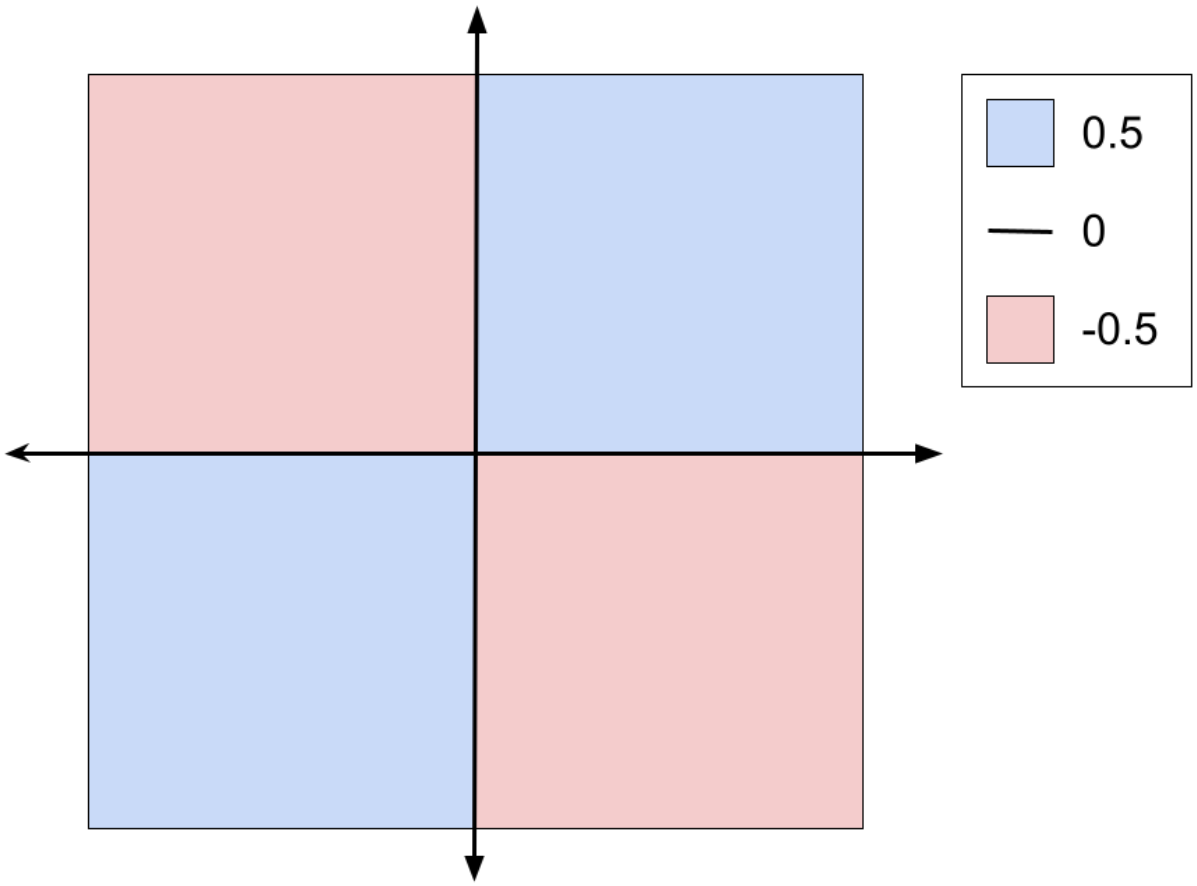

Figure 5.3: A visualization of the new more symmetric XOR function defined in Eq. (5.11) over all of phase space.

We first took this to be the target qubit response function. However, we eventually realized from the plots of the learned phasesthat it might be difficult to learn coefficients such that we could obtain such a sudden change from -0.5 to $+0.5$ at $x \cdot p = 0$, especially because the target function output was slightly asymmetric here, so we added an intermediate region at $x \cdot p = 0$ where the function would take an intermediate value of 0. This is given by the revised XOR function definition in Eq. (5.11):

$$XOR(x,p) = \begin{cases} \frac{1}{2}, & x \cdot p > 0 \\ 0, & x \cdot p = 0 \\ -\frac{1}{2}, & x \cdot p < 0. \end{cases} \tag{5.11}$$

Moreover, this new qubit response function is shown in Fig. 5.3.

Note that both XOR qubit response functions are indeed dependent on both the x and p quadratures nontrivially, since there does not exist a way to decouple these qubit response functions into independent functions of x and p. As such, if we can implement a good approximation to these XOR qubit response functions with BiQSP, then we will already have shown the ability to solve a new kind of problem using this QSP-based method for designing

qubit response functions. Although being able to sense whether an oscillator's position and momentum have the same sign may not, in itself, be a useful sensing ability, success on this example would indicate the ability to learn BiQSP phases to implement nontrivial bivariable qubit response functions, some of which certainly have useful applications.

The last piece necessary to perform the learning of the phase sequences for best approximating this qubit response function with BiQSP is the loss function to minimize. Because we are aiming for a particular target value for every grid point, we choose to take the mean of some distance metric between the current function value of F and the target value over all grid points. Two reasonable choices are the squared error and the absolute value of the difference.

We denote the target qubit response function T. In the first case, our loss function is just the usual mean squared error (MSE), in which case for a grid of N gridpoints (x_i, y_i), we have

$$\begin{aligned} MSE(\phi_0, \{\phi_j^{(\kappa)}\}, \{\phi_j^{(\lambda)}\}) &= \frac{1}{N}\sum_{i=0}^{N-1}(F(x_i, y_i) - T(x_i, y_i))^2 \\ &= \frac{1}{N}\sum_{i=0}^{N-1}\sum_{r,s=-d}^{d}(f_{r,s}e^{-i\frac{r\kappa x_i}{2}}e^{-i\frac{s\lambda y_i}{2}} - T(x_i, y_i))^2. \end{aligned} \tag{5.12}$$

However, we choose to take the latter, so our loss function is

$$\begin{aligned} \mathcal{L}(\phi_0, \{\phi_j^{(\kappa)}\}, \{\phi_j^{(\lambda)}\}) &= \frac{1}{N}\sum_{i=0}^{N-1}|F(x_i, y_i) - T(x_i, y_i)| \\ &= \frac{1}{N}\sum_{i=0}^{N-1}\sum_{r,s=-d}^{d}\left|f_{r,s}e^{-i\frac{r\kappa x_i}{2}}e^{-i\frac{s\lambda y_i}{2}} - T(x_i, y_i)\right|. \end{aligned} \tag{5.13}$$

Finally, as mentioned earlier, we choose to set the length scale by $\kappa = \lambda = 2$ for our learning.

5.5 Preliminary Results

In order to go about this numerical optimization procedure, we make use of the recursive formulae that we derived for the constructive proof that BiQSP, as we have defined it, implements a bivariable Laurent polynomial transformation on w and v.

In particular, we implement with the Python package `PyTorch` a recursive algorithm using tensors to calculate the Fourier coefficients f and g of polynomials F and G from the initial phase ϕ_0 and the two sequences of phases $\{\phi_j^{(\kappa)}\}$ and $\{\phi_j^{(\lambda)}\}$ in a manner that is autodifferentiable. We then define a grid of points in phase space, and using these f and g coefficients, we evaluate the polynomials F and G on these grid points. Finally, we define an appropriate loss function according to Eq. (5.13) in order to evaluate the proximity of the function evaluations to those for the desired qubit response function, and we perform gradient descent on the initial phase ϕ_0 and the phases in the phase sequences $\{\phi_j^{(\kappa)}\}$ and

$\{\phi_j^{(\lambda)}\}$ using `PyTorch` autodifferentiation in order to find phase sequences that result in a better approximation to the desired qubit response function.

Before we begin to discuss the results of training BiQSP polynomials in this manner in order to approximate the XOR qubit response function of position and momentum defined earlier, we must first make some notes about some details of the training procedure.

The first note is that because the BiQSP qubit response function is a polynomial of $v = e^{-i\frac{\kappa}{2}\hat{x}}$ and $w = e^{-i\frac{\lambda}{2}\hat{p}}$, it is necessarily periodic with periods of $\frac{4\pi}{\kappa}$ in the position quadrature and $\frac{4\pi}{\lambda}$ in the momentum quadrature. As such, in order to avoid redundant evaluation and impose minimal necessary constraints on the learned function, we limit our grid of points for evaluation and training to range from $-\frac{\pi}{2}$ to $\frac{\pi}{2}$ while taking $\kappa = \lambda = 2$.

The second note is also in relation to the choice of grid points for evaluating and optimizing the qubit response function. In particular, it is not reasonable to consider grid points for evaluation with spacing smaller than $\frac{2\pi}{d_{\max}}$, where $d_{\max}$ is the maximum degree of v or w in the Laurent polynomial, or equivalently, the depth d to which we perform the recursive calculation of coefficients. For example, if we take BiQSP according to the definition given in Eq. (5.4) with $d = 3$ (i.e., seven phases with one initial phase ϕ_0 and three phases in each of the phase sequences $\{\phi_j^{(\kappa)}\}$ and $\{\phi_j^{(\lambda)}\}$), then $d_{\max}$ should be 3. Note that because we are taking the grid points to span the range from $-\frac{\pi}{2}$ to $\frac{\pi}{2}$, this means that we cannot have grid spacing closer than $\frac{2\pi}{d}$, or that we cannot divide the range into more than $\frac{d}{2}$ parts, or that we cannot set the number of grid points in this range, including the endpoints, to be more than $\frac{d}{2} + 1$.

With these preliminaries in mind, we begin to present the qubit response functions for the phase sequences learned by gradient descent.

As outlined in the statement of the problem, we began by learning phases corresponding to the slightly asymmetric XOR function defined in Eq. (5.10). As per the requirements laid out in Sec. 5.4, we set out to learn 31 phases to best replicate this XOR function on a 7×7 grid of points spaced evenly from $-\frac{\pi}{2}$ to $\frac{\pi}{2}$ in both x and p. We then evaluate the function and plot both the real and imaginary parts. We find phases that produce a qubit response function achieving a loss value of 0.1756, and the real and imaginary parts of this qubit response function are shown in Fig. 5.4a and Fig. 5.4b of Fig. 5.4, respectively.

Overall, these plots look very promising. The quadrants where x and p have the same sign indeed have F evaluating to complex numbers with real part close to $+0.5$, and the quadrants where x and p have opposite signs indeed have F evaluating to complex numbers with real part close to -0.5. Moreover, most of the imaginary parts of the evaluations of F on the grid points are close to 0, which is desired, since ideally, F would be a real function.

However, we note that most of the largest deviations from the imaginary part being zero fall on the two axes of phase space where $x \cdot p = 0$. This, combined with the observation that the definition of the XOR function in Eq. (5.10) is not quite symmetric about 0, leads us to consider the hypothesis that the asymmetry of the target qubit response function could be difficult for the BiQSP model to fit. As such, we slightly redefine the target XOR qubit response function to make it more symmetric, as given by Eq. (5.11), and we attempt to learn phases for this case in order to test our hypothesis.

With the new definition of the XOR function from Eq. (5.11) used as the target function, we train again and find slightly different phases that result in a slightly different qubit

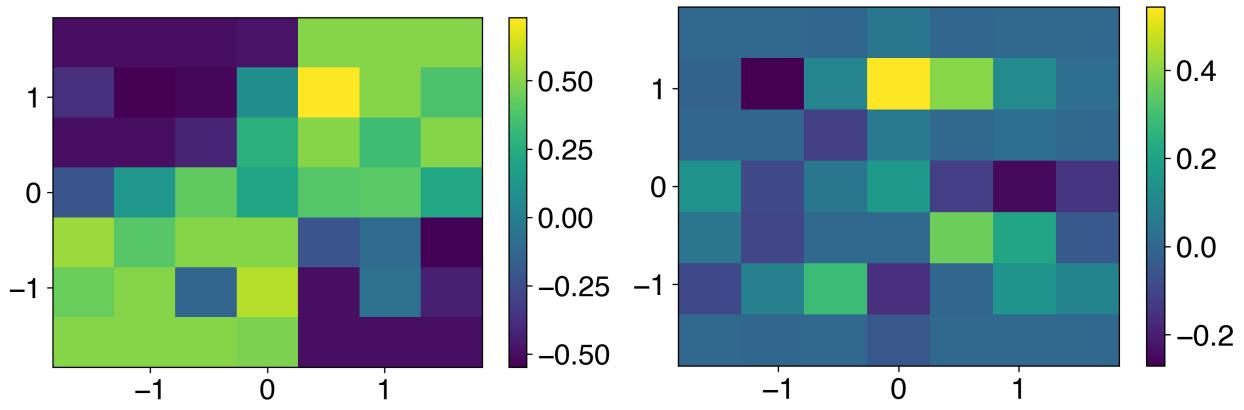

(a) Real Part (b) Imaginary Part

Figure 5.4: Real (Fig. 5.4a) imaginary (Fig. 5.4b) parts of the learned XOR qubit response function from Eq. (5.10) with 31 phases.

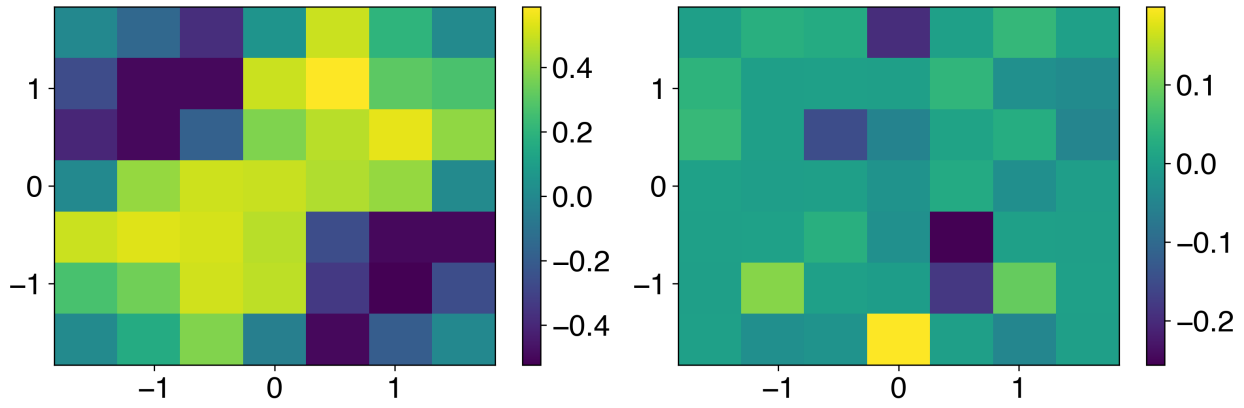

(a) Real Part (b) Imaginary Part

Figure 5.5: Real (Fig. 5.5a) and imaginary (Fig. 5.5b) parts of the learned XOR qubit response function from Eq. (5.11) with 31 phases.

response function that achieves a slightly reduced loss of 0.1601, a first indication that this target might be easier to fit. This new qubit response function's real and imaginary parts are shown in Fig. 5.5a and Fig. 5.5b of Fig. 5.5, respectively.

We see that indeed, there are some improvements in the fit to the desired XOR qubit response function. In particular, the same behavior of having the real part of F evaluate to near 0.5 in the quadrants where x and p have the same sign is mostly retained. Moreover, we do see significant improvement in the imaginary part of F approaching 0 on the grid points, with the maximum magnitude of the imaginary part of F being significantly reduced from 0.533 to 0.194 with this slightly refined XOR qubit response function target. However, there are also some new problems, the most evident being that at the most extreme values of both position and momentum, the function has real part relatively close to zero, meaning that the qubit response function in these regions distant from the origin is not reliable.

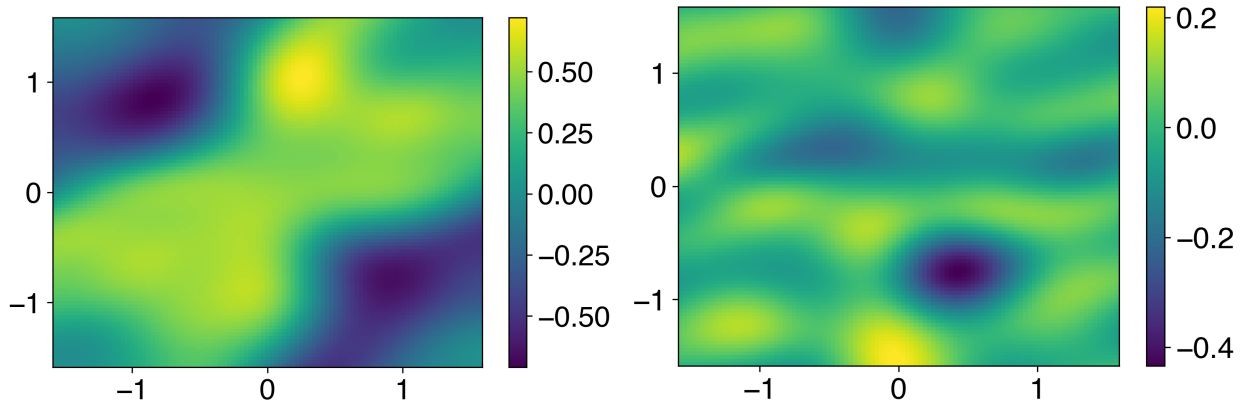

(a) Real Part

(b) Imaginary Part

Figure 5.6: The real and imaginary parts of the optimized approximation of the XOR qubit response function F using 31 phases and evaluated on a 101×101 grid.

Note that the phases learned using each XOR function are given in Table 5.1.

Description	Phases
Asymmetric XOR 5.10	[4.2019, 4.7977, 4.7894, 0.3479, 2.0239, 5.0255, 0.5019, 6.2364, 4.6936, 3.4036, 6.3521, 1.2807, 0.1656, 4.6411, 2.2243, 6.3811, 1.6247, 5.9110, 4.1491, 2.2454, 5.3564, 1.3311, 7.2322, 3.0642, 0.3707, 5.7935, 4.5443, 1.8386, 2.1276, 0.5653, 3.0908]
Symmetric XOR 5.11	[1.9920, 6.2481, 3.2494, 5.8234, 4.4495, 1.3569, 4.8765, -0.1311, 1.6432, 4.9559, 1.4580, 2.8103, 1.4615, 4.8713, 4.9725, 4.2071, 4.6967, 0.0284, 3.4227, 5.6285, 2.7981, 3.5775, 5.9856, 1.4454, 6.2989, 2.1114, 3.1377, 3.9845, 3.0854, 5.3177, 5.3347]

Table 5.1: 31-phase BiQSP phases learned for each kind of target XOR function, both the slightly asymmetric one and the symmetric one.

One final question of interest is how F behaves at points between these grid points. In order to investigate this question, we take the same function F as defined by the coefficients that we had learned, and rather than evaluating the function only on the grid points that were used to train it, we instead evaluate it on a 101×101 grid in the same range from $-\frac{\pi}{2}$ to $\frac{\pi}{2}$. The results for the real and imaginary parts are shown in Fig. 5.6a and Fig. 5.6b of Fig. 5.6, respectively.

We see in these figures that although we only trained the qubit response functions on the 7×7 grid of points from $-\frac{\pi}{2}$ to $\frac{\pi}{2}$, the function retains approximately the values that one would expect from interpolation in the interstitial space, and hence achieves many of the desired goals. The regions distant from the origin remain a concern, as F evaluates to nearly zero there, but otherwise, the function behaves approximately as expected, with real parts near $+0.5$ where x and p have the same sign and real parts near -0.5 where they do

not. Moreover, the imaginary parts are still near 0, albeit a bit greater than on the original 7×7 grid points alone.

We repeat much of this analysis for a 41-phase BiQSP solution evaluated on a 9×9 grid of points, and the results are given in Appendix H.

The loss for this 41-phase BiQSP is slightly greater than for the 31-phase BiQSP despite it having more phases and hence a greater range of qubit response functions that it can express. This highlights a couple of potential shortcomings of our analysis and this numerical optimization approach for learning BiQSP sequences. Specifically, because there are so many phases involved, the optimization is quite complex with many local minima in which the gradient descent method can become trapped. In order to minimize the effects of this difficulty, we initialized the gradient-descent optimization with many distinct random initial phase sequences so that, with greater probability, one of these initial sequences would be in the vicinity of the global minimum and would be able to find it without becoming trapped in one of the many local minima that exist in the rugged optimization landscape. We then retained the best of these phase sequences after 250 rounds of gradient descent and continued to optimize them. This being said, we still might not have found true global minima, and this problem is exacerbated with an increased number of phases, which could explain why the 41-phase BiQSP has a slightly greater loss than the 31-phase BiQSP despite having more expressivity. This numerical optimization problem could benefit from increased computing resources and time, and we hope to continue exploring it in the future.

5.6 Conclusions

In conclusion, we have demonstrated that bivariable quantum signal processing produces Laurent polynomials of the position and momentum quadratures. Although we have not yet proven that all Laurent polynomials are achievable with the form of BiQSP that we presented, and this remains to be shown in future work, we have demonstrated with numerical simulations that BiQSP can achieve good approximations to the XOR function, a nontrivial qubit response function in phase space. The best methods for numerical optimization of the BiQSP phases toward achieving general qubit response functions of position and momentum beyond baseline gradient descent also remains a question for investigation.

Even with these open questions, we conclude that BiQSP is a promising framework for learning how to experimentally realize new varieties of qubit response functions not achievable with quantum signal processing on a single variable alone. These new bivariable qubit response functions could be used to realize yet unrealized quantum algorithms or to sense different properties of quantum states, and these prospects make it a promising research direction.

Chapter 6

Using Qubit-oscillator Systems to Construct Quantum Error-Correction Codes

Quantum computation is subject to significant environmental noise, resulting in errors on the quantum states used for computation. This noise can thus significantly degrade the ability to perform complex computational tasks on quantum devices, especially as more complex computations often require longer operation time and consequently offer increased potential for accumulation of physical errors. As research advances toward applying quantum computation techniques to problems of interest, addressing the problem of carrying them out in the presence of errors becomes increasingly imperative.

We first discuss approaches currently being taken to address the problem of quantum noise in Sec. 6.1. Next, we discuss the burgeoning field of dissipation engineering and its applications to quantum error-correction in Sec. 6.2. After laying this groundwork for understanding the application of dissipation engineering to quantum error-correction, we describe our proposed scheme for using dissipation engineering to stabilize a relatively new kind of quantum error-correcting code in Sec. 6.3. We next describe the methodology that we employ to analyze the performance of our quantum error-correcting protocol in Sec. 6.4. In Sec. 6.5, we present the results of our simulations analyzing the performance of the error-correcting protocol. Finally, in Sec. 6.6, we present the conclusions of our analysis and future directions for this quantum error-correcting codes research.

This research was performed with the Nippon Telegraph and Telephone Corporation (NTT) under the supervision of Dr. Suguru Endō and in collaboration with Dr. Tomohiro Shitara. It will likely be expanded slightly and submitted for publication within the next several months.

6.1 Introduction

In an effort to address the challenge of noise corrupting information stored in quantum states, and inspired by an idea developed in the field of classical computation, researchers in the field began to explore methods for quantum error correction (QEC). The classical

inspiration in error correction is exemplified by the repetition code, which produces error-protected logical units by the replication of bits, as an error on one bit can be corrected by a simple majority vote on the set. Naïvely, this result does not seem translatable to quantum computation, since the no-cloning theorem for qubits precludes the possibility of replicating a qubit's state [Die82; Par70; WZ82].

However, it has been shown that quantum entanglement can enable the quantum equivalent of a repetition code, and the theoretical three-qubit bit-flip code and three-qubit phase-flip codes provide models for this [NC10]. We will not provide a complete explanation and refer anyone interested in additional details to *Quantum Computation and Quantum Information* by Michael Nielsen and Isaac Chuang [NC10]. However, we will provide an overview of these codes. The general idea is that we perform the encoding given in Eq. (6.1), replacing each of the two basis qubits with three entangled basis qubits of the same kind to form a single logical unit that is better protected against noise:

$$|0\rangle \to |0_L\rangle \equiv |000\rangle \tag{6.1a}$$

$$|1\rangle \to |1_L\rangle \equiv |111\rangle. \tag{6.1b}$$

Here, we use the notation of subscript L to denote a logical qubit, as opposed to the standard physical qubit denoted without the subscript. Note that a logical qubit can be, and often is, comprised of multiple physical qubits.

These substitutions imply that the state $\alpha|0\rangle + \beta|1\rangle$ would be encoded as $\alpha|000\rangle + \beta|111\rangle$. This transformation can be accomplished by passing the state to be encoded into a circuit with two additional ancilla qubits, each initialized to $|0\rangle$, and performing a controlled-NOT gate on each qubit controlled on the first qubit, effectively copying its $|0\rangle$ or $|1\rangle$ basis state over to the other two qubits. Then, by performing an appropriate projective measurement on the resulting state at some point in the future, we can determine whether there has been a bit-flip, or Pauli-X, error on *one* of the three qubits and correct it as necessary. The three-qubit phase-flip code is achieved in essentially the same way, except that we use $|+\rangle$ and $|-\rangle$ in place of $|0\rangle$ and $|1\rangle$. This suffices because a phase flip transforms $|+\rangle$ to $|-\rangle$ and vice-versa, making a phase-flip error treatable as a bit-flip error in the $\{|+\rangle, |-\rangle\}$ basis. Moreover, the conversion from the three-qubit bit-flip code is simple; we only need to prepare the three-qubit bit-flip code and then perform a Hadamard gate on each of the three qubits.

Combining these two codes, Peter Shor proposed in 1995 a 9-qubit quantum error-correcting code (QECC) that could correct an arbitrary error on any single qubit [Sho95]. Instead of copying the qubit state, Shor's encoding employs the three-qubit-code idea of distributing the quantum state nonlocally via entanglement over the nine qubits of the code state. His code does so in such a way that a single error of any kind on any *one* qubit cannot irreversibly destroy the information stored in the entire state. Several other quantum codes were subsequently devised using a similar approach, including Andrew Steane's 7-qubit code [Ste96] and a 5-qubit code that was proven to be the shortest possible code that can correct a general single-qubit quantum error [Ben+96; Laf+96].

As should be evident from the fact that each of these codes requires many qubits to correct an arbitrary error on any single qubit, one disadvantage of codes based only on qubits is that they necessarily leverage entanglement of *many* physical qubits to robustly encode a *single* logical qubit. With concatenation of quantum codes to allow correction of more general

errors, the number of physical qubits necessary for realizing a single logical qubit becomes even more daunting [KL96]. This has motivated the development of an alternative type of QECC known as a bosonic QECC, so named because it makes use of a *continuous-variable* bosonic mode. Bosonic QECCs generally utilize only a very small number of continuous-variable modes.

These bosonic QECCs are generally classified according to their symmetries, either rotational or translational. Rotation-symmetric codes are exemplified by cat codes [GCB20]. The two-legged cat code [Leg+13] has basis states defined as in Eq. (6.2):

$$|0_{L,\,\mathrm{cat}}\rangle \propto |\alpha_{\mathrm{cat}}\rangle + |-\alpha_{\mathrm{cat}}\rangle \tag{6.2a}$$

$$|1_{L,\,\mathrm{cat}}\rangle \propto |\alpha_{\mathrm{cat}}\rangle - |-\alpha_{\mathrm{cat}}\rangle, \tag{6.2b}$$

where α_{cat} is the amplitude of the cat state. Note that the state $|0_{L,\,\mathrm{cat}}\rangle$ is just the same as the cat state that we defined in Eq. (2.32). Two-legged cat codes have an error-biased code property; in particular, they are very robust to phase errors but susceptible to photon-loss errors. However, higher-order rotation codes, such as four-legged cat codes, do allow for detecting and correcting photon-loss errors. We note that the logical zero and one states in cat codes are perfectly orthogonal to each other, which means that they can be perfectly distinguished. However, as we mentioned, the standard two-legged cat code is susceptible to photon-loss noise, which causes bit-flip errors on this code.

On the other hand, translation-symmetric bosonic QECCs are exemplified by one of the oldest bosonic QECCs, the 2001 Gottesman-Kitaev-Preskill (GKP) code [GKP01]. The zero and one basis states of the ideal GKP code are defined as in Eq. (6.3):

$$|0_{L,\,\mathrm{gkp}}\rangle \propto \sum_{k,\,l=-\infty}^{\infty} e^{-i\pi kl} |2k\alpha_{\mathrm{gkp}} + l\beta_{\mathrm{gkp}}\rangle \tag{6.3a}$$

$$|1_{L,\,\mathrm{gkp}}\rangle \propto \sum_{k,\,l=-\infty}^{\infty} e^{-i\pi(kl+l/2)} |(2k+1)\alpha_{\mathrm{gkp}} + l\beta_{\mathrm{gkp}}\rangle, \tag{6.3b}$$

where for the square GKP code we set $\alpha_{\mathrm{gkp}} = \sqrt{\frac{\pi}{2}}$ and $\beta_{\mathrm{gkp}} = i\sqrt{\frac{\pi}{2}}$. Although this ideal GKP code is not physically practical because it would require infinite energy to realize, finite-energy variants using finitely-squeezed coherent states have been proposed and are used in practice [NCB22; GP21; RSG20]; in particular, one of these applies an envelope decaying exponentially in $\hat{n}$ to the ideal GKP code basis states [RSG20]. The Knill-Laflamme error-correction matrix of the GKP code indicates that this finite-energy variant has excellent performance against photon-loss noise in a broad range of parameter regimes [Alb+18]. In addition, the associated dissipation-engineering error-correction strategy offers an experimentally-friendly protocol for error suppression with only a single additional ancilla qubit, which results in the extension of the lifetime of GKP-encoded logical qubits in comparison with the lifetime of physical qubits [RSG20; Siv+23]. However, a deficiency of the finite-energy approximate GKP code is that its zero and one code states are *not* orthogonal, a fact that inevitably incurs computation errors.

Another newer code that is both rotationally and translationally symmetric and shares benefits of both the cat code and the GKP code is the squeezed-cat code [SMS22]. A

squeezed-cat code is defined by its amplitude α_{sc} and its squeezing parameter ζ_{sc}. We assume that squeezing always takes place orthogonal to the direction of displacement by taking $\zeta_{\text{sc}} = |\zeta_{\text{sc}}|e^{i\theta/2}$ and $\alpha_{\text{sc}} = |\alpha_{\text{sc}}|e^{i\theta}$. Without loss of generality, we set $\theta = 0$ in the analysis that follows so that α_{sc} is always real. The basis states of a squeezed-cat code with amplitude α_{sc} and squeezing parameter ζ_{sc} are then defined as in Eq. (6.4).

$$|0_{L,\text{sc}}\rangle \propto |\alpha_{\text{sc}}, \zeta_{\text{sc}}\rangle + |-\alpha_{\text{sc}}, \zeta_{\text{sc}}\rangle \tag{6.4a}$$
$$|1_{L,\text{sc}}\rangle \propto |\alpha_{\text{sc}}, \zeta_{\text{sc}}\rangle - |-\alpha_{\text{sc}}, \zeta_{\text{sc}}\rangle, \tag{6.4b}$$

where $|\alpha_{\text{sc}}, \zeta_{\text{sc}}\rangle$ denotes a squeezed coherent state with displacement parameter α_{sc} and squeezing parameter ζ_{sc}, as defined in Eq. (2.31). The squeezed-cat code shares with the standard cat code the desirable property of having perfectly orthogonal basis states, and it shares with the GKP code the property of robustness to photon-loss noise. Note that the bias for the phase error is retained, while the squeezing effect increases the distinguishability of encoded logical states like $\{|+_{L,\text{sc}}\rangle, |-_{L,\text{sc}}\rangle\}$ without worsening the robustness of the code to photon-loss noise.

However, the existing methods for correcting errors on the squeezed-cat code are dissipative stabilization schemes necessitating strong nonlinearity and complex couplings, which are challenging requirements for current systems for practical quantum computation [HQ23; Xu+23b]. Motivated by the experimentally simple scheme for the realization of dissipative error-correction on the finite-energy GKP code that we describe in this work [RSG20], we propose an extension to the dissipation-engineering error-correction approach for the squeezed-cat code.

6.1.1 Outline

This section is organized as follows. First, we introduce and explain the field of dissipation engineering for error-correction, then review an illustrative example of dissipation engineering for stabilization to the finite-energy GKP code subspace, in Section 6.2. Then we present our original contribution to the field of dissipation engineering, a unitary and corresponding sharpen-trim protocol Trotterization for stabilization to the squeezed-cat code subspace in Sec. 6.3. Next, we present our methodology for evaluating the efficacy of the error-correction protocols in Sec. 6.4. Using this methodology, we review the results obtained by utilizing these dissipation-engineering protocols to correct for photon-loss noise in both the GKP code and the squeezed-cat code in Section 6.5. Finally, we provide conclusions, discussion, and outlook on future work in Section 6.6.

6.2 Dissipation Engineering

As was already mentioned, one of the biggest obstacles to quantum information science is decoherence, which arises due to a system's interactions with its environment [AGP08]. The resulting dissipation from these interactions tends to destroy interesting quantum effects that underlie advantages in quantum computation, cryptography, and simulation [NC10; Fey82]. However, about fifteen years ago, proposals began to emerge using dissipation as a quantum

resource rather than regarding it as a stumbling block that quantum innovation would need to hurdle [VWI09]. More recently yet, dissipation engineering has been proposed as a tool for addressing many other areas of interest in quantum computation, such as quantum sensing, quantum simulation, and the focus of our work, quantum error-correction [HMM22].

In this section, we first address the sharpen-trim protocol in Sec. 6.2.1 and then review how this protocol emerges naturally from the Trotterization of a unitary operator for the engineered dissipation of an oscillator coupled with an ancillary qubit to the GKP code subspace in Sec. 6.2.2.

6.2.1 Sharpen-Trim

The sharpen-trim protocol is a dissipation-engineering technique designed for stabilizing grid states. It was first introduced in a 2020 work authored by Campagne-Ibarcq, Eickbusch, and Touzard et al. regarding stabilization of such states in a superconducting cavity [Cam+20] and is comprised of alternating sharpening steps, which sharpen the peaks of the grid state, and trimming steps, which trim extent and hence prevent spreading of the grid state peaks and envelope in phase-space. Although the original idea was proposed in the context of stabilizing grid states in a superconducting cavity, this framework has further natural extensions and has been applied to the stabilization of grid states in other platforms for quantum computation.

Some of these extensions have been explored in the more recent 2020 work authored by Royer et al. regarding the stabilization of GKP states using dissipation-engineering techniques [RSG20]. In particular, this work derives a unitary operator for the stabilization of the finite-energy GKP manifold using a bath comprised of a single qubit that is periodically reset and shows how different Trotterizations of this unitary operator can be implemented with simple quantum circuits using only controlled-displacement operations and qubit resets. The simplest such Trotterization, a first-order Trotterization, produces the same sharpen-trim protocol outlined in Campagne-Ibarcq, Eickbusch, and Touzard et al. [Cam+20], and we review the derivation of this result here.

6.2.2 Sharpen-Trim for the Finite-energy GKP Manifold

In their work, Royer et al. derive a unitary for stabilizing the finite-energy GKP manifold using engineered dissipation given a system comprised of an oscillator coupled to a single ancillary qubit, then Trotterize this unitary in order to obtain the sharpen-trim protocol [RSG20]. We now review their derivation in order to provide a blueprint for analyzing dissipation engineering schemes.

Because we are analyzing a scheme for the engineered dissipation of the finite-energy GKP code, we begin by considering the stabilizers of the ideal GKP code, $\hat{T}_{x,0} = e^{il_{\text{gkp}}\hat{x}}$ and $\hat{T}_{p,0} = e^{-il_{\text{gkp}}\hat{p}}$, where l_{gkp} is the lattice constant of the GKP code. For now, we will focus on the $\hat{T}_{x,0}$ stabilizer, but $\hat{T}_{p,0}$ can be treated similarly.

In order to treat finite-energy GKP states analytically, we use the envelope operator in the number operator $\hat{E}_\Delta - \exp\{-\Delta^2\hat{a}^\dagger\hat{a}\}$ so that we have

$$|\mu_\Delta\rangle = \mathcal{N}_\Delta \hat{E}_\Delta |\mu_0\rangle, \tag{6.5}$$

where $\mu \in \{0, 1\}$, Δ parametrizes the size of the GKP state, and $\mathcal{N}_\Delta$ is a normalization factor.

In order to stabilize these finite-energy GKP states, we need to transform the stabilizers for the ideal GKP code. In particular, we can easily check that the finite-energy stabilizers can be obtained via a transformation induced by the envelope operator:

$$\hat{T}_{x,\Delta} = \hat{E}_\Delta \hat{T}_{x,0} \hat{E}_\Delta^{-1} = e^{i l_{\text{gkp}} (c_\Delta \hat{x} + i s_\Delta \hat{p})}, \tag{6.6}$$

where we take the convention from Royer et al. of defining $c_\Delta = \cosh \Delta^2$, $s_\Delta = \sinh \Delta^2$, and $t_\Delta = \tanh \Delta^2$. As one would hope, the finite-energy states are exact $+1$ eigenstates of these finite-energy stabilizers (i.e., $\hat{T}_{x,\Delta} |\mu_\Delta\rangle = |\mu_\Delta\rangle$).

Now, toward engineering dissipation to the finite-energy GKP manifold, we find the annihilation operator for the x-quadrature of the finite-energy GKP manifold $\hat{d}_{x,\Delta}$. We do so by transforming this stabilizer for which the finite-energy GKP states are $+1$ eigenstates with the natural logarithm to produce a different operator for which the finite-energy GKP states are eigenstates with eigenvalue 0:

$$\begin{aligned} \hat{d}_{x,\Delta} &= -\frac{i}{l_{\text{gkp}} \sqrt{2 s_\Delta c_\Delta}} \ln \hat{T}_{x,\Delta} \\ &= \frac{1}{\sqrt{2}} \left(\frac{\hat{x}_{\left[2\pi/(l_{\text{gkp}} c_\Delta)\right]}}{\sqrt{t_\Delta}} + i \hat{p} \sqrt{t_\Delta} \right). \end{aligned} \tag{6.7}$$

Here, the subscript $[2\pi/(l_{\text{gkp}} c_\Delta)]$ on $\hat{x}$ indicates modularity of the $\hat{x}$ operator, since the complex logarithm is multivalued.

We can then couple the system to a bath in order to dissipate according to this annihilation operator in order to drive the state toward the ground state manifold, which is the finite-energy GKP manifold:

$$\hat{H}_{x,\Delta} = \Gamma_x \left[\hat{d}_{x,\Delta} \hat{b}_\tau + \hat{d}_{x,\Delta}^\dagger \hat{b}_\tau \right], \tag{6.8}$$

where $\hat{b}_\tau$ is a annihilation operator for the bath that satisfies $\left[\hat{b}_\tau, \hat{b}_{\tau'}\right] = \delta(\tau - \tau')$. Now, because we repeatedly reset the environment in this dissipative error-correction scheme so that the bath can be implemented by a single qubit, and because the excitation in the environment is low, we can replace the annihilation operator by $\hat{b}_\tau \to \frac{1}{\sqrt{2}} (\hat{\sigma}_x + i \hat{\sigma}_y)$.

Substituting this explicit form for $\hat{b}_\tau$ and expanding, we find

$$\hat{U} = \exp\left\{ -i \hat{H}_{x,\Delta} \delta t \right\} = \exp\left\{ -i \sqrt{\frac{\Gamma_x \delta t}{t_\Delta}} \left(\hat{x}_{\left[l_{\text{gkp}}/(2 c_\Delta)\right]} \hat{\sigma}_x + \hat{p} \hat{\sigma}_y t_\Delta \right) \right\}. \tag{6.9}$$

Note that we need to eliminate the modularity of the modular position operator $\hat{x}_{\left[2\pi/(l_{\text{gkp}} c_\Delta)\right]}$ for hardware-efficient implementation. We can eliminate this modularity if we choose δt in such a way that

$$e^{-i \sqrt{\frac{\Gamma_x \delta t}{t_\Delta}} \hat{x} \hat{\sigma}_x} = e^{-i \sqrt{\frac{\Gamma_x \delta t}{t_\Delta}} \left(\hat{x} + \frac{2\pi}{l_{\text{gkp}} c_\Delta} \hat{I} \right) \hat{\sigma}_x} \tag{6.10}$$

up to a global phase.

The smallest value of $\sqrt{\frac{\Gamma_x \delta t}{t_\Delta}}$ for which this equation is satisfied is

$$\sqrt{\frac{\Gamma_x \delta t}{t_\Delta}} = \frac{1}{2} l_{\text{gkp}} c_\Delta, \tag{6.11}$$

so we impose this as a condition on $\sqrt{\frac{\Gamma_x \delta t}{t_\Delta}}$ to eliminate the modularity of the position operator $\hat{x}$.

Substituting this value into the unitary obtained earlier, we find

$$\begin{aligned} \hat{U} &= \exp\left\{-\frac{1}{2} i l_{\text{gkp}} c_\Delta (\hat{x}\hat{\sigma}_x + \hat{p}\hat{\sigma}_y t_\Delta)\right\} \\ &= \exp\left\{-\frac{i l_{\text{gkp}} c_\Delta \hat{x}\hat{\sigma}_x}{2} - \frac{i l_{\text{gkp}} s_\Delta \hat{p}\hat{\sigma}_y}{2}\right\} \end{aligned} \tag{6.12}$$

By then Trotterizing this unitary with two different orderings, we obtain the eponymous sharpen and trim steps of the position x-quadrature part of the sharpen-trim protocol:

$$\hat{U}_x^{(ST)} = \begin{cases} e^{\frac{-i l_{\text{gkp}} s_\Delta \hat{p}\hat{\sigma}_y}{2}} e^{\frac{-i l_{\text{gkp}} c_\Delta \hat{x}\hat{\sigma}_x}{2}} & \text{(6.13a)} \\ e^{\frac{-i l_{\text{gkp}} c_\Delta \hat{x}\hat{\sigma}_x}{2}} e^{\frac{-i l_{\text{gkp}} s_\Delta \hat{p}\hat{\sigma}_y}{2}}. & \text{(6.13b)} \end{cases}$$

We can then repeat this process for the momentum p-quadrature in order to obtain the complete sharpen-trim protocol in both quadratures:

$$\hat{U}_p^{(ST)} = \begin{cases} e^{\frac{i l_{\text{gkp}} c_\Delta \hat{p}\hat{\sigma}_x}{2}} e^{\frac{-i l_{\text{gkp}} s_\Delta \hat{x}\hat{\sigma}_y}{2}} & \text{(6.14a)} \\ e^{\frac{-i l_{\text{gkp}} s_\Delta \hat{x}\hat{\sigma}_y}{2}} e^{\frac{i l_{\text{gkp}} c_\Delta \hat{p}\hat{\sigma}_x}{2}}. & \text{(6.14b)} \end{cases}$$

The circuits implementing the GKP code sharpen and trim operators for both the x- and p-quadratures are shown in Fig. 6.1.

6.3 Sharpen-Trim for the Squeezed-cat Manifold

Although its proximity to the origin in phase space limits its vulnerability to photon-loss error, the squeezed-cat code introduced in Sec. 6.1, like other bosonic QECCs, can incur photon-loss error. However, the existing methods for correcting errors on the squeezed-cat code are dissipative stabilization schemes necessitating strong nonlinearity and complex couplings, both challenging requirements for contemporary systems that make its realization more difficult [HQ23; Xu+23b]. As such, we ask whether there might be a simpler approach to error-correction on the squeezed-cat code.

We propose error-correction on the squeezed-cat code using a variant of the sharpen-trim protocol. In Sec. 6.3.1, we walk through the derivation of the sharpen-trim protocol for the squeezed-cat manifold, drawing on insights from and making references to the derivation for the sharpen-trim protocol of the finite-energy GKP code. Then in Sec. 6.3.2, we briefly discuss limitations of the sharpen-trim protocol, both for the finite-energy GKP code and also for the squeezed-cat code.

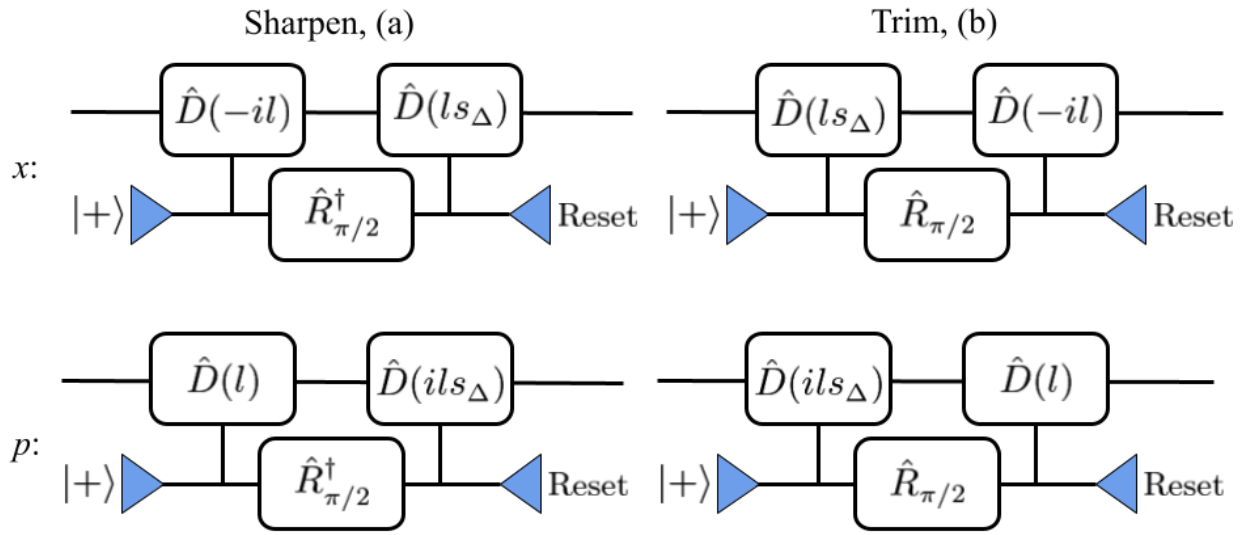

Figure 6.1: Circuits showing the sharpen and trim components of the sharpen-trim protocol for the GKP code in both quadratures, where we abbreviate l_{gkp} by l for brevity. Here, time flows from left to right, and the top wire represents the continuous-variable bosonic state on which the GKP code is being realized, while the bottom wire represents the ancilla qubit. The first column, denoted "Sharpen, (a)," depicts the sharpen circuit component for each quadrature, while the second column, denoted "Trim, (b)," depicts the trim component. The top row, denoted "x," depicts the sharpen and trim circuit components for the position quadrature x, while the bottom row, denoted "p," depicts those for the momentum quadrature p. The gate denoted $\hat{R}_{\pi/2}$ represents a rotation of the ancilla qubit about the x-axis by a phase of $\pi/2$ (i.e., $\hat{R}_{\pi/2} = \exp\{-i\hat{\sigma}_x\pi/4\}$).

6.3.1 Derivation of Sharpen-Trim for the Squeezed-cat Manifold

Having illustrated the derivation for the stabilization of the finite-energy GKP code, we proceed to consider stabilization of the squeezed-cat code with finite squeezing. As in the case of the finite-energy GKP code, to approach determining the stabilizers for the finite energy squeezed-cat code, we begin by considering the stabilizers for the ideal squeezed-cat code whose code states we denote $|\mu_{\mathrm{sc},0}\rangle$ for $\mu \in \{0, 1\}$. The logical $\hat{X}_{\mathrm{sc},0}$ operator for the squeezed-cat code of amplitude α_{sc} (i.e., the operator that maps $|0_{\mathrm{sc}}\rangle$ to $|1_{\mathrm{sc}}\rangle$ and vice versa) is given by $\hat{X}_{\mathrm{sc},0} = -i\hat{D}\left(i\frac{\pi}{4\alpha_{\mathrm{sc}}}\right)$ [End+24]. Because $\hat{X}^2_{\mathrm{sc},0} = \hat{I}_{\mathrm{sc},0}$, we have that $(\hat{X}^2_{\mathrm{sc},0})^2 = \hat{D}\left(i\frac{\pi}{\alpha_{\mathrm{sc}}}\right)$ is a stabilizer for this ideal squeezed-cat code. Substituting the definition of the displacement operator from Eq. (2.29) and taking the notation $\hat{T}_{\mathrm{sc},x,0}$ for this ideal x-quadrature stabilizer of the squeezed-cat subspace, we find

$$\hat{T}_{\mathrm{sc},x,0} = e^{i\frac{\pi\sqrt{2}}{\alpha_{\mathrm{sc}}}\hat{x}}. \tag{6.15}$$

However, our finite-energy squeezed-cat code has a finite squeezing parameter of $-\ln\sqrt{\tanh\Delta^2}$ rather than an infinite squeezing parameter. This corresponds to adding an envelope $\hat{E}_\Delta = \exp\{-\Delta^2\hat{a}^\dagger\hat{a}\}$, as in the finite-energy GKP case. Thus, we find the corresponding finite-energy stabilizer

$$\hat{T}_{\mathrm{sc},x,\Delta} = \hat{E}_\Delta\hat{T}_{\mathrm{sc},x,0}\hat{E}_\Delta^{-1} = e^{i\frac{\pi\sqrt{2}}{\alpha_{\mathrm{sc}}}(c_\Delta\hat{x}+is_\Delta\hat{p})}. \tag{6.16}$$

From here, we note that this expression is identical to that of Eq. (6.6) but with $\frac{\pi\sqrt{2}}{\alpha_{\mathrm{sc}}}$ in place of l_{gkp}, so we can immediately write the unitary for dissipation in this quadrature:

$$\begin{aligned}\hat{U} &= \exp\left\{-i\frac{\pi\sqrt{2}}{2\alpha_{\mathrm{sc}}}c_\Delta(\hat{x}\hat{\sigma}_x + \hat{p}\hat{\sigma}_y t_\Delta)\right\} \\ &= \exp\left\{-\frac{i\pi\sqrt{2}c_\Delta\hat{x}\hat{\sigma}_x}{2\alpha_{\mathrm{sc}}} - \frac{i\pi\sqrt{2}s_\Delta\hat{p}\hat{\sigma}_y}{2\alpha_{\mathrm{sc}}}\right\}.\end{aligned} \tag{6.17}$$

Now, Trotterizing this unitary, we can additionally obtain the sharpen-trim operators for the stabilization of the squeezed-cat subspace in this quadrature:

$$\hat{U}_x^{(ST)} = \begin{cases} e^{\frac{-i\pi\sqrt{2}s_\Delta\hat{p}\hat{\sigma}_y}{2\alpha_{\mathrm{sc}}}}e^{\frac{-i\pi\sqrt{2}c_\Delta\hat{x}\hat{\sigma}_x}{2\alpha_{\mathrm{sc}}}} & \text{(6.18a)} \\ e^{\frac{-i\pi\sqrt{2}c_\Delta\hat{x}\hat{\sigma}_x}{2\alpha_{\mathrm{sc}}}}e^{\frac{-i\pi\sqrt{2}s_\Delta\hat{p}\hat{\sigma}_y}{2\alpha_{\mathrm{sc}}}}. & \text{(6.18b)} \end{cases}$$

Note that because for the for the squeezed-cat code, the other quadrature does not have the same translational symmetry that exists with displacements in the momentum p quadrature, these are the only operators that we can obtain from translational symmetry. The circuit for realizing this new sharpen-trim protocol for the squeezed-cat code is shown in Fig. 6.2.

6.3.2 Limitations

Note that both this squeezed-cat code sharpen-trim protocol and that for the finite-energy GKP code do have limits to their applicability. In particular, as the squeezing parameter of

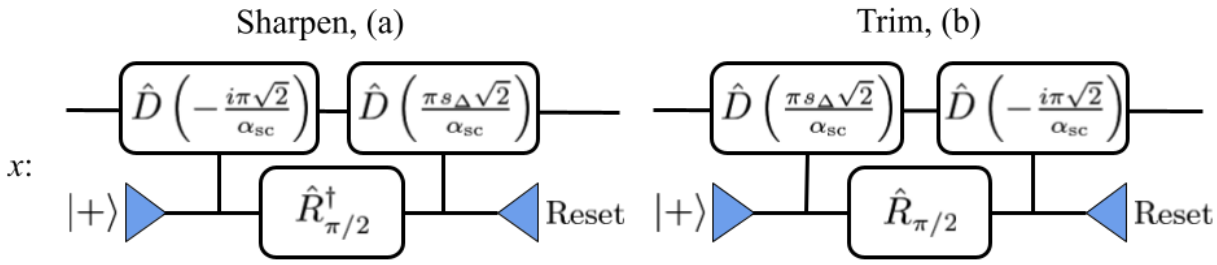

Figure 6.2: Circuits showing the sharpen and trim components of the sharpen-trim protocol for the squeezed-cat code in the x quadrature. Here, time flows from left to right, and the top wire represents the continuous-variable bosonic state on which the GKP code is being realized, while the bottom wire represents the ancilla qubit. The first column, denoted "Sharpen, (a)," depicts the sharpen circuit component, while the second column, denoted "Trim, (b)," depicts the trim component. Note that because the squeezed-cat code only has translational symmetry with displacements in the p quadrature, we only have a sharpen-trim protocol for the x quadrature. The gate denoted $\hat{R}_{\pi/2}$ represents a rotation of the ancilla qubit about the x-axis by a phase of $\pi/2$, as in Fig. 6.1.

the code to be corrected becomes larger (i.e., as it approaches the ideal squeezed-cat or GKP code with infinite-energy code states), the number of iterations of the sharpen-trim protocol required to dissipate back to the code manifold increases significantly. This, in turn, degrades the quality of the error-correction, since physical errors on both the oscillator and the ancilla qubit accumulate over the many necessary iterations of the sharpen-trim protocol, which has the effect of increasing the potential for incurring additional logical errors. Thus, even when using the sharpen-trim protocol, one must consider the trade-off between the benefits of using a code with greater squeezing parameter (e.g., increased robustness to photon-loss noise for the squeezed-cat code and decreased readout error for the GKP code) and the costs of decreasing the efficacy of error-correction by requiring a greater number of sharpen-trim iterations.

6.4 Methodology

Now that we have presented both the dissipation-engineering approach for error correction on the finite-energy GKP code from Royer et al. [RSG20], as well as our new dissipation-engineering approach for error correction on the finite-energy squeezed-cat code, we present how we will evaluate both of these codes with their respective dissipation-engineering approaches to error correction.

First, we will discuss our choices for code parameters in Sec. 6.4.1. Then we will discuss our choices for the quantum noise for which we will simulate the performance of these two codes in Sec. 6.4.2.

6.4.1 Code Parameter Choices

In order to make the finite-energy squeezed-cat code that we consider as comparable with the finite-energy GKP code as possible, we assume identical parameters for the two codes wherever possible.

For example, both finite-energy codes are parametrized by a parameter Δ that maximal occupancy, and hence the size, of the code states. As $\Delta \to 0$, the codes approach the ideal, though unphysical due to having infinite energy, codes. In order to work with nearly ideal codes, we choose $\Delta^2 = 0.05$.

Moreover, we choose the amplitude of the finite-energy squeezed-cat code to be such that it uses the same sharpen-trim operators in the one quadrature that the finite-energy GKP code uses in that same quadrature. As we saw in the derivation of the sharpen-trim operators for the finite-energy squeezed-cat code, this occurs for $l_{\text{gkp}} = \frac{\pi\sqrt{2}}{\alpha_{\text{sc}}}$, or $\alpha_{\text{sc}} = \frac{\pi\sqrt{2}}{l_{\text{gkp}}}$. We choose to use the square GKP code described in Sec. 6.1, which has $\alpha_{\text{gkp}} = \sqrt{\frac{\pi}{2}}$, $\beta_{\text{gkp}} = i\sqrt{\frac{\pi}{2}}$, and $l_{\text{gkp}} = 2\sqrt{\pi}$. This then implies that we must have $\alpha_{\text{sc}} = \sqrt{\frac{\pi}{2}}$.

6.4.2 Noise Choices

Common errors on bosonic codes like the QECC that we are considering in this work include such errors as photon-loss error, dephasing error, and displacement error. In this work, we choose to focus on photon-loss error, as it is more often incurred on bosonic codes. We probe a variety of photon-loss error magnitudes κt, simulating them by evolving the states under the null Hamiltonian and taking the collapse operator to be the annihilation operator on the oscillator $\hat{a}$ for different time durations. Here, κ denotes the photon-loss noise rate of the cavity in units of s^{-1}, and t denotes the duration of the exposure to this noise in s, such that κt is a unitless measure of the amount of photon-loss noise to which the encoded state is exposed.

Additionally, in a discussion of the sharpen-trim protocol by Grimsmo and Puri [GP21], they remark that while the sharpen-trim protocol is relatively robust to phase flips on the ancilla qubit, it is potentially sensitive to bit flips on the qubit, such as those caused by thermal relaxation. In order to account for the effects of this potential source of error in the sharpen-trim protocol, we first consider the expected extent of thermal relaxation on the ancilla qubit. As is done in the research by Royer et al. [RSG20], we consider only ancilla errors occurring during the controlled-displacement gates of the sharpen-trim protocol. In an experimental work from Sivak et al. [Siv+23] regarding stabilization of a finite-energy GKP code, it is given that the duration of a controlled-displacement gate in their experiment is 448 ns, while the thermal relaxation time $\bar{T}_1^t$ of the transmon qubits that they use as ancilla qubits is 280 µs. Given this information and the fact that our controlled displacements are of magnitudes $\frac{\pi\sqrt{2}}{\alpha_{\text{sc}}} \approx 3.545$ and $\frac{\pi s_\Delta \sqrt{2}}{\alpha_{\text{sc}}} \approx 0.1773$, we estimate that the coefficient λ of the collapse operator $\hat{I}_{\text{sc}}\hat{\sigma}_-$ (representing thermal relaxation of the ancilla qubit) in the Lindblad master equation is in the range 2.836×10^{-3} – 5.669×10^{-2}. We simulate the sharpen-trim protocol with ancilla errors by employing the `QuTiP` package of `Python` and, in particular, its `mesolve` function. Specifically, we simulate the qubit rotations and qubit reset steps noiselessly, but for the controlled-displacement steps, we use `mesolve` to simulate

the Lindbladian for the controlled-displacement operator with collapse operator $\sqrt{\lambda}\hat{I}_{\text{sc}}\hat{\sigma}_{-}$. We perform these simulations of the sharpen-trim protocol for values of λ spanning the range that we estimated and an order of magnitude greater but observe deviations in logical purity and logical fidelity of at most 0.1% from those values obtained with entirely noiseless simulations, also carried out using the `QuTiP` package. As such, we perform all of our subsequent simulations without ancilla noise in order to save simulation time.

6.4.3 Evaluation Metrics

With all of the preliminaries settled about parameters of the finite-energy squeezed-cat and GKP codes to be compared, as well as the noise from which to simulate recovery, we proceed to discuss the metrics that we will use to investigate how the performance of our new finite-energy squeezed-cat code error-correction method compares with that for the existing method with the finite-energy GKP code.

The key idea of our approach is using measurements of the ideal logical Pauli operations that an experimentalist would use to reconstruct the logical state that the code is encoding, so we provide details about the exact logical Pauli operations that we measure, as well as how we use them to reconstruct the logical states and evaluate the recovery procedures.

6.4.3.1 Logical Pauli Operations

With regard to the measurements that we choose to make in order to reconstruct the logical qubit state, we opt to measure the logical Pauli operators for the ideal codes. We make this decision because it best aligns with the methodology that would be undertaken in practice for this process.

We recognize that noise can distort the encoded states significantly and hence result in some of an encoded state's support leaving the code subspace, as well as that this can result in complex measurements with significant imaginary parts that result in the reconstruction of unphysical qubits. As such, we measure the real part of the logical Pauli operators and use these values to reconstruct the logical qubit state. Note that measuring the real part of the logical Pauli operator is readily achievable by employing the Hadamard test.

To be precise, we specify the logical Pauli operators that we measure for each code. We use the subscript "L" to indicate that these Pauli operators are for the logical qubit, as well as the subscripts "gkp" and "sc" to distinguish the operators for the finite-energy GKP code and the finite-energy squeezed-cat code, respectively.

The logical Pauli operators for the finite-energy GKP state are as follows [GP21]:

$$\hat{Z}_{L,\,\text{gkp}} = \hat{D}(\beta_{\text{gkp}}) \tag{6.19a}$$

$$\hat{X}_{L,\,\text{gkp}} = \hat{D}(\alpha_{\text{gkp}}) \tag{6.19b}$$

$$\hat{Y}_{L,\,\text{gkp}} = -i\hat{Z}_{L,\,\text{gkp}}\hat{X}_{L,\,\text{gkp}}. \tag{6.19c}$$

The logical Pauli operators for the finite-energy squeezed-cat state used in this work are

those given in the research of Endo et al. [End+24]:

$$\hat{Z}_{L,\mathrm{sc}} = e^{i\pi\hat{a}^\dagger\hat{a}} \tag{6.20a}$$

$$\hat{X}_{L,\mathrm{sc}} = -i\hat{D}\left(i\frac{\pi}{4\alpha_{\mathrm{sc}}}\right) \tag{6.20b}$$

$$\hat{Y}_{L,\mathrm{sc}} = -i\hat{Z}_{L,\mathrm{sc}}\hat{X}_{L,\mathrm{sc}}. \tag{6.20c}$$

Note, however, that as Endo et al. remark, these logical Pauli operators are only exact logical Pauli operators for the ideal squeezed-cat code with infinite squeezing parameter, which is why they have no dependence on a squeezing parameter ζ_{sc}. This means that they are only approximations of the logical Pauli operators for the squeezed-cat code with finite squeezing parameter and, moreover, that these approximations best approximate the actual logical Pauli operators when considering squeezed-cat codes of greater amplitude α_{sc} and squeezing parameter ζ_{sc}. Recall that we do use the ideal logical Pauli X operator given above in our derivation of the dissipator to the finite-energy squeezed-cat code manifold. We are able to do so because we conjugate this ideal logical Pauli X operator with the envelope operator $\hat{E}_\Delta$, which has the effect of inducing the finite squeezing parameter $-\ln\sqrt{\tanh\Delta^2}$ on the state.

6.4.3.2 Logical Qubits

Given the measurements of these logical operators, we can proceed to reconstruct the logical qubit states that are encoded with each code and evaluate them for purity and for fidelity to the original encoded logical qubit.

We first reconstruct the logical qubit density matrix from the logical Pauli measurements using the following formula:

$$\hat{\rho}_L = \frac{1}{2}\left\{\hat{I} + \mathrm{Re}\left(\langle\hat{X}_L\rangle\right)\hat{X} + \mathrm{Re}\left(\langle\hat{Y}_L\rangle\right)\hat{Y} + \mathrm{Re}\left(\langle\hat{Z}_L\rangle\right)\hat{Z}\right\}, \tag{6.21}$$

where here, $\hat{I}$, $\hat{X}$, $\hat{Y}$, and $\hat{Z}$ refer to the general Pauli matrices and not to logical Pauli matrices, while $\hat{X}_L$, $\hat{Y}_L$, and $\hat{Z}_L$ refer to the logical Pauli operators for the respective code, $\langle\hat{A}\rangle$ denotes the measurement of operator $\hat{A}$, and the measurements of these operators are taken with respect to the state for which the logical density matrix is being constructed.

For reference, we now briefly explain the ideas of purity and fidelity, then define the formulae that we use for computing them using the logical qubits in our evaluation.

Purity The *purity* γ of a state provides information about how mixed a state is (i.e., the extent to which we have exact information about the quantum system). The purity of a normalized quantum state satisfies

$$\frac{1}{d} \leq \gamma \leq 1, \tag{6.22}$$

where d denotes the dimension of the Hilbert space in which the state is defined.

We compute the purity γ_L of the reconstructed logical qubit $\hat{\rho}_L$ by

$$\gamma_L = \mathrm{tr}\left(\hat{\rho}_L^2\right), \tag{6.23}$$

where tr denotes the trace of the density matrix.

Fidelity The *fidelity* F is a metric between two quantum states that quantifies their "closeness". For any two density matrices $\hat{\rho}$ and $\hat{\sigma}$, their fidelity satisfies $0 \leq F(\hat{\rho}, \hat{\sigma}) \leq 1$, as well as $F(\hat{\rho}, \hat{\sigma}) = F(\hat{\sigma}, \hat{\rho})$.

Suppose that we denote the initial encoded state prior to noise or error-correction by $\hat{\rho}'_L$. Then the desired fidelity is computed as

$$F(\hat{\rho}_L, \hat{\rho}'_L) = \left(\mathrm{tr} \sqrt{\sqrt{\hat{\rho}_L} \hat{\rho}'_L \sqrt{\hat{\rho}_L}} \right)^2 . \tag{6.24}$$

6.5 Results

Having lain all of the groundwork with respect to specifying the codes under consideration and detailing the methods being used to evaluate the performance of the error-correction protocols, we now proceed to present the results from the numerical simulations that we performed to compare the performance of the squeezed-cat code with our new error-correction protocol to that of the GKP code with error correction.

We organize our results as follows. First, we present the results of our simulations of the sharpen-trim protocol used for quantum error-correction on both codes, with all of the sharpen-trim iterations performed at the conclusion of the noise process, in Sec. 6.5.1. Then we consider an alternative approach to application of the sharpen-trim error-correction protocol in which the protocol is applied periodically, and we present the results of our simulations for this variant of error-correction protocol for both codes in Sec. 6.5.2. Finally, we discuss intended future directions in Sec. 6.5.3.

6.5.1 Post-noise Sharpen-Trim

We begin by presenting the results of our simulations for implementing the sharpen-trim protocols for error-correction on both the finite-energy squeezed-cat code and the finite-energy GKP code. We perform all of our simulations with Fock number $N = 400$, as this N exceeds the number of photons expected in both the squeezed-cat and GKP code basis states that we simulate, and we have observed convergence of the quantities of interest for this Fock number. As described in Sec. 6.4, we first simulate photon-loss noise of various amounts κt incident on a logical qubit encoded with each of the two codes and evaluate the quality of the logical encoding relative to the original logical state. We then simulate performing an appropriate number of sharpen-trim iterations (five for the GKP encoding and ten for the squeezed-cat encoding) on the resulting physical states and again evaluate the quality of the logical encoding with respect to that of the original logical state after error-correction.

Because the performance on a single random encoded logical state is not necessarily representative of the performance for all possible encoded logical states, we perform this same procedure for ten random logical states encoded with each of the two quantum error-correcting codes in order to obtain a better sample and build up statistics. We choose the number of logical states sampled to be ten primarily due to computational constraints, as the resources available for simulation are limited to my local machine. In order to obtain results frequently enough so that we can feed back on them as we plan research directions,

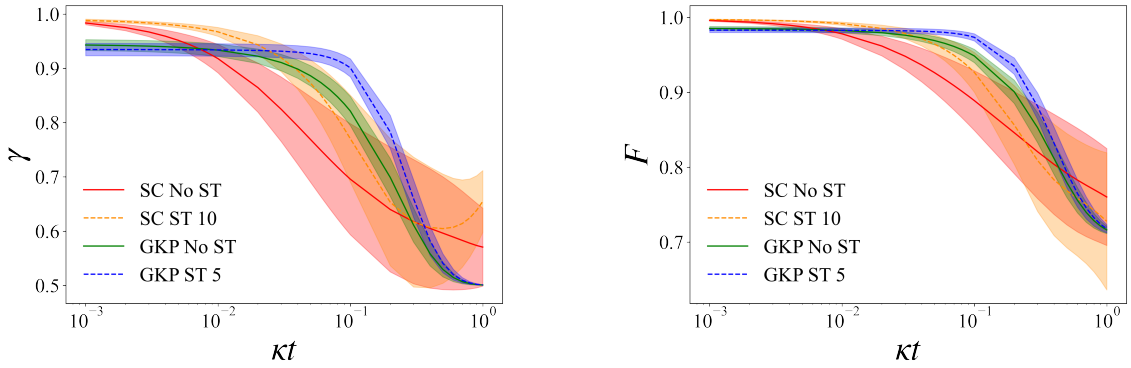

(a) Purity vs. Noise

(b) Fidelity vs. Noise

Figure 6.3: Logical purity (Fig. 6.3a) and logical fidelity (Fig. 6.3b) of ten random logical states encoded with both the squeezed-cat code and the GKP code against cavity photon-loss noise κt for $0.001 \leq \kappa t \leq 1$. For the squeezed-cat code, ten iterations of the sharpen-trim protocol are performed, and for the GKP code, five iterations of the sharpen-trim protocol are performed. This discrepancy in the number of iterations exists because the GKP-code sharpen-trim includes twice as many gates as that for the squeezed-cat code. The error bands are of width equal to one standard deviation of the measured values for the ten random states. Here, "ST" followed by a number denotes the application of sharpen-trim with that number of iterations of sharpen-trim performed, and "No ST" indicates no application of the sharpen-trim error-correction protocol.

we choose to simulate with ten random logical states, in which case the simulation for obtaining the data used to produce a single plot of this work requires approximately ten hours of computation time at full computational resource utilization. In order to generate these ten random logical states, we utilize the function `rand_ket_haar` in the `QuTiP` package of `Python` to obtain a Haar random pure state of dimension 2. Repeating this process ten times, we find ten random logical states. Once we have completed the generation of the ten random states, we compute the performance (logical purity and logical fidelity relative to the encoded logical states) across these ten logical states encoded with both the squeezed-cat and the GKP code, both after the photon-loss noise and then following the application of the appropriate number of iterations of the sharpen-trim protocol. Finally, we plot these average values of these two performance metrics with error bars of one standard deviation against the photon-loss noise κt in Fig. 6.3.

Here, we see that the respective sharpen-trim protocols do indeed improve the quality of the encoded logical states for their respective encodings after photon-loss noise has occurred. Moreover, we see that the squeezed-cat code with its sharpen-trim protocol does perform better than the GKP code with its sharpen-trim protocol as proposed in the work of Royer et al. [RSG20] in both logical purity and logical fidelity restoration for small photon-loss noise $\kappa t \lessapprox 0.02$.

However, for larger photon-loss noise κt, we observe that the sharpen-trim error-correction protocol for the squeezed-cat encoding actually worsens the restoration of the logical state

following the photon-loss noise. This effect perhaps seems a bit counterintuitive, since the squeezed-cat sharpen-trim protocol is designed to restore the encoded state to the squeezed-cat code manifold; as such, we would naïvely expect that the restoration of the logical state should only improve following the application of the sharpen-trim protocol. However, this is not necessarily the case. As the photon-loss noise incurs physical error on the state, there is a point at which this physical error becomes a logical error (i.e., it fundamentally changes the logical state encoded by the physical state). Once this transition occurs, even if the sharpen-trim error-correction protocol is performed, the physical state is not restored to encode its original logical state but instead the new logical state encoded following the physical error. Because this transition is more likely to occur with larger photon-loss noise κt, we see a degradation in the quality of the logical-state restoration in this large κt regime.

6.5.2 Periodic Sharpen-Trim

Motivated by this explanation, we consider how we can prevent the physical state from reaching this transition so that the sharpen-trim protocol can remain effective for error-correction even for large photon-loss noise κt. Toward this goal, we propose an approach inspired by the quantum Zeno effect. In order to slow the transition of the physical state under the effect of the photon-loss noise, we perform the same number of iterations of the sharpen-trim protocol on each encoding that we performed in Sec. 6.5.1 but now distribute these iterations of the sharpen-trim error-correction protocol throughout the period during which this noise is incident on the encoded states, terming this the "periodic" sharpen-trim error-correction protocol. In this manner, we hope to slow the evolution of the encoded logical states under the error such that they never reach the critical point at which an unrecoverable logical error occurs. As discussed earlier, we expect the greatest impact for the largest photon-loss noise κt, since for these larger values of κt, the states more quickly accrue logical errors that are unrecoverable with the sharpen-trim error-correction protocol, meaning that more frequent application of the sharpen-trim error-correction protocol to slow this process should be most beneficial in this case.

In order to test this hypothesis and the overall efficacy of the periodic sharpen-trim approach, we simulate photon-loss noise at various photon-loss noise values κt as before but now perform the *periodic* error-correction protocol, distributing the same number of sharpen-trim error-correction iterations over five applications. As in Sec. 6.5.1, we account for a variety of encoded logical states by performing our error-correction analysis for ten random logical states encoded using both the squeezed-cat and GKP codes, plotting their average logical purity and logical fidelity to the original logical state with error bands of single-standard-deviation width, as before. The results are shown in Fig. 6.4.

We indeed see with ten random states encoded using the squeezed-cat and GKP codes that the squeezed-cat code with our new sharpen-trim error-correction protocol does outperform the GKP code with the error-correction protocol proposed in the work of Royer et al. [RSG20] for both small photon-loss noise ($\kappa t \lessapprox 0.02$), as observed in Sec. 6.5.1, and now also large photon-loss noise ($\kappa t \gtrapprox 0.8$), although the latter is only true for some random states, as indicated by the error bands. Moreover, we do observe that the improvement in logical state restoration with periodic sharpen-trim is present across the whole photon-loss noise regime, but we also see that the most significant improvement over the single

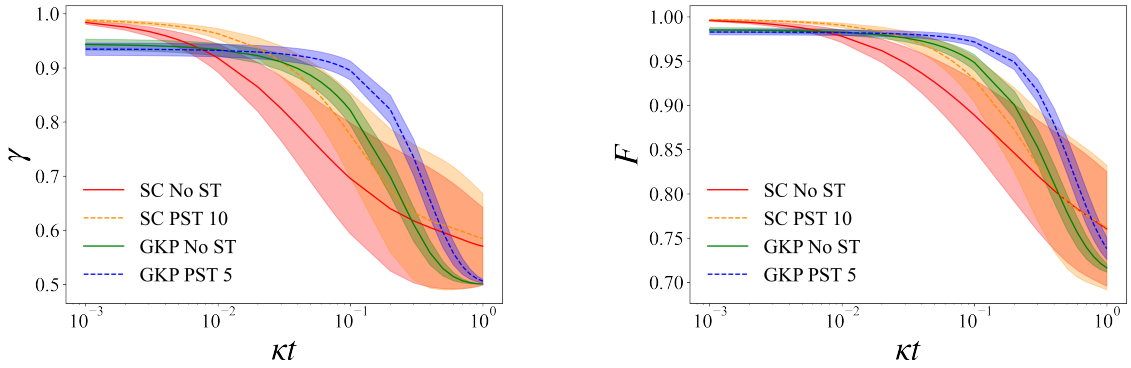

(a) Purity vs. Noise

(b) Fidelity vs. Noise

Figure 6.4: Logical purity (Fig. 6.4a) and logical fidelity (Fig. 6.4b) of ten random logical states encoded with both the squeezed-cat code and the GKP code against cavity photon-loss noise κt for $0.001 \leq \kappa t \leq 1$. For the squeezed-cat code, ten iterations of the sharpen-trim protocol are performed, and for the GKP code, five iterations of the sharpen-trim protocol are performed. Here, "PST" followed by a number denotes that number of iterations of sharpen-trim distributed periodically to form the periodic sharpen-trim protocol.

application occurs for larger noise κt, as we predicted.

6.5.3 Future Directions

In this work, we introduced one application of dissipation engineering to quantum error-correction of the squeezed-cat code based on the sharpen-trim protocol. The way in which we derived the sharpen-trim protocol for the squeezed-cat code was by Trotterization of a unitary operator for dissipating to the squeezed-cat code manifold. Besides the first-order Trotterization that results in the sharpen-trim protocol, there are other second-order Trotterizations, such as the so-called big-small-big and small-big-small Trotterizations, with similarly simple experimental implementations that have been proposed for error-correction of the finite-energy GKP encoding in the work by Royer et al. [RSG20]. As such, in the future, we would like to explore the efficacy of the error-correction protocols corresponding to these second-order Trotterizations and analyze how they compare with the sharpen-trim protocol.

Additionally, we are interested in exploring the performance of the finite-energy squeezed-cat code in comparison with the finite-energy GKP code when their respective sharpen-trim error-correction protocols are employed for codes using different values of the amplitude and squeezing parameter. This is a direction of particular interest because the squeezed-cat code is known to become more robust to photon-loss noise as its amplitude decreases and its squeezing parameter increases [Pan+23], so we hypothesize that squeezed-cat codes with lesser amplitude and greater squeezing parameter might be more desirable and hence utilized more frequently in practical applications.

We also understand that purity and fidelity are not the only metrics by which we can

evaluate the performance of our sharpen-trim protocol for correcting the effects of photon-loss noise on the encoding of a logical state. In particular, we have considered the possibility that the entanglement fidelity could be a better metric for evaluation, since the noise on the physical state might leave the logical state pure while dephasing its entanglement with some other reference system. As such, we would also like to explore how well the entanglement fidelity of the logical state is restored by our sharpen-trim protocol for the squeezed-cat code in much the same way that we have investigated the restoration of the logical purity and logical fidelity.

Regarding the readout of the logical state from the finite-energy GKP and squeezed-cat codes, there has also been some recent research suggesting higher-fidelity methods that make use of measurement operators better tailored to the finite-energy nature of the physical code states [HA21]. As such, we are interested in extending the method for higher-fidelity readout presented in this work for the finite-energy GKP code to the squeezed-cat code. Subsequently, we would like to explore whether we see similarly strong performance of our approach to correcting errors on logical states encoded with the squeezed-cat code when these higher-fidelity readout methods are employed.

6.6 Conclusion

Among QECCs, the squeezed-cat code is a strong choice for encoding quantum data, as it combines the strengths of the translationally-symmmetric GKP code with the strengths of the rotationally-symmetric standard cat code; it has orthogonal code states while also being inherently robust to photon-loss noise because of its compactness and proximity to the origin in phase space. Moreover, in this work, we have demonstrated via simulations that even when photon-loss error does occur, our new experimentally-realizable dissipation engineering approach can correct this error and restore the logical state being encoded. This method for quantum error-correction of the squeezed-cat qubit is significantly simpler than other existing approaches, as it uses only oscillator displacements controlled on a single ancilla qubit, and is thus quite practical for implementation on near-term quantum devices. Specifically, we demonstrate that the performance of the squeezed-cat code for logical-state restoration using our dissipation-engineering error-correction protocol even exceeds that for the finite-energy GKP code corrected using the analogous protocol introduced in Royer et al. [RSG20] under experimentally-realistic conditions in a few key regimes of the photon-loss noise κt, especially when the error-correction protocol is applied several times throughout the computation.

Chapter 7

Conclusion

In summary, we have employed machine learning and other high-level computational techniques for the design of applications of a system consisting of a qubit coupled to an oscillator to implementing fundamental components of quantum technology. Although we do not address nearly all of the potential applications of this system to quantum technology, we have presented a number of research projects spanning quantum computation, quantum sensing, and quantum error-correction for which we have performed optimization and simulations using classical computation and have thus demonstrated the potential of the qubit-oscillator system for employment toward all of these applications. In this manner, we have successfully used high-level computational techniques to efficiently design applications of the system to quantum technology, and in doing so, we have made significant steps toward answering the main question of this thesis. Further research can build on this work by exploring potential applications for other systems to quantum technology in a similar manner.

We have not yet completed the work outlined in Chapter 5 regarding bivariable quantum signal processing (BiQSP), as we still aim to prove that given Laurent polynomial coefficients for a qubit response function, there exist BiQSP phases that realize a qubit response function with these coefficients. Moreover, there still remains the question of whether or not learning the BiQSP phases that produce a qubit response function most closely matching the values of the the desired qubit response function on a set of grid points is the most effective way of learning the phases for that qubit response function or if there might be a more effective alternative approach. We would like to further explore these questions in the future.

The same is true of the work outlined in Chapter 6. Although we did extensively test the performance of our squeezed-cat sharpen-trim protocol against that of the GKP sharpen-trim protocol for a variety of encoded logical states, we have not yet tested the performance of other Trotterizations of the dissipation unitary for the error-correction of the squeezed-cat code, and so this is another direction that we would like to further explore in the future. Additionally, we believe that the squeezed-cat code has additional benefits for error correction when the amplitude of the code states is smaller, and so we intend to further investigate in this direction as well in the near future.

Appendix A

Definition of the Generalized Gell-Mann Matrices

In general, for a $d \times d$ Hermitian matrix H, we can find a set of basis matrices, such that H can be written as a linear combination of the basis matrices. Denote E_{ij} as the $d \times d$ matrix with the (i, j)-th element being 1 and the rest are zeros. Recall that for the 2×2 dimensional case where there are four Pauli matrices, i.e., I, σ_z, σ_x, σ_y. In analogy to σ_z, we can define $(d-1)$ diagonal matrices M_j^Z in the following way

$$M_j^Z = \sqrt{\frac{2}{j(j-1)}}\left(\sum_{k=1}^{j-1} E_{kk} - (j-1)E_{jj}\right), \tag{A.1}$$

where $2 \leq j \leq d$. Similarly, there are $d(d-1)/2$ real matrices M_{jk}^X

$$M_{jk}^X = E_{jk} + E_{kj} \quad (2 \leq j < k \leq d) \tag{A.2}$$

in analogy to σ_x, and another $d(d-1)/2$ imaginary matrices M_{jk}^Y

$$M_{jk}^Y = -iE_{jk} + iE_{kj} \quad (2 \leq j < k \leq d) \tag{A.3}$$

analogous to σ_y. Simple counting suggests that there are a total of $d^2 - 1$ such basis matrix (without the identity matrix). It can be verified that they are traceless and orthonormalized to each other. Moreover, they are closed under the commutation

$$[M_j^Z,\, M_k^Z] = 0, \tag{A.4}$$

$$[M_j^Z,\, M_{lm}^X] = i\sqrt{\frac{2}{j(j-1)}}\left(\sum_{k=1}^{j-1}(\delta_{km}M_{kl}^Y + \delta_{lk}M_{km}^Y) - (j-1)(\delta_{mj}M_{jl}^Y + \delta_{lj}M_{jm}^Y)\right), \tag{A.5}$$

$$[M_j^Z,\, M_{lm}^Y] = i\sqrt{\frac{2}{j(j-1)}}\left(\sum_{k=1}^{j-1}(\delta_{mk}M_{kl}^X - \delta_{lk}M_{mk}^X) - (j-1)(\delta_{mj}M_{jl}^X - \delta_{lj}M_{mj}^X)\right), \tag{A.6}$$

$$[M^X_{jk},\, M^X_{lm}] = i\delta_{kl}M^Y_{jm} + i\delta_{jl}M^Y_{km} + i\delta_{mj}M^Y_{kl} + i\delta_{mk}M^Y_{jl}, \tag{A.7}$$

$$[M^Y_{jk},\, M^Y_{lm}] = -\,\delta_{kl}M^X_{jm} + \delta_{jl}M^X_{km} + \delta_{mj}M^X_{kl} - \delta_{mk}M^X_{jl}, \tag{A.8}$$

$$[M^X_{jk},\, M^Y_{lm}] = i\delta_{km}M^X_{jl} - i\delta_{jl}M^X_{km} + i\delta_{mj}M^X_{kl} - i\delta_{lk}M^X_{mj}. \tag{A.9}$$

Appendix B

Decomposing an Arbitrary Rotation into Two Rotations in the xy-plane

We will demonstrate here that it is possible to decompose any arbitrary $SO(3)$ rotation into two rotations in the xy-plane.

We begin with the well-known fact that any $SO(3)$ rotation $R_{\vec{r}}(\theta)$ can be decomposed into two reflections, denoted with the letter S, about planes p_1 and p_2 intersecting at an angle $\frac{\theta}{2}$, where $\vec{r} = p_1 \cap p_2$. This can be expressed as follows:

$$R_{\vec{r}}(\theta) = S(p_1) \circ S(p_2). \tag{B.1}$$

Composing a reflection with itself produces the identity, and thus, we can insert two reflections about plane p into Eq. (B.1) and rewrite it as

$$R_{\vec{r}}(\theta) = S(p_1) \circ S(p) \circ S(p) \circ S(p_2). \tag{B.2}$$

We would like to decompose arbitrary rotations into pairs of red sideband pulses, each of which is restricted to rotation about an axis in the xy-plane, so we choose p to be the xy-plane. With this choice, we find

$$R_{\vec{r}}(\theta) = R_{\vec{r}_1}(\theta_1) R_{\vec{r}_2}(\theta_2), \tag{B.3}$$

where $\vec{r}_1 = p_1 \cap p$ and $\vec{r}_2 = p \cap p_2$, and $\frac{\theta_i}{2} = |\angle(p_i, p)|$, the angle between the planes p and p_i for $i = 1, 2$. We can always choose the planes p_1 and p_2 to be different from the xy-plane, so we are guaranteed to find a decomposition of the arbitrary $SO(3)$ rotation $R_{\vec{r}}(\theta)$ into two red sideband pulses using this method.

Appendix C

Subroutine on Decomposition of Rotations in to the xy-plane

With Appendix B in mind, following is a detailed subroutine to decompose any rotation $R_{\hat{r}}(\theta)$ into rotations with rotation axes lying in the xy-plane:

1. If $\hat{r}$ is already in the xy-plane (i.e., its z-component is equal to zero), then there is no need for decomposition, and the rotation can be made directly.

2. If $\hat{r}$ is not in the xy-plane, then find a unit vector $\hat{r}_1^{\perp}$ that is perpendicular to $\hat{r} = \langle r_1, r_2, r_3 \rangle$. Because the z-component r_3 is nonzero, such a vector is given by

$$\hat{r}_1^{\perp} = \frac{1}{\sqrt{r_1^2 + r_3^2}} \langle -r_3, 0, r_1 \rangle. \tag{C.1}$$

3. Find a second unit vector $\hat{r}_2^{\perp}$ that is perpendicular to both $\hat{r}$ and $\hat{r}_1^{\perp}$ by taking

$$\vec{r}_2^{\perp} = \frac{\hat{r} \times \hat{r}_1^{\perp}}{\|\hat{r} \times \hat{r}_1^{\perp}\|}. \tag{C.2}$$

4. For any value of $\phi \in \mathbb{R}$, $0 \leq \phi < 2\pi$, take the unit normal vectors

$$\hat{n}_1 = \hat{r}_1^{\perp} \cos(\phi) + \hat{r}_2^{\perp} \sin(\phi) \tag{C.3}$$

$$\hat{n}_2 = \hat{r}_1^{\perp} \cos\left(\phi + \frac{\theta}{2}\right) + \hat{r}_2^{\perp} \sin\left(\phi + \frac{\theta}{2}\right), \tag{C.4}$$

   where a reflection through the plane with normal vector $\hat{n}_1$ followed by a reflection through the plane with normal vector $\hat{n}_2$ is equivalent to a rotation about $\hat{r}$ by an angle of θ.

5. Next, as per the discussion in Appendix B, two reflections about the xy-plane (which together are equivalent to the identity transformation) are inserted, and this sequence is recomposed into a sequence of two rotations about unit vectors $\hat{r}_1$ and $\hat{r}_2$ in the xy-plane.

In particular, define $\hat{z} = \langle 0,\, 0,\, 1 \rangle$ to be the unit normal vector to the xy-plane, and take

$$\hat{r}_1 = \frac{\hat{n}_1 \times \hat{z}}{\|\hat{n}_1 \times \hat{z}\|} \tag{C.5}$$

$$\theta_1 = 2\cos^{-1}\left(\hat{n}_1 \cdot \hat{z}\right) \tag{C.6}$$

$$\hat{r}_2 = \frac{\hat{z} \times \hat{n}_2}{\|\hat{z} \times \hat{n}_2\|} \tag{C.7}$$

$$\theta_2 = 2\cos^{-1}\left(\hat{z} \cdot \hat{n}_2\right). \tag{C.8}$$

It is guaranteed that $\hat{r}_1$ and $\hat{r}_2$ lie in the xy-plane because they must, by definition, be perpendicular to $\hat{z}$. Moreover, these choices give the equivalence

$$R_{\hat{r}}(\theta) \leftrightarrow \{R_{\hat{r}_1}(\theta_1),\, R_{\hat{r}_2}(\theta_2)\} \tag{C.9}$$

of the sequence of rotations $\{R_{\hat{r}_1}(\theta_1),\, R_{\hat{r}_2}(\theta_2)\}$ about axes in the xy-plane with the original rotation $R_{\hat{r}}(\theta)$, as desired.

Appendix D

Proof of bosonic QSP Theorem 3

Denote the set of eigenvalues and eigenvectors of the generator $h(\hat{x}, \hat{p})$ in Lemma 2 to be λ and $|\lambda\rangle$ such that

$$h(\hat{x}, \hat{p}) |\lambda\rangle = \lambda |\lambda\rangle . \tag{D.1}$$

Since $h(\hat{x}, \hat{p})$ is Hermitian, we have $\lambda \in \mathbb{R}$. Moreover, for an infinite-dimensional oscillator, $\{\lambda\}$ can be inherently continuous. Furthermore, we assume that $\{|\lambda\rangle\}$ forms a (over)complete basis for the oscillator (for example, in the case of a continuous displacement operator whose eigenstates are coherent states) for achieving universal control of the oscillator. However, the bosonic QSP formalism still works in the subspace expanded by $\{|\lambda\rangle\}$.

Now, consider the action of W_z on an arbitrary qubit-oscillator entangled state, where the oscillator state is given by $\frac{1}{\sqrt{2}}(|0\rangle |\Psi_0\rangle_{\text{osc}} + |1\rangle |\Psi_1\rangle_{\text{osc}})$. Expand the oscillator state under the $\{|\lambda\rangle\}$ basis to find

$$\begin{aligned}
&W_z \frac{1}{\sqrt{2}} (|0\rangle |\Psi_0\rangle_{\text{osc}} + |1\rangle |\Psi_1\rangle_{\text{osc}}) \\
=&e^{-ih(\hat{x},\hat{p})\sigma_z} \frac{1}{\sqrt{2}} (|0\rangle |\Psi_0\rangle_{\text{osc}} + |1\rangle |\Psi_1\rangle_{\text{osc}}) \\
=&e^{-ih(\hat{x},\hat{p})\sigma_z} \frac{1}{\sqrt{2}} \left(|0\rangle \int d\lambda c_{0,\lambda} |\lambda\rangle + |1\rangle \int d\lambda c_{1,\lambda} |\lambda\rangle \right) \\
=&\frac{1}{\sqrt{2}} \left(|0\rangle \int d\lambda e^{-i\lambda} c_{0,\lambda} |\lambda\rangle + |1\rangle \int d\lambda e^{i\lambda} c_{1,\lambda} |\lambda\rangle \right) \\
=&\int d\lambda |\lambda\rangle \frac{1}{\sqrt{2}} \left(|0\rangle e^{-i\lambda} c_{0,\lambda} + |1\rangle e^{i\lambda} c_{1,\lambda} \right) \\
=&\int d\lambda |\lambda\rangle \otimes e^{-i\lambda\sigma_z} \left[\frac{c_{0,\lambda} |0\rangle + c_{1,\lambda} |1\rangle}{\sqrt{2}} \right] .
\end{aligned} \tag{D.2}$$

Therefore, W_z acts individually on each 2×2 subspace labeled by the eigenvalue λ of $h(\hat{x}, \hat{p})$ in a similar spirit to that of qubitization of a finite-dimensional block-encoding. From Eq. (D.2), repeatedly applying W_z and a single-qubit rotation $e^{i\theta_j\sigma_x}$ will result in the application of QSP

to each individual 2×2 subspace:

$$
\begin{aligned}
& e^{i\theta_d \sigma_x} \prod_{j=0}^{d-1} W_z e^{i\theta_j \sigma_x} \frac{1}{\sqrt{2}} (|0\rangle |\Psi_0\rangle_{\text{osc}} + |1\rangle |\Psi_1\rangle_{\text{osc}}) \\
= & \int d\lambda \, |\lambda\rangle \otimes e^{i\theta_d \sigma_x} \prod_{j=0}^{d-1} e^{-i\lambda\sigma_z} e^{i\theta_j \sigma_x} \left[\frac{c_{0,\lambda} |0\rangle + c_{1,\lambda} |1\rangle}{\sqrt{2}} \right]. \qquad \text{(D.3)}
\end{aligned}
$$

In the 2×2 subspace for each λ, we identify the following sequence of SU(2) rotations

$$
U_{\lambda, \vec{\theta}} = e^{i\theta_d \sigma_x} \prod_{j=0}^{d-1} e^{-i\lambda\sigma_z} e^{i\theta_j \sigma_x}. \qquad \text{(D.4)}
$$

This is nothing but the usual single-qubit QSP sequence under the W_z-convention [Mar+21], where the signal being transform is a Pauli-Z rotation parameterized by the eigenvalue λ. To be more concrete, applying the single-qubit QSP theorem to $U_{\lambda, \vec{\theta}}$, we have

$$
U_{\lambda, \vec{\theta}} = \begin{bmatrix} F(\omega_\lambda) & iG(\omega_\lambda) \\ iG(\omega_\lambda^{-1}) & F(\omega_\lambda^{-1}) \end{bmatrix}, \qquad \text{(D.5)}
$$

where $\omega_\lambda = e^{-i\lambda}$, $F(\omega_\lambda) = \sum_{j=-d}^{d} f_j \omega_\lambda^j$, $G(\omega_\lambda) = \sum_{j=-d}^{d} g_j \omega_\lambda^j$ are Laurent polynomials of degree-d with real coefficients f_j, $g_j \in \mathbb{R}$. The unitarity condition on $U_{\lambda, \vec{\theta}}$ also requires that for all λ,

$$
F(\omega_\lambda) F(\omega_\lambda^{-1}) + G(\omega_\lambda) G(\omega_\lambda^{-1}) = 1. \qquad \text{(D.6)}
$$

The reverse direction of the QSP theorem also means that given arbitrary degree-d real Laurent polynomial $F(\cdot)$, $G(\cdot)$ satisfying Eq. (D.6), there exists a sequence of phase angles $\vec{\theta}$ such that a circuit constructed from $U_{\lambda, \vec{\theta}}$ can implement the given $F(\cdot)$, $G(\cdot)$.

The above single-qubit QSP result applies for each individual eigenspace of the oscillator labeled by λ. Performing the integral over all λ, it follows that the overall sequence in Eq. (4.13) performs a Laurent polynomial transformation on $e^{-ih(\hat{x}, \hat{p})}$, hence proving Theorem 3. The last step of elevating from qubit QSP to the hybrid qubit-oscillator continuous-variable case resembles the spirit of deriving quantum eigenvalue transform [Mar+21], with the difference that in our case the spectra of the oscillator is continuous while in the usual multi-qubit case the eigenspectra being discrete.

Appendix E

Proof that the response function is a polynomial of the sensed signal

We prove in this section that the QSPI response function, as defined in Eq. (4.23), is a degree-d polynomial transformation of the new signal $v = e^{i(2\kappa)\beta}$ within a restricted range $[-\frac{\pi}{2\kappa}, \frac{\pi}{2\kappa}]$ and the polynomial is real.

Using the Laurent polynomial expressions in Eq. (4.14) and explicitly evaluating the integration with respect to x, we can write Eq. (4.23) as a series sum

$$\mathbb{P}(M =\downarrow |\beta) = \sum_{n,\,n',\,m,\,m'=-d}^{d} A_{n,\,n',\,m,\,m'}, \tag{E.1}$$

where

$$\begin{aligned} A_{n,\,n',\,m,\,m'} = &(f_n f_{n'} + g_n g_{n'})(f_m f_{m'} + g_m g_{m'})^* \\ &\times e^{-\frac{1}{4}\kappa^2(n-n'-m+m')^2} e^{-i\kappa(n-m)\beta}. \end{aligned} \tag{E.2}$$

The following property can be verified:

$$A_{n,\,n',\,m,\,m'} = A^*_{m,\,m',\,n,\,n'}. \tag{E.3}$$

Therefore, we can rearrange the sum for the QSPI response function to be

$$\begin{aligned} \mathbb{P}(M =\downarrow |\beta) &= \frac{1}{2} \sum_{n,\,n',\,m,\,m'=-d}^{d} (A_{n,\,n',\,m,\,m'} + A^*_{m,\,m',\,n,\,n'}) \\ &= \frac{1}{2} \left(\sum_{n,\,n',\,m,\,m'=-d}^{d} A_{n,\,n',\,m,\,m'} + \sum_{n,\,n',\,m,\,m'=-d}^{d} A^*_{m,\,m',\,n,\,n'} \right) \\ &= \frac{1}{2} \left(\sum_{n,\,n',\,m,\,m'=-d}^{d} A_{n,\,n',\,m,\,m'} + \sum_{n,\,n',\,m,\,m'=-d}^{d} A^*_{n,\,n',\,m,\,m'} \right) \\ &= \sum_{n,\,n',\,m,\,m'=-d}^{d} \Re A_{n,\,n',\,m,\,m'}, \end{aligned} \tag{E.4}$$

where we have renamed variables $m \leftrightarrow n$ and $m' \leftrightarrow n'$ from the second line to the third line, and $\Re\cdot$ denotes the real part.

Next, we prove that $\mathbb{P}(M =\downarrow |\beta)$ is a degree-d Laurent polynomial of $v = e^{i(2\kappa)\beta}$ in the range $[-\frac{\pi}{2\kappa}, \frac{\pi}{2\kappa}]$.

Because f_n, g_n are each coefficients of Laurent polynomials from QSP, it follows that f_n, $g_n \neq 0$ only for even n if d is even, or f_n, $g_n \neq 0$ only for odd n if d is odd. This means $A_{n,n',m,m'} \neq 0$ only when m, n have the same parity and m', n' have the same parity, which further suggests the variable substitution

$$m = n + 2s, \quad m' = n' + 2r, \tag{E.5}$$

where $-d \leq s, r \leq d$. Substituting this back into Eq. (E.2), we have

$$\begin{aligned} A_{n,n',n+2s,n'+2r} = &(f_n f_{n'} + g_n g_{n'}) \\ &(f_{n+2s} f_{n'+2r} + g_{n+2s} g_{n'+2r}) \\ &e^{-\kappa^2 (r-s)^2} e^{i(2\kappa)s\beta}. \end{aligned} \tag{E.6}$$

Further, substituting this back into Eq. (E.1), we obtain

$$\begin{aligned} &\mathbb{P}(M =\downarrow |\beta) \\ &= \sum_{n,n',s,r=-d}^{d} (f_n f_{n'} + g_n g_{n'})(f_{n+2s} f_{n'+2r} + g_{n+2s} g_{n'+2r}) \\ &\quad \times e^{-\kappa^2 (r-s)^2} e^{i(2\kappa)s\beta} \\ &= \sum_{s=-d}^{d} c_s(\kappa) v^s, \end{aligned} \tag{E.7}$$

where $v = e^{i(2\kappa)\beta}$ and

$$\begin{aligned} c_s(\kappa) = &\sum_{n,n',r=-d}^{d} (f_n f_{n'} + g_n g_{n'}) \\ &(f_{n+2s} f_{n'+2r} + g_{n+2s} g_{n'+2r}) e^{-\kappa^2 (r-s)^2}, \end{aligned} \tag{E.8}$$

with f_n, $g_n \in \mathbb{R}$, $c_s \in \mathbb{R}$.

Because the new signal operator v has an effective momentum of 2κ, this means that $\mathbb{P}(M =\downarrow |\beta)$ will be periodic with a reduced period of $[-\frac{\pi}{2\kappa}, \frac{\pi}{2\kappa}]$. It follows that the QSPI response function $\mathbb{P}(M =\downarrow |\beta)$ is a degree-d Laurent polynomial in the operator $v = e^{i(2\kappa)\beta}$.

Appendix F

Recursive relationship between the QSP coefficients

The probability of making the wrong decision can be efficiently computed classically from the original QSP phase angles. First, by using the following recursive relationship, all the QSP coefficients f_n, g_n as stated in Theorem 3 can be computed from the phase angles. Second, the series sum in Eq. (4.33) can be evaluated explicitly using the computed f_n, g_n, without loss of numerical precision.

$$f_r^{(d+1)} = \begin{cases} \cos\theta_{d+1} f_{r-1}^{(d)}, & r = d, d+1 \\ -\sin\theta_{d+1} g_{r+1}^{(d)}, & r = -d, -d-1 \\ \cos\theta_{d+1} f_{r-1}^{(d)} - \sin\theta_{d+1} g_{r+1}^{(d)}, & |r| \leq (d-1) \end{cases} \tag{F.1}$$

$$g_r^{(d+1)} = \begin{cases} \sin\theta_{d+1} f_{r-1}^{(d)}, & r = d, d+1 \\ \cos\theta_{d+1} g_{r+1}^{(d)}, & r = -d, -d-1 \\ \sin\theta_{d+1} f_{r-1}^{(d)} + \cos\theta_{d+1} g_{r+1}^{(d)}, & |r| \leq (d-1) \end{cases} \tag{F.2}$$

Appendix G

Proof of Heisenberg scaling for QSPI binary decisions

From Fig. 4.5, the decision error probability can be approximately written as a sum of two contributions in the following way

$$p_{\text{err}} \approx \epsilon \left(\frac{\pi}{\kappa} - 2\sigma \right) + \frac{\sigma}{2}, \tag{G.1}$$

where ϵ is the approximation error to an ideal step function from a polynomial function. The first term in Eq. (G.1) is obtained from such an imperfect polynomial approximation in the region of $[-\frac{\pi}{2\kappa}, \frac{\pi}{2\kappa}]$, excluding the rising and falling edges $[\beta_{\text{th}} - \sigma/2, \beta_{\text{th}} + \sigma/2] \cup [-\beta_{\text{th}} - \sigma/2, -\beta_{\text{th}} + \sigma/2]$; the second term in Eq. (G.1) is from erroneous decisions when the displacement β lies within the rising or falling edge.

Rearranging Eq. (G.1), this means that the error in the polynomial approximation to $P_{\text{ideal}}^{\text{sign, sin}}$ is

$$\epsilon \approx \frac{p_{\text{err}} - \frac{\sigma}{2}}{\frac{\pi}{\kappa} - 2\sigma}. \tag{G.2}$$

From Ref. [Mar+23], to achieve an ϵ-approximation to the sign function in regions excluding $[-\sigma/2, \sigma/2]$ requires a polynomial of degree $d = \gamma(\epsilon, \sigma)$ for

$$\gamma(\epsilon, \sigma) := 2 \cdot \left\lceil \max \left(\frac{e}{\sigma} \sqrt{W\left(\frac{8}{\pi\epsilon^2}\right) W\left(\frac{512}{e^2\pi}\frac{1}{\epsilon^2}\right)}, \sqrt{2} W\left(\frac{8\sqrt{2}}{\sqrt{\pi}\sigma\epsilon} \sqrt{W\left(\frac{8}{\pi\epsilon^2}\right)} \right) \right) \right\rceil + 1, \tag{G.3}$$

where $W(\cdot)$ is the Lambert W function. Assuming $\sigma = O(p_{\text{err}})$ and for small p_{err}, substitute Eq. (G.2) into Eq. (G.3) and use a Taylor expansion on the Lambert W function in order to obtain Eq. (4.40) in the main text.

Appendix H

Results for 41 Phases Trained on a 9×9 Grid

As mentioned in Chapter 5, we repeated much of the analysis presented there for 31-phase BiQSP with 41 phases trained on a 9×9 target grid. We present the results of this supplementary analysis here. We did not repeat the analysis for the slightly asymmetric XOR function given in Eq. 5.10, as we had already shifted to using the symmetric XOR function given in Eq. 5.11 by this point.

For the asymmetric XOR function given in Eq. 5.11, we achieve a loss of 0.2155 and find the following qubit response function plots Fig. H.1a and Fig. H.1b of Fig. H.1 for the real and imaginary parts, respectively.

The real and imaginary parts of the finer-grid evaluation of the qubit response function are shown in Fig. H.2a and Fig. H.2b of Fig. H.2, respectively.

Note that, as mentioned in Chapter 5, the loss function for this qubit response function is a bit greater than for the 31-phase BiQSP for the reasons that we give in Chapter 5.2.

The BiQSP phases achieving this qubit response function are given in Table H.1.

Description		Phases
Symmetric XOR	5.11	[5.0870, 3.8817, 5.0512, 1.5792, 5.1918, 3.6297, 5.4102, 5.3284, 1.3099, 5.5671, 4.7964, 1.2086, 4.3467, 6.3379, 5.5033, 1.6697, 0.9855, 1.6711, 4.9414, 3.9580, 4.3727, 3.3942, 1.2229, 2.9802, 0.1725, 4.3998, 4.5407, 0.9028, 0.3202, 5.4757, 6.2410, 2.0768, 4.8046, 2.6349, 0.3457, -0.0230, 2.8366, 5.1122, 2.4947, 0.9951, 5.1257]

Table H.1: 41-phase BiQSP phases learned for the symmetric target XOR function given in Eq. 5.11

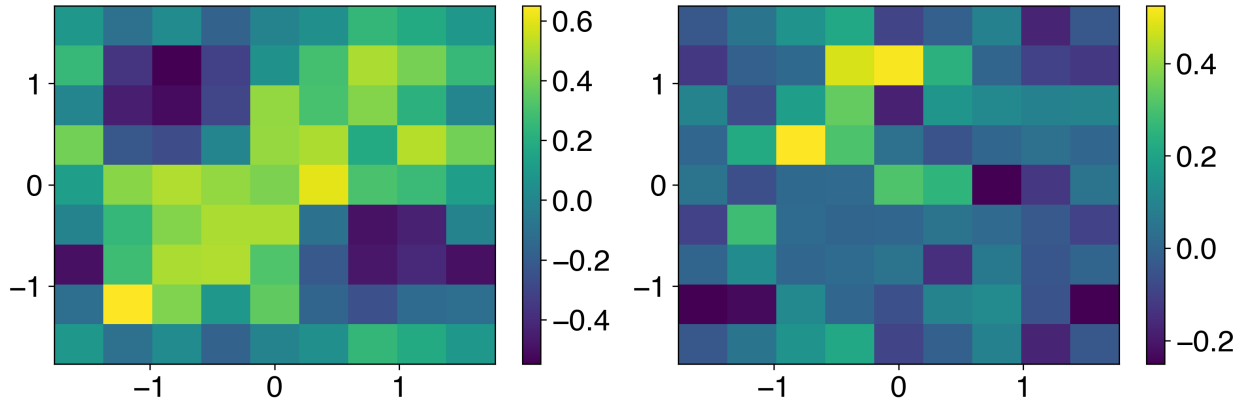

(a) Real Part (b) Imaginary Part

Figure H.1: Real (Fig. H.1a) and imaginary (H.1b) parts of the learned symmetric XOR qubit response function from Eq. 5.11 with 41 phases.

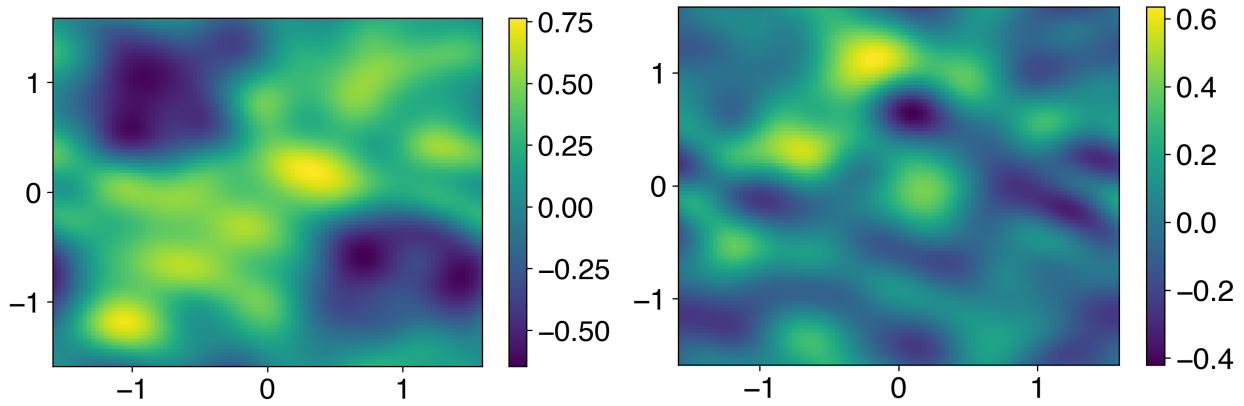

(a) Real Part (b) Imaginary Part

Figure H.2: The real (Fig. H.2a) and imaginary (Fig. H.2b) parts of the optimized approximation of the XOR qubit response function F using 41 phases and evaluated on a 101×101 grid.

References

[Ifr+00] Georges Ifrah, E. F. Harding, David Bellos, Sophie Wood, and Harding E. F. *The Universal History of Computing: From the Abacus to Quantum Computing*. USA: John Wiley & Sons, Inc., 2000.

[Lev13] Steven Levy. *The Brief History of the ENIAC Computer*. Ed. by Smithsonian Magazine. [Online; posted November 2013]. Nov. 2013. URL: https://www.smithsonianmag.com/history/the-brief-history-of-the-eniac-computer-3889120/.

[Wie83] S. Wiesner. "Conjugate coding". In: *ACM SIGACT News* 15 (1 1983), pp. 78–88. DOI: 10.1145/1008908.1008920. URL: https://dl.acm.org/doi/pdf/10.1145/1008908.1008920.

[Ben82] Paul A. Benioff. "Quantum mechanical Hamiltonian models of discrete processes that erase their own histories: Application to Turing machines". In: *Intl. Journal of Theo. Phys.* 21.3 (Apr. 1, 1982), pp. 177–201. DOI: 10.1007/BF01857725. URL: https://doi.org/10.1007/BF01857725.

[Fey82] Richard P. Feynman. "Simulating physics with computers". In: *Intl. Journal of Theo. Phys.* 21.6 (June 1, 1982), pp. 467–488. DOI: 10.1007/BF02650179. URL: https://doi.org/10.1007/BF02650179.

[LB99] S. Lloyd and S. L. Braunstein. "Quantum Computation over Continuous Variables". In: *Phys. Rev. Lett.* 82 (8 Feb. 1999), pp. 1784–1787. DOI: 10.1103/PhysRevLett.82.1784. URL: https://link.aps.org/doi/10.1103/PhysRevLett.82.1784.

[MKB+19] K. C. McCormick, J. Keller, S. C. Burd, et al. "Quantum-enhanced sensing of a single-ion mechanical oscillator". In: *Nature* 572.7767 (2019), pp. 86–90. DOI: 10.1038/s41586-019-1421-y. URL: https://doi.org/10.1038/s41586-019-1421-y.

[BSB+19] S. C. Burd, R. Srinivas, J. J. Bollinger, et al. "Quantum amplification of mechanical oscillator motion". In: *Science* 364.6446 (2019), pp. 1163–1165. ISSN: 0036-8075. DOI: 10.1126/science.aaw2884. URL: https://science.sciencemag.org/content/364/6446/1163.

[NCS18a] M. Y. Niu, I. L. Chuang, and J. H. Shapiro. "Qudit-Basis Universal Quantum Computation Using $\chi^{(2)}$ Interactions". In: *Phys. Rev. Lett.* 120 (16 Apr. 2018), p. 160502. DOI: 10.1103/PhysRevLett.120.160502. URL: https://link.aps.org/doi/10.1103/PhysRevLett.120.160502.

[GKP01] Daniel Gottesman, Alexei Kitaev, and John Preskill. "Encoding a qubit in an oscillator". In: *Phys. Rev. A* 64 (1 June 2001), p. 012310. DOI: 10.1103/PhysRevA.64.012310. URL: https://link.aps.org/doi/10.1103/PhysRevA.64.012310.

[FNM+19] C. Flühmann, T. L. Nguyen, M. Marinelli, et al. "Encoding a qubit in a trapped-ion mechanical oscillator." In: *Nature* 566 (2019), pp. 513–517. DOI: 10.1038/s41586-019-0960-6.

[GLC+19] Y. Y. Gao, B. J. Lester, K. S. Chou, et al. "Entanglement of bosonic modes through an engineered exchange interaction". In: *Nature* 566.7745 (2019), pp. 509–512. DOI: 10.1038/s41586-019-0970-4. URL: https://doi.org/10.1038/s41586-019-0970-4.

[Mas+19] Gleb Maslennikov, Jaren Gan, Ko-Wei Tseng, Chi Huan Nguyen, and Dzmitry Matsukevich. "Towards Continuous Variables Quantum Computing with Trapped Ions". In: *2019 Conference on Lasers and Electro-Optics Europe and European Quantum Electronics Conference*. Optica Publishing Group, 2019.

[PAS23] PASQAL. "PASQAL Announces Partnership to Develop the Foundations of a Photonic Quantum Processor Powered by Neutral Atom Technology". In: *PASQAL* (Oct. 2023). URL: https://www.pasqal.com/articles/pasqal-announces-partnership-to-develop-the-foundations-of-a-photonic-quantum-processor-powered-by-neutral-atom-technology.

[Pfi19] Olivier Pfister. "Continuous-variable quantum computing in the quantum optical frequency comb". In: *Journal of Phys. B: Atomic, Molecular and Optical Phys.* 53.1 (Nov. 2019), p. 012001. DOI: 10.1088/1361-6455/ab526f. URL: https://dx.doi.org/10.1088/1361-6455/ab526f.

[SQJ18] Ingrid Strandberg, Fernando Quijandria, and GöRan Johansson. "Continuous Variable Quantum Computing in Circuit QED". In: *APS March Meeting Abstracts*. Vol. 2018. APS Meeting Abstracts. Jan. 2018, E39.008, E39.008.

[RA21] Federico Rueda and Sonia Lopez Alarcon. "Continuous Variable Quantum Compilation". In: *2021 Intl. Conference on Comp. Sci. and Comp. Intelligence (CSCI)*. Dec. 2021, pp. 1765–1770. DOI: 10.1109/CSCI54926.2021.00335.

[Par+20] Adrian Parra-Rodriguez, Pavel Lougovski, Lucas Lamata, Enrique Solano, and Mikel Sanz. "Digital-analog quantum computation". In: *Phys. Rev. A* 101.2 (Feb. 2020). ISSN: 2469-9934. DOI: 10.1103/physreva.101.022305. URL: http://dx.doi.org/10.1103/PhysRevA.101.022305.

[Mar24] Ana Martin. *Digital-Analog Quantum Computing and Algorithms*. 2024. arXiv: 2401.10622 [quant-ph].

[YN03] J. Q. You and Franco Nori. "Quantum information processing with superconducting qubits in a microwave field". In: *Phys. Rev. B* 68 (6 Aug. 2003), p. 064509. DOI: 10.1103/PhysRevB.68.064509. URL: https://link.aps.org/doi/10.1103/PhysRevB.68.064509.

[Wal+04] A. Wallraff, D. I. Schuster, A. Blais, L. Frunzio, R. S. Huang, J. Majer, S. Kumar, S. M. Girvin, and R. J. Schoelkopf. "Strong coupling of a single photon to a superconducting qubit using circuit quantum electrodynamics". In: *Nature* 431.7005 (Sept. 1, 2004), pp. 162–167. DOI: 10.1038/nature02851. URL: https://doi.org/10.1038/nature02851.

[Joh+06] J. Johansson, S. Saito, T. Meno, H. Nakano, M. Ueda, K. Semba, and H. Takayanagi. "Vacuum Rabi Oscillations in a Macroscopic Superconducting Qubit *LC* Oscillator System". In: *Phys. Rev. Lett.* 96 (12 Mar. 2006), p. 127006. DOI: 10.1103/PhysRevLett.96.127006. URL: https://link.aps.org/doi/10.1103/PhysRevLett.96.127006.

[Lei+03] D. Leibfried, R. Blatt, C. Monroe, and D. Wineland. "Quantum dynamics of single trapped ions". In: *Rev. Mod. Phys.* 75 (1 Mar. 2003), pp. 281–324. DOI: 10.1103/RevModPhys.75.281. URL: https://link.aps.org/doi/10.1103/RevModPhys.75.281.

[Man+03] Olaf Mandel, Markus Greiner, Artur Widera, Tim Rom, Theodor W. Hänsch, and Immanuel Bloch. "Controlled collisions for multi-particle entanglement of optically trapped atoms". In: *Nature* 425.6961 (Oct. 1, 2003), pp. 937–940. DOI: 10.1038/nature02008. URL: https://doi.org/10.1038/nature02008.

[RBH01] J. M. Raimond, M. Brune, and S. Haroche. "Manipulating quantum entanglement with atoms and photons in a cavity". In: *Rev. Mod. Phys.* 73 (3 Aug. 2001), pp. 565–582. DOI: 10.1103/RevModPhys.73.565. URL: https://link.aps.org/doi/10.1103/RevModPhys.73.565.

[Chi+04] I. Chiorescu, P. Bertet, K. Semba, Y. Nakamura, C. J. P. M. Harmans, and J. E. Mooij. "Coherent dynamics of a flux qubit coupled to a harmonic oscillator". In: *Nature* 431.7005 (Sept. 1, 2004), pp. 159–162. DOI: 10.1038/nature02831. URL: https://doi.org/10.1038/nature02831.

[Mor+21] Lorenzo Moro, Matteo G. A. Paris, Marcello Restelli, and Enrico Prati. "Quantum compiling by deep reinforcement learning". In: *Comm. Phys.* 4.1 (Aug. 6, 2021), p. 178. DOI: 10.1038/s42005-021-00684-3. URL: https://doi.org/10.1038/s42005-021-00684-3.

[Cim+23] Valeria Cimini, Mauro Valeri, Emanuele Polino, Simone Piacentini, Francesco Ceccarelli, Giacomo Corrielli, Nicolò Spagnolo, Roberto Osellame, and Fabio Sciarrino. "Deep reinforcement learning for quantum multiparameter estimation". In: *Adv. Photonics* 5.1 (2023), p. 016005. DOI: 10.1117/1.AP.5.1.016005. URL: https://doi.org/10.1117/1.AP.5.1.016005.

[Zen+23] Yexiong Zeng, Zheng-Yang Zhou, Enrico Rinaldi, Clemens Gneiting, and Franco Nori. "Approximate Autonomous Quantum Error Correction with Reinforcement Learning". In: *Phys. Rev. Lett.* 131 (5 July 2023), p. 050601. DOI: 10.1103/PhysRevLett.131.050601. URL: https://link.aps.org/doi/10.1103/PhysRevLett.131.050601.

[NC10] Michael A. Nielsen and Isaac L. Chuang. *Quantum Computation and Quantum Information*. Cambridge University Press, 2010. URL: https://www.cambridge.org/core/books/quantum-computation-and-quantum-information/01E10196D0A682A6AEFI

[Cav81] C. Caves. "Quantum-mechanical noise in an interferometer". In: *Phys. Rev. D* 23 (8 Apr. 1981), pp. 1693–1708. DOI: 10.1103/PhysRevD.23.1693. URL: https://link.aps.org/doi/10.1103/PhysRevD.23.1693.

[Aas+13] J. Aasi et al. "Enhanced sensitivity of the LIGO gravitational wave detector by using squeezed states of light". In: *Nature Photonics* 7.8 (July 2013), pp. 613–619. ISSN: 1749-4893. DOI: 10.1038/nphoton.2013.177. URL: http://dx.doi.org/10.1038/nphoton.2013.177.

[Liu+21] Yuan Liu, Jasmine Sinanan-Singh, Matthew T. Kearney, Gabriel Mintzer, and Isaac L. Chuang. "Constructing qudits from infinite-dimensional oscillators by coupling to qubits". In: *Phys. Rev. A* 104 (3 Sept. 2021), p. 032605. DOI: 10.1103/PhysRevA.104.032605. URL: https://link.aps.org/doi/10.1103/PhysRevA.104.032605.

[JC63] E.T. Jaynes and F.W. Cummings. "Comparison of quantum and semiclassical radiation theories with application to the beam maser". In: *Proceedings of the IEEE* 51.1 (1963), pp. 89–109. DOI: 10.1109/PROC.1963.1664.

[TV02] Carmen M. Tesch and Regina de Vivie-Riedle. "Quantum computation with vibrationally excited molecules". In: *Phys. Rev. Lett.* 89.15 (2002), p. 157901. URL: https://journals.aps.org/prl/abstract/10.1103/PhysRevLett.89.157901.

[AM76] Neil W. Ashcroft and Nathaniel David Mermin. *Solid state physics*. 1st ed. Thomson Learning, 1976.

[BGO20] Alexandre Blais, Steven M. Girvin, and William D. Oliver. "Quantum information processing and quantum optics with circuit quantum electrodynamics". In: *Nature Phys.* 16.3 (2020), pp. 247–256. URL: https://www.nature.com/articles/s41567-020-0806-z.

[CLY97] Isaac L. Chuang, Debbie W. Leung, and Yoshihisa Yamamoto. "Bosonic quantum codes for amplitude damping". In: *Phys. Rev. A* 56.2 (1997), p. 1114. URL: https://journals.aps.org/pra/abstract/10.1103/PhysRevA.56.1114.

[CMM99] Paul T. Cochrane, Gerard J. Milburn, and William J. Munro. "Macroscopically distinct quantum-superposition states as a bosonic code for amplitude damping". In: *Phys. Rev. A* 59.4 (1999), p. 2631. URL: https://journals.aps.org/pra/abstract/10.1103/PhysRevA.59.2631.

[Mic+16] Marios H. Michael, Matti Silveri, R. T. Brierley, Victor V. Albert, Juha Salmilehto, Liang Jiang, and Steven M. Girvin. "New class of quantum error-correcting codes for a bosonic mode". In: *Phys. Rev. X* 6.3 (2016), p. 031006. URL: https://journals.aps.org/prx/abstract/10.1103/PhysRevX.6.031006.

[NCS18b] Murphy Yuezhen Niu, Isaac L. Chuang, and Jeffrey H. Shapiro. "Hardware-efficient bosonic quantum error-correcting codes based on symmetry operators". In: *Phys. Rev. A* 97.3 (2018), p. 032323. URL: https://journals.aps.org/pra/abstract/10.1103/PhysRevA.97.032323.

[Alb+18] Victor V. Albert, Kyungjoo Noh, Kasper Duivenvoorden, Dylan J. Young, R. T. Brierley, Philip Reinhold, Christophe Vuillot, Linshu Li, Chao Shen, S. M. Girvin, et al. "Performance and structure of single-mode bosonic codes". In: *Phys. Rev. A* 97.3 (2018), p. 032346. URL: https://journals.aps.org/pra/abstract/10.1103/PhysRevA.97.032346.

[NGJ20] Kyungjoo Noh, S. M. Girvin, and Liang Jiang. "Encoding an oscillator into many oscillators". In: *Phys. Rev. Lett.* 125.8 (2020), p. 080503. URL: https://journals.aps.org/prl/abstract/10.1103/PhysRevLett.125.080503.

[Got99] Daniel Gottesman. "Fault-Tolerant Quantum Computation with Higher-Dimensional Systems". In: *Chaos Solitons and Fractals* 10.10 (1999), pp. 1749–1758. URL: https://www.sciencedirect.com/science/article/abs/pii/S0960077998002185.

[Zho+03] D. L. Zhou, B. Zeng, Z. Xu, and C. P. Sun. "Quantum computation based on d-level cluster state". In: *Phys. Rev. A* 68.6 (2003), p. 062303. URL: https://journals.aps.org/pra/abstract/10.1103/PhysRevA.68.062303.

[BV05] Samuel L. Braunstein and Peter Van Loock. "Quantum information with continuous variables". In: *Rev. Mod. Phys.* 77.2 (2005), p. 513. URL: https://journals.aps.org/rmp/abstract/10.1103/RevModPhys.77.513.

[Pir+06] Stefano Pirandola, Stefano Mancini, David Vitali, and Paolo Tombesi. "Continuous variable encoding by ponderomotive interaction". In: *The European Phys. Journal D - Atomic, Molecular, Optical and Plasma Phys.* 37.2 (2006), pp. 283–290. URL: https://link.springer.com/article/10.1140/epjd/e2005-00306-3.

[Mot+17] Keith R. Motes, Ben Q. Baragiola, Alexei Gilchrist, and Nicolas C. Menicucci. "Encoding qubits into oscillators with atomic ensembles and squeezed light". In: *Phys. Rev. A* 95.5 (2017), p. 053819. URL: https://journals.aps.org/pra/abstract/10.1103/PhysRevA.95.053819.

[Flü+19] Christa Flühmann, Thanh Long Nguyen, Matteo Marinelli, Vlad Negnevitsky, Karan Mehta, and J. P. Home. "Encoding a qubit in a trapped-ion mechanical oscillator". In: *Nature* 566.7745 (2019), pp. 513–517. URL: https://www.nature.com/articles/s41586-019-0960-6.

[Ofe+16] Nissim Ofek, Andrei Petrenko, Reinier Heeres, Philip Reinhold, Zaki Leghtas, Brian Vlastakis, Yehan Liu, Luigi Frunzio, S. M. Girvin, Liang Jiang, et al. "Extending the lifetime of a quantum bit with error correction in superconducting circuits". In: *Nature* 536.7617 (2016), pp. 441–445. URL: https://www.nature.com/articles/nature18949.

[Has+21] Jacob Hastrup, Kimin Park, Jonatan Bohr Brask, Radim Filip, and Ulrik Lund Andersen. "Universal unitary transfer of continuous-variable quantum states into a few qubits". In: *arXiv preprint arXiv:2106.12272* (2021). URL: https://arxiv.org/abs/2106.12272.

[SK93] Bruce W. Shore and Peter L. Knight. "The Jaynes-Cummings model". In: *Journal of Modern Optics* 40.7 (1993), pp. 1195–1238. URL: https://www.tandfonline.com/doi/abs/10.1080/09500349314551321.

[LE96] Chi K. Law and Joseph H. Eberly. "Arbitrary control of a quantum electromagnetic field". In: *Phys. Rev. Lett.* 76.7 (1996), p. 1055. URL: https://journals.aps.org/prl/abstract/10.1103/PhysRevLett.76.1055.

[MM13] Brian Mischuck and Klaus Mølmer. "Qudit quantum computation in the Jaynes-Cummings model". In: *Phys. Rev. A* 87 (2 Feb. 2013), p. 022341. DOI: 10.1103/PhysRevA.87.022341. URL: https://link.aps.org/doi/10.1103/PhysRevA.87.022341.

[Str12] Frederick W. Strauch. "All-resonant control of superconducting resonators". In: *Phys. Rev. Lett.* 109.21 (2012), p. 210501. URL: https://journals.aps.org/prl/abstract/10.1103/PhysRevLett.109.210501.

[San05] Marcelo França Santos. "Universal and deterministic manipulation of the quantum state of harmonic oscillators: a route to unitary gates for Fock State qubits". In: *Phys. Rev. Lett.* 95.1 (2005), p. 010504. URL: https://journals.aps.org/prl/abstract/10.1103/PhysRevLett.95.010504.

[Kra+15] Stefan Krastanov, Victor V. Albert, Chao Shen, Chang-Ling Zou, Reinier W. Heeres, Brian Vlastakis, Robert J. Schoelkopf, and Liang Jiang. "Universal control of an oscillator with dispersive coupling to a qubit". In: *Phys. Rev. A* 92 (4 Oct. 2015), p. 040303. DOI: 10.1103/PhysRevA.92.040303. URL: https://link.aps.org/doi/10.1103/PhysRevA.92.040303.

[CC00] Andrew M. Childs and Isaac L. Chuang. "Universal quantum computation with two-level trapped ions". In: *Phys. Rev. A* 63.1 (2000), p. 012306. URL: https://journals.aps.org/pra/abstract/10.1103/PhysRevA.63.012306.

[Gul+03] Stephan Gulde, Mark Riebe, Gavin P. T. Lancaster, Christoph Becher, Jürgen Eschner, Hartmut Häffner, Ferdinand Schmidt-Kaler, Isaac L. Chuang, and Rainer Blatt. "Implementation of the Deutsch–Jozsa algorithm on an ion-trap quantum computer". In: *Nature* 421.6918 (2003), pp. 48–50. URL: https://www.nature.com/articles/nature01336?free=2.

[Sch+03] F. Schmidt-Kaler, H. Häffner, S. Gulde, M. Riebe, G. P. T. Lancaster, T. Deuschle, C. Becher, W. Hänsel, J. Eschner, C. F. Roos, et al. "How to realize a universal quantum gate with trapped ions". In: *Appl. Phys. B* 77.8 (2003), pp. 789–796. URL: https://link.springer.com/article/10.1007/s00340-003-1346-9.

[VC05] Lieven M. K. Vandersypen and Isaac L. Chuang. "NMR techniques for quantum control and computation". In: *Rev. Mod. Phys.* 76.4 (2005), p. 1037. URL: https://journals.aps.org/rmp/abstract/10.1103/RevModPhys.76.1037.

[PK06] Brent Pryor and Navin Khaneja. "Fourier decompositions and pulse sequence design algorithms for nuclear magnetic resonance in inhomogeneous fields". In: *The Journal of Chem. Phys.* 125.19 (2006), p. 194111. URL: https://aip.scitation.org/doi/abs/10.1063/1.2390715.

[GS20] Aaron Z. Goldberg and Aephraim M. Steinberg. "Transcoherent states: Optical states for maximal generation of atomic coherence". In: *PRX Quantum* 1.2 (2020), p. 020306. URL: https://link.aps.org/doi/10.1103/PRXQuantum.1.020306.

[BOB05] Gavin K. Brennen, Dianne P. O'Leary, and Stephen S. Bullock. "Criteria for exact qudit universality". In: *Phys. Rev. A* 71.5 (2005), p. 052318. URL: https://journals.aps.org/pra/abstract/10.1103/PhysRevA.71.052318.

[BK08] Reinhold A. Bertlmann and Philipp Krammer. "Bloch vectors for qudits". In: *Journal of Phys. A: Mathematical and Theoretical* 41.23 (2008), p. 235303. URL: https://iopscience.iop.org/article/10.1088/1751-8113/41/23/235303/meta.

[Min21] G. Mintzer. *qo-qudit*. https://github.com/mitquanta/qo-qudit. 2021.

[LCW98] Daniel A. Lidar, Isaac L. Chuang, and K. Birgitta Whaley. "Decoherence-free subspaces for quantum computation". In: *Phys. Rev. Lett.* 81.12 (1998), p. 2594. URL: https://journals.aps.org/prl/abstract/10.1103/PhysRevLett.81.2594.

[Sin+23] Jasmine Sinanan-Singh, Gabriel L. Mintzer, Isaac L. Chuang, and Yuan Liu. *Single-shot Quantum Signal Processing Interferometry*. 2023. arXiv: 2311.13703 [quant-ph].

[CC16] LIGO Scientific Collaboration and Virgo Collaboration. "Observation of Gravitational Waves from a Binary Black Hole Merger". In: *Phys. Rev. Lett.* 116 (6 Feb. 2016), p. 061102. DOI: 10.1103/PhysRevLett.116.061102. URL: https://link.aps.org/doi/10.1103/PhysRevLett.116.061102.

[Bot+22] Tobias Bothwell, Colin J. Kennedy, Alexander Aeppli, Dhruv Kedar, John M. Robinson, Eric Oelker, Alexander Staron, and Jun Ye. "Resolving the gravitational redshift across a millimetre-scale atomic sample". In: *Nature* 602.7897 (2022), pp. 420–424.

[Rou+23] Tanya S. Roussy, Luke Caldwell, Trevor Wright, William B. Cairncross, Yuval Shagam, Kia Boon Ng, Noah Schlossberger, Sun Yool Park, Anzhou Wang, Jun Ye, et al. "An improved bound on the electron's electric dipole moment". In: *Science* 381.6653 (2023), pp. 46–50.

[GLM04] Vittorio Giovannetti, Seth Lloyd, and Lorenzo Maccone. "Quantum-Enhanced Measurements: Beating the Standard Quantum Limit". In: *Science* 306.5700 (2004), pp. 1330–1336. DOI: 10.1126/science.1104149. eprint: https://www.science.org/doi/pdf/10.1126/science.1104149. URL: https://www.science.org/doi/abs/10.1126/science.1104149.

[Boi+08] Sergio Boixo, Animesh Datta, Matthew J. Davis, Steven T. Flammia, Anil Shaji, and Carlton M. Caves. "Quantum Metrology: Dynamics versus Entanglement". In: *Phys. Rev. Lett.* 101 (4 July 2008), p. 040403. DOI: 10.1103/PhysRevLett.101.040403. URL: https://link.aps.org/doi/10.1103/PhysRevLett.101.040403.

[Til+10] Todd Tilma, Shinichiro Hamaji, W. J. Munro, and Kae Nemoto. "Entanglement is not a critical resource for quantum metrology". en. In: *Phys. Rev. A* 81.2 (Feb. 2010), p. 022108. ISSN: 1050-2947, 1094-1622. DOI: 10.1103/PhysRevA.81.022108. URL: https://link.aps.org/doi/10.1103/PhysRevA.81.022108 (visited on 01/31/2023).

[Bra+18] Daniel Braun, Gerardo Adesso, Fabio Benatti, Roberto Floreanini, Ugo Marzolino, Morgan W. Mitchell, and Stefano Pirandola. "Quantum-enhanced measurements without entanglement". en. In: *Rev. Mod. Phys.* 90.3 (Sept. 2018), p. 035006. ISSN: 0034-6861, 1539-0756. DOI: 10.1103/RevModPhys.90.035006. URL: https://link.aps.org/doi/10.1103/RevModPhys.90.035006 (visited on 01/30/2023).

[BW00] D. W. Berry and H. M. Wiseman. "Optimal States and Almost Optimal Adaptive Measurements for Quantum Interferometry". In: *Phys. Rev. Lett.* 85.24 (Dec. 2000), pp. 5098–5101. ISSN: 1079-7114. DOI: 10.1103/physrevlett.85.5098. URL: http://dx.doi.org/10.1103/PhysRevLett.85.5098.

[Gór+20] Wojciech Górecki, Rafał Demkowicz-Dobrzański, Howard M. Wiseman, and Dominic W. Berry. "π-Corrected Heisenberg Limit". In: *Phys. Rev. Lett.* 124.3 (Jan. 2020). ISSN: 1079-7114. DOI: 10.1103/physrevlett.124.030501. URL: http://dx.doi.org/10.1103/PhysRevLett.124.030501.

[Mar+22] Christian D. Marciniak, Thomas Feldker, Ivan Pogorelov, Raphael Kaubruegger, Denis V. Vasilyev, Rick van Bijnen, Philipp Schindler, Peter Zoller, Rainer Blatt, and Thomas Monz. "Optimal metrology with programmable quantum sensors". en. In: *Nature* 603.7902 (Mar. 2022). Number: 7902 Publisher: Nature Publishing Group, pp. 604–609. ISSN: 1476-4687. DOI: 10.1038/s41586-022-04435-4. URL: https://www.nature.com/articles/s41586-022-04435-4 (visited on 01/30/2023).

[Bol+96] J. J . Bollinger, Wayne M. Itano, D. J. Wineland, and D. J. Heinzen. "Optimal frequency measurements with maximally correlated states". In: *Phys. Rev. A* 54 (6 Dec. 1996), pp. 4649–4652. DOI: 10.1103/PhysRevA.54.R4649. URL: https://journals.aps.org/pra/pdf/10.1103/PhysRevA.54.R4649.

[Ram50] Norman F. Ramsey. "A Molecular Beam Resonance Method with Separated Oscillating Fields". In: *Phys. Rev. (U.S.) Superseded in part by Phys. Rev. A, Phys. Rev. B: Solid State, Phys. Rev. C, and Phys. Rev. D* 78.6 (1950), pp. 695–699. ISSN: 0031-899X.

[Kau+21] Raphael Kaubruegger, Denis V. Vasilyev, Marius Schulte, Klemens Hammerer, and Peter Zoller. "Quantum Variational Optimization of Ramsey Interferometry and Atomic Clocks". In: *Phys. Rev. X* 11.4 (Dec. 2021). DOI: 10.1103/physrevx.11.041045. URL: https://doi.org/10.1103%2Fphysrevx.11.041045.

[Des+23] Eloi Descamps, Nicolas Fabre, Arne Keller, and Perola Milman. *Quantum metrology using time-frequency as quantum continuous variables: sub shot-noise precision and phase space representation.* en. arXiv:2210.05511 [quant-ph]. Jan. 2023. URL: http://arxiv.org/abs/2210.05511 (visited on 01/30/2023).

[Pen+16] M. Penasa, S. Gerlich, T. Rybarczyk, V. Métillon, M. Brune, J. M. Raimond, S. Haroche, L. Davidovich, and I. Dotsenko. "Measurement of a microwave field amplitude beyond the standard quantum limit". In: *Phys. Rev. A* 94 (2 Aug. 2016), p. 022313. DOI: 10.1103/PhysRevA.94.022313. URL: https://link.aps.org/doi/10.1103/PhysRevA.94.022313.

[DTW17] Kasper Duivenvoorden, Barbara M. Terhal, and Daniel Weigand. "Single-mode displacement sensor". en. In: *Phys. Rev. A* 95.1 (Jan. 2017), p. 012305. ISSN: 2469-9926, 2469-9934. DOI: 10.1103/PhysRevA.95.012305. URL: https://link.aps.org/doi/10.1103/PhysRevA.95.012305 (visited on 01/30/2023).

[Gil+21] Kevin A. Gilmore, Matthew Affolter, Robert J. Lewis-Swan, Diego Barberena, Elena Jordan, Ana Maria Rey, and John J. Bollinger. "Quantum-enhanced sensing of displacements and electric fields with two-dimensional trapped-ion crystals". In: *Science* 373.6555 (2021), pp. 673–678.

[Tse+19] M. Tse, Haocun Yu, N. Kijbunchoo, A. Fernandez-Galiana, P. Dupej, L. Barsotti, C. D. Blair, D. D. Brown, S. E. Dwyer, A. Effler, et al. "Quantum-Enhanced Advanced LIGO Detectors in the Era of Gravitational-Wave Astronomy". In: *Phys. Rev. Lett.* 123 (23 Dec. 2019), p. 231107. URL: https://link.aps.org/doi/10.1103/PhysRevLett.123.231107.

[Dar+18] Shakib Daryanoosh, Sergei Slussarenko, Dominic W. Berry, Howard M. Wiseman, and Geoff J. Pryde. "Experimental optical phase measurement approaching the exact Heisenberg limit". In: *Nature Comm.* 9.1 (Nov. 2018). ISSN: 2041-1723. DOI: 10.1038/s41467-018-06601-7. URL: http://dx.doi.org/10.1038/s41467-018-06601-7.

[Wan+19] W. Wang et al. "Heisenberg-limited single-mode quantum metrology in a superconducting circuit". In: *Nature Comm.* 10.1 (Sept. 2019). ISSN: 2041-1723. DOI: 10.1038/s41467-019-12290-7. URL: http://dx.doi.org/10.1038/s41467-019-12290-7.

[Gie22] Karol Gietka. "Harnessing center-of-mass excitations in quantum metrology". In: *Phys. Rev. Res.* 4.4 (2022), p. 043074.

[Kir+11] M. Kira, S. W. Koch, R. P. Smith, A. E. Hunter, and S. T. Cundiff. "Quantum spectroscopy with Schrödinger-cat states". In: *Nature Phys.* 7 (Sept. 2011), pp. 799–804. DOI: 10.1038/NPHYS2091. URL: https://www.nature.com/articles/nphys2091.

[ZZS18] Quntao Zhuang, Zheshen Zhang, and Jeffrey H. Shapiro. "Distributed quantum sensing using continuous-variable multipartite entanglement". en. In: *Phys. Rev. A* 97.3 (Mar. 2018), p. 032329. ISSN: 2469-9926, 2469-9934. DOI: 10.1103/PhysRevA.97.032329. URL: https://link.aps.org/doi/10.1103/PhysRevA.97.032329 (visited on 01/30/2023).

[Kwo+22] Hyukgun Kwon, Youngrong Lim, Liang Jiang, Hyunseok Jeong, and Changhun Oh. "Quantum Metrological Power of Continuous-Variable Quantum Networks". In: *Phys. Rev. Lett.* 128 (18 May 2022), p. 180503. DOI: 10.1103/PhysRevLett.128.180503. URL: https://link.aps.org/doi/10.1103/PhysRevLett.128.180503.

[Li+23] Haoya Li, Yu Tong, Hongkang Ni, Tuvia Gefen, and Lexing Ying. "Heisenberg limited Hamiltonian learning for interacting bosons". In: *arXiv preprint arXiv:2307.04690* (2023). URL: https://arxiv.org/abs/2307.04690.

[Hua+23] Hsin-Yuan Huang, Yu Tong, Di Fang, and Yuan Su. "Learning Many-Body Hamiltonians with Heisenberg-Limited Scaling". In: *Phys. Rev. Lett.* 130 (20 May 2023), p. 200403. DOI: 10.1103/PhysRevLett.130.200403. URL: https://link.aps.org/doi/10.1103/PhysRevLett.130.200403.

[DGN22] Yulong Dong, Jonathan Gross, and Murphy Yuezhen Niu. "Beyond Heisenberg Limit Quantum Metrology through Quantum Signal Processing". In: *arXiv preprint arXiv:2209.11207* (2022). URL: https://arxiv.org/abs/2209.11207.

[Zho+18] Sisi Zhou, Mengzhen Zhang, John Preskill, and Liang Jiang. "Achieving the Heisenberg limit in quantum metrology using quantum error correction". In: *Nature Comm.* 9.1 (2018), p. 78.

[Sug+23] Sho Sugiura, Arkopal Dutt, William J. Munro, Sina Zeytinoğlu, and Isaac L. Chuang. "Power of sequential protocols in hidden quantum channel discrimination". In: *arXiv preprint arXiv:2304.02053* (2023).

[RC21] Zane M. Rossi and Isaac L. Chuang. "Quantum hypothesis testing with group structure". In: *Phys. Rev. A* 104 (1 July 2021), p. 012425. DOI: 10.1103/PhysRevA.104.012425. URL: https://link.aps.org/doi/10.1103/PhysRevA.104.012425.

[Ros+22] Zane M. Rossi, Jeffery Yu, Isaac L. Chuang, and Sho Sugiura. "Quantum advantage for noisy channel discrimination". In: *Phys. Rev. A* 105 (3 Mar. 2022), p. 032401. DOI: 10.1103/PhysRevA.105.032401. URL: https://link.aps.org/doi/10.1103/PhysRevA.105.032401.

[ZZ19] Quntao Zhuang and Zheshen Zhang. "Physical-Layer Supervised Learning Assisted by an Entangled Sensor Network". In: *Phys. Rev. X* 9 (4 Oct. 2019), p. 041023. DOI: 10.1103/PhysRevX.9.041023. URL: https://link.aps.org/doi/10.1103/PhysRevX.9.041023.

[Xia+21] Yi Xia, Wei Li, Quntao Zhuang, and Zheshen Zhang. "Quantum-Enhanced Data Classification with a Variational Entangled Sensor Network". In: *Phys. Rev. X* 11 (2 June 2021), p. 021047. DOI: 10.1103/PhysRevX.11.021047. URL: https://link.aps.org/doi/10.1103/PhysRevX.11.021047.

[Mey+23] Johannes Jakob Meyer, Sumeet Khatri, Daniel Stilck França, Jens Eisert, and Philippe Faist. "Quantum metrology in the finite-sample regime". In: *arXiv preprint arXiv:2307.06370* (2023). URL: https://arxiv.org/abs/2307.06370.

[Tan+08] Si-Hui Tan, Baris I. Erkmen, Vittorio Giovannetti, Saikat Guha, Seth Lloyd, Lorenzo Maccone, Stefano Pirandola, and Jeffrey H. Shapiro. "Quantum Illumination with Gaussian States". In: *Phys. Rev. Lett.* 101 (25 Dec. 2008), p. 253601. DOI: 10.1103/PhysRevLett.101.253601. URL: https://link.aps.org/doi/10.1103/PhysRevLett.101.253601.

[Pir+19] Stefano Pirandolo, Riccardo Laurenza, Cosmo Lupo, and Jason L. Pereira. "Fundamental limits to quantum channel discrimination". In: *npj Quantum Info.* 5 (50 2019).

[OS10] Alan V. Oppenheim and Ronald W. Schafer. *Discrete-time signal processing*. 3rd ed. Prentice Hall signal processing series. Pearson, 2010.

[PM72] T. Parks and James McClellan. "Chebyshev approximation for nonrecursive digital filters with linear phase". In: *IEEE Transactions on Circuit Theory* 19.2 (1972), pp. 189–194.

[Ant18] Andreas Antoniou. *Digital filters: analysis, design, and signal processing applications*. McGraw-Hill Education, 2018.

[LYC16] Guang Hao Low, Theodore J. Yoder, and Isaac L. Chuang. "Methodology of resonant equiangular composite quantum gates". In: *Phys. Rev. X* 6.4 (2016), p. 041067. URL: https://journals.aps.org/prx/abstract/10.1103/PhysRevX.6.041067.

[LC19] Guang Hao Low and Isaac L. Chuang. "Hamiltonian simulation by qubitization". In: *Quantum* 3 (2019), p. 163. URL: https://quantum-journal.org/papers/q-2019-07-12-163/.

[Kik+23] Yuta Kikuchi, Conor Mc Keever, Luuk Coopmans, Michael Lubasch, and Marcello Benedetti. "Realization of quantum signal processing on a noisy quantum computer". In: *npj Quantum Info.* 9.1 (2023), p. 93.

[RC22] Zane M. Rossi and Isaac L. Chuang. "Multivariable quantum signal processing (M-QSP): prophecies of the two-headed oracle". In: *Quantum* 6 (2022), p. 811. URL: https://quantum-journal.org/papers/q-2022-09-20-811/.

[Don+22] Yulong Dong, Lin Lin, Hongkang Ni, and Jiasu Wang. "Infinite quantum signal processing". In: *arXiv preprint arXiv:2209.10162* (2022).

[Ros+23] Zane M. Rossi, Victor M. Bastidas, William J. Munro, and Isaac L. Chuang. "Quantum signal processing with continuous variables". In: *arXiv preprint arXiv:2304.14383* (2023).

[MW23] Danial Motlagh and Nathan Wiebe. "Generalized quantum signal processing". In: *arXiv preprint arXiv:2308.01501* (2023).

[Lan23] Lorenzo Laneve. "Quantum signal processing over SU (N): exponential speed-up for polynomial transformations under Shor-like assumptions". In: *arXiv preprint arXiv:2311.03949* (2023).

[RCC23] Zane M. Rossi, Jack L. Ceroni, and Isaac L. Chuang. "Modular quantum signal processing in many variables". In: *arXiv preprint arXiv:2309.16665* (2023).

[Mar+23] John M. Martyn, Yuan Liu, Zachary E. Chin, and Isaac L. Chuang. "Efficient fully-coherent quantum signal processing algorithms for real-time dynamics simulation". In: *The Journal of Chem. Phys.* 158.2 (2023).

[WDL22] Jiasu Wang, Yulong Dong, and Lin Lin. "On the energy landscape of symmetric quantum signal processing". In: *Quantum* 6 (2022), p. 850.

[Mar+21] John M. Martyn, Zane M. Rossi, Andrew K. Tan, and Isaac L. Chuang. "Grand unification of quantum algorithms". In: *PRX Quantum* 2.4 (2021), p. 040203. URL: https://journals.aps.org/prxquantum/abstract/10.1103/PRXQuantum.2.040203.

[Yu+22] Zhan Yu, Hongshun Yao, Mujin Li, and Xin Wang. "Power and limitations of single-qubit native quantum neural networks". In: *Advances in Neural Info. Proc. Sys.* 35 (2022), pp. 27810–27823.

[Hal+05] P. C. Haljan, K.-A. Brickman, L. Deslauriers, P. J. Lee, and C. Monroe. "Spin-Dependent Forces on Trapped Ions for Phase-Stable Quantum Gates and Entangled States of Spin and Motion". In: *Phys. Rev. Lett.* 94 (15 Apr. 2005), p. 153602. DOI: 10.1103/PhysRevLett.94.153602. URL: https://link.aps.org/doi/10.1103/PhysRevLett.94.153602.

[Eic+22] Alec Eickbusch, Volodymyr Sivak, Andy Z. Ding, Salvatore S. Elder, Shantanu R. Jha, Jayameenakshi Venkatraman, Baptiste Royer, Steven M. Girvin, Robert J. Schoelkopf, and Michel H. Devoret. "Fast universal control of an oscillator with weak dispersive coupling to a qubit". In: *Nature Phys.* 18.12 (2022), pp. 1464–1469. URL: https://www.nature.com/articles/s41567-022-01776-9.

[Hel69] Carl W. Helstrom. "Quantum detection and estimation theory". In: *Journal of Stat. Phys.* 1 (1969), pp. 231–252. URL: https://link.springer.com/article/10.1007/BF01007479.

[Yan21] Sung-Moon Michael Yang. *Modern Digital Radio Communication Signals and Systems*. 2nd ed. Springer, 2021.

[CW12] Andrew M. Childs and Nathan Wiebe. "Hamiltonian simulation using linear combinations of unitary operations". In: *Quantum Info. & Comp.* 12.11-12 (2012), pp. 901–924.

[Ber+15] Dominic W. Berry, Andrew M. Childs, Richard Cleve, Robin Kothari, and Rolando D. Somma. "Simulating Hamiltonian Dynamics with a Truncated Taylor Series". In: *Phys. Rev. Lett.* 114.9 (Mar. 2015). ISSN: 1079-7114. URL: http://dx.doi.org/10.1103/PhysRevLett.114.090502.

[Haa19] Jeongwan Haah. "Product Decomposition of Periodic Functions in Quantum Signal Processing". en. In: *Quantum* 3 (Oct. 2019). arXiv:1806.10236 [quant-ph], p. 190. ISSN: 2521-327X. DOI: 10.22331/q-2019-10-07-190. URL: http://arxiv.org/abs/1806.10236 (visited on 01/03/2023).

[Bla+04] Alexandre Blais, Ren-Shou Huang, Andreas Wallraff, S. M. Girvin, and R. J. Schoelkopf. "Cavity quantum electrodynamics for superconducting electrical circuits: An architecture for quantum computation". In: *Phys. Rev. A* 69 (6 June 2004), p. 062320. DOI: 10.1103/PhysRevA.69.062320. URL: https://link.aps.org/doi/10.1103/PhysRevA.69.062320.

[Mon+96] Christopher Monroe, Dawn M. Meekhof, Brian E. King, and David J. Wineland. "A "Schrödinger cat" superposition state of an atom". In: *Science* 272.5265 (1996), pp. 1131–1136.

[GW04] Jeffrey S. Geronimo and Hugo J. Woerdeman. "Positive extensions, Fejér-Riesz factorization and autoregressive filters in two variables". In: *Annals of Math.* (2004), pp. 839–906. URL: https://www.jstor.org/stable/3597329.

[Cha+20] Rui Chao, Dawei Ding, Andras Gilyen, Cupjin Huang, and Mario Szegedy. *Finding Angles for Quantum Signal Processing with Machine Precision*. en. arXiv:2003.02831 [quant-ph]. Mar. 2020. URL: http://arxiv.org/abs/2003.02831 (visited on 01/08/2023).

[MLS23] G. Mintzer, Y. Liu, and J. Sinanan-Singh. *Quantum Signal Processing Interferometry*. https://github.com/yuanliu1/QSP-Interferometry. 2023.

[KV16] Yigit Cagatay Kuyu and Fahri Vatansever. "A new intelligent decision making system combining classical methods, evolutionary algorithms and statistical techniques for optimal digital FIR filter design and their performance evaluation". In: *AEU-Intl. Journal of Electronics and Comm.* 70.12 (2016), pp. 1651–1666.

[Pek34] C. L. Pekeris. "The Rotation-Vibration Coupling in Diatomic Molecules". In: *Phys. Rev.* 45 (2 Jan. 1934), pp. 98–103. DOI: 10.1103/PhysRev.45.98. URL: https://link.aps.org/doi/10.1103/PhysRev.45.98.

[Rib+18] Raphael F. Ribeiro, Luis A. Martínez-Martínez, Matthew Du, Jorge Campos-Gonzalez-Angulo, and Joel Yuen-Zhou. "Polariton chemistry: controlling molecular dynamics with optical cavities". In: *Chem. Sci.* 9.30 (2018), pp. 6325–6339.

[Xio23] Wei Xiong. "Molecular Vibrational Polariton Dynamics: What Can Polaritons Do?" In: *Accounts of Chem. Res.* 56.7 (2023), pp. 776–786.

[Xu+23a] Han Xu, Benran Wang, Haidong Yuan, and Xin Wang. "Quantum hypothesis testing via robust quantum control". In: *arXiv preprint arXiv:2309.05592* (2023).

[Bra+23] Anthony J. Brady, Alec Eickbusch, Shraddha Singh, Jing Wu, and Quntao Zhuang. "Advances in Bosonic Quantum Error Correction with Gottesman-Kitaev-Preskill Codes: Theory, Engineering and Applications". In: *arXiv preprint arXiv:2308.02913* (2023).

[DJK15] Rafal Demkowicz-Dobrzański, Marcin Jarzyna, and Jan Kołodyński. "Quantum limits in optical interferometry". In: *Progress in Optics* 60 (2015), pp. 345–435.

[EMD11] B. M. Escher, Ruynet Lima de Matos Filho, and Luiz Davidovich. "General framework for estimating the ultimate precision limit in noisy quantum-enhanced metrology". In: *Nature Phys.* 7.5 (2011), pp. 406–411.

[DKG12] Rafał Demkowicz-Dobrzański, Jan Kołodyński, and Mădălin Guţă. "The elusive Heisenberg limit in quantum-enhanced metrology". In: *Nature Comm.* 3.1 (2012), p. 1063.

[Zho+19] Sisi Zhou, David Layden, Mengzhen Zhang, John Preskill, Paola Cappellaro, and Liang Jiang. "Error-corrected quantum sensing". In: *Optical, Opto-Atomic, and Entanglement-Enhanced Precision Metrology*. Vol. 10934. SPIE. 2019, pp. 148–161.

[Liu+24] Y. Liu, J. M. Martyn, J. Sinanan-Singh, S. Singh, S. M. Girvin, and I. L. Chuang. "Toward Mixed Analog-Digital Quantum Signal Processing: Quantum AD/DA Conversion and the Fourier Transform". In: *In preparation* (2024).

[Die82] D. Dieks. "Communication by EPR devices". In: *Phys. Lett. A* 92.6 (1982), pp. 271–272. ISSN: 0375-9601. DOI: https://doi.org/10.1016/0375-9601(82)90084-6. URL: https://www.sciencedirect.com/science/article/pii/0375960182900846.

[Par70] James L. Park. "The concept of transition in quantum mechanics". In: *Foundations of Phys.* 1.1 (Mar. 1, 1970), pp. 23–33. DOI: 10.1007/BF00708652. URL: https://doi.org/10.1007/BF00708652.

[WZ82] W. K. Wootters and W. H. Zurek. "A single quantum cannot be cloned". In: *Nature* 299.5886 (Oct. 1, 1982), pp. 802–803. DOI: 10.1038/299802a0. URL: https://doi.org/10.1038/299802a0.

[Sho95] Peter W. Shor. "Scheme for reducing decoherence in quantum computer memory". In: *Phys. Rev. A* 52 (4 Oct. 1995), R2493–R2496. DOI: 10.1103/PhysRevA.52.R2493. URL: https://link.aps.org/doi/10.1103/PhysRevA.52.R2493.

[Ste96] A. M. Steane. "Error Correcting Codes in Quantum Theory". In: *Phys. Rev. Lett.* 77 (5 July 1996), pp. 793–797. DOI: 10.1103/PhysRevLett.77.793. URL: https://link.aps.org/doi/10.1103/PhysRevLett.77.793.

[Ben+96] Charles H. Bennett, David P. DiVincenzo, John A. Smolin, and William K. Wootters. "Mixed-state entanglement and quantum error correction". In: *Phys. Rev. A* 54 (5 Nov. 1996), pp. 3824–3851. DOI: 10.1103/PhysRevA.54.3824. URL: https://link.aps.org/doi/10.1103/PhysRevA.54.3824.

[Laf+96] Raymond Laflamme, Cesar Miquel, Juan Pablo Paz, and Wojciech Hubert Zurek. "Perfect Quantum Error Correcting Code". In: *Phys. Rev. Lett.* 77 (1 July 1996), pp. 198–201. DOI: 10.1103/PhysRevLett.77.198. URL: https://link.aps.org/doi/10.1103/PhysRevLett.77.198.

[KL96] Emanuel Knill and Raymond Laflamme. *Concatenated Quantum Codes*. 1996. arXiv: quant-ph/9608012 [quant-ph].

[GCB20] Arne L. Grimsmo, Joshua Combes, and Ben Q. Baragiola. "Quantum Computing with Rotation-Symmetric Bosonic Codes". In: *Phys. Rev. X* 10 (1 Mar. 2020), p. 011058. DOI: 10.1103/PhysRevX.10.011058. URL: https://link.aps.org/doi/10.1103/PhysRevX.10.011058.

[Leg+13] Zaki Leghtas, Gerhard Kirchmair, Brian Vlastakis, Robert J. Schoelkopf, Michel H. Devoret, and Mazyar Mirrahimi. "Hardware-Efficient Autonomous Quantum Memory Protection". In: *Phys. Rev. Lett.* 111 (12 Sept. 2013), p. 120501. DOI: 10.1103/PhysRevLett.111.120501. URL: https://link.aps.org/doi/10.1103/PhysRevLett.111.120501.

[NCB22] Kyungjoo Noh, Christopher Chamberland, and Fernando G.S.L. Brandão. "Low-Overhead Fault-Tolerant Quantum Error Correction with the Surface-GKP Code". In: *PRX Quantum* 3 (1 Jan. 2022), p. 010315. DOI: 10.1103/PRXQuantum.3.010315. URL: https://link.aps.org/doi/10.1103/PRXQuantum.3.010315.

[GP21] Arne L. Grimsmo and Shruti Puri. "Quantum Error Correction with the Gottesman-Kitaev-Preskill Code". In: *PRX Quantum* 2 (2 June 2021), p. 020101. DOI: 10.1103/PRXQuantum.2.020101. URL: https://link.aps.org/doi/10.1103/PRXQuantum.2.020101.

[RSG20] Baptiste Royer, Shraddha Singh, and S. M. Girvin. "Stabilization of Finite-Energy Gottesman-Kitaev-Preskill States". In: *Phys. Rev. Lett.* 125.26 (Dec. 2020). ISSN: 1079-7114. DOI: 10.1103/physrevlett.125.260509. URL: http://dx.doi.org/10.1103/PhysRevLett.125.260509.

[Siv+23] V. V. Sivak et al. "Real-time quantum error correction beyond break-even". In: *Nature* 616.7955 (Apr. 1, 2023), pp. 50–55. DOI: 10.1038/s41586-023-05782-6. URL: https://doi.org/10.1038/s41586-023-05782-6.

[SMS22] David S. Schlegel, Fabrizio Minganti, and Vincenzo Savona. "Quantum error correction using squeezed Schrödinger cat states". In: *Phys. Rev. A* 106 (2 Aug. 2022), p. 022431. DOI: 10.1103/PhysRevA.106.022431. URL: https://link.aps.org/doi/10.1103/PhysRevA.106.022431.

[HQ23] Timo Hillmann and Fernando Quijandría. "Quantum error correction with dissipatively stabilized squeezed-cat qubits". In: *Phys. Rev. A* 107 (3 Mar. 2023), p. 032423. DOI: 10.1103/PhysRevA.107.032423. URL: https://link.aps.org/doi/10.1103/PhysRevA.107.032423.

[Xu+23b] Qian Xu, Guo Zheng, Yu-Xin Wang, Peter Zoller, Aashish A. Clerk, and Liang Jiang. "Autonomous quantum error correction and fault-tolerant quantum computation with squeezed cat qubits". In: *npj Quantum Info.* 9.1 (Aug. 3, 2023), p. 78. DOI: 10.1038/s41534-023-00746-0. URL: https://doi.org/10.1038/s41534-023-00746-0.

[AGP08] Panos Aliferis, Daniel Gottesman, and John Preskill. "Accuracy threshold for postselected quantum computation". In: *Quantum Info. Comp.* 8.3 (Mar. 2008), pp. 181–244. ISSN: 1533-7146.

[VWI09] Frank Verstraete, Michael M. Wolf, and J. Ignacio Cirac. "Quantum computation and quantum-state engineering driven by dissipation". In: *Nature Phys.* 5.9 (Sept. 1, 2009), pp. 633–636. DOI: 10.1038/nphys1342. URL: https://doi.org/10.1038/nphys1342.

[HMM22] Patrick M. Harrington, Erich J. Mueller, and Kater W. Murch. "Engineered dissipation for quantum information science". In: *Nature Rev. Phys.* 4.10 (Aug. 2022), pp. 660–671. ISSN: 2522-5820. DOI: 10.1038/s42254-022-00494-8. URL: http://dx.doi.org/10.1038/s42254-022-00494-8.

[Cam+20] P. Campagne-Ibarcq et al. "Quantum error correction of a qubit encoded in grid states of an oscillator". In: *Nature* 584.7821 (Aug. 2020), pp. 368–372. ISSN: 1476-4687. DOI: 10.1038/s41586-020-2603-3. URL: http://dx.doi.org/10.1038/s41586-020-2603-3.

[End+24] Suguru Endo, Keitaro Anai, Yuichiro Matsuzaki, Yuuki Tokunaga, and Yasunari Suzuki. "Projective squeezing for translation symmetric bosonic codes". In: *arXiv preprint arXiv:2403.14218* (2024).

[Pan+23] Xiaozhou Pan, Jonathan Schwinger, Ni-Ni Huang, Pengtao Song, Weipin Chua, Fumiya Hanamura, Atharv Joshi, Fernando Valadares, Radim Filip, and Yvonne Y. Gao. "Protecting the Quantum Interference of Cat States by Phase-Space Compression". In: *Phys. Rev. X* 13 (2 Apr. 2023), p. 021004. DOI: 10.1103/PhysRevX.13.021004. URL: https://link.aps.org/doi/10.1103/PhysRevX.13.021004.

[HA21] Jacob Hastrup and Ulrik Lund Andersen. "Improved readout of qubit-coupled Gottesman–Kitaev–Preskill states". In: *Quantum Sci. and Tech.* 6.3 (June 2021), p. 035016. ISSN: 2058-9565. DOI: 10.1088/2058-9565/ac070d. URL: http://dx.doi.org/10.1088/2058-9565/ac070d.